CMP (Centre for Microsystems and Photonics)
Department of Electronic and Electrical Engineering
University of Strathclyde

OPTICAL TECHNIQUES FOR EXAMINING MECHANICAL MATERIALS

by

BORJA SORAZU LUCIO

A thesis presented in fulfilment of the requirements for the degree of Doctor of Philosophy and accepted on the recommendation of:

Prof. R. Tatam, *external examiner*
Prof. W. Johnstone, *internal examiner*
Prof. B. Culshaw, *internal examiner* & *supervisor*

November 2006

Declaration

Signature: Date: 22 November 2006

If you cry for the missing Sun,
the tears will not let you see the stars.

John Kare

The world is my homeland,
and science is my religion.

Christian Huygens

Look back during the last year
and tell me, can you remember a smile,
a tear and a new friendship?
Then be sure that this year was worth it.

John Kare

ABSTRACT

Advances in sensors-actuators technology and signal processing are revolutionizing Structural-Health Monitoring and Non-destructive Testing with the integration of sensing-actuating capabilities into the structure.

We demonstrate ultrasonic guided-wave detection capabilities of four optic fibre sensors (OFS) and experimentally address their damage detection and location potential, based on their sensing high directivity. Various signal processing methods that look into perturbations caused over guided-waves propagation characteristics are discussed for damage detection and location applications.

We model the modulation that the acoustic wave pressure field induces over the sensing property of an integrating OFS. The basic trends predicted, for varying sensor length, distant and orientation to the ultrasonic source, are experimentally confirmed. The model characterizes the directivity pattern of these sensors with obvious implications in damage location. We also prove that a polarimetric sensor exhibits similar integration behaviour than an interferometric system.

The unparallel remote inspection capabilities and broadband (spatial and temporal) ultrasonic generation and detection features attainable by combination of laser generation and interferometric detection are demonstrated. An all-optical remote inspection tool for materials is constructed and experimentally applied to aluminium samples. The processing of the detected ultrasonic data by 2D-Fourier transform and reassigned-spectrogram provides high quality and high resolution information of the structurally localized and global dispersion characteristics. This is utilized to demonstrate sensitivity to temperature changes and to illustrate hole-damage detection.

Finally an inversion technique is applied to the broadband dispersion information allowing accurate and repeatable estimation of elastic and geometrical properties of the structure. The technique provides values of Young's modulus (E) 71.0GPa, Poisson's ratio (v) 0.352, and plate thickness (d) 1.16 mm, experimentally validated within an error of 1% for E, and 2% for v and d.

Monitoring the deviation of these values with respect to an undamaged signature can be used as indicator of structural damage or deterioration.

ACKNOWLEDGEMENTS

A PhD is not only the result of the three or four years of experiments and theoretical work that it takes to accomplish it, but the global contribution of one youth dedicated to learn.

The huge number of people who have influenced me during all these years are too many to be able to mention here in two pages, but I must recognize the contribution and influence of those that I remember most.

I start with the first teacher that in school opened my eyes to the beauty and the mystery of science. Constantino Valdivielso, you knew how to amaze us kids. Thank you for using your great influence over our knowledge seeking minds in the best possible way.

During my high school years, I discovered by a fortunate incident the TV series COSMOS by Carl Sagan, it was then when I decided to study, among all the interesting scientific degrees, for the degree of Physics at the University of the Basque Country. I am not the first one to be so enormously influenced by this TV series, and in recognizing Carl Sagan's great mastery in explaining and showing the amazement of science.

At university I learnt so much from so many, please forgive me if I do not mention your names explicitly but be sure I remember you all. My special thanks go to Arias, the Optics lecturer. Your classes were astonishing, not only funny and relaxing but an incredible source of knowledge. It was such an impressive experience to see your delight teaching us the marvellous secrets of Optics that no wonder I chose it as my PhD subject. You have influenced me in so many ways that I could never thank you enough.

During the last years of my university degrees, I had the pleasure of being taught by two of the most friendly lecturers I ever met; Juan Mari Collantes and Joaquin Portilla. Thank you for being so close to the students and most importantly thanks for all your help, your advice and your friendship. If I am writing this thesis today it is mainly because of you.

I cannot forget those incredible friends I met during my university years: Ivan, Agurtzane, Gerardo…thanks for being always there when I needed you most and for not forgetting about me during this period of far relationship. Believe me when I tell you that it is an honour to be able to call you my friends.

The PhD in Glasgow has been, without doubt, the most influential stage of my life so far. I have matured as a person. I have known so many people from so many cultures. I have visited different countries and learned so many things. Glasgow has given me so much; the most wonderful, clever and interesting woman, Dania I love you and this thesis is totally dedicated to you. Some really amazing friends; Nugi, Ardi, Irfan and all PPI…thank you all

for those incredible times we enjoyed together, for letting me taste your magnificent Indonesian culture and food, and for teaching me how to play badminton. Glasgow, you also gave me back my favourite sport: basketball…cheers guys for those incredible games.

A special acknowledgement goes to those who have been my new family in a foreign land- The Optoelectronics Division in the University of Strathclyde.

Brian thanks for giving me the opportunity to work under your supervision. Your guidance and support, but most importantly your friendship, has been invaluable during all these years. Aileen thanks for your warm spirit, your strength and optimism inspired and helped me so many times. Gillian thanks for treating me in such a friendly way and for trusting me from the first day we met. Daniel thanks for sharing your knowledge and the experience of your family with me. I will never forget that week in the Highlands. Yao thanks for all those conversations late in the university and for letting me being part of your marvellous culture. We have had so much fun in those trips around Scotland and the week in Spain. Sofiane thanks for sharing so many of your experiences with me, you taught me more that what you think. Graham and Dong thanks for all your lessons, for your patience with all my questions and for your help both in the lab and personally, this thesis wouldn't have been what it is without you. Atique thanks for walking together the path of mysteries of Lamb waves and signal processing, I am sure all would have been more difficult without you. Kevin thanks for teaching me how to play golf and for all those arguments we had, I cannot imagine how boring the office would have been without you. Andrew you came to the group almost when I was leaving however it seems I know you forever, thanks for your kindness and friendship. Amy thanks for being always there when I most needed to chat, it was a great pleasure to have all those endless conversations about books, cinema, television and origami. It took long to develop our friendship but I must say it was worth it. George it was amazing to ask you questions, you seemed to have an answer for everything. Carol and Sadie thanks for your patience and for your invaluable help. Although I could continue indefinitely I must give a big thanks to Walter, Alistair, Anartz, Joanna, Dorn, Hee Su, Gordon, Colin, Deepak and all of you I met in Strathclyde. Thanks all very much, because of you I almost did not feel homesick, and when I did you were always there to comfort me.

I leave for the end the most important and sincere of all the acknowledgements, my family that have always been there when I most needed them. None of this would have been possible without your support, your advice and your love. Julen and Mikel follow your dreams. Aita and Ama all this is for you and please forgive me for those Christmas times when I was absent, I love you all.

THESIS FUNDING SUPPORT

The four years of research needed to accomplish the work of this thesis would have not been able without the financial support provided by:

- University of Strathclyde for their PhD scholarship funding between 2001/2004.
- Basque Government (Spain) PhD research scholarship 2004/2005 through '*Programa de Formación de Investigadores del Departamento de Educación, Universidades e Investigación*'.

The author would like to thank both institutions for their support.

TABLE OF CONTENTS

ABBREVIATIONS

2D	Two Dimensional
2D-FT	Two Dimensional Fourier Transform
3D	Three Dimensional
A/D	Analogue/Digital
AM	Amplitude Modulated
ANSYS	FE analysis software packet
AOM	Acousto-Optic Modulator
ASCE	American Society of Civil Engineers
CCD	Charged-coupled device camera
CFPI	Con-focal Fabry-Perot Interferometer
CW	Continuous wave laser
DFT	Discrete Fourier Transform
DHS	Downhill simplex algorithm
DLA	Digital linear actuator
DWT	Discrete Wavelet Transform
ECL	External Cavity Laser
EMAT	Electromagnetic Acoustic Transducer
EMI	Electromagnetic Interference
EOM	Electro-Optic Modulator
F	Finesse (of an optical cavity)
FBG	Fibre Bragg Gratings
FE	Finite Elements
FFPI	Fibre Fabry-Perot Interferometer
FFT	Fast Fourier Transform
FPI	Fabry-Perot Interferometer
FSR	Free spectral range
FWHM	Full width half maximum
GRIN	Graded refractive index
HF	High Frequency
HP	High pass
IR	Infrared radiation
LDV	Laser Doppler velocimeter

LSP	Gradient method and line search algorithm for nonlinear least-squares problem
MATLAB	Matrix Laboratory, high-performance language for technical computing
MEMS	Micro-Electromechanical Systems
MZ	Mach-Zehnder interferometer
NDT	Non-Destructive Testing
NDE	Non-Destructive Evaluation
OCT	Optical Coherence tomography
ORMOCER®	Organically modified ceramics
PD	Photodetector
PI	Proportional integral controller
P-wave	Pressure wave
PM	Phase Modulation
PT	Pulse thermography
PZT	Plumbum (lead) Zirconate Titanate piezoelectric ceramic
RF	Radio Frequency
RMS	Root Mean Square
SF	Sensitivity factor
SH-wave	Shear Horizontal wave
SHM	Structural Health Monitoring
SMART layer	Stanford Multi-Actuator-Receiver Transduction layer
SNR	Signal to noise ratio
STFT	Short Time Fourier Transform
SV-wave	Shear Vertical wave
TOF	Time of Flight
VOA	Variable optical attenuator
WDM	Wavelength Division Multiplexing

LIST OF SYMBOLS

$\cdot$	Scalar product
$\times$	Vectorial product
$\|\ \|$	Absolute values
$\|e_i\rangle$	Base vector of the polarization states algebra in Jone's algebra
$\|>$	Jone's algebra vector representation
$<\|>$	Polarization state projection in Jone's algebra representation
$\otimes$	Convolution operator
*	Complex conjugate
^{T}	Transposition operator
A_1, A_2	Arbitrary constants
A_M	Approximation at level M in wavelet decomposition
A	Spacing between Comb transducer elements
$\overline{a}_X$, $\overline{a}_Z$	Lamb wave acceleration components normalized against the vertical displacement in the surface of the plate
B	Magnetic flux
c, c_{ph}	Lamb wave phase velocity
c_g	Lamb wave group velocity
c_L, c_T	Longitudinal and transversal mode wave velocity
c_p	Phase velocity
c_s	Specific heat
c_R	Rayleigh wave phase velocity
D	Induced electrical displacement in piezoelectric materials
D_{11}, D_{22}	In-plane dipolar forces
D_{33}	Out-of-plane dipolar force
D_m	Detail coefficients in the wavelet decomposition
d	Plate's thickness (or piezoelectric coupling for piezo materials)
$\overline{d}$	Lamb wave constant given by $\pi \cdot f \cdot d / c_T$
$d\Phi$	Ultrasonic wave induced phase difference in the interferometric sensor
E	Young's modulus (or electric field for piezoelectric materials)
$F[]$	Fourier transform operator

F_s	Sampling frequency
f	Frequency
$f_{carrier}$	Carrier frequency of a burst signal
f_r	Normalized bias frequency
f_{rate}	Burst rate of a burst signal
f_u	Ultrasonic frequency
$\hat{f}$	Frequency reassigned coordinate
$f{\cdot}th$	Frequency:thickness product
G	Lamb wave dispersion function
H	Hessian matrix
$\Im$	Imaginary part
I_o	Incident optical intensity
J	Eddy current density
k	Wavenumber as $1/\lambda$ (or AC coupling coefficient for FBGs)
k_L, k_T, k_R, $k_{S,A}$	Longitudinal, transversal, Rayleigh and Lamb waves wavenumber (as ω/c_L, ω/c_T, ω/c_R and ω/c respectively)
k_{jc}, k_{jt}	Electric field coefficients for the jth directional coupler (subindex c is for coupling and the subindex t is for the transmission)
k_p	Electromechanical coupling factor for piezoelectric materials
L	Total length of the grating in a FBG
n_{eff}	Effective refractive index of an optical fibre
p_{11}, p_{12}	Pockel's components of the strain optic tensor
q_R, s_R	Rayleigh wave constants given by $\sqrt{k_R^2 - k_L^2}$ and $\sqrt{k_R^2 - k_T^2}$ respectively
$q_{S,A}$, $s_{S,A}$	Lamb wave constants given by $\sqrt{k_{S,A}^2 - k_L^2}$ and $\sqrt{k_{S,A}^2 - k_T^2}$ respectively
$\overline{q}$, $\overline{s}$	Constants associated with Lamb wave acceleration components, defined as $\sqrt{1-(c/c_L)}$ and $\sqrt{1-(c/c_T)}$ respectively
r	Wave propagated distance (or the optical intensity reflectivity for FBGs)
$R(\alpha)$	Radiation directivity
$\Re$	Real part
S	Strain (for piezoelectric materials)

s_E, s_v	Sensitivity of Lamb modes phase velocity to small changes of E and v
s^E	Mechanical compliance (for piezoelectric materials)
T	Temperature
T_s	Time sampling period
T	Mechanical stress applied to piezoelectric material
t	Time
$\hat{t}$	Time reassigned coordinate
T_C	Curie temperature
u, v, w	Displacement component in the X, Y and Z direction respectively
u_S, u_A	In-plane particle displacement for symmetric and antisymmetric Lamb wave modes
$\hat{u}_r$, $\hat{u}_\theta$	Radial and tangential unitary vectors for polar coordinates
V	Visibility of interference
v_{ph}	Phase velocity
W_{il}	Weighting factor for the inversion process
$W_x(t, f)$	Wigner-Ville distributions of a time signal x
w_S, w_A	Out-of-plane particle displacement for symmetric and antisymmetric Lamb wave modes
$\bar{x}$, $\bar{z}$	Horizontal and vertical position normalized against λ_S
$x(t)$, $x[n]$	Continuous signal and sampled discrete signal
$\vec{\nabla}$	Gradient operator, in Cartesians is given by $\frac{\partial}{\partial x}\hat{i}+\frac{\partial}{\partial y}\hat{j}+\frac{\partial}{\partial z}\hat{k}$
∇^2	Laplace operator, in Cartesians is given by $\frac{\partial^2}{\partial x^2}+\frac{\partial^2}{\partial y^2}+\frac{\partial^2}{\partial z^2}$
Δc, Δk	Phase velocity and wavenumber irresolvable error
$\Delta\Phi$	Optical phase difference between interferometer arms
$\Delta\bar{\phi}$	Normalized variation of fibre optical phase in wavefront integration model
$\Delta\bar{\phi}_{pp}$	Peak to peak value of $\Delta\bar{\phi}$
Δx	Space sampling period
Λ	FBG's grating period
α	Attenuation coefficient of a wave
β	Propagation constant (or parameter associated to a Kaiser window)
Γ	Confinement factor for optical fibres

γ	Degree of coherence of a laser source
δ	Skin depth (or detuning factor in FBGs)
$\delta()$	Dirac Delta function
δ_ω	Thermal diffusion length
ε	Strain
ε^T	Dielectric permittivity
ζ	Distance from fibre segment to ultrasonic source
ζ_0	Distance from centre of fibre to ultrasonic source
θ	Angle of punctual acoustic source respect to normal direction of fibre axis
θ_i, θ_r	Incident and reflected angle
λ	Wavelength
λ_S	Ultrasonic wavelength
λ_B	Bragg wavelength
λ_R	Rayleigh wave wavelength
λ, μ	Lame constants
μ_0, μr	Permeability of free space and relative permeability
ν	Poisson's ratio
ξ	Lamb wave constant given by c_T^2/c_L^2
ρ	Density
ς	Lamb wave constant given by c_T^2/c^2
σ	Electrical conductivity (or arbitrary angles)
$\hat{\sigma}$	DC coupling coefficient in FBGs
σ_{th}	Thermal conductivity
σ_{xx}, σ_{xy}…	Stress components (first suffix represents the direction of the stress and the second suffix is the plane in which it is acting)
σ_t, σ_ω	Time and frequency deviation
ω	Angular frequency
ω_S	Ultrasonic angular frequency
ϕ	Scalar potential
Φ_d	Environmental perturbation induced phase difference in interferometer
Φ_{PZT}	Phase shift caused by the PZT cylinder in the interferometer reference arm
Φ_S	Amplitude of ultrasonic wave induced phase difference in interferometer
ψ	Vector potential
$\psi_{m,n}$	Discrete wavelets

Chapter 1

INTRODUCTION
An Overview to SHM and NDT

1.1 THESIS BACKGROUND

Structural health monitoring (SHM) [2] and damage detection involves the use of in-situ, non-destructive sensing and analysis of structural characteristics for the purpose of detecting changes that may indicate damage or degradation. Its growing applicability covers from civil and structural engineering (bridge dynamic loading, post-earthquake damage evaluation of high-rise buildings, ground transportation sectors) to aerospace industry and marine engineering.

One of the main ideas in SHM is to integrate within the inspected structure non-destructive testing (NDT) methods and in service monitoring of the mechanical properties, objectives that SHM shares with smart structures. However in many important SHM applications, where the structure is under extreme temperature and/or stress conditions, difficult to access structural areas or for very small (micro or nano) systems, structurally embedded, contact sensors are not possible.

Between the available NDT techniques, the most promising and developed appears to be the acousto-ultrasonics, where a stress and/or strain wave inducing probe and a stress and/or strain detecting probe are required. Lamb waves, as the most reliable, efficient and suitable acoustic waves for plate-like structures, can provide information of the structure's entire thickness through large distances. They are sensitive to the principal material elastic properties as well as to structural loading or defects within the material.

In addition optical fibre technology appears as one of the most promising candidates for being integrated as a monitoring sensor system of large area structures in general, and in composite structures in particular. Optical fibre sensors can support extreme operation conditions, they are immune to electromagnetic interference, their small dimensions, lightweight characteristic and geometrical flexibility makes them very suitable for nonobtrusive integration in composite, concrete and metallic structures. Optical transmission

lines are low power and lossless in comparison with electrical systems and they are highly sensitive to ultrasonic waves in a broad variety of sensing ways.

In this chapter we provide a detailed overview of the two fields within which this thesis is framed; SHM and NDT. We look into the different techniques to them applied and we compare them, highlighting the advantage that acousto-ultrasonic and optical fibre sensors provide over the other techniques.

It is through the combination of acousto-ultrasonics and optical fibre sensing, the way in which this thesis looks to contribute to SHM and NDT of materials.

1.2 STRUCTURAL HEALTH MONITORING

In order to understand what Structural Health Monitoring (SHM) is about, we need first to understand what the words Health and Monitoring mean from structural engineering point of view:

Structural Health is related to the ability to function/perform and maintain the structural integrity through the entire life-cycle of the structure [1]. It is similar to the health of a life organism, where the organism is the structure and its life is the structure's life-cycle.

Monitoring is the process of keeping a record in a regular basis with the purpose of assessing the current damage state of the structure and to predict its performance and remaining useful life (*prognosis*) under expected future loading conditions.

In consequence SHM consists in the acquisition of periodically sampled dynamic response measurements of structural data from a network of sensors, and its posterior validation and analysis in order to assess harmful perturbations in the structural performances by the presence of damages or by normal operation, and therefore ensure the structural integrity. Its final aim is to optimize the structural lifetime and utility.

The current feasibility and applicability of Structural Health Monitoring to a broad spectrum of engineering disciplines, has made of it an emerging and promising research field as probed by the huge number of publications and conferences dedicated solely to this subject (e.g. some conference references are [2-4]). Aerospace, civil and mechanical engineering infrastructures appear as the most directly beneficiaries of SHM developments.

1.2.1 Configuration of a Structural Health Monitoring system

In order to accomplish its numerous and multifaceted tasks, a SHM system is a complex structure composed of multidisciplinary components as shown in Figure 1.1 (based in [5,6]).

The first stage of a SHM system is its architectural design, at this point the usage conditions of the monitored structure are considered and it is decided the level of monitoring priority of the different structural components, their layout and the way they interact. This information is used to define the types of damage to look for, and it affects the decision of the sensors and actuators density and position distribution. At this point of design, an important decision must be made as if a *real-time* or *discontinuous* SHM configuration is selected; where a real-time configuration monitors the structure continuously during operation meanwhile in the discontinuous configuration the monitoring data only can be accessed after operation.

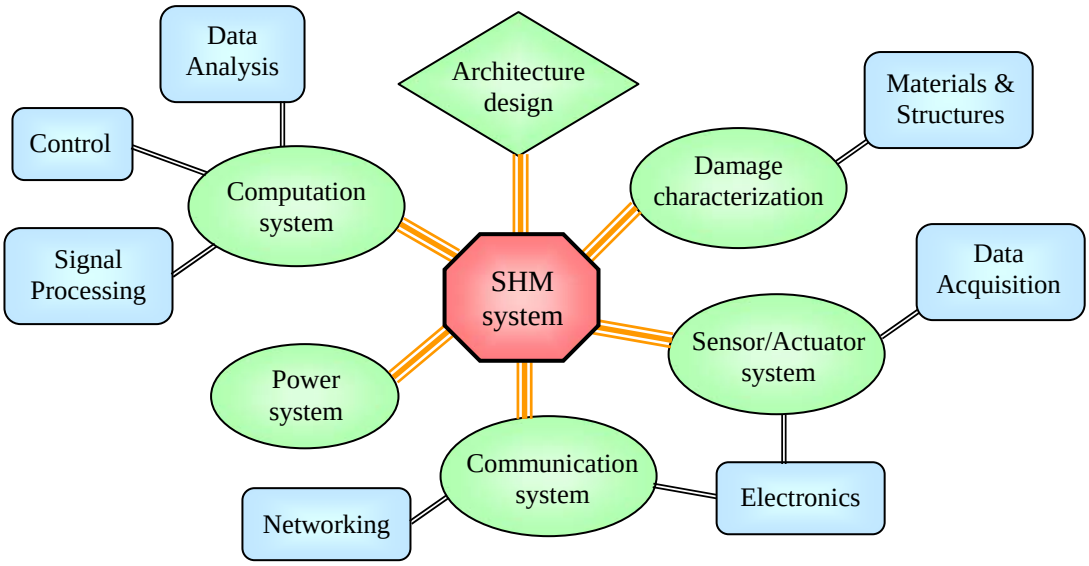

Figure 1.1: Components of a SHM system and fields involved.

In the next level a SHM system deals with one of its main task, which is damage detection and evaluation. Because all materials and structures present defects at the nano/microstructural level in the form of impurities, imperfections or even voids produced during manufacturing. It is important for the SHM system to characterize what is defined as damage and when the monitored structure is damaged. In order to accomplish this, it is necessary to distinguish three levels of the damage evolution [6]; defect, damage and fault.

- *Defect* is any imperfection inherent in the material, being always present in a nano/microstructural level. Because any engineering structure is designed taking these imperfections into consideration, at this level the structure can operate perfectly.
- *Damage* is any change in the structure's material and geometrical properties which cause the system to perform below an ideal condition. However it can still function satisfactorily. All damage always begins at the material level and under adequate loading conditions it evolves to component and system level, developing into a fault.

- *Fault* is when the structure no longer performs satisfactorily, so a remedial action has to be undertaken.

These stages have an obvious evolution an relationship, as shown in the next Figure:

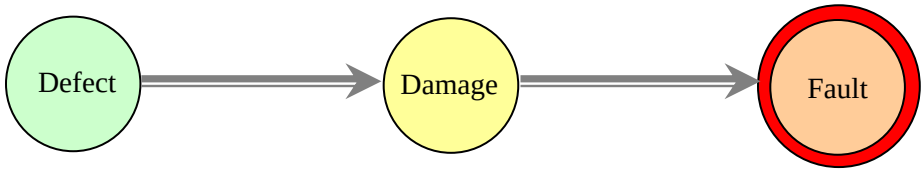

Figure 1.2: Damage evolution in a structure.

In order to be able, in practice, to distinguish these stages and particularly to know when a structure is no longer operative, an important knowledge of Materials and Structural Engineering is required. A SHM system should identify the presence of damage and its severity and advice for correction before the appearance of a fault.

After characterizing the kind of damage that can be presented in the structure a proper sensing method and sensor and actuator system must be selected. Here an important decision is to determine the sensors placement and to choose between *active sensing*, where the sensing system requires an external perturbation of the structure for its damage presence interrogation or *passive sensing* where no artificial energy is required as it detects the perturbation of the ambient conditions caused by the presence of damage. Reference [7] shows that because active sensing interacts with the structure it is more reliable than passive sensing which just 'listen' to the structure. In this stage an adequate knowledge of sensors, electronics and data acquisition is of relevant importance. The sensing system will be constituted of a considerably amount of units, proportional to the complexity and size of the structure under monitoring. As a result a communication system is needed not only for the transferring of data between the sensing units but also to transfer the full data collected by the sensors to the processing or computation system and to convert this data from analogue into a digital format. The computation system may present two different architectures; *centralized* processing unit or a *distributed* group of more local processing units. In any case the computation system is the brain of the SHM system, which deciphers and interprets the data collected by the sensor system. In most cases the computation system is built over the next four levels:

- *Pre-processing*: The data collected by the sensor system is *de-noised* and filtered and in some cases a data dimension reduction and transformation is also applied.

- *Feature extraction*: In this stage the components of the signal data including the damage signature are magnified and the components associated to the normal operating conditions of the undamaged structure are reduced or filtered.
- *Pattern processing*: At this stage different algorithms are applied to the feature data previously extracted in order to assess the extent and severity of the damage. It can also include the location of the damage within the structure.
- *Decision/Intervention*: Based in the information of the previous level, this stage decides if any action should be taken and it controls the execution of these actions carried out by the actuators system (which could consist in human intervention for the simplest SHM system to more complex electroresponsive devices). In some cases it can even estimate the operative life of the structure until failure.

The disciplines of data analysis, signal processing and control engineering are of special relevance in the computation system level.

Advances in any of the multiple disciplines involved in a SHM system favour its development. In the last two decades we have seen marvellous improvements in networking communication, with special relevance to the wireless technology. Additionally optical fibre sensors have shown a great adaptability to the measurement of almost all kind of parameters and their ability to be integrated into most materials, with the Fibre Bragg gratings as a clear protagonist. On the other hand a lot of new signal processing and data analysis methods are continuously emanating from the mathematical and artificial intelligence communities, some examples are the wavelets analysis, principal component analysis or genetic algorithms. Finally since the development of the first electronic digital computer in the late 1930's we have never seen such processing power increase capabilities as those in the last decade. All this modern advances are some of the reasons that are making SHM to emerge strongly within the whole Engineering community.

1.2.2 Contribution of a SHM system to engineering structures

A SHM system contributes in two different ways to the improvement of engineering structures. The first contribution is of a *safety* improvement, as it provides a permanent monitoring of the structure from when it is manufactured until the end of its service life. This permanent knowledge of the structural conditions contrasts with the conventional cyclical inspection procedures where the inspection of the system it is only carried out during beforehand scheduled routines, whether evidence of damage is present or not. Damage could initiate between the inspection intervals, and grow until a fatal failure is caused, before even

being detected. A SHM not only identify the presence of damage in the structure at any time but also can give information of its evolution and verify if the structure is capable of performing the functions it was intended for, under the current and future expected usage conditions and to predict when this performance could no longer meet customer or user requirements. In which case SHM can suggests scheduling of the structural repair, replacement of parts or even ascertain the end of the structural utile life.

The second main SHM contribution comes as structure's *cost improvement*. Transportation and civil engineering structures require extensive maintenance directed not only to the health and usage monitoring but also, to a great extent, to repair and replacement of the damaged components. This expensive and extensive maintenance is due to the complexity of the systems (in both their design and their use of high performance, new technology materials) and to the strict safety and efficiency regulations dominating markets that relates with human lives. In order to better understand the cost improvement of SHM we will look into a particular case, the aircraft industry. The aircraft industry as one of the most innovative industries is continuously introducing new materials and technologies. In this industry as in many others, engineers design the structures based on two main design approaches:

- *Safe-life* design, it is orientated to the design of ideal structures. This means that the structure is designed with the main intention of having the structure damage free through all its lifetime. Once the service time for which the structure was originally designed has come to an end, the structure must be taken out of service, no matter if any kind of evident damage is present or not. This design principle manifestly requires providing a huge margin of safety for the structure's design, so most of the times in which the structure has been taken out of service, it could still provide an adequate performance during an additional considerable percentage of the original lifetime. This makes the safe-life design philosophy economically ineffective.
- *Damage-tolerant* design, in contrast to the previous design philosophy allows the structure to develop damage as long as it does not affect the overall performance of the structure. In order for this to be accomplished the undamaged part of the structure must be able to sustain the loads and functions that the damaged part cannot cope with any more. In this design principle the structure must be submitted to a cyclic inspection and maintenance servicing.

The oldest safe-life principle has nowadays been dominated by the damage-tolerant one, mainly because of the requirement of new lightweight structures. As the damage-tolerant design does not require a big margin of safety design it increases the allowable stress

conditions, leading to a reduction of structural cross-sections and so to a reduction in structural weight. This would benefit in production costs as less material is needed and in the operation costs as less weight leads to less consumption and/or increment of the transportable weight load. The permanent knowledge of the structure condition provided by a SHM system highly benefits a damage-tolerant design. Because not only replaces a regular maintenance with an as needed maintenance, but it also indicates whether the presence of a damage requires immediate repair in order to avoid its development towards more critical and costly proportions or if its repair can be postponed until a more global repair requirement is scheduled. Additionally the damage information provided by the SHM system will benefit in the *downtime cost*, as it reduces the time that the structure is taken out of service, and it will benefit in the human error costs and structure dismantling costs.

1.2.3 Future of Structural Health Monitoring towards Smart Structures

SHM and Smart structures share the same objectives, this is to integrate within the inspected structure non-destructive testing methods and in service monitoring of the mechanical properties. Moreover, as described in [8] they also share a similar components configuration as that shown in Figure 1.1. It is not difficult then to believe that their future is to merge into a common discipline. For this to happen, the structure requires of adaptable capabilities and the SHM system must instruct this adaptability in response to the monitoring information and external circumstances.

A *Smart Structure* [9, 10] consist in a structure that can react to the environment in which they operate in order to enhance their functionality and survivability. This concept is applicable and desirable in all engineering industries, from all kind of transportation and civil engineering to domestic appliances, intelligent clothes and toys. Born as a modern field of research at the beginning of the 1980s with the development of ‘smart skins’ that integrated radar antennas into the skins of military aircrafts. It soon expanded into provide a whole aircraft health monitoring capabilities integrated into the aircraft structure, and it was called ‘smart structures’ research. Almost immediately other engineering disciplines absorbed the concept, with civil, marine and transportation engineering being the most relevant examples.

In their fusion SHM will provide the “smartness” virtue to the structure, in the way of instructing the structure to adequately adapt and react to the environment in order to increase its performance and operational lifetime. The implementation of smart structures should have a very effective and beneficial impact in a high diversity of applications, being the most evident for the near future; composite structures, aircraft industry and large civil structures.

This impact would be orientated into their design, production or construction and its maintenance as explained next.

Composites are engineering materials made from two or more components. One component is often a strong fibre that gives the materials its tensile strength. The other component (called *matrix*) is often a resin, such as polyester or epoxy that binds the fibres together, transferring load from broken fibres to unbroken ones and between fibres that are not oriented along lines of tension. Composite structures are characterized for having one of the highest strength:weight ratios. Their high performance and very demanding fabrication specifications, make them very desirables to have an integrated monitoring system since fabrication. Furthermore because structure composite technology is still relatively immature, the structures based in these very new materials are not yet very commonly used as structural elements. In consequence there are not too many engineering data collected regarding their long-term performance and failure conditions. As a result the structures based in composites must be overdesigned with big safety margins making an insufficiently use of the light weight and high strength characteristics of these materials. Again a proper capitalization of these material's properties would be achieved with a real-time monitoring.

On the other hand, an important percentage of the currently used civil and aerospace infrastructures are not only in need of renewal but they are working beyond their design lifetime. The reason for this is a major concentration of infrastructures made during a concentrated period of time. This is the case of many European countries after the Second World War, but also of many developing Asian nations which experienced rapid economical growth, as it is the case of Japan. For instance (as extracted from [11]), Japan built most of its currently used highway bridges between 1960 and 1985. The consequences of this high time concentration of built infrastructures is affecting Japan now, where most bridges experience damage and deterioration and are in need of retrofit/repair more or less at the same time. This effects can be extended to most civil and aerospace infrastructures of many developed countries, including USA, taking the modern society to what [11] calls "mass-maintenance age". The enormous investments that the replacement and repair of these infrastructures would require in the near future, demands them to be in service for a considerable extended period. Based on this, it is not a surprise to read the conclusions of the '2005 Report Card for America's Infrastructure' [12] issued by ASCE (American Society of Civil Engineers), that valuates the U.S. infrastructure as an overall poor condition. A relevant summary of this report is given in Table 1.1. Although this analysis is directly applied to the USA infrastructures it can be extended to infrastructures state conditions from many others developed countries.

The consequences of such poor infrastructure conditions are nowadays more evident than ever before, just months after the big crisis that hurricane Katrina has caused in New Orleans. A full city, in the richest country in the world, appeared submerged under water because of the deteriorating levels of the network of dams and levees in the region and by extension in all the country [13]. The cost in lives (more than one thousand lives) and property hugely surpasses the initially estimated maintenance and improvement costs (0.5 billion dollars in 10 years).

Infrastructure	Comments	2005 Grade
Bridges	In 2003, 27.1 % of USA's 590750 bridges rated structurally deficient or functionally obsolete. Estimated cost of $9.4 billion a year for 20 years to eliminate all bridge deficiencies.	C
Dams	Since 1998, the number of unsafe dams has risen by 33% to more than 3500. Estimated cost of $10.1 billion over the next 12 years to address only the critical dams.	D
Drinking water	Very old water transportation and treatment systems require of replacement, not only because they are failing but also to comply with safe drinking water regulations. It is estimated that $11 billion annually are required.	D-
Navigable Waterways	Of the 257 locks on the more than 12,000 miles of inland waterways, nearly 50% are functionally obsolete. By 2020, number will increase to 80%. Estimated cost of $125 billion to replace them.	D-
Rails	The freight railroad industry needs $175-$195 billion over the next 20 years to maintain existing infrastructure and expand for freight growth. Additionally the passenger market requires expansion of the railroad network and maintenance estimated in $60 billion over same period. This is a total of $12-13 billion per year.	C-
Roads	Poor road conditions cost U.S. motorists $54 billion a year in repairs and operating costs. Without mentioning the cost of $63.2 billion a year to American economy derived from the 3.5 billion hours a year that Americans are stuck in traffic. It is a total of $117 per year.	D
Aviation	It is estimated that more than $10.5 billion a year is invested in civil aircraft maintenance. With a considerable portion of this cost dedicated to inspection. This cost considerably increases with aircraft's life.	D+

Table 1.1: Estimation of America's Infrastructure conditions in 2005. Evaluation values are: **A** = Excellent, **B** = Good, **C** = Mediocre, **D** = Poor, **E** = Failing and **F** = Incomplete

SHM is one of the technologies that will make possible the elongation of the infrastructures lifetime in a safe and cost effective way. The addition of Smart Structures into these civil infrastructures and integration into new infrastructures will importantly affect the decrement of their maintenance and repair budgets. For instance in civil and military aviation infrastructure this improvement could save around 20% of maintenance and repair costs [1].

In conclusion, the SHM, in its approach towards a Smart Structure, is evolving on the direction of integrating the monitoring capabilities unobtrusively within the structure. The integrated sensor system will consist of a distributed system of active sensor units; each one completed with a local mechanical excitation source, a processing unit and a communication unit [14]. Each unit will have damage detection capabilities and through cross-correlation of the whole unit array data, damage location is provided by an external centralized data storage and processing unit where monitoring of the full system is carried out. In addition future SHM systems will be also completed with an actuator system which will act adequately in response to the detected damage, controlled by the centralized processing unit, in order to improve and maintain its performance, integrity and remaining useful life.

Nowadays there are several sensor technologies that make the nonobtrusive integration a possibility. The ones with higher potential are Micro-Electromechanical Systems (MEMS), optical fibre sensors and modern piezoelectric sensor technologies such as small piezoceramics and piezoelectric paints (more of this in Chapter 2).

This thesis aims to look into this future of SHM, for this reason we have chosen to work with optical fibre sensors towards nondestructive testing of materials. In comparison with the other two options for constituting integrated sensor systems, optical fibres have the benefits of immunity to electromagnetic fields, extremely high sensitivity, broadband signal detection spectrum, environmental ruggedness, low power requirements, lightweight, geometric flexibility, long lifetime and compatibility with modern telecommunication data transmission systems. In addition optical fibres are probably the most suitable for integration in modern carbon and glass fibre composites structures, commonly used in aerospace, automotive and marine industries and they are beginning to emerge as serious contenders in civil industries. An optical fibre is totally compatible with reinforcing fibres. When embedded into the composite material, optical fibre sensors will have very little impact upon strengths, breaking strains or overall mechanical properties, provided that the fibre is oriented appropriately with the reinforcing fibres. And provided that the optical fibre is less than 10% of the composite material’s thickness and it is coated with a resin-compatible material [15].

Optical fibres allow point sensors, integrating sensors, multiplexed sensors and fully distributed sensors geometries easily adaptable to the sizes of civil infrastructures (for instance as shown in Chapter 2 we have used; FBG as multiplexed point sensor, polarimetric system as an integrated sensor and examples of fully distributed systems are those based on Raman scattering for temperature measurement or based on Brillouin scattering for strain measurement).

As pointed in [10] “the development of smart structures in the near future will almost certainly involve the use of fiber-optic sensing”.

Finally, in order to develop a successful SHM system it is vital to allow Nondestructive testing (NDT) methods to become and integral part of the structure to be monitored. A SHM system applies NDT in order to identify damage and detect possible failure in the structure. In the next section we introduce the concept of Nondestructive testing, we describe the currently most used methods and concentrate into those few with the aptitude to be integrated into a smart structure.

1.3 NON-DESTRUCTIVE TESTING OF MATERIALS

The British Institute of Non-Destructive Testing defines Non-Destructive Testing of materials (NDT) as the branch of engineering concerned with all methods of detecting and evaluating flaws in materials. The flaws may be cracks or inclusions in welds and castings, or variations in structural properties which can lead to loss of strength or failure in service [19]. An essential feature of NDT is that the test process must not produce any damaging effect on the material under test.

It is important to notice the differences between SHM and NDT. A SHM system uses NDT as part of its monitoring functions. Meanwhile NDT is a series of discrete tests that look for an image (visual, ultrasonic or any other way) of the structure under inspection, to find flaws or defects by changes in several physical properties. SHM interpret the information obtained from the NDT method used to estimate in a permanent way the health of the structure, for which it looks to changes of properties that could or not be physical.

Damage detection, characterization and location are relevant to all the engineering disciplines not only for safety issues but also because of performance and cost efficiency improvements. This vast interest in NDT can be seen in the several international conferences dedicated exclusively to this subject, e.g. [16,17].

The work of such multidisciplinary community aiming to a common objective has developed a great number and diversity of Non-destructive damage detection techniques based in different physical phenomena and properties. What is more, the continues advances in physics, mathematics, electronics, computer power, system modelling, signal processing and sensors have not only improved existing techniques but also help in the development of new ones, and it will continue to do so in the future.

It is not the intention of this thesis to review all the present Non-destructive testing methods. However in order to understand the choices taken in this project it would be helpful at least to review the most commonly used techniques [1,5,20-23].

Civil engineering, transportation engineering and mechanical engineering industries are very familiar with; visual inspection, liquid penetrant inspection, acoustic emission inspection, holographic inspection, shearography inspection, thermography inspection, Eddy current, magnetic particle inspection, radiography inspection, vibration and modal analysis inspection and ultrasonic inspection. A summary of these techniques is shown in Table 1.2 where their possibility as a SHM system in the near future is evaluated. A more detailed description of the basic operation principles of these techniques as well as their associated advantages, disadvantages and main applications can be found in the literature [24-30].

Method	Applications	Advantages	Disadvantages	SHM Potential
Visual Inspection	Surface defects	Inexpensive No data analysis Portable All materials	Limited detection sensitivity Time consuming Operator interpretation Accessibility required	None
Liquid Penetrant	Surface defects	Inexpensive No data analysis Portable Nonporous materials Sensitive to small defects	No detection if defect filled. Contact method Accessibility required	None
Acoustic Emission	Monitoring development of surface/internal discontinuities	Inexpensive Fast scan of large areas Portable Sensitive to small defects	Passive technique (requires load) Reduced repeatability Complex data analysis	Lightweight No power need Large area inspection Triangulation possible Structural integration
Holography	Surface/sub-surface defects	Non-contact and remote inspection Fast scan of large areas High sensitivity Easy data analysis	Relatively expensive Vibration isolation required Requires load	None
Shearography	Surface/sub-surface defects	Non-contact and remote inspection Fast scan of large areas High sensitivity Easy data analysis	Relatively expensive Requires load	None
Thermography	Surface/sub-surface defects	Non-contact and remote inspection	Relatively expensive High energy required Poor penetration	None

		Fast scan of large areas Easy data analysis		
Eddy Current	Surface/sub-surface crack detection	Non-contact Sensitive to small cracks Lightweight & portable Relatively inexpensive	Very complex data analysis High energy required Conductive materials only Requires calibration High qualified personnel Poor penetration Small area monitoring (requires scanning)	None
Magnetic Particle	Surface/sub-surface defects	Easy operation No data analysis Sensitive to small defect Inexpensive Non-contact Portable	Ferromagnetic materials only Accessibility required Contact method	None
Radiography	Surface and internal discontinuities	Internal inspection No data analysis Easy operation	Safety hazard Limited detection sensitivity Relatively expensive Time consuming Operator interpretation Accessibility to both sides required	None
Vibration/Modal Analysis	Global structural analysis	Applicable to complex structures Inexpensive Portable Fast scan of large areas	Complex data analysis Very limited detection sensitivity High sensitive to boundary conditions	Lightweight Low power required Small area inspection Structural integration
Ultrasonic (conventional scanning)	Surface and internal defects	Internal inspection Inexpensive Portable Sensitive to small defect Relative fast scan of large areas	Small area monitoring (requires scanning) Complex data analysis Contact method, requires couplant	None
Ultrasonic (guided waves method)	Surface and internal defects	Internal inspection Inexpensive Portable Sensitive to small defect Non-contact and remote inspection possible Fast scan of large areas	Very complex data analysis Plate-like structures	Lightweight Medium power required Strip area inspection Large area coverage Triangulation possible Structural integration

Table 1.2: Summary of the most common NDT techniques.

If we evaluate these methods from their potential implementation in a SHM system, only three of them can be considered seriously; acoustic emission, modal analysis and ultrasonic guided waves. Between these three, modal analysis as a global method has a limited size detection sensitivity and it does not provide much information about the damage location and characterization. Its sensitivity to changes in the boundary conditions (e.g structure's geometrical dimensions and loads) makes it less attractive than the other two options. Acoustic emission and ultrasonic inspection are in fact related in the way that both use ultrasounds as the physical scanning property. Both could use very similar detection sensors and very similar signal processing tools for data interpretation. However the biggest difference is that acoustic emission is a passive inspection method, where the damage is only sensed when a primary load level is exceeded. This means that acoustic emission is based in the worsening of an already existing damage, making of it a very unrepeatable method. Ultrasonic inspection, in contrast, is an active method which requires an external source of energy to generate the ultrasonic signal used for the inspection. Ultrasonic inspection with guided waves solves the problems of the other two methods and combined with non-contact optical generation of ultrasounds provides remote inspection capabilities. It also benefits from the applicability of inexpensive and lightweight sensing arrays that can be integrated to the structure under test achieving large area inspections. Between the possible sensing arrays optical fibre sensors are the highest potential candidates for their incomparable advantages against the more conventional electronic and electrical counterparts (as described in Chapter 2), with particular relevance on composite and concrete structures.

Ultrasonic NDT provides a sensitive method of inspection in most materials; metallic, non-metallic, magnetic or nonmagnetic, in opposition to other NDT methods which are particular to specific materials.

Ultrasonic guided waves carry huge information about the damaged structure, being able to contribute in all the goals required in damage detection:

- Determination of the presence of damage in the specimen.
- Estimation of the severity of the damage.
- Differentiate various types of damages.
- Location of the damage.
- Estimation of the dimensions of the damage.

All the inspection benefits that ultrasonic guided waves provides has made it eligible as the NDT method use within this thesis.

Yet the main disadvantage of ultrasonic guided waves is the complexity of the analysis of the obtained data for the extraction of all the relevant information. That is why we have had to wait to the modern advances in computer power and in Signal Processing techniques in order to see the big boom that in the last years has raised ultrasonic guided waves as one of the most promising NDT methods. This thesis also contributes in the analysis of this complex data in different applications.

In the next sections we look into the origins of the NDT technique and introduce the different methods used to generate and detect ultrasonic waves.

1.3.1 Non-Destructive Testing with ultrasounds

Sound testing is probably one of the oldest and most accessible Non-Destructive Testing tools used for detection of hidden defects [31]. For instance internal defect in forgings or casting can be detected as a change in the ringing note when the specimen is hit with a hammer. In a similar way anyone can test their porcelains and glasses for cracks by tapping it with their fingernails and listening to the sound, if it is “dull” then it indicates presence of cracks. This technique probably was already used by the inventors of ceramics more than 11 thousands years ago. However the transition from the audible sound to the ultrasound, in order to decrease detectable damage dimensions, could not be possible without the modern technology that replaces hammer and ear with piezo-electric, transducers, optical fibres and lasers.

The principle of the ultrasonic testing is that solid materials are good conductors of sound waves [18]. The sound wave generated by means of a mechanical interaction with the structure, propagates as a vibration perturbation from one region of the space to another. Any major disturbance of the structure homogeneity will alter this vibration’s properties (amplitude, frequency, phase velocity…) and create new vibration fields as reflection and transmission waves. The wave perturbation is stronger the smaller the wavelength of the wave, provided that the wavelength is the order or smaller than the disturbance dimensions. Because acoustic waves in solids have propagating velocities of the order of *km/s* then in order to detect disturbances smaller than centimetre dimensions, the frequency range must be over hundreds of *kHz*. Any sound frequency over the human ear audible region (10 *Hz* to 20 *kHz*) is considered *ultrasound*.

Through-transmission and reflection technique

Non-Destructive material testing with ultrasounds started, from a theoretical point of view, more than 60 years ago when the Soviet scientist Sergei Y. Sokolov, proposed in 1928 a

through-transmission technique for flaw detection in metals [32, 33]. In this method ultrasonic source and receiver are located in opposite sides of the material under test. The variations in ultrasonic energy transmitted across the metal are used to locate and measure the flaw, since the presence of the flaw in between the transmitter and receiver will scatter part of the input ultrasonic energy decreasing the part arriving to the receiver (fig. 1.3).

Sokolov also suggested a *reflection technique*, where source and receiver are located in the same side of the material. In this case the incident ultrasonic pulse wave is transmitted from one side of the sample and reflected back from the far side to the receiver, this pulse is named *backwall echo*. The time of arrival depends on the dimensions of the material and velocity of the ultrasounds in that material.

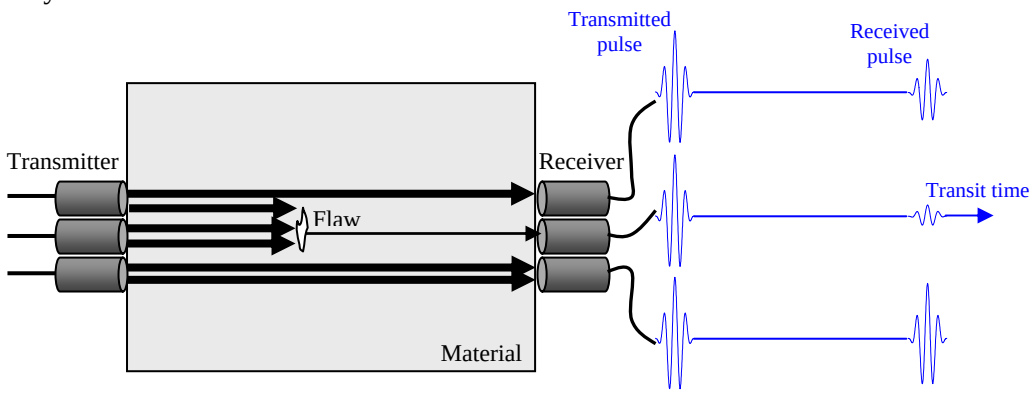

Figure 1.3: Through-transmission technique for flaw detection

The presence of a flaw in the propagation path is shown as new pulses arriving before the backwall echo. These pulses, named *flaw echos*, are reflections from the flaw. In this way a map of the material can be generated to illustrate the location and geometry of the flaws (fig. 1.4). When the same probe is used to generate the ultrasound and receive the reflected wave, the reflection technique is called *pulse-echo*. If the reflection is received by another transducer then it is called *pitch-catch*.

Although the theory was suggested by Sokolov in the early 30s, the technology needed to generate the short pulses necessary to measure the small propagation time of the reflected echoes was not available until the Second World War.

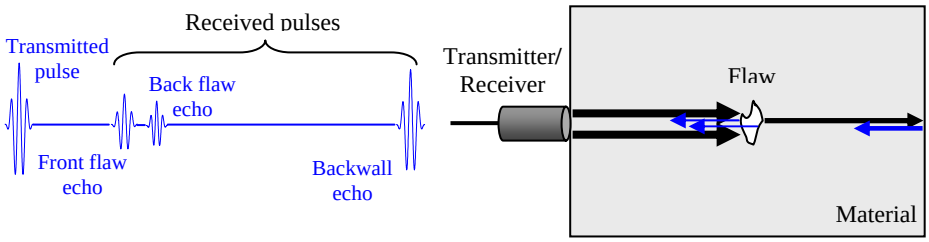

Figure 1.4: Reflection technique for flaw detection

This is why we have to wait until the early 1940s to see Floyd Firestone in USA and Donald Sproule in the UK initiate independently and in the highest of the secrecies the industrial use of ultrasonic testing [34-37]. It is at this time when the industrial material testing was born, not just for flaw detection but also testing of any material imperfection or material characterization. Until then the only methods for internal flaw detection was the hazardous *radiography* (x-ray or radioactive isotopes) *methods*.

Scanning inspection

Looking at the transmitted and reflected waves by means of the previously described techniques constitute the most popular and conventional ultrasonic inspection method, the *scanning inspection*. Depending in the region being scanned, three different scanning inspections can be distinguished; *A-scan* inspects the material at a single point, displaying the incident pulse and the echoes along a transit time plot as shown in fig. 1.4, B-*scan* is a series of A-scans along a line of the material. It gives information of discontinuities as a 'cross sectional view' of the specimen. The display shows the peak of the pulses obtained by each of the A-scans taken and combined according to the probe displacement. The vertical coordinate is the pulses' transit time (fig. 1.5-*left*). *C-scan* is a collection of B-scans, covering a surface section of the specimen. It gives a three dimensional information of the material discontinuities in a 'flat plan view'. The display is a surface contour plot of the intensity sectional information given by the set of performed B-scans (fig. 1.5-*right*).

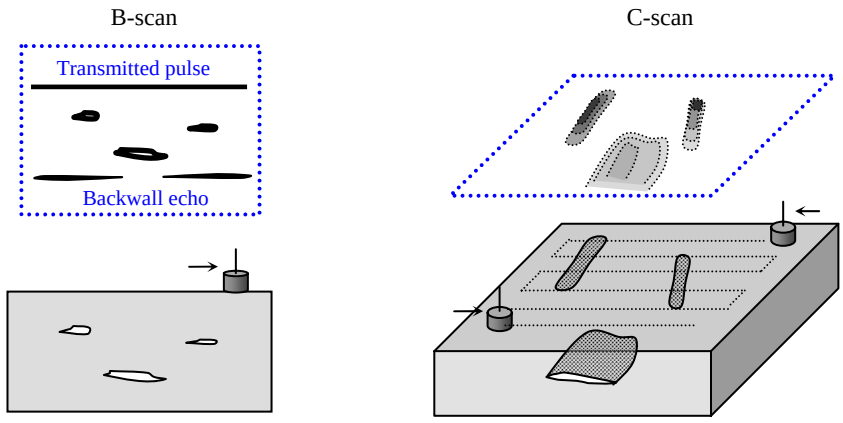

Figure 1.5: B-scan and C-scan principle of scanning and displays.

The ultrasonic waves used by the scanning inspection are *bulk waves* (transversal and longitudinal waves). The C-scan is a flexible and robust technique and has become common NDT technique in innumerable applications where subsurface flaw detection is needed. As mentioned in Table 1.2, beside the Radiography method, the ultrasonic scanning is the only method that can reveal substantial subsurface flaws, with the advantage that this technique

does not suffer from the safety hazards of the former one and the high cost of the used equipment.

Nonetheless conventional ultrasonic inspection also has important drawbacks; it is limited to the test of relatively simple geometries, where accessibility to the structures surface is required and it only interrogate the close region around the area where the probe is positioned, which consequently imply long time scanning of large areas, and if done improperly it can easily miss essential flaws.

Ultrasonic guided waves inspection

These limitations of the conventional ultrasonic methods were overcome when Worlton [38,39] at the end of the 50s recognized the advantages that guided waves offered over the conventionally used bulk waves, for the inspection of thin-plate structures; such as metal plates, airframes, large containers, pipes and tubes.

Although guided ultrasonic waves are properly introduced and discussed in Appendix A, it is interesting to point here the main benefits by them provided to the ultrasonic NDT inspection method:

- Full structure's volume inspection over long distances between the source and the receiver, from a single probe position.
- Greater sensitivity than conventional ultrasonic methods or other NDT methods. And sensitivity to different types of flaws.
- Ability to inspect structures under water, coating, insulation, multi-layer structures or concrete with excellent sensitivity.
- Capability to detect, locate, classify and size defects.
- Their guiding character enables them to follow curvature and reach hidden and/or buried parts.

The work developed in this thesis use guided waves ultrasonic NDT methods, in particular we work with the so-called Lamb waves.

1.3.2 Methods for generation and detection of ultrasounds

From a mechanical shock or friction of a body to more complex physical interactions, quite numerous are the available methods to generate and detect ultrasounds in solid media. These methods are based in many different physical properties. Between all the existing methods it is the piezo-electric effect the most widely used for ultrasonic transduction mainly due to the fact that the same probe can be used both for generation and for detection at the same time.

They are also the ones that produce the best signals and they have a great potential for structural integration beneficed by their simultaneous sensor and actuator behaviour. Though optical methods have several advantages over the contact piezo-electric transducers that make them desirable in certain applications, as listed in Chapter 2. An interesting review of the different possible physical effects used until now for the transmission and reception of ultrasonic waves can be found in [31,40], however as new physical interactions are discovered and new technologies developed, new effects will add to this list in the future:

- Mechanical effect.
- Piezo-electric effect
- Thermal effect
- Electrostatic methods
- Electrodynamic methods
- Magnetostrictive methods
- Optical methods

In this thesis we have worked with the piezo-electric effect and thermal effect for contact and non-contact ultrasonic guided wave generation in plate like structures, as shown in Chapter 2. Piezo-electric effect and several optical methods were also used for the ultrasonic detection as shown in same chapter.

1.4 OBJECTIVES

It is the main objective of this work to contribute into the development of NDT optical techniques applied to SHM of structures. In order this to be accomplished we have had to complete a numerous of related tasks as pointed next:

- Introduce and review the current developments in SHM and NDT.
- Understand and characterize the generation, propagation and detection stages of ultrasonic guided waves in plate-like structures. This information will help to better understand the interaction of these ultrasonic signals with defects.
- Development and confirmation of a theoretical model for the modulation that the acoustic wave pressure field induces over the sensing property of an integrating OFS. Allowing characterization of integration sensors directivity pattern with application in damage location.

- Review of the state of the art in optical fibre sensors for ultrasound detection, and application of various optical fibre sensors for damage detection and location.
- Development and testing of an all-optical, non-contact technique for the monitoring of the elastic and geometrical properties of mechanical materials.
- Development and implementation of signal processing tools to extract the information that characterizes the elastic and geometrical properties of mechanical materials.
- Validation of these processing tools over the experimentally obtained complex ultrasonic data.
- Apply this technique for the monitoring of the materials temperature changes and damage detection potential.

1.5 OUTLINE OF THE THESIS

The main objective of the thesis here presented has been to combine the advantages and structural integration capabilities of ultrasonic guided waves NDT technique with the unrivalled acoustic wave sensing performance and nonintrusive structural integration characteristics of modern optical fibre sensor technology. In this way we contribute into the future of SHM by integrating NDT monitoring technology into structural materials.

The order in which the different chapters are presented, follows a thematic division of the produced work in two main areas; application of optical fibre sensors for ultrasonic guided waves NDT, addressing their damage detection and location potential based on their sensing high directivity. And development and construction of a complete non-contact, all-optical tool for the remote inspection of mechanical materials. Its experimental application included the measurement of physical and geometrical properties of plate-like structures for SHM. Each of these main contents is preceded by a series of introductory chapters and complemented with multiple appendices at then end of the thesis, to provide the necessary background and conceptual information required for a better and complete understanding of the work.

Chapter 2 focuses on the detection and generation techniques of ultrasonic guided waves. We start looking into the conventional contact transducers based on the piezoelectric effect highlighting their more serious limitations and comparing them with the advantages provided by modern optical systems. In order to take full advantage of the non-contact and remote inspection characteristics that optical techniques provide for SHM applications we present and analyse various optical techniques for both ultrasonic generation and detection. The optical ultrasonic sources studied are Q-switched high power laser source and a low power

CW alternative. Later we concentrate on the various optical fibre ultrasonic detection methods used in this thesis; Fibre Bragg gratings, Mach-Zehnder and modified Mach-Zehnder optical fibre interferometers and fibre optic polarimetric sensor. Followed by a comparison of their performance parameters and sensing aspects. This chapter is strongly complemented with Appendix A which introduces the propagation characteristics and theory of the elastic waves in solids, with an in-depth investigation in guided acoustic waves (Lamb waves in particular) in order to understand their interaction with defects and their dependence with the elastic properties of materials.

The experimental application of the previous optical fibre ultrasonic sensor systems is fully described in Chapter 3. There we confirm their suitability for ultrasonic wave detection and describe their potential for damage detection and location based in their inherent high sensing directivity.

Chapter 4 describes the analytical and experimental work to develop and validate a computer model of the wavefront integration interaction between a finite length optical fibre sensor (OFS) and an ultrasonic wave. Until this work the modulation that the acoustic wave pressure field induces over the sensing property of an integrating OFS has not been studied in depth, with very few reports published about it. In this model we have analysed the relation between the length of the sensing fibre, its distance to the ultrasound source and its sensitivity to ultrasound detection, for different orientations of the source with respect to the sensing fibre. The predicted basic trends were experimentally confirmed. The model also characterizes the directivity pattern of these sensors with obvious implications in damage location. The unintuitive model prediction of maximum sensitivity for an orientation of the fibre axis non perpendicular to the propagation direction of the ultrasound contrasts with the sensitivity typical of pressure sensors. This prediction was positively verified experimentally. We also prove theoretically that positive and negative changes are produced in the fibre birefringence in a similar way to that expected in the fibre refractive index. Therefore a polarimetric sensor exhibits similar integration behaviour than an interferometric system, as observed experimentally.

Before introducing the second main body of this thesis we present in Chapter 5 the various signal processing tools employed in the analysis of the experimental ultrasonic wave data along this thesis. These include time domain and frequency domain analysis for application in structural damage detection and location, and characterization. Time-frequency analysis and two dimensional Fourier transform (2D-FT) technique to assess the structural condition as shown in Chapter 6. The thorough analysis of the 2D-FT presented in this chapter gives a

novel interpretation of its results and allows understanding that the aliasing effect in the 2D-FT is not as damaging as in 1D. In the other hand wavelets analysis was used for pre-processing of the data as a de-noising instrument. The chapter finishes with the description of various optimization algorithms as used in Chapter 7 for extraction of the material elastic and geometrical properties.

In Chapter 6 we present the creation of a successful non-contact laser generation and detection of ultrasounds tool for the extraction of the structural properties on mechanical materials. The system uses a Q-switch Nd:YAG short pulse high power laser to generate a broadband source of Lamb waves. These waves propagate along a sample plate interacting with its entire volume. A modified Mach-Zehnder surface displacement optical fibre interferometer is used for the remote detection of these waves.

The 2D-FT and the reassigned spectrogram are applied to the obtained data in order to extract the structural information stored in the ultrasonic wave dispersion features. This information is presented as phase and group velocity dispersion curves, and with the help of an ANSYS model simulation we have identified and developed various enhancements in their resolution, contrast and region of definition. For instance in aluminium plate like samples we were able to identify symmetric and antisymmetric Lamb modes until order 5 and in a region within 0 to 4 *mm/mm* wavenumber:thickness product and from 0 to 14 *MHz mm* frequency:thickness product. We also found that meanwhile the dispersion information provided by the 2D-FT can focus the material property analysis to specific areas of the sample under test, the time-frequency analysis analyse the full area between source and receiver. The Lamb wave dispersion information was later successfully applied to temperature change sensitivity with detectable perturbations caused by changes of 100 degrees. This temperature changes implies modifications of less than 7% in the Young's modulus and Poisson's ratio. In a similar way the dispersion information was also suitable for damage detection applications, clearly showing the increment of a hole-through of diameter varying from 0 to 2 *cm*.

Chapter 7 shows the last part of the work done, which is the application of inversion techniques to the obtained dispersion information in order to extract and monitor changes in the materials elastic and geometrical properties, such as Young's modulus E, Poisson's ratio v and plate's thickness d. The presented inversion technique is based in the minimization of the differences between the phase velocity values of the experimental dispersion curves and theoretical ones obtained for changing values of E, v and d, defined as error function. Followed by an in-depth analysis of the optimization algorithms, the used error function and

its weighting factors we were able to identify those regions of the experimental dispersion curves more suitable for the inversion technique. The convergence of the inversion algorithms was also improved by means of a new technique for simple extraction of an accurate initial estimation of the elastic and geometrical properties based in complementary frequency:thickness product information.

The technique provides values of $E = 71.0 GPa$, $v = 0.352$, and $d = 1.16\ mm$, being able to achieve a worst case scenario error of 1% for *E*, and 2% for *v* and *d*.

The final Chapter 8 is a review of the full work here presented, where the most relevant conclusions of all the previous chapters are highlighted and discussed, pointing in the direction of future recommended work to be carried out.

1.6 REFERENCES

[1] Staszewski W. J., Boller C., and Tomlinson G. R. *Health Monitoring of Aerospace Structures: Smart Sensor Technologies and Signal Processing*, Eds. Chichester: Jon Wiley & Sons Inc, 2003.

[2] 1st and 2nd *European Workshops on Structural Health Monitoring*, 2002 and 2004

[3] 1st, 2nd, 3rd, 4th and 5th *International Workshops on Structural Health Monitoring* from 1997 to 2005.

[4] 1st to 12th *SPIE Symposiums on Smart Structures and Materials* from 1994 to 2005

[5] Kessler S. S. and Spearing S. M. *Structural Health Monitoring of composite materials using piezoelectric sensors*, Materials Evaluation, submitted 2005.

[6] Worden K. and Dulieu-Barton J. M. *An overview of intelligent fault detection in systems and structures*, Structural Health Monitoring, vol. **3(1)**, pp. 85-98, 2004.

[7] Boller C., Biemans C., Staszewski W. J., Worden K. and Tomlinson G. *Structural damage monitoring based on an actuator-sensor system*, Proceedings of SPIE Smart Structures and Integrated Systems conference, Newport, USA, 1999.

[8] Asundi A. K. *Smart Structures research at NTU*, School of Mechanical and Production Engineering, Nayyang Technological University, Singapore.

[9] Culshaw B. *Smart Structures and Materials*, Artech House Books, 1996.

[10] Dakin J. and Culshaw B. *Optical Fibre Sensors: applications, analysis and future trends*, Chapter 16, vol. 4, Artech House, 1997.

[11] Fujino Y. and Abe M. *Structural Health Monitoring –current status and future*, Proceedings of the 2nd European workshop in SHM, pp. 3-10, 2004.

[12] http://www.asce.org/reportcard/2005/

[13] Lucas G. *Central Valley vulnerable to flooding Katrina a reminder of deteriorating levees in California*, San Francisco Chronicle, 9th September 2005.

[14] Farrar C. R., Sohn H. and Doebling S. W. *Structural Health Monitoring at Los Alamos laboratory*, 13th International Congress and Exhibition on Condition Monitoring and Diagnostic Engineering Management (COMADEM 2000), Houston, TX, USA, December 3-8, 2000.

[15] Culshaw B. and Gardiner P. T. *Smart Structures – the relevance of fibre optics*, Fiber and integrated optics, vol. **2**, pp. 353-373, 1993.

[16] 1st to 10th *SPIE Symposiums on Non-Destructive Evaluation for Health Monitoring and Diagnostics* from 1996 to 2005

[17] 1st to 44th *British Conference on Non-Destructive Testing* from 1962 to 2005

[18] http://www.ndt.net/article/v05n09/berke/berke1.htm

[19] http://www.bindt.org/

[20] Hull B., John V. *Nondestructive Testing*, Macmillan, UK, 1998.

[21] Nikou V., Mendez P.F., Masubuchi K. and Eagar T. W. *NDT techniques for inspecting welds in the space environment*, Insight, submitted 2003.

[22] Munns J. and Georgiou *Non-destructive testing methods for adhesively bonded joint inspection - a review*, Insight, vol. **37(12)**, pp. 941-952, 1995.
[23] Khan M. A. U. *Non-destructive testing applications in commercial aircraft maintenance*, Proceedings of the 7th European Conference on Non-Destructive Testing, vol. **4**, 1999.
[24] Vest C. V. *Holographic interferometry*, John Wiley & Sons, New York, 1979.
[25] Miller R. K., McIntire P. *Non-Destructive Testing Handbook*, 2nd edition, Vol. 5: *Acoustic Emission Testing*, American Society for Non-Destructive Testing, 1987.
[26] Maldague X. *Introduction to NDT by Active Infrared Thermography*, Materials Evaluation vol. **6(9)**, pp. 1060-1073, 2002.
[27] Zweschper Th., Dillenz A., Riegert G. and Busse G. *Lockin thermography methods for the NDT of CFRP aircraft components*, NDT.net, vol. **8(2)**, 2003.
[28] Nieminen A. O. and Koenig J. L. *NMR imaging – a promising new adhesive evaluation technique*, J. Adhesion Sci. Technol., vol. **2** (6), pp. 407-414, 1988.
[29] Vallen H. *AE Testing Fundamentals,Equipment, Applications*, , NDT.net, vol. **7(9)**, 2002.
[30] Doebling S. W., Farrar C. R., Prime M. B. and Shevitz D. W. *Damage identification and Health Monitoring of structural and mechanical systems from changes in their vibration characteristics: a literature review*, Los Alamos National Laboratory, Technical report LA-13070-MS, 1996.
[31] Krautkramer J., Krautkramer H. *Ultrasonic Testing of Materials*, Springer-Verlag, New York, 1990.
[32] Sokolov S.Y. *On the problem of the propagation of ultrasonic oscillations in various bodies*, Elek. Nachr. Tech., vol. **6**, pp. 454-460, 1929.
[33] Sokolov S.Y. *Ultrasonic methods of detecting internal flaws in metal articles*, Zavodskaya Laoratoriya, vol. **4**, pp.1468-1473, 1935.
[34] Firestone F.A. US-Patent 2 280 226 - *Flaw Detecting Device and Measuring Instrument*, April 1942.
[35] Firestone F.A. *The supersonic reflectoscope, an instrument of inspecting the interior of solid parts by means of sound waves*, J. Acoust. Soc. Am., vol. **17**, pp. 287-299, 1945.
[36]Desch C. H., Sproule D. O. and Dawson W. J. *The detection of cracks in steel by means of supersonic waves*, J. Iron Steel Inst., vol. **153**, pp. 319-352, 1946.
[37]Sproule D. O. *Improvements in/or relating to apparatus for flaw detection and velocity measurements by ultrasonic echo methods*, GB Pat. 774675, 1952.
[38]Worlton D. C. *Ultrasonic testing with Lamb waves*, Non-Destructive Testing, vol. **15**, pp. 218-222, 1957.
[39] Worlton D. C. *Experimental confirmation of Lamb waves at Megacycles frequencies*, Journal of Applied Physics, vol. **32**, pp. 967-971, 1961.
[40] Moulson A. J. and Herbert J. M. *Electroceramics: Materials, properties, applications*, Chapman & HallLondon, 1990.

Chapter 2

DETECTION & GENERATION OF ULTRASOUNDS

2.1 INTRODUCTION

We have already seen that ultrasonic waves are a very important tool for SHM and NDT applications. But in order to use them first we need a way to generate and detect them within the inspected structural material. Precisely this is the subject of the present chapter.

Until the discovery of the LASER during the 60s, the only way to generate and detect ultrasonic waves was by means of contact transducers. Their requirement of a *couplant* cause serious limitations in their operability; for instance variability in the sensitivity and in the bandwidth, limited velocities in the scanning of the sample, etc (we will see more later). Most of these drawbacks are solved with the non-contact optical ultrasonic generation and detection systems. Even the contact optical ultrasonic detection systems provide various important advantages over the conventional contact transducers; for instance a bigger temporal and spatial resolutions, lightweight characteristics, immunity to electromagnetic radiation, flat spectral response, etc.

Despite the inherent superiority of optical generation and detection of ultrasound, it is still a 'modern' technique compared with the more classical and consolidated contact transducer techniques. This is why its presence in the commercial industry is not yet a reality. It is more complex and expensive than contact transducers, which still dominate the vast majority of ultrasound applications and will do so in the middle-to-near future.

We start this chapter introducing the piezoelectric based contact transducers for ultrasonic generation and detection applications, and later we highlight the main limitation associated with them. The comparison with the advantages that optical techniques provide lead us into the main body of this chapter, which deals with the various optical detection and generation systems that we have used along this thesis. The optical systems used for ultrasonic detection are; fibre Bragg gratings, all fibre interferometric systems based in two different Mach-

Zehnder configurations and a polarimetric system. We characterize and describe each of these systems and subsequently we compare them.

The optical generation of ultrasound is based on high power, very short pulsed laser sources, and low power continuous wave (CW) lasers. The combination of non-contact optical techniques for both the ultrasonic generation and detection stages provides a completely remote inspection tool that can operate in corrosive, high temperature and radioactive environments [1]. That is the subject of chapters 6 and 7.

2.2 CONVENTIONAL TRANSDUCERS FOR THE GENERATION AND DETECTION OF ULTRASOUNDS

The vast majority of the contact transducers are based in the piezoelectric effect due to its dual property of providing both ultrasonic waves detection and generation capabilities with a single transducer.

The piezoelectric effect was discovered by the brothers Curie in 1880 [2], by which piezoelectric materials are able to develop an electric polarization when they are submitted to an external stress. With tension and compression generating opposite polarity proportional to the applied stress. This is how piezoelectric materials can be used for ultrasonic waves detection.

In piezoelectric materials the reverse effect is also present, as a physical deformation of the material occurs when it is under an electric potential. The deformation is proportional to the applied electric field and it affects as an elongation or shortening of the material in the direction of the electric field according to its polarity, phenomenon which is known as *inverse-piezoelectric effect*. This is how piezoelectric materials work as ultrasonic actuators.

The acoustic coupling for piezoelectric transducers (both for ultrasonic generation and detection) require of physical contact with the sample media so that the stress can propagate from one to the other, and of an acoustic conductive interface known as *couplant*. The couplant transmit the ultrasound between transducer and sample, and its absence would cause great variations in the transducer sensitivity between other things [3]. The couplant must consist of a low absorption material, in most cases of fluid or viscous constitution, like oil, grease, or honey. Sometimes also a solid couplant can be used, such as a soft metal.

2.2.1 Conventional ultrasonic generation

When a contiguous medium opposes the increase or decrease of the piezoelectric material dimensions due to the physical deformation induced during the inverse-piezoelectric effect,

then a stress field is transmitted to it and an ultrasonic wave is born. The frequency of the transmitted stress is the same than the frequency of the applied electric field.

The first practical application of piezoelectric materials for acoustic wave generation was due to Paul Langevin [4], during the World War I, who used piezoelectric crystal quartz transducers to generate acoustic waves in water in order to detect German submarines, similarly to the way in which the reflection technique (presented in Chapter 1) was used to detect flaws in a structure. Soon after the quartz crystal was replaced by Rochelle salt for similar underwater sound applications, because of its higher electromechanical coupling properties [5]. Rochelle salt was the first crystal discovered with the properties of ferroelectric materials, they present spontaneous polarization along one axis of the crystal and below their Curie temperature these dipoles line up along this axis. Nowadays over 100 different ferroelectric materials are known, and because they are the most sensitive and provide the higher electromechanical coupling of all piezoelectric materials, they are the most commonly used for actuator and sensor applications. Between the different ferroelectric materials the most common used ones are the ceramics such as barium titanate and lead zirconate titanate (better known as PZT, discovered in the 1950s [6]). PZT ceramics provide a high piezoelectric activity and they can be moulded during their preparation into a great variety of shapes. For instance the shapes used in this thesis are; disc shape used for ultrasonic receiving and generating transducer, and hollow cylinder shape used as a phase modulator in the optical fibre interferometric system later described. These PZT ceramic shapes are shown in fig. 2.1 together with their vibration modes used in our applications (axial and radial mode for the disc shape and radial mode for cylinder shape).

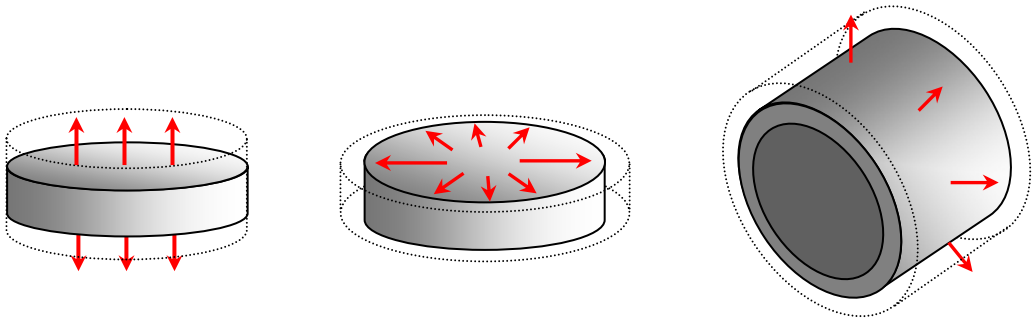

Figure 2.1: PZT used shapes and vibration modes: (*Left*) disc in axial mode. (*Centre*) disc in radial mode. (*Right*) hollow cylinder in radial mode.

Traditionally contact piezoelectric transducers for ultrasonic generation have been divided into two different groups [7,8]; wedge and comb transducers. However modern development

in the piezo-based transducers industry has seen the creation of the piezoelectric wafers, based on very thin piezoelectric ceramics.

2.2.1.1 Wedge transducer

These transducers consist of a piezoelectric material cylinder combined with an angled wedge commonly made of Perspex in a configuration similar to that shown in fig. 2.2. The cylinder piezoelectric actuator is used in axial mode in order to launch longitudinal waves into the structure over which surface the wedge is resting in contact.

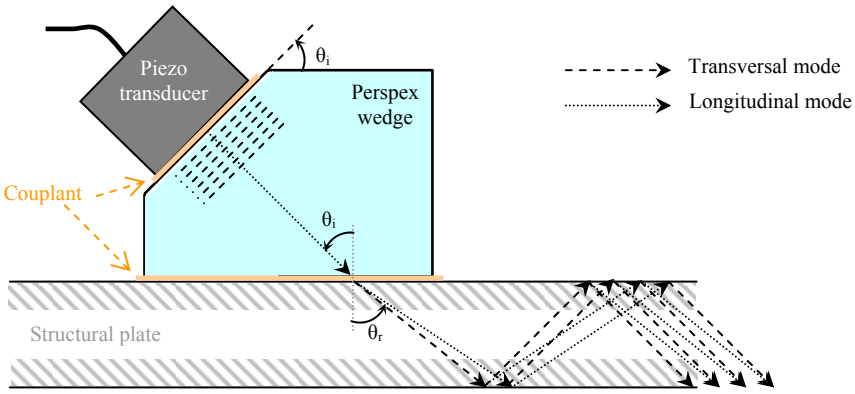

Figure 2.2: In a wedge transducer the phase velocity of the excited Lamb mode is given by the wedge angle and the longitudinal wave velocity in the wedge material.

The launched longitudinal wave is refracted in the interference between the surface of the sample and the wedge, generating also a transversal wave mode. These waves propagate within the plate structure by reflection in its upper and lower surface generating new transversal and longitudinal waves by mode conversion. At some distance from the transducer the interference pattern of these waves no longer allow their individual identification and they propagate as a wave packet. For certain cases of wedge angle, plate thickness and material properties, constructive interference takes place and a guided wave is propagated. In fact depending on the angle of the wedge, different Lamb modes at different wavelength can be selectively launched. Because the refraction of plane bulk waves satisfy *Snell's law* (eqn. 2.1), this law can be used to calculate the resulting phase velocity of the generated Lamb wave or to determine the possible combinations of phase velocity and frequency of the different Lamb modes that could be generated in the structure.

$$\frac{\sin\theta_i}{\sin\theta_r} = \frac{c_i}{c_r} \tag{2.1}$$

Where θ_i and θ_r are the incident and refracted angles of the incident longitudinal mode, respectively. c_i and c_r are the phase velocity of the wave in the wedge and plate respectively.

If a single Lamb mode is to be launched then the reflected angle should be 90^0 (horizontal launch of the wave). Applying eqn. 2.1 the phase velocity of the generated Lamb mode (c_r in that equation) is given by the longitudinal mode phase velocity in the wedge material (c_i in the equation) and by the wedge angle (θ_i) or equivalently $c = c_L / \sin\theta$. Notice that this relation imposes a limitation in the wedge material used. This material must be such that its longitudinal wave velocity is less than the Lamb wave velocity in the structure. The specification of the phase velocity value corresponds to a horizontal line in the material Lamb wave phase velocity dispersion curves, that intersects with multiple modes at different frequencies. The launched Lamb mode will be given by the frequency at which the piezoelectric transducer is excited. For a more detailed discussion see Appendix A and [9].

2.2.1.2 Comb transducer

An array of periodically spaced piezoelectric elements are placed on the structural surface with a couplant medium in between to properly transfer the excited longitudinal waves into the structure, as shown in fig. 2.3.

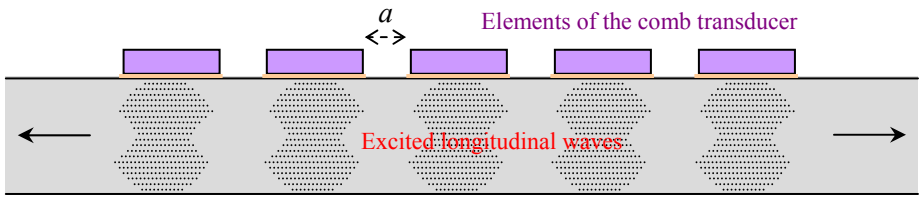

Figure 2.3: In a periodic array or comb transducer the wavelength of the excited Lamb mode is given by the distance between the comb elements.

The *comb* pumps energy into the structure by exciting all the elements in phase or out of phase, generating bulk waves that propagate in both directions along the structure. The spacing between the comb elements a is chosen such that satisfies $2a = \lambda$, with λ being the desired wavelength of the generated Lamb wave. The selected wavelength only determine a slope in the phase velocity dispersion curves and in theory any intersection of this slope with the different Lamb mode curves would allow their excitation as long as the excitation frequency of the comb elements is adequately chosen. It is also possible to change the excited Lamb wave wavelength (or excited slope in the dispersion curves) by using a suitable time delay profiling of the comb elements excitation [8]. Some uses of comb transducers for NDT applications are [10], a more detailed analysis is given in [11].

2.2.1.3 Piezoelectric wafers

Unfortunately the previous conventional ways of generating ultrasounds are relatively too heavy, too big and expensive to be considered as an ultrasonic generation technique for widespread structural deployment in NDT or SHM applications [7]. In recent years a development in the piezo-based transducers has seen a huge improvement on the previous limitations by the creation of *piezoelectric wafers*. Piezoelectric wafers, also called patches, are very thin piezoelectric ceramics with lightweight characteristics that can be created in small dimensions and moulded in a great variety of shapes, the disc shape being the one chosen in this thesis for its omnidirectional radiation characteristics allowing larger interrogation zone for NDT applications. Their dimensions are typically of a few millimetres in diameter and just a few hundred micrometers in thickness, making them very low cost transducers and relatively unobtrusive when bonded or embedded into different structures. The most widely exploited piezoelectric ceramic is the PZT type. Their dominant role in the piezoelectric wafers market is due to their large radial electromechanical coupling factor k_p that characterize the ability to generate large radial displacements, and also because they have a relatively high Curie temperature (temperature above which the material stops being piezoelectric) [12]. This type of ceramic is also chosen for our applications.

The piezoelectric wafers have several advantageous operational differences with respect to the previously described contact transducers:

- In the wedge and comb transducers the coupling transfer of the ultrasound to the structure is weak, with the couplant mainly being water, gel, honey or air. In contrast piezoelectric wafers are strongly coupled to the structure by adhesive bonding (in this work we used Epoxy bonding) or embedding into the structure, thus following the structural dynamics.
- Wedge and comb transducers excite and sense the structural ultrasonic waves indirectly through out-of plane strain by mode conversion of bulk waves interacting with the surfaces of the structure. In contrast the piezoelectric wafers excite and sense the ultrasound in the structure directly through in-plane strain coupling [7] because piezoelectric wafers commonly use their planar mode (also called radial mode for disc PZTs as shown in fig. 2.4-*right*).

The rest of this section concentrates on the operation of PZT disc transducers for ultrasonic generation, as they are the ones used in this thesis.

Figure 2.4 shows the axial and radial vibration modes of a disc shaped PZT transducer, consisting in an elongation or shortening of the material in the direction of the electric field

according to its polarity. The physical deformation of the disc is proportional to the applied electric field. The medium to which the disc is bonded or embedded causes an opposition to this deformation and a stress field is transmitted into the medium.

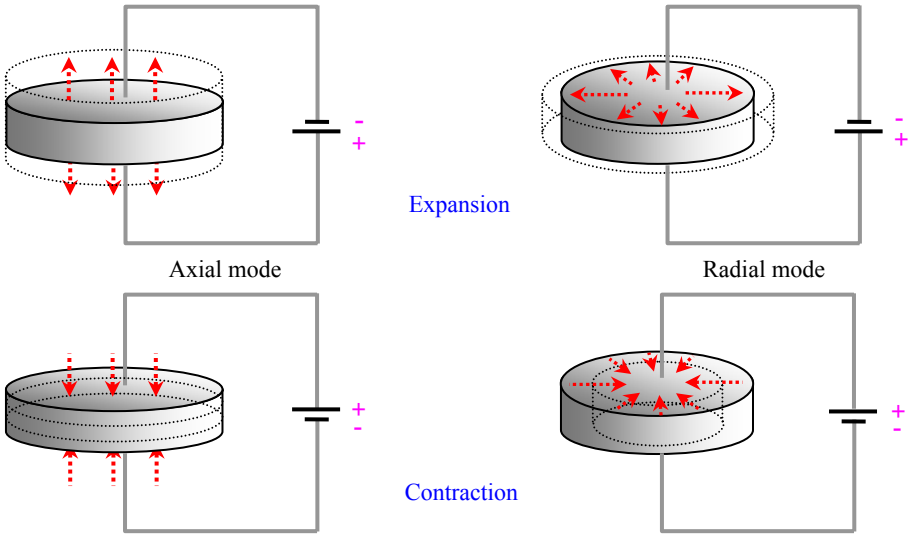

Figure 2.4: Inverse-piezoelectric effect on a disc shape PZT for its axial and radial modes (left and right respectively). (*Top*) The polarity of the applied electric field generates an expansion of the piezoceramic vibration mode. (*Bottom*) Inverse polarity to previous case generates a contraction of the piezoceramic vibration mode. The dashed lines indicate final dimensions.

Notice that although in fig. 2.4 we show the axial and radial vibration modes of the disc PZT transducer independently, in most cases these modes are coupled.

The equation that describes the response of a piezoelectric material during the inverse piezoelectric effect is a tensorial relation between mechanical and electrical variables [13]:

$$S = s^E T + dE \tag{2.2}$$

Where E is the applied electric field, T is the mechanical stress applied to the material, S is the strain and s^E is the mechanical compliance at a particular value of E. The quantities represented in capital letters are vectors and the ones represented in lower case are tensors. For a PZT disc bonded to the surface of a material, if an electric field is applied in the normal direction to the surface the only significant induced strains are in the axial mode [13].

The PZT disc in the same way as any elastic plate can oscillate mechanically in a similar fashion of a classic mass and spring system. The geometry and mechanical properties of the plate define its resonant frequency, such that the largest amplitude of the mechanical oscillations is generated when excited at this frequency. In a piezoelectric material the excitation is done by applying an alternating voltage to its electrodes. In practice the resonant system also include a damping term, which for the case of the oscillating PZT disc is given

in the form of internal friction and energy convection as ultrasonic waves are transmitted to the adjacent structure. Therefore, the mechanical behaviour of a piezoelectric material near resonance can be approximated by an equivalent electrical circuit as shown in fig. 2.5.

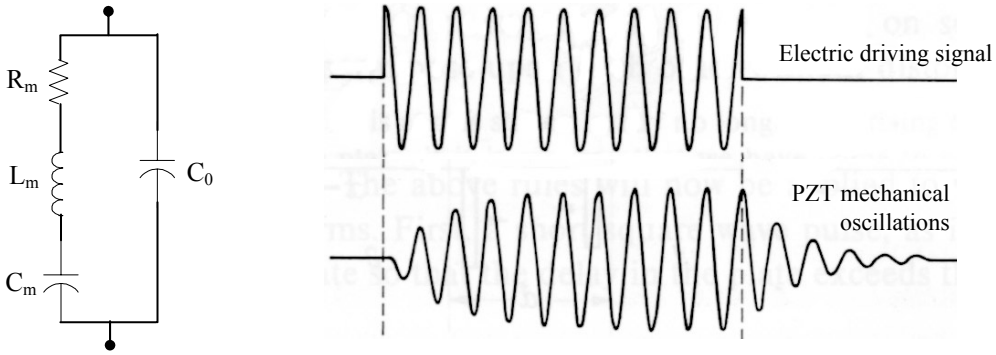

Figure 2.5: (*Left*) electrical equivalent circuit for PZT disc operating near resonance. C_0 is the electrical capacitance, R_m is the mechanical damping and L_m and C_m associated with mechanical resonant properties. (*Right*) Comparison between a toneburst driving electric signal (*top*) and the generated PZT mechanical oscillations (*bottom*).

Based in the described mechanical resonant behaviour of the PZT discs, fig. 2.5-*right* shows the PZT response to a toneburst driving electric signal. At the beginning and end of the driving toneburst the PZT tends to resist any mechanical change, due to its inertia and elastic forces, thus smoothing the oscillation as build-up and decay transients. The effect of these transient oscillations is attenuated by increasing the mechanical damping coefficient of the PZT, so that the actual oscillation of the disc resembles more closely the driving voltage [3]. Alternatively if the driving voltage is windowed then a similar effect can be achieved as explained in Appendix E.

2.2.2 Conventional ultrasonic detection

The detection of ultrasonic waves by conventional piezoelectric transducers is based in the piezoelectric effect. When a stress field is applied over a piezoelectric material, its randomly polarized domain structures [3] respond such that a compression perpendicular to the direction of polarization or tension parallel to the direction of polarization will generate a voltage with polarity opposite to that of the poling voltage. The generated electrical polarity is proportional to the magnitude of the applied stress, with tension and compression causing opposite polarity as shown in fig. 2.6 for the axial and radial vibration modes of a disc shaped piezoelectric material. In this figure the applied stress is represented by red arrows and the induced dipole moment is shown as blue arrow. If an electric circuit is connected to the electrodes of the piezoelectric material, the induced dipole moment causes an electric

transient current to circulate, with compressive and tensile stresses producing currents in opposite sense (as shown by the grey arrow in fig. 2.6). It is obvious the great potential of piezoelectric effect for the detection of the stress field associated to propagating ultrasonic waves.

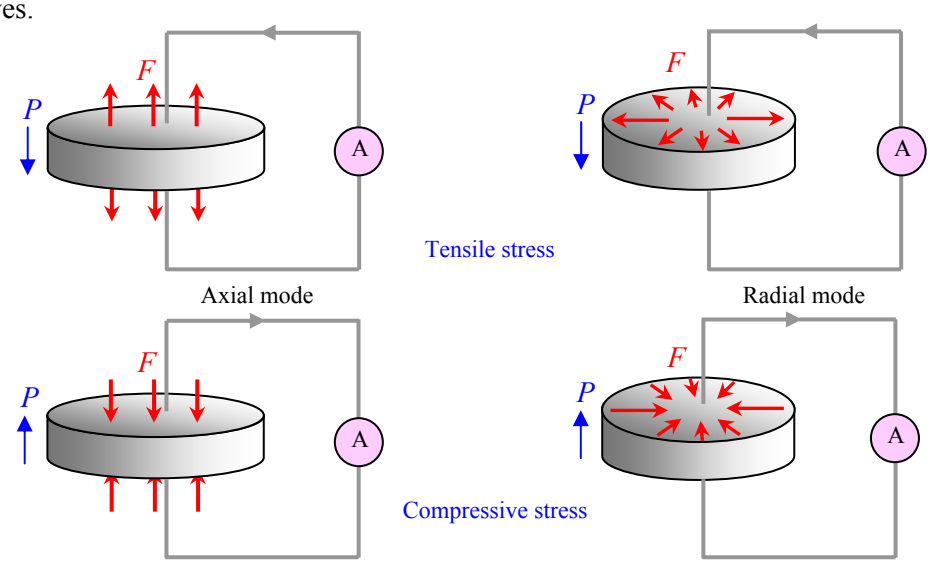

Figure 2.6: Piezoelectric effect on a disc shape PZT for its axial and radial modes (left and right respectively). In red the applied external stress and in blue the induced dipole moment (*Top*) Tensile stress and (*Bottom*) compressive stress produce an opposite sense electric current in an external electric circuit.

2.2.2.1 Piezoceramic sensors

The equation that describes the response of a piezoelectric material during the piezoelectric effect is a tensorial relation between mechanical and electrical variables [13]:

$$D = d \cdot T + \varepsilon^T E \tag{2.3}$$

Where D is the induced electrical displacement, E is the generated electric field, T is the mechanical stress applied to the piezoelectric material, d is the piezoelectric coupling between the electrical and mechanical variables and ε^T is the dielectric permittivity measured at zero mechanical stress ($T = 0$).

The dual characteristic of piezoelectric materials (ultrasonic generation and detection) makes of piezoelectric sensors adequate for structurally integrated NDT applications and smart structures. With the added advantage of modern development that has allowed making them smaller, more reliable and cheaper. Therefore they have become the most widely used NDT sensors for ultrasonic guided waves applications mainly in their piezoceramic version. Piezoceramic sensors have developed into different technologies, with the most important being (together with the piezoceramic wafer previously described):

SMART Layers (or Stanford Multi-Actuator-Receiver Transduction Layer)

SMART layers consist in a network of piezoelectric wafer discs embedded in a think dielectric carrier film [14,15]. This layer can either be surface mounted on existing structures or integrated into a composite structure during fabrication, allowing the creation of a Smart structure by non-destructive assessment of the internal and external states of the structure.

Piezoceramic paint

This piezoceramic sensor is a composite material comprising of finely powdered PZT particles embedded in a polymer matrix [16]. The paint is water based acrylic formulation in which the pigment in conventional paint is substituted by the PZT particles. The passive polymer matrix must have high permeability, high modulus and good adhesion to both PZT and all common structural materials. In fig. 2.7 we show the simple steps needed to create an ultrasonic sensor based in piezoelectric paint (as described in [17]).

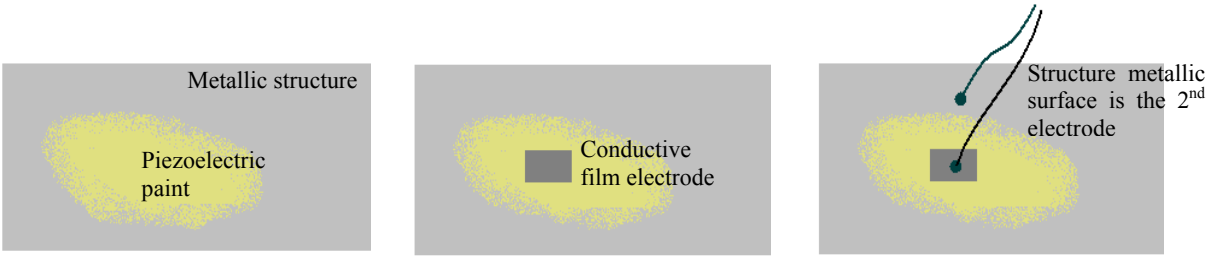

Figure 2.7: Steps for a piezoelectric paint vibration sensor: (*Left*) Piezoelectric paint is sprayed over the surface of a conductive material, (*Centre*) a conductive film is sprayed over the piezoelectric paint layer to form an electrode, (*Right*) attach leads to electrode and structural metal surface (2nd electrode).

When the structure vibrates, the film is stretched with it and an electric charge appears on the electrodes. Piezoelectric paint sensors are very suitable for measuring shock and vibration on large structures.

A PZT wafer in a disc shape fig. 2.1 (for its omnidirectional radiation characteristics) is the contact transducer used in this thesis, for ultrasonic generation and detection, in those applications that require ultrasonic waves of narrow frequency band. Such as the damage detection and location applications described in next chapter, and the experimental work of Chapter 4.

2.3 LIMITATIONS OF CONVENTIONAL TRANSDUCERS AND ADVANTAGES OF OPTICAL TECHNIQUES

Most of the limitations related with conventional contact transducers are due to their need of couplant [18]:

- Variability in the sensitivity and in the bandwidth of the generated ultrasounds; caused by an inhomogeneous distribution of the couplant through the contact surface. Originating problems of repeatability.
- Limited scanning velocities; because it is important to maintain a good and homogenous coupling between transducer and structure.
- Limited temperature application; due to the difficulty to find ultrasonic couplants which will work at temperatures in excess of a few hundreds °C.
- Possible chemical reactions between the couplant and the surface of the sample.
- Contact transducers load the sample's surface, influencing the propagation of the ultrasonic waves.

The important restriction of these drawbacks associated with contact transducers has lead to the development of other type of non-contact ultrasonic transducers that are couplant free. Between them, *EMAT* (Electromagnetic acoustic transducers) are probably the best known [18]. A detailed description of their operation can be found in [3]. Although non-contact, EMAT transducers are restricted to structures with a conductive surface layer and they are susceptible to sensitivity variations due to changes in the separation between probe and sample surface. Additionally EMAT share other important limitations with piezoelectric contact transducers:

- Narrow bandwidth generated ultrasound; because the piezoelectric element in the transducers is a resonant system, generating ultrasonic frequency bandwidths no greater than a few hundreds of kHz. For the same reason, piezoelectric transducers have great sensitivity for single frequency applications at which their resonant frequency is tuned. We will see in next chapter examples of such applications involving damage detection and location.
- Low spatial resolution; no more than a few *mm*, due to the relatively large size of the piezoelectric probes and EMATs. Their size also limits their usability in restricted areas or small specimen applications.
- Susceptible to electromagnetic interference (EMI); the electromagnetic radiation between the source and detection stages of these transducers is frequently a big problem, in addition of pickup of environmental EM radiation [19].

The modern optical systems developed for ultrasonic generation and detection applications not only offer solutions to most of these limitations:

- It provides broadband generation and detection of ultrasound (tens of *MHz*).
- Flat spectral response (due to the absence of resonant coupling conditions).

- Good electromagnetic environment tolerance; optical fibre is made of a dielectric material, thus optical fibre sensors are immune to EMI. This makes optical fibre sensors very eligible to be placed close to high EMI sources like power generators, and to structures inclined to lightening strikes as bridges, tower or aircrafts.
- Lightweight and high spatial resolution. With optical fibre sensors providing spatial resolutions of tens of μm or even better if non-contact interferometric systems are used, given by the spot size of the focused laser beam.
- Great geometrical versatility allowing unobtrusive integration for structural monitoring and great accessibility to restricted areas by use of mirrors or optical fibre to steer the optical beam.
- Adaptability to extreme environment conditions; optical fibre can support temperatures of around 700^0C (with exception of FBGs with no more than 300^0C). However the use of interferometric non-contact optical techniques allows a completely remote inspection (several meters or more) that can operate in corrosive, high temperature and radioactive environments [1]. Notice that for EMAT transducers the distance from the receiver probe to the sample's surface should not be bigger than 1 *mm*, which cannot be considered a remote inspection.
- High speed and repeatable scanning; mainly when a non-contact interferometric optical system is used, as the focused measuring laser beam can be changed quickly and accurately.

They also provide the following added advantages:

- It launches simultaneously bulk, surface and guided waves. It can therefore be used to detect volumetric, surface and subsurface defects.
- The optical beams can reach areas that are difficult to access, if we use optical fibres or mirrors to steer them.
- High degree of absolute accuracy; measurements can in principle be calibrated against the wavelength of the light.

Nonetheless optical systems present also some disadvantages in comparison with their electromechanical counterparts; they are more complex and costly to use, they have safety issues regarding high power laser radiation and they have less sensitivity.

A resume of the most important shortcomings of conventional contact transducers and the benefits that optical systems provide for ultrasonic generation and detection applications are schematically displayed in fig. 2.8.

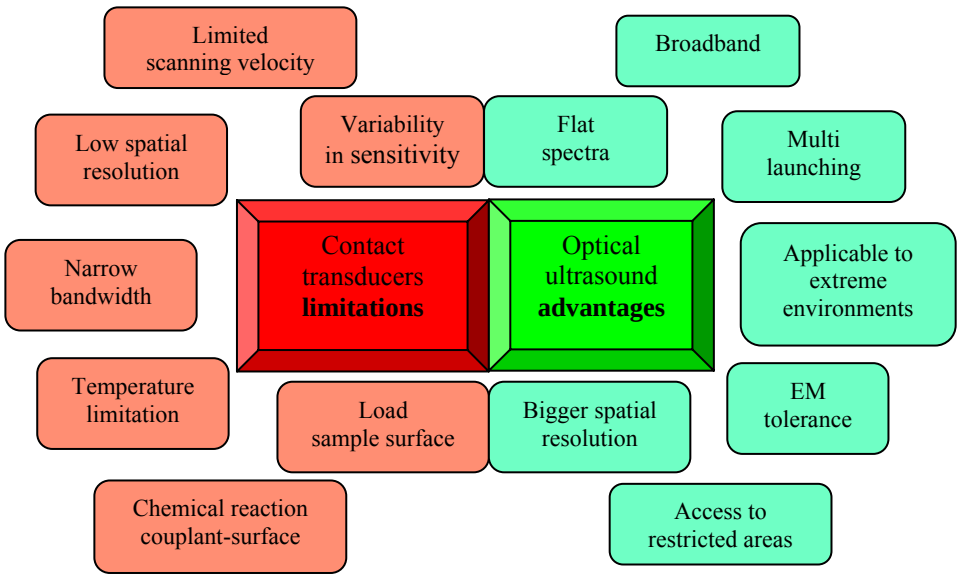

Figure 2.8: Comparison between the most important limitations of the contact transducers (in red) and the advantages of the optical techniques in the application of ultrasonic detection and generation.

2.4 OPTICAL TECHNIQUES FOR THE GENERATION AND DETECTION OF ULTRASOUNDS

The conventional contact transducers dominate the vast majority of industrial applications for ultrasonic generation and detection [20]. However in a small number of cases the limitations associated with contact techniques requires alternative methods. This happens with the two applications that this thesis deals with; non-destructive testing (NDT) of materials including health monitoring of advanced structural composite materials [18,21] and the measurement of material elastic properties [22]. In addition to advantages such as high speed, repeatable scanning and electromagnetic immunity that non-contact optical techniques provide to these applications. Even more vital is the benefits attainable by complementing a non-contact optical detection technique with a non-contact optical generation technique. The broadband as well as flat frequency spectrum response characteristic to optical detection techniques is in this way complemented with broadband generated frequency spectrum which although not flat, falls slowly and monotonically with increasing frequency [23]. The same can be said of the spatial characteristic broad bandwidth, as both the optical generation and detection is based in a laser beam which can be focused to micrometers dimensions, giving to this technique an advantageous position for MEMS technology, cellular biology and acoustic microscopy applications [24]. In the next sections we described the non-contact optical generation of ultrasound techniques used in

this thesis and also we analyse and compare the four optical fibre systems used for ultrasonic detection.

2.4.1 Optical generation of ultrasounds

Laser generation of ultrasound has been discussed extensively in the literature [18,21,25,26], and the intention of this chapter is to provide only a general overview of the subject.

Light is not a mechanical entity, though there are various mechanisms whereby light can be transformed into mechanical motion. The most basic of these mechanisms is the *radiation pressure* where the momentum of the photons in the light beam is changed as they are reflected from or absorbed by a surface. However the principal mechanism involved in laser generation of ultrasound is through the heat that the light beam induces in the material. We shall see next how this heat is generated, restricting our analysis to metal materials as this group of solids is the one used in this thesis.

2.4.1.1 Mechanism for optical generation of ultrasound

When the beam of a laser is directed onto a solid sample, the electromagnetic radiation interacts with electrons in the material close to the surface. Some of this incident radiation is absorbed by the sample by various mechanisms, whilst the remainder of the energy is reflected. The conduction electrons at the surface screen the interior of the material from the beam's radiation, thus the radiation absorption only takes place within a thin layer in the surface named *skin depth* δ. For wavelengths in the near infrared/visible spectrum δ is given by eqn. 2.4 [18].

$$\delta = \left(\pi \sigma \mu_r \mu_0 \nu\right)^{-1/2} \tag{2.4}$$

Where σ and μ_r are the electrical conductivity and relative permeability of the material, μ_0 the permeability of free space and v the frequency of the radiation. Substituting for aluminium with radiation at 1064 *nm* wavelength, then we get a skin depth of 5 *nm* (a small fraction of the optical wavelength).

In a metallic material most of the absorbed radiation is transformed into thermal energy through resistive loses thereby heating the surface of the sample at a skin depth layer. Thermal conductivity distributes this heat through the sample as shown in fig. 2.9 for a Gaussian time dependence pulsed laser of 20 *ns* pulse width and 100 *mJ* energy incident over an area of 10 mm^2 providing a maximum power density of about 2 MW/cm^2. The figure shows how at the beginning of time, when the laser pulse is shot, the temperature increases

as the pulse energy is being absorbed. Once the laser pulse is stopped, the temperature falls as the heat is conduced into the bulk of the material.

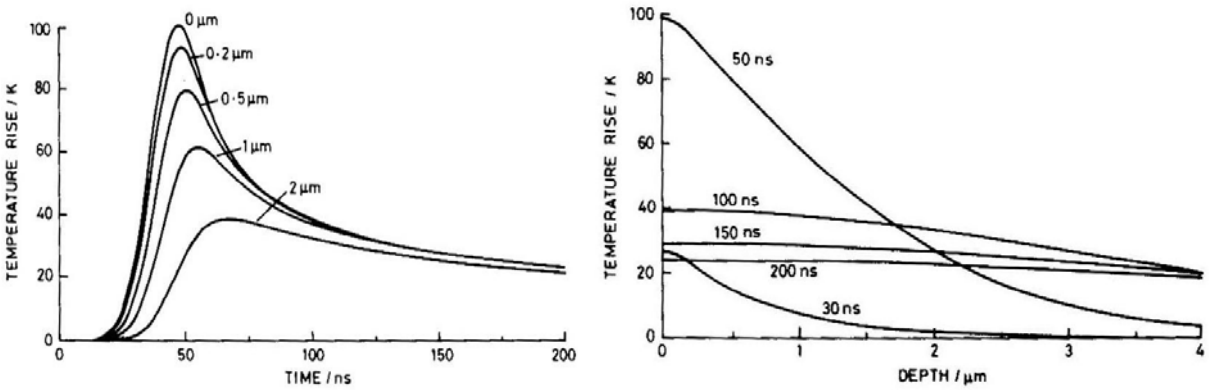

Figure 2.9: Temperature distribution in aluminium for a Gaussian time dependence of a laser pulse with maximum power density 2 MW/cm^2 and duration 20 *nsec*; (*Left*) as a function of time for a range of depths, (*Right*) and as a function of the depth at 50 *nsec* after the pulse is shot. Figure from [18].

The induced temperature gradients generate the stress and strain fields by thermal expansion. Any temporal variation of these stress fields generate, in turns, elastic waves. In order for this stress field variation to take place, the optical beam must be modulated (like in fig. 2.9 where a pulse modulation was assumed) so that the DC component of this modulation causes a steady rise in the material temperature, and the dynamic component produces the acoustic wave. As we can see from the previous figure, the rapid temperature changes occur within a few microns of the surface, extending the effective source depth from the previous skin depth value. The new source depth is given by the thermal diffusion length δ_ω, defined as a function of the radiation frequency ω in eqn. 2.5 [18], where σ_{th} is the thermal conductivity of the material, ρ its density and c_s is the specific heat.

$$\delta_\omega = \sqrt{\frac{2\sigma_{th}}{\omega \rho c_s}} \tag{2.5}$$

The described mechanism of laser generation of ultrasound is exploited in different ways so that two ultrasonic source regimes are distinguished; Thermoelastic regime and ablation or plasma regime. The next sections provide a brief description of each of them.

2.4.1.2 Thermoelastic regime

When the power density of the radiation is below 10^7 W/cm^2 for most metals, then the only ultrasonic generation effect that takes place is the one previously described. Thus the ultrasonic source can be considered as a centre of expansion in the surface of the material.

The simplest model for this ultrasonic source is to neglect thermal diffusion effects and approximate it to a surface point heating expansion source, which is equivalent to a set of three orthogonal pair of forces (*force dipoles*) as shown in fig. 2.10-*left* [27]. The in-plane dipoles are equal ($D_{11} = D_{22}$), however for a free surface solid body and considering the heated area to have zero thickness (or the thickness to be much smaller than the laser spot as it is in our case), the dipole normal to the surface can be neglected ($D_{33} = 0$). The net result is an in-plane stress ultrasonic source. A detailed mathematical analysis of this source is given in [28]. This model deals with sources of finite dimensions by assuming that they are composed of an assembly of point sources over its area. These models predict the major features of laser generated ultrasonic waves [29] and they have been positively experimentally verified in [30,31] for highly focused and nanosecond duration laser sources.

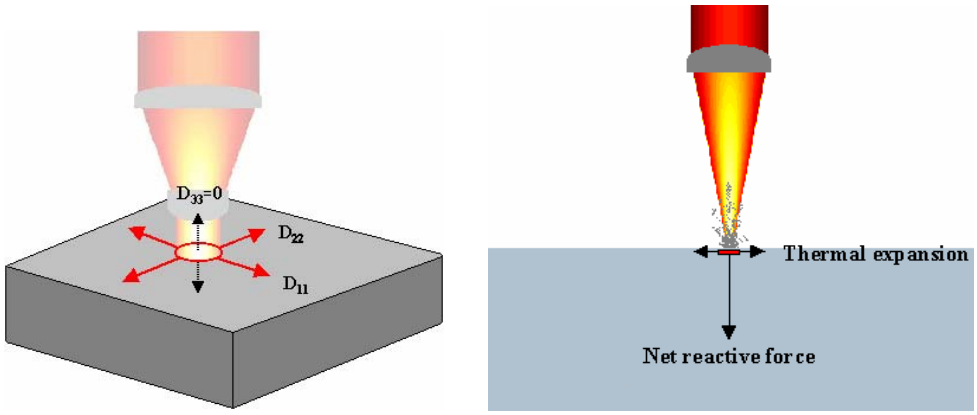

Figure 2.10: Optical generation of ultrasounds: (*Left*) Thermoelastic regime. Ultrasonic source is a centre of expansion with principal stress components parallel to the surface and no perpendicular stress components. (*Right*) Ablation regime. Plasma formation causes a reactive stress predominantly normal to the surface.

In [32] the radial displacement values in the far field are obtained based in the previous model. It can be demonstrated [18] that for low energy levels (such that vaporization of the surface is avoided) a linear relationship exists between the generated sound amplitude and the energy of the light source. In order to generate reasonable ultrasonic wave amplitudes (around 1 *nm*) at a distance of 10 *cm* in the range of frequencies between 100 *kHz* to 10 *MHz* the most effective method appears to be a short-pulsed laser with peak power of *MW* and *nsec* pulse width. This is the approach taken in this thesis, where a Nd:YAG Q-switched laser source of 5 *nsec* pulse width, 850 *mJ* pulse energy and 1064 *nm* wavelength was chosen (for a detailed description of the Q-switching technique see references [33,34]).

In order to improve even further the signal to noise ratio of the generated ultrasonic signals, the laser beam is focused into a line-source rather than a circular spot. In this way more

energy can be injected into the surface while keeping the energy density low enough. The directionality of a line-source with plane waveforms generated parallel to the line decreases the spreading attenuation in comparison with an omnidirectional circular source.

The equivalent mathematical model for the two-dimensional case of an infinitely long and thin line-source excitation has been analysed in [35]. A more accurate model is presented in [36] where thermal diffusion and finite length and width of the line-source is taken into account. It is also recommended the simplified approach developed in [37], that calculates the motion of ultrasonic surface wave pulses generated by the laser irradiation, of arbitrary time dependence, at a point and a finite line of a homogeneous isotropic solid.

The most accurate models [36,37] of thermoelastic excitation that take into account the thermal diffusion disagree with the approximated models only in the near field close to the radiated region, however in the far field (which is satisfied in our experiments) both models are indistinguishable.

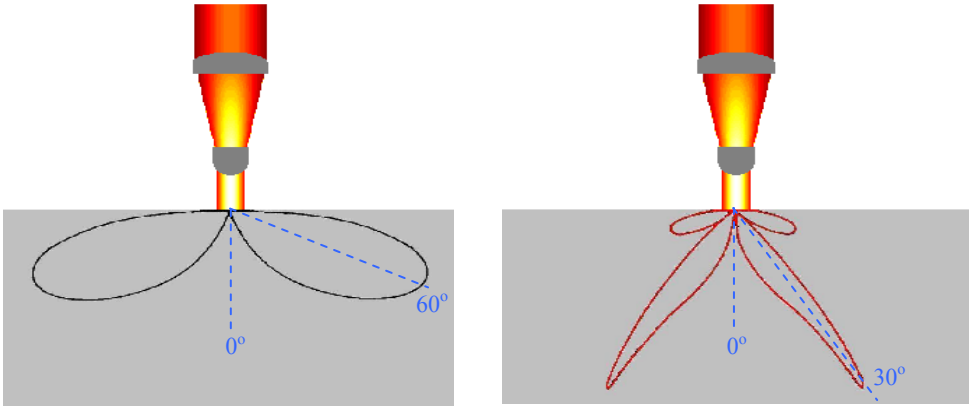

Figure 2.11: Directivity pattern of longitudinal waves (*Left*) and transversal waves (*Right*) for thermoelastic regime source in Aluminium. Amplitudes plotted in arbitrary units.

As predicted by these models, the amplitude of the bulk waves generated by laser generation is found to be a function of the angle measured from the normal to the surface of a semi-infinite metal body. The directivity patterns of the transversal and longitudinal modes induced by both point source and line-source are very similar as shown in [30], provided that the directivity patter of the line-source is determined in a plane perpendicular to the surface of the material and the line itself. These directivity patterns are illustrated in fig. 2.11 for aluminium. They are characterized by having little radiation either perpendicular or parallel to the surface of the metal. Meanwhile the longitudinal mode is predominately radiated at an angle of 60^{o}, the transversal mode has an enhanced directivity at an angle of 30^{o}.

We must notice that both directivity patters are not in the same scale, however for thermoelastic regime both longitudinal and transversal modes are generated with same order of magnitude [3].

2.4.1.3 Ablation regime

When the power density of the radiation is increased by any means (for instance decreasing the pulse duration or the laser spot for a given pulse energy or increasing the pulse energy itself) over a specific threshold which depends in the material (~ 10^7 W/cm^2 for most metals), then its surface starts boiling (as shown in fig. 2.10-*right*). Sample to the depth of several micrometers is vaporized forming plasma [18]. This ablation of material produces a reactive stress predominantly normal to the surface. Thus the ultrasonic source in this regime has its principal stress normal to the surface of the solid body, in contrast to the in-plane stress component of the thermoelastic regime. The difference between the ultrasonic sources of both regimes is evident as well in the far-field directivity pattern of the longitudinal and transversal modes generated by them. Like we did for the thermoelastic regime, we have represented in fig. 2.12 the directivity pattern of both bulk waves for an aluminium semi-infinite body. The longitudinal mode is principally radiated in a direction normal to the surface, whereas the transversal mode is radiated mainly at an angle of 35º.

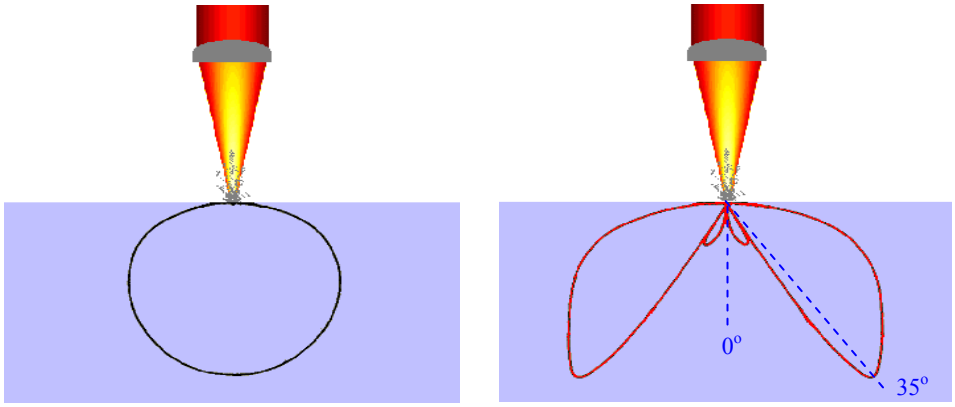

Figure 2.12: Directivity patter of longitudinal waves (*Left*) and transversal waves (*Right*) for ablation regime source in Aluminium. Amplitudes plotted in arbitrary units.

As with the thermoelastic directivity patterns, the ones shown here are not in the same scale, in fact in the ablation regime the amplitude of longitudinal waves radiated normal to the surface are of higher order of magnitude than the transversal modes [3], giving support to the affirmation that the ablation regime is dominant normal to the surface ultrasonic source.

The ablation regime causes inevitably surface damage, however in applications where surface conditions is not important this ultrasonic generation technique can be considered as

non-destructive. In fact as noted in [38] ablation regime by high power short pulsed lasers are inefficient in removing material from target. The reason being that the very high power density of the pulse causes only a small mass of the material to absorb the radiated energy, which vaporizes almost explosively at a very high temperature. The resulting plasma screens the remaining part of the surface from the pulse and the high pressure of the plasma raises the boiling point of the material suppressing new metal loss.

In the ablation regime the generation of compression and surface waves is enhanced by increasing power density, but shear waves will reach a maximum near the onset of plasma and then decrease as the power density increases [18].

2.4.1.4 Conclusions about optical generation of ultrasounds

In conclusion, the thermoelastic source with its dominant in-plane motion will naturally couple more efficiently into symmetric Lamb mode launch because this mode has commonly a main in-plane displacement component (see Appendix A). Whereas the plasma regime with its normal to the surface reaction component couples more efficiently into antisymmetric Lamb modes with a main out-of-plane displacement component associated. The compatibility of the plasma regime out-of-plane reaction component, with the out-of-plane displacement sensitivity of the laser interferometer used in the optical detection stage of this thesis (shown later in this chapter), made us choose an ablation ultrasonic source. With the additional benefit that this regime provides ultrasonic waves of higher amplitude in comparison with the thermoelastic regime as higher power densities are required.

2.4.1.5 Low power laser generation of ultrasound

The optical generation of ultrasound by a short pulse from a Q switched Nd:YAG laser with a pulse energy of significant fraction of a joule, provides high peak temperature increments which allows good optical to acoustic conversion efficiency. But also an important propensity to cause significant surface damage. An alternative examined involve CW low power lasers with modulated output intensity. The low power laser source reduce the maximum temperature increment of the surface thus also the conversion efficiency. Then higher optical energy should be provided to the material, by means of increasing the average laser power (a $1W$ semiconductor laser source is used). Still the amplitude of the generated ultrasound is small and the detected signal will be dominated by thermal noise in the detector system, unless very narrowband sensitive lock-in detection schemes are used [39]. Alternative that has problems of frequency dependent detector positioning. A better approach taken by our group is based on the total random characteristic of the thermal noise,

thus the ultrasonic wave can be separated from the noisy signal by applying a pseudorandom noise modulation technique, which allowed a broadband Lamb wave generation [40] although often not as large as that generated by Q-switched high power pulse lasers. In our case, the laser diode source is modulated with a Golay code [41], chosen for its preferential autocorrelation characteristics for the unipolar signal representation suitable to optical systems intensity modulation. The highly noisy detected signal is cross-correlated with the laser diode driving signal. The overall effect of the code consists in generating a series of impulses into the sample plate which later are averaged during the correlation process, being able in this way to extract the acoustic information from a very noisy signal.

The SNR of the ultrasonic signals generated by low power laser sources can be enhanced by applying elastic constraint at the heated surface as demonstrated in [42] in collaboration with other members of our research group. In this case a light absorbing material with high thermal expansion coefficient (black paint) was chosen to further enhance ultrasonic generation. The main effect of the constrain is to introduce a large stress normal to the surface by a combination of increased absorption and vaporization of the constrain layer.

2.4.2 Optical detection of ultrasounds

All the optical detection systems used in this thesis and presented in the next sections are based on optical fibre technology. There are multiple reasons for doing so; optical fibre systems allow an easier and more flexible handling of the sensing light beam than bulk optical components, and avoid the alignment difficulties of bulk systems. They are portable in opposition to most bulk optic systems, and they are safer because the laser beam is always confined within the fibre, and reduce the optical energy lost and scattering noise due to the laser beam interacting with the surfaces of the bulk optic components. Most importantly optical fibre sensors have the potential of being unobtrusively integrated into the structure under inspection, which is of great advantage for the SHM and NDT applications that this thesis aim to demonstrate. Additionally optical fibre sensors are compatible with modern telecommunication data transmission systems and they are intrinsically low-loss, therefore providing to the monitoring system of a truly remote operation from the processing centre.

The sensing principle of an optical fibre sensor is divided into two groups regarding the way they sense the environmental effects:

- *Extrinsic sensors* (fig. 2.13-*left*): the optical fibre acts as a guide of the light into a transmitting optical system that illuminates a measurand volume in which the light is modulated by different interactions with the environmental signal to be evaluated. Later an

optical fibre is again used to guide the modulated light collected by a receiver optical system towards the photodetector. The optical fibre is used as information carrier by its guided light.

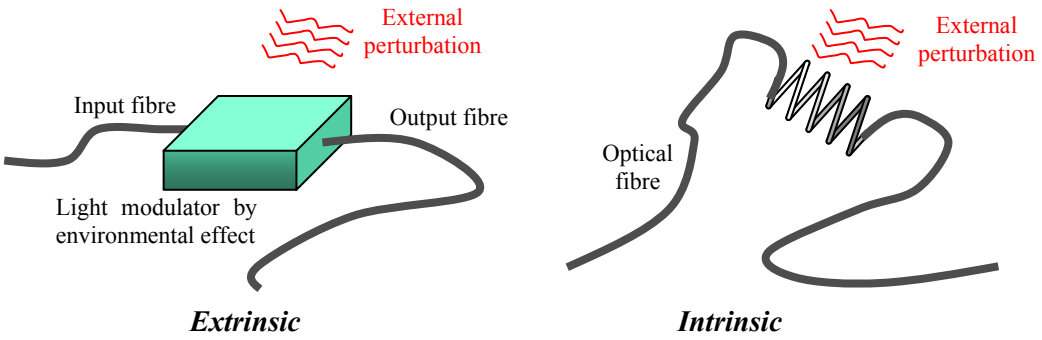

Figure 2.13: Extrinsic and Intrinsic optical fibre sensors.

➢ *Intrinsic sensors* (fig. 2.13-*right*): now the light does not leave the optical fibre that guides it. The physical measurand is encoded as a change in a property of the optical signal being carried in the core of the fibre. The wide range of available optical fibre sensors allow sensing of virtually any environmental effect of interest; strain, temperature, pressure, displacements, vibration, acceleration, speed, rotation, force, humidity, viscosity and surface condition [43].

In this thesis we work with four different optical fibre sensors that are suitable candidates to be part of a fibre optic smart structure application. These are; two different Mach-Zehnder configuration interferometric sensors, polarimetric sensor and fibre Bragg grating sensor. Between them only one of the Mach-Zehnder interferometer configurations (named *modified Mach-Zehnder*) belongs to the extrinsic sensors group and it is also the only one that allows remote detection of ultrasonic waves. The operation of these optical fibre sensors and the principles of their transduction of the measurands involved in ultrasonic sensing applications (strain, displacement and pressure) is the subject of the next sections.

2.4.2.1 Fibre Bragg gratings

Since their demonstration in 1989 by Meltz and co-workers [44], fibre Bragg gratings have seen an explosion of activity and a growing importance and dominance in the optical fibre sensors, smart structures and structural health monitoring communities. This is illustrated by the enormous percentage of papers based in these sensors in comparison with other sensor devices that a literature survey of the main conferences in the previous subjects show [45-47]. The major reasons that make FBGs so prominent not only in ultrasonic detection applications but also in optical communications, sensors and lasers applications [48] is; their very good long term stability and high reliability [49], their multiplexing capabilities and

their multifunctionality to measure strain, pressure and temperature with easy calibration and providing absolute values of these magnitudes.

FBG fabrication is based in the fibre photosensitivity discovered by Hill in 1978 [50], consisting in the permanent change in the refractive index of the core of a guided wave device when irradiated with ultraviolet light. An FBG is a permanent, periodic perturbation of the core's refractive index of an optical fibre by exposing it to a spatially varying pattern of ultraviolet intensity radiation (fig. 2.14).

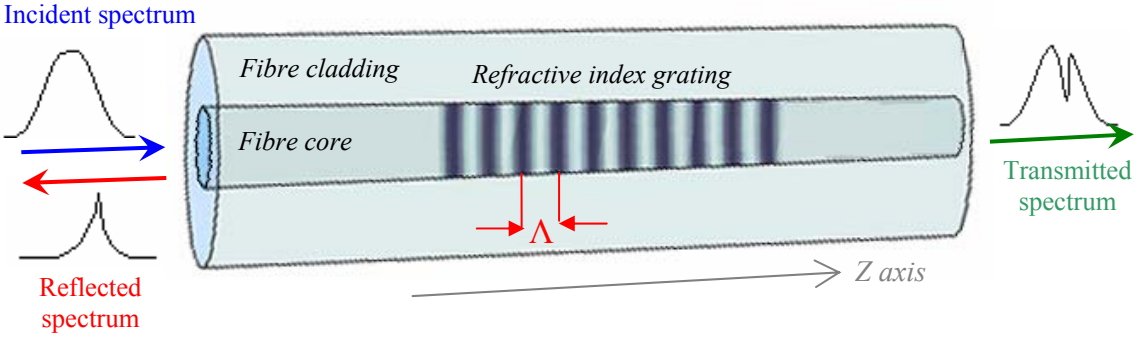

Figure 2.14: Illustration of a uniform fibre Bragg grating, where the fibre core refractive index appears modulated and its filtering effect over an incident pulse of light.

The grating is characterised by its period Λ, amplitude of the refractive index perturbation and length L (usually between 1 to 20 *mm*). For a single mode fibre Bragg grating (as those used in this thesis), when the incident guided mode interact with the gratings, a certain proportion of its light is scattered at each grating plane. Under appropriate conditions, certain scattering directions may be found where the wavelets created at each plane are in phase, if this directions correspond to the backward direction of the single guided mode, then a resonant condition is satisfied and strong scattering occur. As shown in [51] by treating the FBG as an optical diffraction grating, we obtain the coupling between forward and backward guided mode takes place when the light propagates at the Bragg wavelength λ_B defined in eqn. 2.6.

$$\lambda_B = 2n_{eff}\Lambda \tag{2.6}$$

Where n_{eff} is the fibre core effective refractive index (defined by $n_{eff} = n_{fibre\_core}(\lambda_B)/\ n_{air}(\lambda_B)$).

In order to calculate the spectral grating characteristics, that is the spectrum of the reflected and transmitted portions of the incidental light, in most cases *coupled-mode theory* is applied [52]. This theory solves the propagation of the superposition of existing modes in the guided wave under the boundary conditions of the perturbation caused by the presence of the gratings. In the case of a uniform grating this problem has analytical solution as given by the

intensity reflection spectrum r on eqn. 2.7. The intensity reflectivity r represents the relationship between the reflected intensity I_{ref} to the total incident intensity I_0 to the grating. The transmission spectrum can be obtained by $\tau = 1\text{-}r$.

$$r = \frac{I_{ref}}{I_0} = \frac{\sinh^2\left(\sqrt{k^2 - \hat{\sigma}^2}\cdot L\right)}{\cosh^2\left(\sqrt{k^2 - \hat{\sigma}^2}\cdot L\right) - \frac{\hat{\sigma}^2}{k^2}} \tag{2.7}$$

Where $k = \frac{\pi}{\lambda}\cdot v \cdot \delta\overline{n}_{eff}$ is the *AC coupling coefficient*, $\hat{\sigma} = \delta + \frac{2\pi}{\lambda}\delta\overline{n}_{eff}$ is the *DC coupling coefficient* and $\delta = 2\pi n_{eff}\left(\frac{1}{\lambda} - \frac{1}{\lambda_D}\right)$ is the *detuning factor* with λ being the light wavelength and $\lambda_D = 2n_{eff}\Lambda$ is the *design wavelength* for Bragg scattering by an infinitesimally weak grating $\delta n_{eff} \rightarrow 0$. The rest of the parameters are related with the perturbation to the fibre's effective refractive index by the presence of the uniform grating, which if considered along the z axis (taken as the fibre axis as shown in fig. 2.14) this perturbation is given by:

$$\delta n_{eff}(z) = \delta\overline{n}_{eff}(z)\cdot\left[1 + v\cdot\cos\left(\frac{2\pi}{\Lambda}\cdot z\right)\right] \tag{2.8}$$

If the optical fibre has a step-index profile (as in most common cases) then we can relate the effective refractive index modulation δn_{eff} in eqn. 2.8 with the fibre core refractive index modulation δn_{co} by $\delta n_{eff} \approx \Gamma\cdot\delta n_{co}$ where Γ is the *confinement factor*, which gives the ratio of the power guided in the core to the total power of the mode of interest.

$$r_{\max} = \tanh^2(kL) \tag{2.9}$$

By differentiation of eqn. 2.8 respect to the light wavelength we obtain the expression for maximum reflectivity of the grating (given by eqn. 2.10). The maximum occur when $\hat{\sigma} = 0$ so that all reflected waves are phase matched. It is easy to prove that in order to satisfy this condition, the light wavelength must be equal to:

$$\lambda_{\max} = \lambda\big|_{\hat{\sigma}=0} = \lambda_D\left(1 + \frac{\delta\overline{n}_{eff}}{n_{eff}}\right) \approx \lambda_D = 2n_{eff}\Lambda \tag{2.10}$$

Where we have taken into account that in most cases $1 >> \delta\overline{n}_{eff} / n_{eff}$ [53]. Notice that the expression for the wavelength associated to the maximum Bragg grating reflectivity is equal to what it was defined as Bragg wavelength λ_B in eqn. 2.6.

An FBG is in effect a filter for the electromagnetic wave of the light travelling along the fibre line as it reflects the light in a predetermined range of wavelength centred around the

peak value at λ_B. An example of a typical fibre Bragg grating reflectivity spectra is plotted in blue in fig. 2.15. The sidelobes presented at both sides of the centre peak are due to multiple reflexions from and towards the opposite borders of the grating region. Hence an ideal grating infinitely long would have a delta Dirac reflectivity spectra. The particular reflectivity spectra of fig. 2.15 is associated to the FBGs used in the experimental work later presented with $L = 1mm$, $\Lambda = 5.25*10^{-7} - 5.3*10^{-7}\ m$, $n_{eff} = 1.45$, $v = 1$ and $\delta n_{eff} = 4.2*10^{-4}$.

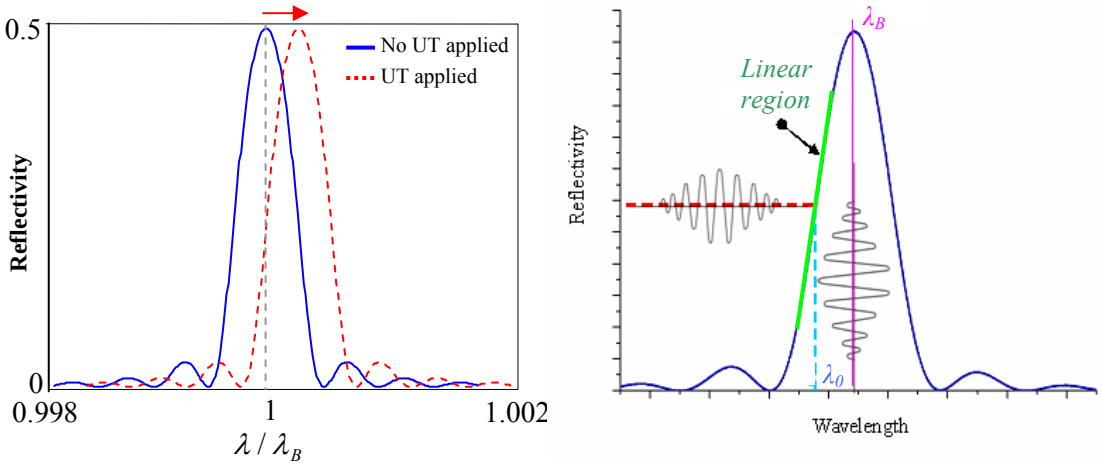

Figure 2.15: (*Left*) Typical reflectivity spectrum of a uniform FBG as a function of the light normalized wavelength respect to the Bragg wavelength (λ_B). Ultrasonic waves cause a horizontal shift of the spectra.

Sensor characteristics of FBGs

The Bragg wavelength as given in eqn. 2.6 is a function of the grating parameters n_{eff} and Λ, which are affected by changes of pressure, strain or temperature applied to the fibre [48]. Therefore the basic principle of operation of optical fibre sensors based in a FBG is to monitor the shift in the Bragg wavelength caused by the changes in the measurand. As calculated in [54] for a grating of $\lambda_B = 1.557\ nm$ inscribed in a Ge/B co-doped fibre, the normalized temperature sensitivity is given by $(1/\lambda_B)\cdot(\partial \lambda_B / \partial T) = 7.06\cdot10^{-6}\ {}^0C^{-1}$, the normalized pressure sensitivity is $(1/\lambda_B)\cdot(\partial \lambda_B / \partial P) = 2.02\cdot10^{-6}\ MPa^{-1}$ and the axial strain sensitivity is $(1/\lambda_B)\cdot(\partial \lambda_B / \partial \varepsilon) = 0.772\cdot10^{-6}\ \mu\varepsilon^{-1}$. These values clearly show that FBGs are not as good pressure sensors as they are for temperature and strain measurements. Therefore here we just concentrate in the last two parameters sensitivity.

Temperature sensitivity

If we consider that all mechanical strains are zero, and only temperature induced strain is present, then the shift of the Bragg wavelength for a given temperature change ΔT is given by [53]:

$$\frac{\Delta\lambda_B}{\lambda_{B0}} = \left(\alpha + \frac{1}{n_{eff}} \frac{\partial n_{eff}}{\partial T} \right) \cdot \Delta T \tag{2.11}$$

Where λ_{B0} is the Bragg wavelength with no strain and at room temperature, α is the thermal expansion coefficient of the fibre. The second term of eqn. 2.11 is related with the thermo-optic effect which is the dominant one. Although α and $\partial\, n_{eff} /\partial T$ depend in the fibre composition, in most common fibres we can approximate α as varying between $0.55\text{-}1.1\cdot10^{-6}$ and $\partial\, n_{eff} /\partial T \approx 10^{-5}\ 1/K$. Hence for a FBG with $\lambda_B = 1.53\ \mu m$ and $n_{eff} = 1.445$, the temperature sensitivity is given by $\Delta\lambda_B / \Delta T = 11\ pm/K$ at room temeperature.

Strain sensitivity

We consider now that the temperature is fixed and a strain field ε_Z travelling along the axis of the grating (axis of the fibre, named axis Z in fig. 2.14). We consider that the strain wavelength is much greater than the length of the FBG (so that at any time the strain can be considered constant along all the grating), then the shift of the Bragg wavelength is given by eqn. 2.12 [55], where v is Poisson's ration and p_{11} and p_{12} are the components of the strain optic tensor.

$$\frac{\Delta\lambda_B}{\lambda_{B0}} = \left(1 - \frac{n_{eff}^2}{2} \left[p_{12} - \nu\left(p_{11} + p_{12} \right) \right] \right) \cdot \varepsilon_z \tag{2.12}$$

For a typical silica fibre $v = 0.17$, $p_{11} = 0.12$ and $p_{12} = 0.27$, thus for same conditions as before $\lambda_{B0} = 1.53\ \mu m$ and $n_{eff} = 1.445$, then the strain sensitivity at room temperature is given by $\Delta\lambda_B / \varepsilon_Z = 1.21\ pm/\mu\varepsilon$.

Ultrasonic wave detection characteristics

Although in a more general case the FBG will be affected by both effects (temperature and strain variations), in ultrasonic detection applications mainly only the strain perturbation effect is of interest and the temperature can be considered fixed or its variations can be compensated by using an extra FBG sensor just for temperature sensing. Therefore in ultrasonic sensing we are mainly interested in the Bragg wavelength shift given by eqn. 2.12, where for a sinusoidal ultrasonic wave of frequency ω_S and wavelength λ_S, the strain can be given by $\varepsilon_Z = \varepsilon_m \cdot \cos(2\pi z/\lambda_S - \omega_S \cdot t)$. When $\lambda_S >> L$ (as it is the case in our experiments) the reflectivity spectra response of the grating keeps it shape and the effect of the ultrasonic strain field is a shift of all the spectra equal to the Bragg wavelength shift as given by eqn. 2.12. This is shown in fig. 2.15-*left* with the reflectivity spectra under no strain given in blue and the spectra under strain is given in red. Although the shift of the spectra is towards

increasing wavelength values, however for a sinusoidal strain field it will oscillate around the Bragg wavelength as the strain oscillates between positive and negative values as shown in fig. 2.15-*right*.

The FBG sensor interrogation method used in this work (see next chapter) for ultrasonic wave detection measures the shift in λ_B indirectly by detecting the modulation on the reflected optical power while the input light wavelength is kept constant in the linear region of the sensor (usually in the region where the reflectivity is between 20 to 80% of the maximum, as shown by a green line in 2.15-*right*).

FBGs are used to measure mainly in-plane strains along its axis and since they are generally so small (few *mm*) compared to the ultrasonic wavelength, they are considered to be point scanning sensors. FBG can be bonded to or embedded in the sample to be scanned to form a contact detection system. Because FBGs are characterised by very low insertion loss they are suitable for multiplexing in series along a fibre and are thus ideal for multiple sensor applications, where time and wavelength division multiplexing can be applied [56].

2.4.2.2 All-fibre interferometric systems

In an interferometric system the measurand is encoded as an optical phase modulation of the light propagating within the interferometer. The interferometer achieves the phase demodulation in different ways regarding the particular type of interferometer used; two-beam interferometer, birefringent interferometer, multiple beam interferometer, etc [57]. We concentrate this section in the first type as it is the kind of interferometer used in our experimental work.

The *two-beam interferometer* in an all-fibre Mach-Zehnder configuration is shown schematically in fig. 2.16. The light from a highly coherent source is coupled into the system input fibre and then divided at the first directional coupler into the two fibre arms of the interferometer. One of the optical paths, named *sensing arm*, is optimized for sensitivity to the environmental effect of interest and it is the light that propagates within that suffers the phase modulation by interaction with the ultrasonic wave. While the second optical path, named *reference arm*, is as environmentally isolated as possible and it presents various optical components in order to maximize the phase change and so the interferometric sensitivity (as shown later). Both interferometric arms are combined coherently at the end of the system in a second directional coupler, to produce a fluctuating light intensity due to constructive and destructive interference as the relative phase of the signal and reference beams changes. This optical intensity fluctuation is carried to two photodetectors to convert it into a more manageable electronic signal.

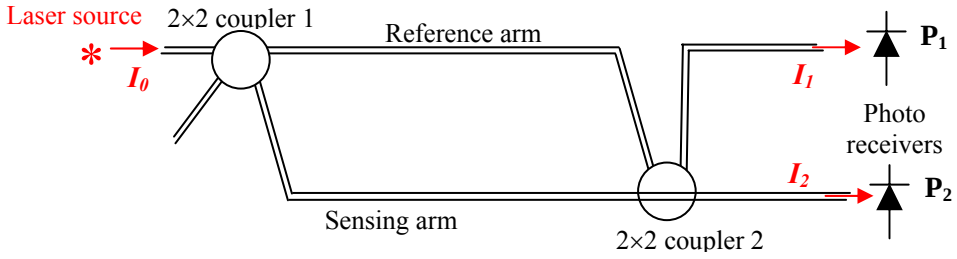

Figure 2.16: The two-beam all-fibre interferometer in a Mach-Zehnder configuration.

This approach allows the measurement of extremely small phase differences between both combined beams as induced by the measurand.

Through a detailed analysis of the propagation of the electric field of the input light beam towards the two output photodetectors, which is commonly found in the literature [57], one can obtain that the optical power arriving to each of them is given by eqn. 2.13, if polarization effects are ignored (in practice this is a good approximation, however under other detection principles; f.i. the polarimetric sensor (as shown later) the polarization effects can be dominant).

$$I_i = I_0\left[k_{1c}{}^2 \cdot k_{2c}{}^2 + k_{2t}^2 \cdot k_{1t}^2 \pm 2 \cdot \gamma \cdot k_{1c} \cdot k_{2c} \cdot k_{1t} \cdot k_{2t} \cdot \cos(\Delta\phi)\right] \tag{2.13}$$

Where the sign - is for photodetector 1 and sign + for the photodetector 2, which basically means that their inputs are in exact antiphase. The rest of the parameters are defined as; I_0 input power from the laser, k_{jc} and k_{jt} are the electric field coefficients for the jth directional coupler (where the subindex c is for the coupling of the beam from one arm to the other, and the subindex t is for the transmission of the beam within the same arm) in both cases they are real numbers. We have considered that the couplers add π / 2 radians during coupling [57]. γ is the degree of coherence of the source. $\Delta\Phi$ is the difference on the optical phase delay of the beams at the end of both arms, which can be rewritten as the integral effect of the difference in their optical path length as:

$$\Delta\phi = \frac{2\pi}{\lambda_0}\left[\int_{\text{Sensing arm}} ndl - \int_{\text{Reference arm}} ndl\right] \tag{2.14}$$

Where λ_0 is the wavelength of the laser source in vacuum, n is the fibre refractive index and dl is a length element of the fibre. The expression for the optical intensity in the photoreceivers can be further simplified by considering 50% couplers without losses so that $k_{jc} = k_{jt} = 1/\sqrt{2}$ and by defining the *visibility of the interference V* as:

$$V = \frac{I_{\max} - I_{\min}}{I_{\max} + I_{\min}} = \gamma \tag{2.15}$$

We can see that the visibility of the interference is equal to the degree of source coherence, being a reason for an interferometric sensor to require a very good quality laser source. It can be proved [57] that γ =1 if the coherence time of the laser source is much bigger than the differential propagation delay time between reference and sensing arms. The laser source used in our experimental interferometers (as described in Chapter 3) is characterised for having a very stable frequency with a long coherence length, this allows the length of the reference and sensing arms not to require a perfect match.

The simplified expressions of the light in the photodetectors are given by:

$$I_i = \frac{I_0}{2}\left[1 \pm \cos(\Delta\phi)\right] \tag{2.16}$$

A differential combination of the electric signals given by both photodetectors would produce a photocurrent *i* output equal to:

$$i = \varepsilon\, I_0 \cos(\Delta\phi) \tag{2.17}$$

Where ε is the responsivity of the photodetector. We can now rewrite the differential phase shift between both arms of the interferometer as a combination of a slow varying phase shift Φ_d (due to environmental perturbations acting in both arms that includes any phase difference between due for instance to a length mismatch) and the term due to the interaction of the ultrasonic wave with the sensing arm $d\Phi$ (therefore $\Delta\Phi = \Phi + d\Phi$). For a sinusoidal propagating acoustic wave, we can rewrite $d\Phi = \Phi_S \sin(\omega_S t)$, for ω_S being the ultrasonic frequency and where the amplitude of the induced phase difference Φ_S can be correctly assumed to be small. Therefore the varying photocurrent given by the photodetectors for a detected ultrasonic signal perturbation would be given by:

$$di \propto \varepsilon\, I_0 \sin(\phi_d) \cdot \phi_S \sin(\omega_S t) \tag{2.18}$$

Active homodyne demodulation

The greatest sensitivity of a homodyne interferometer occurs when it operates in *quadrature*, at which the optical path phase difference between reference and sensing arm correspond to $\Phi_d = (2m+1)\cdot\pi/2$ for *m* being an integer. In this case we have that $\sin(\Phi_d)$ =1 and then *di* caused by $d\Phi$ is maximum (from eqn. 2.18). Opposite would happen if $\Phi_d = m\cdot\pi$ as *di* would be zero, causing a vanishing of the detected ultrasonic signal (shown in fig. 2.17 from [43]).

However in a practical interferometer, the environmental perturbation will cause the phase of the reference arm to slowly change so that Φ_d changes with time, causing a continuous drift of the interferometer sensitivity. The more the sensitivity drift the longer the length of the reference arm. For instance optical fibres at an optical wavelength of 1 μm, are affected by temperature with an optical phase shift sensitivity of 100 $rad/\mathrm{m}\cdot{}^{0}C$, by pressure as 10 $rad/\mathrm{m}\cdot bar$, by strain as 10 $rad/\mathrm{m}\cdot\mu\varepsilon$ and by rotation as 0.05 $rad/m^2\cdot rad\cdot s$ [58]. This problem is commonly corrected in homodyne interferometers by actively control the phase in the reference arm compensating the environmental low frequency perturbations. This is done by adding a piezoelectric cylinder that stretch the reference arm fibre around it, thus modulating the reference optical path length and so the phase of the light within it [59].

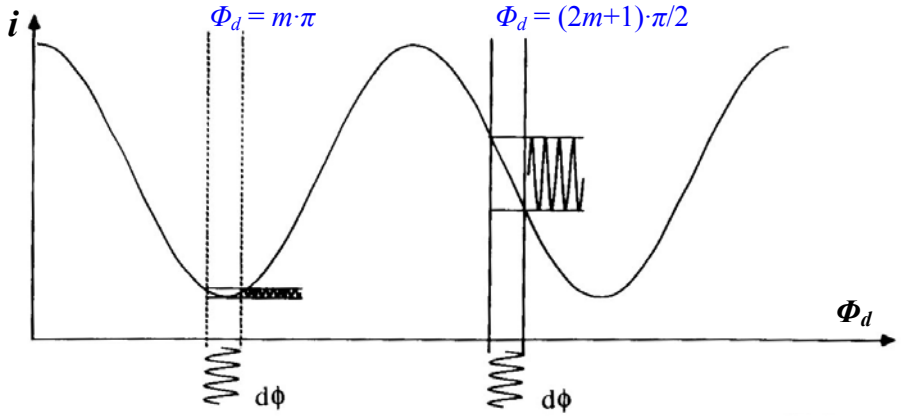

Figure 2.17: Two-beam homodyne signal amplitude in relation to its operation point.

If we name Φ_{PZT} the phase shift caused by the PZT cylinder in the reference arm. Then if the photodetectors output is low pass filtered, the obtained signal would be given by:

$$i = \varepsilon I_0 \cdot \cos\left(\phi_d - \phi_{PZT}\right) \tag{2.19}$$

If the interferometer is held in quadrature, then Φ_d - Φ_{PZT} = (2m+1)·π/2 and the low frequency output of the interferometer would cancel. However small low frequency deviations from quadrature (by environmental perturbation) would generate a bipolar low frequency interferometric output:

$$\Delta i\big|_{Quadrature} = -\varepsilon I_0 \cdot \left(\phi_d - \phi_{PZT}\right) \tag{2.20}$$

The bipolar output signal in eqn. 2.20 experiences a sign change when passing through quadrature, becoming a very useful error signal fed into the PZT cylinder as a feedback voltage by an electronic servo loop. The high frequency output signal from the interferometer in the small-angle approximation for the ultrasonic signal modulation $d\Phi$, is directly proportional to the ultrasound in a similar way as in eqn. 2.20 with $d\Phi$ instead of (Φ_d - Φ_{PZT}). This active demodulation approach is commonly known as low-gain mode of

operation [43] and it is the one chosen in this thesis, because it has the advantage of a high frequency response (limited only by the photodetector) and it has the lowest noise floor typically achievable with homodyne interferometric sensors [43]. In addition decoupling the high and low frequency detection circuits allow a greater gain to be applied to the ultrasound signal by the high frequency detector, due to the removal of the higher magnitude DC component [60].

Maximize phase change by adding optical components in the reference arm

The previous derivation of the optical intensity arriving to the photodetectors was considered for a neglectable attenuation in the arms of the interferometer or at least an identical attenuation. If a different attenuation is considered for reference and sensing arm, the visibility of the interference decreases [43], in a similar way if we include the effects of the polarization state of the beams propagating in both arms we would notice that the best sensitivity would be achieved if the interfering beams have the same polarization state.

Hence in most cases a more accurate scheme of the two-beam interferometer is the one shown in fig. 2.18, where the reference arm includes not only the PZT cylinder phase modulator as previously described (together with a description of the feedback control loop) but in addition it also contain two other components to maximize the phase change elucidated. These components are:

- *Polarization controller*: it allows adjusting the polarization of the light in the reference arm to be matched to that of the signal arm, maximizing the light interference in the output.
- *Variable optical attenuator (V.O.A.)*: to match the light intensity in the reference arm with that in the sensing arm obtaining maximum visibility of the interference fringes.

In the other hand the sensing arm in fig. 2.18 presents two different configurations. The one named *a)* is a pure Mach-Zehnder sensing arm configuration, consisting in a single fibre bonded to the surface or embedded within the plate where the ultrasound is propagating. The configuration identified as *b)* is slightly different and it resembles the sensing behaviour of a Michelson interferometer because the sensing beam is focussed and reflected from the surface under inspection (which acts as a moving mirror). Nevertheless because the sensing and reference beam do not return back through the sensing and reference arm to interfere, it is not a pure Michelson interferometer. We have named this configuration as modified Mach-Zehnder interferometer. Next we look in more detail how the interaction with the ultrasonic wave takes place in each configuration.

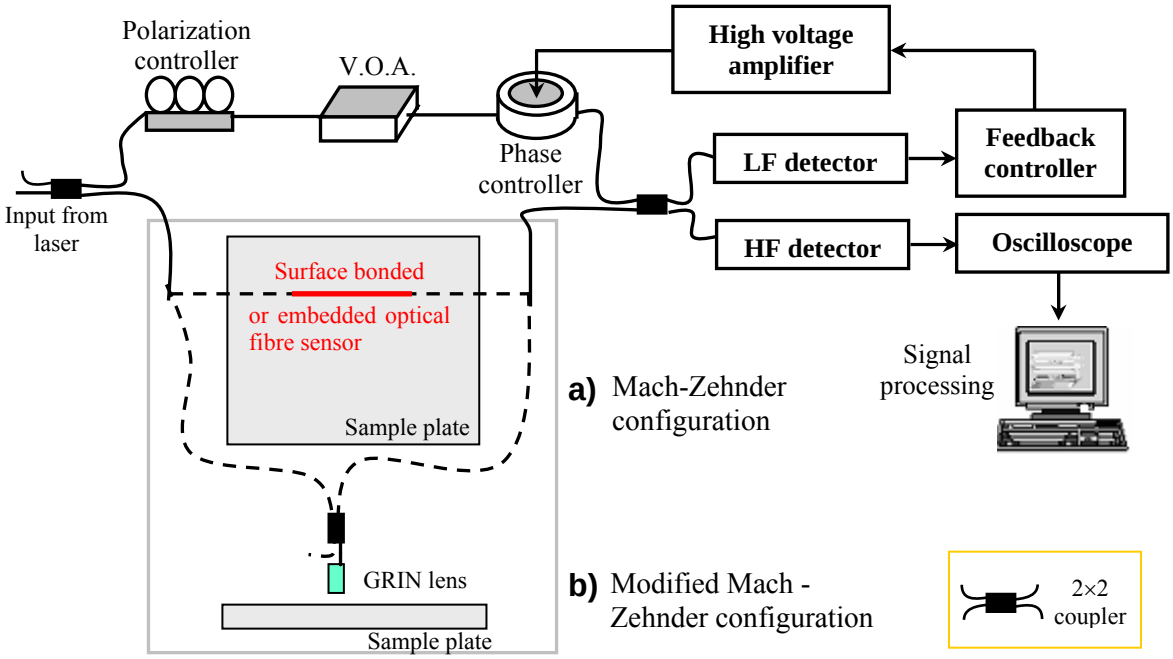

Figure 2.18: Schematic of the fibre interferometric ultrasonic detection systems: *a*) *Mach-Zehnder configuration*, where the optical fibre sensing arm is bonded on the surface or embedded into the structure. *b*) *Modified Mach-Zehnder configuration*, where the light of the sensing arm is focused onto the surface of the plate and its scattered light collected. The optical components in the reference arm are needed to optimize the system performance. V.O.A. is a variable optical attenuator.

2.4.2.2.1 Mach-Zehnder configuration

In this configuration a finite length of the sensing arm optical fibre is bonded to the surface or embedded into the structural material under inspection. The transduction mechanism is based in the *strain-optic effect* by which pressure field of the acoustic wave acting on the optical fibre produces a modulation of its refractive index n causing a difference in the optical phase with respect to the reference arm as defined by eqn. 2.14. A more detailed analysis of this interaction can be seen in Chapter 4 where a mathematical model of this transduction is presented.

This is obviously an intrinsic sensor and it is sensitive to both in-plane and out-of-plane stress field components. It is also an integrating sensor, because the sensor length is much bigger than the ultrasonic wavelength therefore it is modulated by a finite size of the ultrasonic wavefront rather than by only one point of it. The complexity of this integration interaction is described in Chapter 4, however this complexity comes in exchange of its advantage that one such detector transducer with one ultrasonic source cover a larger scanned area than the single strip from source to sensor provided by point scanning sensors.

This sensor configuration is a contact technique because the sensing fibre is fixed in position, however it provides good repeatability with minimal variation in the acoustic coupling at the interface.

Finally it has been demonstrated experimentally that the interferometer operation when the sensing fibre is embedded is between 10 to 20 times more sensitive to Lamb waves than when it is bonded [61].

2.4.2.2.2 Modified Mach-Zehnder configuration

In this extrinsic sensor configuration, the beam propagating in the optical fibre of the sensing arm is connected through a directional coupler into a pigtailed optical fibre GRIN lens assembly (as shown in fig. 2.18*b*). The GRIN lens focuses the sensing beam perpendicularly onto the surface of the plate where the ultrasound is propagating. This adds an air gap into the sensing pathway. The scattered light from the sample was again collected back by the same GRIN lens into the sensing arm optical fibre and then recombined in the second directional coupler to interfere with the reference beam.

The modulation of the phase of the light in the sensing arm for this interferometric configuration is caused by a change in the physical length of the air gap added to the sensing arm as the sensing light beam reflects from the surface of the sample subjected to ultrasonic out-of-plane displacements (as by the configuration in fig. 2.18*b*). Other orientations of the GRIN lens sensing probe (f.i. at 45 degrees) would allow the detection of in-plane surface displacement in addition to the out-of-plane one. However this would require additional measurement beam collection optics in order to separate both components as shown in [61]. The complexity of such systems and because the out-of-plane displacement serves our need made us chose the single configuration previously presented.

In this configuration the V.O.A. in the reference arm is of great importance because due to the fact that the sensing light beam has to leave the optical fibre to interact with the surface of the plate it suffers a substantial optical loss. This loss has to be compensated by a similar loss in the light in the reference arm (via the V.O.A.) to improve the visibility of the interference and so the sensitivity of the system. The sensitivity is also proportional to the total optical power collected in the interference recombination of sensing and reference beam (see eqn. 2.18), because the dominant noise source of this interferometers is usually the shot noise of the photodetector used [62], which is improved by increasing the incident optical power. Therefore this interferometric configuration requires an effort to achieve effective re-collection of the scattered light, for that a highly reflective sample surface and short focal length GRIN lens is used. The high reflectivity of the sample surface can be achieved by

polishing it or, as done in our experiments, by bonding a highly reflective film (3M Optical Enhancement Films) layer which provides a reflectance of 95%. Because this layer is very thin (63 μm thick) it guaranties no perturbation on the propagating Lamb waves at the frequencies of interest.

The present optical system has much in common with optical coherence tomography (OCL), first demonstrated in 1991 [63]. OCL is an interferometric, non-invasive optical tomographic imaging technique, widely accepted in ophthalmology and other biomedical applications, offering millimetre penetration (approximately 2-3 *mm* in tissue) with sub-micrometre axial and lateral resolution. These resolutions are achieved by applying low-coherence interferometry. In contrast to the conventional interferometry with long coherence length (as that used in all the interferometric systems here presented), in OCT the interference is shortened to a distance of micrometres thanks to the use of broadband light sources.

A special feature of the modified Mach-Zehnder interferometer optical fibre sensor, compared to the other systems here described, is that it is the only one allowing a non contact and remote detection of the propagating ultrasonic wave. The advantages of this detection system appear enormously increased when combined with an also non-contact optical technique for ultrasonic generation. In that case a complete non-contact and remote inspection tool is created which has no rival in applications involving hazardous environments and extreme conditions like for instance process monitoring and on-line quality control during fabrication of high specifications composite materials [18]. The development of such a tool and its application for measuring elastic property of materials has been one of the main targets of this thesis as presented in chapters 6 and 7.

Finally the modified Mach-Zehnder configuration is a point-to-point scanning sensor because the scanning part of the sensor is a highly focused sensing beam. This sensor provides a very high spatial resolution (few μm or less), which is fundamental for the elastic property measurements applications for which it is intended.

2.4.2.3 Polarimetric sensor

The experimental ultrasonic signals obtained with the Mach-Zehnder interferometric system were found to be to some degree dependent on the polarisation state of the light in the optical fibre sensor. Effectively when an acoustic wave interacts with an optical fibre bonded onto its surface (or embedded within it), the fibre is subjected to a pressure field that changes not only the effective refractive index of its core but also the birefringence of the fibre. The Mach-Zehnder interferometer is designed to mainly monitor the changes that take place in the refractive index of the sensing fibre although it is in a smaller degree also affected by the

birefringence modulation of the fibre. An optical system was designed to be more suited for monitoring the induced birefringence, based in polarimetry.

The polarimetric system consist simply of a length of standard, single mode, non-birefringent optical fibre either bonded to the surface or embedded within the sample plate under test. The sensing principle is based on the modulation of the polarization state of the propagating light within it, due to the birefringence that the ultrasonic wave pressure field induces in the fibre. A better understanding of the induced birefringence is gained by studying the Lamb wave particle motion around the diameter of the optical fibre sensor as shown in Chapter 4. That analysis shows that the compressions and the expansions caused by the plate's particle movements around the fibre, causes compression and expansion pressures with two main orthogonal components, which are parallel and perpendicular to the plate where the fibre is bonded or embedded. This two main pressure axis constitute the two polarization axes of the induced birefringence.

The changes in the polarization state of the light emerging from the fibre sensor is converted into optical intensity modulation by the various optical components of the polarimetric sensor system, as shown in the set-up of fig. 2.19. Its operation is described next.

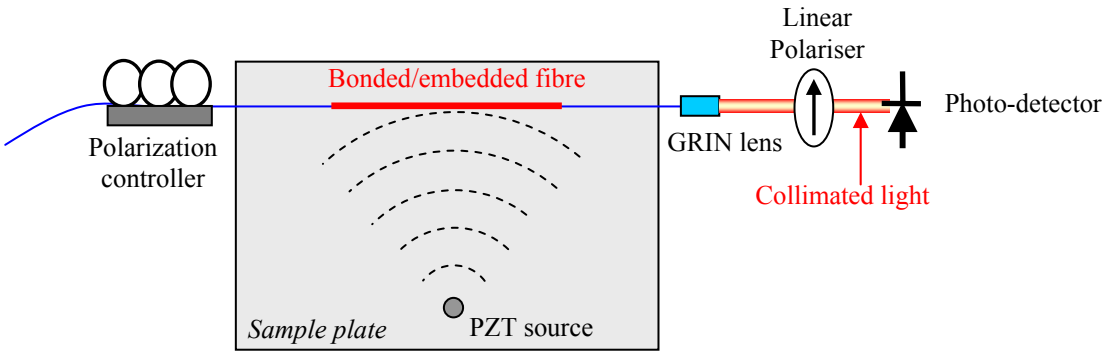

Figure 2.19: Polarimetric sensor system for Lamb wave detection. The acoustic wave pressure field modulates the polarization states of the light within the sensing fibre, which is converted into an optical intensity modulation by the polariser and then transformed into a voltage modulated signal by a photodiode. The polarization controller is used for optimizing the system sensitivity.

A linearly polarised laser source is connected via an optical fibre polarisation controller to the optical fibre sensor which is bonded to the surface or embedded into the sample plate. The output of the sensor fibre is terminated into a GRIN lens that collimates the propagating light, later directed through a rotable linear polariser that acts as an analyser. The analyzer only let pass the component of the incident light with its electric vector projected in the orientation of the linear polarizer, filtering out the rest (as explained in Appendix C). The modulation of the polarization state of the light in the sensor causes a modulation in the

quantity of the light component projected in the orientation of the polariser and so also in the optical intensity passing through it. Finally the light filtered through the polarizer is collected by a photodiode that converts the optical intensity modulated signal into a more manageable electrical voltage modulated signal.

The operation of a polarimetric system can be compared with that of an interferometric system, where the reference and sensing arms of the interferometer are now both birefringent axes that characterize the modulation in the polarization state of the light propagating through the fibre. It is the relation between the changes that the stress field causes in the refractive index of both main polarization axes that gives the ultrasonic wave stress field signal in the polarimetric system. Similar occurs in an interferometric system, where it is the relative changes between sensing and reference arm what gives the ultrasonic signal. Meanwhile in the interferometric system the sensing and reference signals are apart one from another thus only the sensing arm is disrupted by the ultrasonic wave. However in the polarimetric sensor both sensing and reference signals are disrupted by the ultrasound, therefore the difference caused is less accentuated than in the interferometer. In consequence, the sensitivity of the polarimetric system would not be as good as in an interferometric system as shown in table 2.2 [64].

The operability of the polarimetric set-up (as seen on fig. 2.19) is very simple in comparison with the previous optical fibre ultrasonic detection systems. Also because it only uses inexpensive components it makes it a very attractive optical option for ultrasound detection.

The ultrasonic signal amplitude produced by the polarimetric system set-up is found to be dependent both on the state of polarisation of the optical fibre sensor input light and the orientation of the polariser. In Appendix C, we present a theoretical analysis of the polarimetric system sensitivity dependency with the polarization state of the light in the fibre sensor and the orientation of the linear polarizer. Under the simplifying assumptions of an induced linear birefringence, a propagating monochromatic and plane wave light and considering that the changes in the light polarization state are only caused by the changes in the phase difference between the two electric field components and not in their amplitude. We show that the most sensitive operation of the polarimetric system is achieved when the polarization state of the light at the output of the fibre sensor is circular. In practice however we observed that the maximum fringe amplitude was observed with a slightly elliptical polarization. The slight discrepancy is due to the fact that (as mentioned in [65]) the induced birefringence is not purely linear but it has a slight circular component. Nevertheless the optimization of the detected signal is carried out empirically, by manipulating a polarisation

controller before the sensing fibre and adjusting the orientation of the polariser plate until maximum amplitude of the ultrasonic signal is achieved.

More about this system and pictures of its experimental set-up are shown in Chapter 4.

2.4.2.4 Comparison of the three optical fibre detection systems

Table 2.1 compares the general sensing aspects of the four optical fibre sensor systems described in previous section.

FBG	*MZ Interferometer*	*Modified MZ Interf.*	*Polarimetric sensor*
Contact	Contact	Non-contact	Contact
Absolute measurements		Absolute measurements	
In-plane displacement	Both displacements	Out-plane displacement	Both displacements
Strain sensitive	Stress sensitive	Strain sensitive	Stress sensitive
Point to point scanning	Integration scanning	Point to point scanning	Integration scanning
2^{nd} best spatial resolution		Best spatial resolution	
		Problems with low reflective surface	

Table 2.1: Comparison of the main characteristics of the 4 optical detection of ultrasound techniques.

- FBG and Michelson analyse only one point of the propagating ultrasonic wavefront. In contrast the integration techniques analyse a finite size. Which means that in NDT, a single integration scanning sensor will cover an area of the structure that would require an array of multiple point-to-point sensors. However the detected signal for the integration sensor is far more complicate than that for a point-to-point sensor.

- All the integrating sensors and the FBG are contact systems and suffer from the same disadvantages of the conventional contact transducers. The coupling of the ultrasonic wave to the fibre sensor will depend highly in the way they are bonded to or embedded in the structure. In contrast the modified MZ interferometer allows a completely remote inspection when also combined with laser ultrasound generation.

- The modified MZ interferometer is the most sensitive of the optical fibre detection systems described. But it is only sensitive to out-of-plane displacements of the ultrasonic wave (in the simple configuration in which we have applied it). In contrast FBG sensors are sensitive to in-plane displacement, and in a more complete way the other two integration sensors are sensible to both in-plane and out-of-plane displacement.

- Because the modified MZ interferometer sensing beam can be focused to a very small spot, it provides the biggest spatial resolution of all the optical sensing techniques.

O F Sensor	Temp. range (^{o}C)	Strain / Displacement sensitivity	Broadband (*MHz*)	Multisensing potential	Multiplex. potential	Embed ability
Modified MZ interferometer	High ~1000	< 0.01 *nm*	>0 - >25	Moderate	High	High
Mach-Zehnder interferometer	High ~1000	< 0.4 *nm*	>0 - >25	Moderate	High	High
Polarimetric sensor	Medium ~700	< 5 μm	>0 - ~25	High	Low	High
Fibre Bragg grating sensor	Low / Medium < 300	~ 0.01 $\mu\varepsilon$	>0 - ~1	High	Very High	High

Table 2.2: Fibre Optic Sensors for Smart Structure applications (Strain/Displacement sensitivity given for dynamic strain range).

In Table 2.2 we compare the performance parameters of the described optical fibre sensors for strain and temperature measurement applications. The way the temperature affects the sensing properties of the interferometric, polarimetric and FBG systems is very different, giving a very different temperature range for each sensor. For instance the temperature limitation of both interferometric systems is related to the temperature at which the fibre core's dopants start diffusing in considerable amounts towards the cladding decreasing the refractive index difference between core and cladding. This causes the optical fibre to loose its optical waves guiding properties. This phenomenon happen at around 800-1000 ^{0}C, much before the silica fibre melting point (around 1600-2000 ^{0}C). The polarimetric system however will be affected by smaller temperatures, but high enough to cause a stress relief in the mechanical state of the optical fibre such that the optical fibre lose its birefringence properties, this happen around 700 ^{0}C. Finally the FBGs' temperature limitation is given by the temperature at which the refractive index modulation induced in the fibre's core starts to diffuse out, this depends in the type of FBG; for type I, which are the most used in telecommunications and sensor applications, and in particular for gratings fabricated in the draw tower the temperature limitation is around 200-300 ^{0}C [56,67], however this maximum will depend considerably on the required minimum reflectivity and in its required stability, which will be improved if the FBG is pre-annealed for a certain time at high temperatures (higher than the operational temperature). Most of the structural inspection for aircraft, automotive or civil industry occurs in the temperature range between -50 to +100 ^{0}C, so for this applications all the previous optical fibre sensors are adequate. However for more temperature restrictive applications, i.e. monitoring of engines or turbines or during the fabrication process of composite structures the temperatures could reach several hundred degrees or even a thousand, at these temperatures FBG are the only ones not suitable.

The strain sensitivity of the four selected optical fibre sensors is given in different dimensions; in displacement for the interferometric and polarimetric systems and in strain for the FBG as these are the magnitudes that each system measures directly. The strain sensitivity of the interferometric systems can vary depending in their configuration and electronic equipment, so we present the experimental sensitivity of the interferometers used by us. The modified Mach-Zehnder interferometer can provide an in-plane displacement sensitivity of around 0.01 *nm*, and an out-plane displacement sensitivity of around 0.05 *nm*. The Mach-Zehnder however provides an out-plane maximum sensitivity of 25 $\mu rad/nm$, which for common interferometric level noise of around 10 μrad gives a displacement sensitivity of 0.4 *nm* [61]. For a common singlemode and uniform FBG the strain sensitivity is given by the typical values of FBGs dynamic strain response of around 1.2 $pm/\mu\varepsilon$ in the region of 1550 *nm* optical wavelength [66,68], and by the smallest detectable Bragg wavelength shift. In our experiments the tuneable laser used had a linewidth of 0.8 *fm* at 1550 *nm.* Considering only optical limitations this value gives the minimum detectable wavelength shift, which for the previous dynamic strain response for the FBG, corresponds to a minimum detectable strain of 0.6 $n\varepsilon$. However in practice other noises apart of optical ones take place (e.g. electrical noise), so experimentally the reproducible Bragg wavelength shift resolution is around 0.01 *pm* (for 128 times averaged measurements) [53], which gives a practical dynamic strain sensitivity of around 8 $n\varepsilon$.

The detectable frequency broadband of the interferometric systems is mainly limited by their electronic detection system, however for optical fibre diameters of 125 μm (common single mode fibre, used in our systems) at frequencies in the few tens of *MHz* a series of radial mechanical resonances occur that affect considerably the system sensitivity. This resonance effect starts appearing around 25-35 *MHz* [19,69] although it depends upon the optical fibre composition. In the case of singlemode and uniform FBG the detectable frequency broadband will be limited by the grating period Λ, such that strain wavelengths smaller than the grating period could hardly be detected (as explained next).

It is important to realize that an FBG measures directly the strain, in contrast to the interferometric and the polarimetric systems which measure pure displacements. It does not matter the length of the grating in the FBGe, as long as the ultrasonic wavelength is bigger than the grating, the temperature does not change and the grating period (Λ) is kept constant then the change of the Bragg wavelength (λ_B) is directly proportional to the applied strain (ε) as expressed by $\Delta\lambda_B / \lambda_B = k \cdot \varepsilon$, where k is a constant. For a given change in the applied strain the Bragg wavelength of the grating shifts a same quantity independently of the length of the grating itself. This is not the case in the interferometric and polarimetric systems. In the

interferometric systems it is the difference in the optical length between the sensing and reference arm what is measured. Particularly in the modified Mach-Zehnder interferometer is a physical length difference what cause the change in the optical length and in the Mach-Zehnder is a change in the sensing fibre refractive index what causes this optical length change. In the interferometric systems as we increase the sensing length of the fibre, even for a fixed strain value will have different interference signal. The reason is that the interferometric systems integrate the effect of the optical length change along all the sensing fibre length. Even more if the strain wavelength is smaller than the sensing fibre length, then additive and subtractive optical length effects take place giving very different results for very small sensing fibre length changes. Similar integration effect takes place in the polarimetric system, where in this case the measured phenomenon is the effect that the strain or stress field have over the main birefringent axis of the sensing optical fibre. Again this effect is integrated along all the sensing length of the fibre.

The FBG gives the average strain along the grating length. If the strain wavelength (λ_S) is >> than the grating length then the strain perturbation can be considered static and uniform along the grating and the grating behaves ideally as a point strain gauge. In this case the strain will cause a shift of the Bragg wavelength proportional to its value without perturbation of the reflectivity spectra [70,71]. When the strain wavelength is comparable to the grating length, the supposition of the uniform strain along the grating does not hold any more as different sections of the sensing grating see a different applied strain. In this case the shape of the FBG's reflectivity spectra is modified. If the strain wavelength decrease under the grating length size then the grating behave as an integrating sensor, where the positive and negative parts of the strain wavelengths will compensate each other, reducing the overall effect over the reflectivity spectra. In fact if λ_S << grating length (condition that it is satisfied when λ_S is the order of Λ) then the shape and shift of the reflectivity spectra is practically unchanged and so high frequencies are hardly detectable [55]. In conclusion the detectable frequency broadband of the FBGs is limited to wavelengths in the order of the grating length, which for ultrasonic signals means maximum detectable frequencies of a few *MHz*.

2.5 CONCLUSIONS

This chapter has discussed the great advantages that modern optical fibre sensor technology can provide over the current industrially applied conventional contact transducers for ultrasonic generation and detection applications. We have presented and analysed the ultrasonic sources due to high power Q-switched laser generation and offer a low power CW alternative. We saw that the thermoelastic regime generated ultrasonic waves that couple

more efficiently into symmetric Lamb modes, whereas the ablation regime couples better into antisymmetric Lamb modes.

The optical detection of ultrasound, in this thesis, has been based on optical fibre sensor technology. Four have been the optical fibre sensors used in this work and in this chapter we have described their principles of operation and characteristics. These are; FBG sensor, two different configurations of an all-fibre Mach-Zehnder interferometer and a polarimetric sensor. We have compared their performance parameters and their different sensing characteristics and seen that although some provide better qualities than the others in different aspects, however none of them can be confirmed as the single best option, depending more in the specific application. For instance meanwhile the FBGs provide better multiplexing capabilities than the polarimetric sensor and higher spatial resolution, the polarimetric sensor provide a range of temperature applicability double than that of the FBG sensors and a broader frequency response. A single polarimetric sensor can cover a much larger area for detecting acoustic waves, but its much more complex signal response respect to FBG sensors make the detected data difficult to analyse. Additionally the polarimetric sensor inspection technique is cheaper and easier to operate than the FBG sensors based one.

2.6 REFERENCES

[1] Monchalin J-P *Optical detection of ultrasound*, IEEE Trans. on ultrasonics, ferroelectrics, and frequency control, **UFFC-33(5)**, pp. 485-499, 1986.

[2] Curie P. and Curie J. *Development par pression de l'électricité polaire dans les cristaux hémièdres a fecs inclinées*, Comptes Rendus, vol. **91**, pp. 291-295, 1880.

[3] Krautkramer J. and Krautkramer H. *Ultrasonic Testing of Materials*, Springer-Verlag, New York, 1990.

[4] Langevin P., Journal of Physics (Paris), Colloque **C6(**suppl. no. **11-12)**, 1922.

[5] Mason W. P. *Piezoelectricity, its history and applications*, J. Acoust. Soc. Am., vol. **70(6)**, pp. 1561-1566, 1981.

[6] Moulson A. J. and Herbert J. M. *Electroceramics: Materials, properties and applications*, Chapman & Hall, 1990.

[7] Giurgiutiu V. and Cuc A. *Embedded non-destructive evaluation for structural health monitoring, damage detection and failure prevention*, Shock and vibration digest, vol. **37(2)**, pp.83-105, 2005.

[8] Rose J. L. *A baseline and vision of ultrasonic guided wave inspection potential*, Journal of pressure vessel technology, vol. **124**, pp. 273-282, 2002.

[9] Viktorov I. A. *Rayleigh and Lamb waves – Physical theory and applications*, Plenum Press, New York, 1967.

[10] Rose J.L., Pelts S. P. and Quarry M. J. *A comb transducer model for guided wave NDE*, Ultrasonics, vol. **36**, pp. 163-169, 1998.

[11] Takeuchi M. and Yamanouchi K. *Theoretical analysis of comb transducers for surface acoustic waves*, Japanese Journal of Applied Physics, vol. **22**, Suppl. 22-3, pp. 154-156, 1983.

[12] *Damage assessment in smart composite structures: DAMASCOS*, EU Project # BE974213, 2001.

[13] Giurgiutiu V., Bao J. and Zhao W. *Active sensor wave propagation health monitoring of beam and plate structures*, Proc. of SPIE's 8th Int. Symp. on Smart Struct. and Mat., California, 2001.

[14] Lin M. and Chang F-K *Composite structures with built-in diagnostics*, Materials today, vol. **2(2)**, 1999.

[15] Lin M., Kumar A., Qing X. and Beard S. J. *Advances in utilization of structurally integrated sensor networks for health monitoring in commercial applications*, Proceedings of SPIE's 9th Int. Symposium on Smart Structures and Materials, California, 2002.
[16] White J. R., Poumeyrot B., Hale J. M. and Stephenson R. *Piezoelectric paint: ceramic-polymer composites for vibration sensors*, Journal of Material Science, vol. **39(9)**, pp. 3105-3114, 2004.
[17] http://www.ncl.ac.uk/mech/piezoelectric
[18] Scruby, C.B. and Drain, L.E. *Laser ultrasonics: Techniques and applications,* Adam Hilger, 1990.
[19] Culshaw B., Pierce S. G. and Staszewski W. J. *Condition monitoring in composite materials: an integrated system approach*, Proceedings Instn. Mech. Engrs., vol. **212(I)**, pp. 189-202, 1998.
[20] Sorazu B., Thursby G., Culshaw B., Dong F., Pierce S. G., Yang Y. and Betz D. *Optical generation and detection of ultrasounds*, Strain, vol. 39(3), pp. 111-114, 2003.
[21] Davies S. J., Edwards C., Taylor G. S., and Palmer S. B. *Laser-generated ultrasound: its properties, mechanisms and multifarious applications*. App. Physics, vol. **26**, pp. 329-348, 1993.
[22] Hayashi Y., Ogawa S., Cho H. and Takemoto M. *Non-contact estimation of thickness and elastic properties of metallic foils by the wavelet transform of laser generated Lamb waves*, NDT&E Intern., vol. **32**, pp. 21-27, 1999.
[23] Scruby C. B. *Some applications of laser ultrasound*, Ultrasonics, vol. 27, pp. 195-209, 1988.
[24] Atherton K., Culshaw B., Dong F., Jun P., Pierce S. G. and Swift C. *Generation and detection of broadband laser generated ultrasound from low power laser sources*, Photonics 2000, Calcutta (India), 2000.
[25] White R. M. *Generation of elastic waves by transient surface heating*, Journal of Applied Physics, vol. **34(12)**, pp. 3559-3567, 1963.
[26] Hutchins D. *Ultrasonic generation by pulsed laser*, (Academic, New York) Physical Acoustics, vol. XVIII, 1988.
[27] Scruby C. B., Dewhurst R. J., Hutchins D. A. and Palmer S. B. *Quantitative studies of thermally generated elastic waves in laser-irradiated metals*, J.l of app. physics, vol. **51(12)**, pp. 6210-6216, 1980.
[28] Rose L. R. F. *Point-source representation for laser-generated ultrasound*, J. Acoust. Soc. Am. vol. **75**, pp. 723, 1984.
[29] Sanderson T., Ume C. and Jarzynski J. *Laser generated ultrasound: a thermoelastic analysis of the source*, Ultrasonics, vol. **35**, pp. 115-124, 1997.
[30] Hutchins D. A., Dewhurst R. J. and Palmer S. B. *Directivity patterns of laser-generated ultrasound in aluminium*, J. Acous. Soc. Am., vol. **70(5)**, pp. 1362-1369, 1981.
[31] Cooper J. A. *PhD thesis*, Hull University, 1985.
[32] Achenbach J. D. *Wave propagation in elastic solids*, Amsterdam:North-Holland, 1973.
[33] McClung F.J. and Hellwarth R.W. *Giant optical pulsations from ruby*, Journal of Applied Physics, vol. **33(3)**, pp. 828-829, 1962.
[34] Smith G. F. *The early laser years at Hughes Aircraft Company*, IEEE J. Quantum Electron., vol. **20(6)**, pp. 577-584, 1984.
[35] Bernstein J. and Spicer J. *Line source representation for laser-generated ultrasound in aluminum*, J. Acoust. Soc. Am., vol. **107**, pp. 1352-1357, 2000.
[36] Arias I. and Achenbach J. D. *Thermoelastic generation of ultrasound by line-focused laser irradiation*, International J. of Solids and Structures, vol. **40**, pp. 6917-6935, 2003.
[37] Achenbach J. D. *Simplifications for the calculation of surface wave pulses generated by laser-irradiation*, J. Acoust. Soc. Am., vol. **116(3)**, pp. 1481-1487, 2004.
[38] Ready J. F. *Effects of high power laser radiation*, New York:Academic, 1971.
[39] Takamatsu H., Nishimoto Y. and Nakai Y. *Photodisplacement measurement by interferometric laser probe*, Japanese J. of Appl. Physics, vol. **29(12)**, pp. 2847-2850, 1990.
[40] Pierce S. G. and Culshaw B. *Laser generation of ultrasonic Lamb waves using low power optical sources*, IEE Proc. Part A: Science, Meas. and Technology, vol. **145(5)**, pp. 244-249, 1998.
[41] Dixon R. C. *Spread spectrum systems*, John Wiley & Sons, Chapter 3, pp. 53-92, 1976.
[42] Atique S., Culshaw B., Thursby G., Dong F., Sorazu B. and Park H. S. *Generation of ultrasound for material testing using low power diode laser*, 2nd Euro. Workshop on Struc. Health Monit., Germany, 2004.
[43] Udd E. *Fiber Optic Sensors: An introduction for engineers and scientists*, Wiley-Interscience, 1991.

[44] Meltz G., Morey W. W. and Glenn W. H. *Formation of Bragg gratings in optical fibers by a transverse holographic method*, Optics Letters, vol. **14(15)**, pp. 823-825, 1989.
[45] 1st and 2nd *European Workshops on Structural Health Monitoring*, 2002 and 2004.
[46] 9th to 12th *SPIE Symposiums on Smart Structures and Materials*, from 2002 to 2005.
[47] 15th to 18th *International Conference on Optical Fibre Sensors*, from 2002 to 2005.
[48] Culshaw B. and Dakin J. *Optical Fiber Sensors: Components and subsystems, Vol. 3*, Artech House, 1996.
[49] See refs. in page 26 of the Proceedings of the 2nd European workshop on SHM 2004.
[50] Hill K. O., Fuiji Y., et. al. *Photosensitivity in optical fiber waveguide: Application to reflection filter fabrication*, App. physics lett., vol. **32(10)**, pp. 647-649, 1978.
[51] Erdogan T. *Fiber Grating Spectra*, J. Lightwave Technology, vol. **15(8)**, pp. 1277-1294, 1997.
[52] Kogelnik H. *Theory of optical waveguides*, Guided-wave optoelectronics, T. Tamir Ed., New York:Springer-Verlag, 1990.
[53] Betz D. *Application of optical fibre sensors for Structural Health and Usage Monitoring*, PhD Thesis, University of Sheffield, Sheffield, 2004.
[54] Xu M. G., Reekie L., Chow Y. T. and Dakin J. P. *Optical in –fibre grating high pressure sensor*, Electron. Lett., vol. **29**, pp. 398-399, 1993.
[55] Coppola G., Minardo A., et. al *Analysis of feasibility on the use of Fiber Bragg Grating sensors as ultrasound detectors*, Smart Structures and Materials 2001: Sensory Phenomena & Meas. Instr. for Smart Structures and Materials, Proc. of SPIE, vol. **4328**, pp. 224-232, 2001.
[56] Othonos A., Kalli K. *Fiber Bragg Gratings: Fundamentals and applications in telecommunications and sensing*, Artech House, 1999.
[57] Culshaw B. and Dakin J. *Optical Fiber Sensors: Systems and applications, Vol. 2*, Artech House, 1989.
[58] Culshaw B. and Dakin J. *Optical Fiber Sensors: Principles and components, Vol. 1*, Artech House, 1988.
[59] Jackson D. A., Priest R., Dandridge A. and Tveten A. B. *Elimination of drift in a single-mode optical fibre interferometer using a piezo-electrically stretched coiled fibre*, Applied Optics, vol. **19**, pp. 2926, 1980.
[60] Pierce S. G., Philp W. R., Gachagan A., McNab A., Hayward H. and Culshaw B. *Surface-bonded and embedded optical fibre as ultrasonic sensors*, Appl. optics, vol. **35(25)**, pp. 5191-5197, 1996.
[61] Dong F., Atherton K., Pierce S. G. and Culshaw B. *Measurement of in-plane and out-of-plane displacements for ultrasonic flaw detection*, 5th European Conference on Smart Structures and Materials, Proceeding of SPIE, vol. **4073**, pp. 324-331, 2000.
[62] Yong Y. *Surface-bonded optical fiber works as ultrasonic sensor*, MPhil Thesis, University of Strathclyde, Glasgow, 2002.
[63] Huang D, Swanson EA, et. al. *Optical coherence tomography*, Science, vol. **254(5035)**, pp. 1178-1181, 1991.
[64] Lopez-Higuera J. M. *Handbook of optical fibre sensing technology*, John Wiley & Sons, West Sussex, 2002.
[65] Thursby G., Sorazu B., Dong F., Betz D. and Culshaw B. *Damage Detection in Structural Materials using a Polarimetric Fibre Optic Sensor*, 10th Int. Symp. on Smart Struc. and Mat. SPIE, San Diego, 2003.
[66] Friebele E. J., Askins C. G., Bosse A. B., Kersey A. D., Patrick H. J. and Pogue W. R. *Optical fiber sensors for spacecraft applications*, Smart Materials and Structures, vol. **8**, pp. 813-838, 1999.
[67] Nellen Ph., Mauron P., et. al. *Reliability of fiber Bragg grating based sensors for downhole applications*, Sensors and Actuators A, vol. **103**, pp. 364-376, 2003.
[68] Betz D., Trutzel M. N., Staudigel L. , Martin W. and Krumpholz O. *Fiberoptic smart sensing of component deformations in adaptive wings*, Proceedings of the 22nd International Congress of Aerospace Sciences, 2000.
[69] Hall T. J. and Howard D. *Interaction of high frequency sound with fibre guided coherent light*, Electronics Letters, vol. **14(19)**, pp. 620-621, 1978.
[70] Fisher N. E., O'Neil S. E., et. al. *Response of in-fibre Bragg gratings to focused ultrasonic fields*, 12th Conference on Optical Fibre Sensors, pp. 190-193, 1997.
[71] Fisher N. E., Webb D. J., et. al. *Ultrasonic field and temperature sensor based on short in-fibre Bragg gratings*, Electr. Letters, vol. **34(11)**, pp. 1139-1140, 1998.

Chapter 3

ULTRASONIC DAMAGE DETECTION & LOCATION EXPERIMENTS

3.1 INTRODUCTION

The suitability of the optical fibre sensors, described in previous chapter, for the detection of ultrasonic Lamb waves has already been proved numerous times in the literature, for some examples see [1] for FBG sensors, [2] for Mach-Zehnder interferometer, [3] for the modified Mach-Zehnder interferometer and [4] for the polarimetric sensor. In this section we start with the description of the experimental equipment and realization of each detection technique described in Chapter 2. We present the optical fibre surface-bonding technique developed in order to achieve reproducible initial bonding conditions. Later we present an experimental comparison of the ultrasonic signals obtained by each of these sensors under identical ultrasonic launch conditions. We finish this chapter by applying some of the present optical detection techniques of ultrasound to various experimental applications involving hole-like damage detection in aluminium and Perspex sheets and damage location.

3.2 EXPERIMENTAL EQUIPMENT & REALIZATION OF THE ULTRASONIC DETECTION TECHNIQUES

This section describes the experimental instrumentation and realization of the optical fibre ultrasonic detection systems described in previous chapter as developed not only for the experiments in this chapter but also along the rest of this thesis.

3.2.1 Fibre Bragg Gratings

As described in previous chapter, the optical interrogation of the gratings is based in the modulation of the optical power reflected back from the grating. If the wavelength of the laser source is set to a certain part of the grating spectrum (mainly in the linear region of the sensor, usually at about 20 to 80 % of the gratings' maximum reflectivity), any shift of the spectrum (due to the strain field of the propagating ultrasound) will as a consequence

modulate the reflected optical power at the photo-receiver. Figure 3.1 shows a schematic of the interrogation configuration, where we consider multiple FBGs inscribed in a single fibre, as in the fibre rosette configuration used in the damage location application shown later in this chapter.

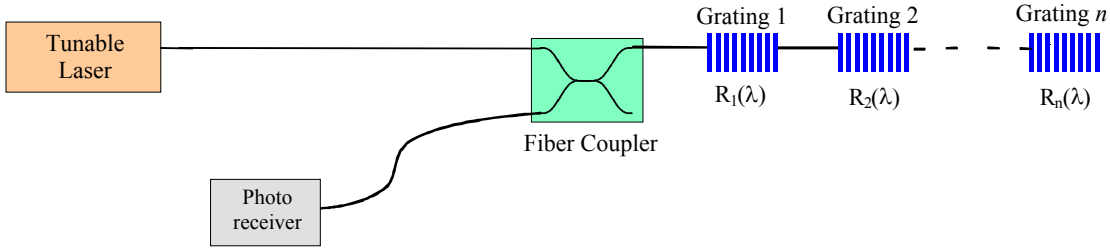

Figure 3.1: Interrogation setup for ultrasonic sensing applications of FBG, operating in WDM mode.

A Radians Innova INTUM 1500 external cavity laser (ECL) diode of low noise and extremely narrow linewidth (around 100 kHz) characteristics, with wide tuning range of about 100 nm in the 1500 nm range, acts as optical source for the FBG interrogation. The reflected optical power is detected by a high sensitivity and variable amplification photodetector, the variable amplification is useful when multiple FBGs of different reflectivity are used (i.e. the FBGs rosette used in the damage location application).

Our gratings were written in bare fibre that was recoated using a ORMOCER® coating (organically modified ceramics, produced via a sol-gel route they have a far higher modulus than the more commonly used polymer recoating materials) in order to ensure optimal strain transfer from the structure to the fibre [5]. The FBGs have a length of 1 *mm* and a narrow linewidth for their reflectivity spectra (FWHM = 0.5*nm*), with a reflectivity of about 15%.

The FBGs were bonded directly onto the surface of the plate using a very thin layer of cyanoacrylate glues which as described in [5] are often desirable because of their ease of processing and their optimized characteristics for strain sensor applications. It is essential that the glue does not surround the whole fibre, else birefringence effects could destroy the simple wavelength-strain relation.

3.2.2 All-fibre interferometric systems

The interferometric system used in this thesis is an experimental system designed and built within our research group for previous projects. The interferometric system was built based on two configurations; Mach-Zehnder and modified Mach-Zehnder. These configurations only differ in the interferometer sensing arm structure as described later. The common interferometer body is described next. Notice that the successful accomplishment of the work

in this thesis very much depended in the correct and stable operation of this device, so a perfect knowledge of its operation was required, which lead to my contribution into some improvements towards its stability.

The interferometer is fully optical fibre build. The system working principles and the function of its different components has been fully treated in Chapter 2. Here we just deal with the parameters characterization of the used components.

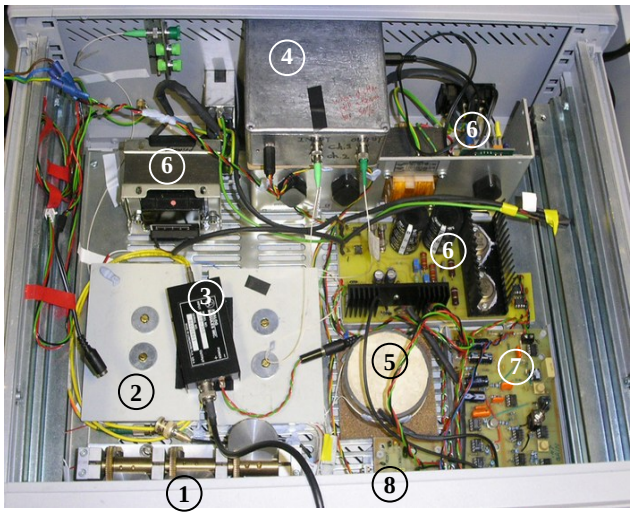

Figure 3.2: Modified Mach-Zehnder interferometer: 1) Polarisation controller, 2) 2x2 couplers, 3) High frequency photodetector, 4) variable optical attenuator (VOA), 5) Phase modulator, 6) interferometric power supply, 7) Control feedback circuit, 8) Low frequency photodetector.

The laser light to the interferometer system is a pigtailed diode pumped Nd:YAG (Lightwave Electronics, Series 126) with a CW axial mode output at 1319 *nm* (shown as number 3 in fig. 3.2). This laser provided a highly stable frequency output with a long coherence length, so that a high sensitivity could be achieved without requiring the lengths of the reference and sensing arms to be matched. The laser output is coupled into an optical fibre pigtail and passed through a variable optical attenuator to reduce its 50 mW power to the required level (in our case ~15 mW) before entering the interferometric system shown in fig. 3.2 (too much power could saturate the photodetectors used, for instance the high frequency photodetector saturates at 1mW input power). In this figure we can see the three main components of the reference arm; polarization controller, variable optical attenuator and a cylindrical PZT phase modulator. The first two components are used to maximize the phase change elucidated as described in Chapter 2. Meanwhile the last component is required to compensate the low-frequency drifting due to the long length of the interferometric arms, so that the interferometer can be hold in its most sensitive and linear operation point (quadrature) by automatic low-frequency feedback control of the phase modulator.

The detection system of the interferometer consisted of a low frequency InGaAs Photodiode (Hamamatsu) with a preamplifier, for stabilization of the system via feedback controller of the phase modulator. This photodetector system has a 16 *kHz* high frequency cut-off and 30 *dB* gain. Also we used a high frequency InGaAs PIN photodiode with a high gain and ultra low noise amplifier module (Analog Modules series 710 type 712-8w/ETX75FC-S) to monitor broadband ultrasonic signals as those used in Chapter 6. The detector low frequency cut-off is 200 *Hz* with a gain equal to 60 *dB*. It provides a detection bandwidth of 60 *MHz*, although we limit the output detected by an oscilloscope to a bandwidth of 15 *MHz* due to the increasing noise of the detector at higher frequency values and because of the flat bandwidth response of the interferometer in this region [6].

We distinguish two different configurations of the present interferometric system based on the characteristics of the sensing arm:

Mach-Zehnder configuration

This configuration has the simplest of sensing arms possible. It consists on a finite length of single mode non-birefringent optical fibre that is bonded to the surface or embedded into the structural material. For simplicity, in this thesis the fibre was always bonded onto the surface, using an epoxy cast. The bonding technique is described later in this chapter.

This configuration provides an out-plane maximum sensitivity of 25 *μrad*/*nm*, which for common interferometric level noise of around 10 *μrad* gives a displacement sensitivity of 0.4 *nm* [3], and it is also sensitive to the in-plane ultrasonic stress field.

Modified Mach-Zehnder configuration

In this configuration the laser beam in the interferometric sensing arm is transmitted to the sample surface through a fibre pigtailed GRIN lens assembly, delivering typically around 1.5 *mW* optical power. The GRIN lens has a focus length of 8.6 *mm*, a back reflection < 40 *dB* and a focused spot diameter of 40 μm, which in comparison with the smallest experimentally detected ultrasonic wavelengths of around 0.5 *mm* qualifies it as being a point detector. The same GRIN lens collects the scattered light from the surface of the plate back to the interferometer. The interferometer sensitivity can be improved by effective re-collection of the scattered light, hence a small piece of a highly reflective film (3M Optical Enhancement Films) was bonded into the surface of the plate where the interferometric beam was focused. This layer provided a reflectance of 95% and was only 63 *μm* thick. Its thickness being 5% of the overall plate thickness and 10% of the smallest propagating ultrasonic wavelength, it can correctly be assumed that its presence does not unduly perturb the displacement fields associated with the propagating Lamb waves.

This configuration can provide an out-of-plane displacement sensitivity in the order of 0.05 *nm* as described in [3]. And it is the configuration used for measuring the out-of-plane surface displacement of the sample for the application shown in Chapter 6, where a remote and broadband (spatial and temporal) ultrasonic sensing device is required.

3.2.3 Polarimetric sensor

This optical detection system is probably the simplest of all. A sensing single mode fibre is again bonded to the surface of the sample using an epoxy cast as described in next section, the fibre is terminated in a GRIN lens in order to collimate the propagating light. The rest of components of the system (its configuration is shown in fig. 2.19) consist in a common polarization controller (adapted for a 1550 *nm* optical wavelength), and a conventional rotable linear polarizer at which the collimated light from the sensing fibre output is directed. The filtered light interacts at the end with a high frequency InGaAs photodiode, which converts the optically modulated signal into an electrical one. The electric signal is high pass filtered to clean environmental low frequency noise and amplified. The final ultrasonic signal is recorder in a Tektronix digital oscilloscope where it can be averaged for signal to noise ratio enhancement and transferred to a computer for data analysis.

As described in previous chapter the obtained ultrasonic signal amplitude is found to be dependent both on the state of polarisation of the optical fibre sensor input light and the orientation of the polariser, such that the most sensitive operation of the polarimetric system is achieved when the polarization state of the light at the output of the fibre sensor is circular.

The polarisation state will inevitably change between the polarisation controller and the sensing fibre, which itself will not be entirely non-birefringent due to stresses produced by the embedding/bonding processes.

Nevertheless the optimization of the detected signal is carried out empirically, by manipulating the polarisation controller until maximum amplitude of the detected ultrasound is achieved and then adjusting the orientation of the polariser plate for a new maximum amplitude, this process is repeated until no farther improvement in the ultrasonic amplitude is observed (which usually happen after 2 cycles).

3.3 OPTICAL FIBRE SURFACE-BONDING PROCEDURE

In previous chapter we mentioned that the Mach-Zehnder interferometer proved to be 10 to 20 times more sensitive to ultrasonic wave detection when the sensing optical fibre was embedded into the structure rather than surface-bonded. The high complexity associated to the optical fibre embedding process made us concentrate the work of this thesis into surface-

bonded applications. However we have encountered experimentally that the ultrasonic signals obtained from surface-bonded optical fibre sensors are highly dependant on the bonding conditions. We have experimented with different kind of bonding materials (nail varnish, several types of sealants, tapes, plasticine…) with a detailed analysis presented in [7]. The conclusion of these experiments was that the obtained ultrasonic signals were non-repeatable due to the irreproducible initial bonding conditions associated.

In order to improve the reproducibility of the initial bonding conditions we decided to cast the optical fibre into a resin mould prior to attachment to the plate under inspection. The resin chosen was a two component epoxy known as Epotek 301 made by Epoxy Technology [8]. This epoxy adhesive features very low viscosity, good pot life, good handling characteristics and excellent optical properties and it was designed primarily for optical filters. Epotek 301 also has good adhesion to many different types of substrates including glass, metals and most plastics, which makes of it very adequate for our applications of optical fibre bonding onto aluminium and Perspex plates.

The fabrication of the optical fibre casts consist in the next steps:

- A mould is made with the shape of half cylinder of length given by the length of the optical fibre to be bonded.
- The optical fibre is then fixed onto the mould being very careful of keeping it under tension so that the fibre is not bending, and that the fibre is near the plane surface of the mould.
- The liquid Epotek 301 is poured into the mould and let to cure overnight at room temperature.

Once the cast is cured with the optical fibre within, the plane surface of the cast is bonded onto the plate by applying a thin layer of the same epoxy adhesive and then laying the cast over it with a slight uniform pressure and letting it cure overnight again.

Figure 3.3 shows one of such optical fibre casts, of 11.3 *cm* long, after curing and bonded onto the surface of a Perspex plate. A diagram of the section view of this cast is shown in fig. 4.3 of next chapter.

The ultrasonic signals detected under this bonding condition were found to be reliable and repeatable. Thus this bonding technique was used in all experiments concerning the polarimetric sensor and the Mach-Zehnder interferometer.

Figure 3.3: Optical fibre cast into an epoxy resin mould surface-bonded onto a Perspex plate.

3.4 INSTRUMENTATION FOR ULTRASONIC GENERATION BASED ON PZT DISCS TRANSDUCERS

In the experiments presented in this chapter and in Chapter 4 the ultrasonic generation is based in PZT wafer disc contact transducers. The reason being that the involved applications are characterized for requiring ultrasonic waves of narrow frequency band, for which PZT contact transducers are very suitable and provide great sensitivity. We have also used non contact optical generation techniques for the spatial and temporal broadband applications described in Chapters 6 and 7, therefore the equipment description of such generation systems is introduced in those chapters.

The damage detection and location applications for which the ultrasonic generation was carried by disc PZT transducers mainly analyze the fastest S_0 Lamb mode at low frequencies at which the mode is non dispersive. Thus the thickness to diameter radio of the discs was chosen in order to uncouple the axial and radial vibration modes. The thickness was chosen to be 400 *μm* fixing the frequency of the first axial mode resonant frequency at 5.5 *MHz*. Meanwhile a diameter of 10 *mm* is designed to situate the first radial vibration mode at around 235 *kHz* (although the exact value depends on the thickness and material of the plate to which the PZTs are bonded) [9]. The chosen design parameters, for the *Ferroperm PZ29* PZT discs used, provide an optimized coupling to in-plane motion at low frequencies, which perfectly complements the main in-plane motion component of the S_0 mode (particularly at low frequency:thickness product values) as seen in Appendix A.

In order to generate the sinusoidal tone burst driving signals for the PZT discs, a HP 33120A signal generator was used, the limited voltage amplitude of this instrument required the use of a RF power amplifier so that the PZTs could generate detectable ultrasonic signals. The ENI (Electronic Navigation Instruments) 2100L power amplifier was used, which provided a

50 *dB* amplification (maximum output power of 100 *W*) and a frequency range from 10 *KHz* to 12 *MHz*.

3.5 COMPARISON OF ULTRASONIC SIGNALS OBTAINED BY THE OPTICAL FIBRE DETECTORS

Over the surface of an aluminium plate of 1.18 mm thickness we bond a PZT disc wafer acting as an ultrasonic source. At a distance that varies between 32 *cm* and 37 *cm* we bond; a FBG, the reflective layer where the sensing beam of the modified MZ interferometer is focused, the optical fibre sensor of a polarimetric sensor (oriented perpendicularly to the ultrasonic direction of propagation) and at the far end another PZT disc acting as a receiver. The distances between source and sensors guaranty to be in the far field (thus the source can be considered a point) and all the components are far enough from the borders of the plate to avoid reflections during the time interval of analysis. The source is excited by a 4.5 cycles (see Appendix E) sinusoidal toneburst Hanning windowed at two different frequencies (110 *kHz* and 270 *kHz*). These frequencies can only couple into the two basic Lamb modes (S_0 and A_0), which greatly simplifies the detected ultrasonic time data for a direct time analysis.

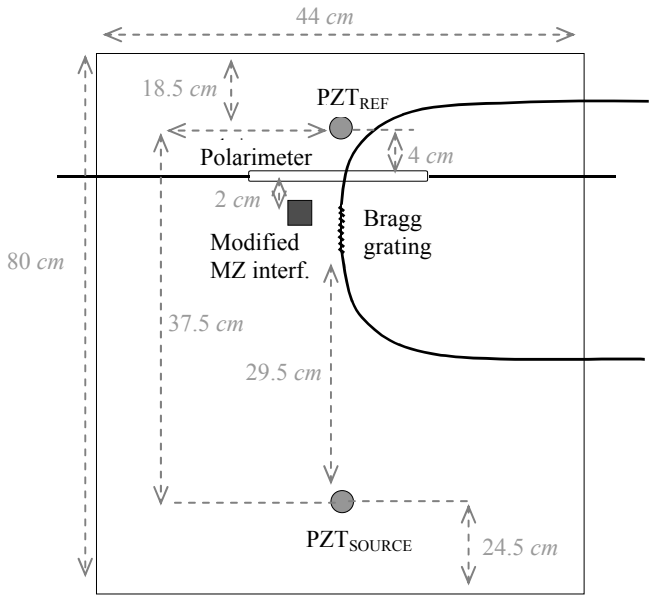

Figure 3.4: Layout of the experiment for the comparison of relative S_0 and A_0 ultrasonic detectors sensitivity.

Because the different sensing techniques measure different modal parameters and the symmetric and antisymmetric modes have different characteristics, different sensors will show differing relative sensitivities to the S_0 and A_0 Lamb modes. The multiple signals obtained from the sensors under identical launch conditions using the plate layout shown in

fig. 3.4 are plotted in fig. 3.5, and their relative amplitudes at the two excited frequencies are calculated in table 3.1.

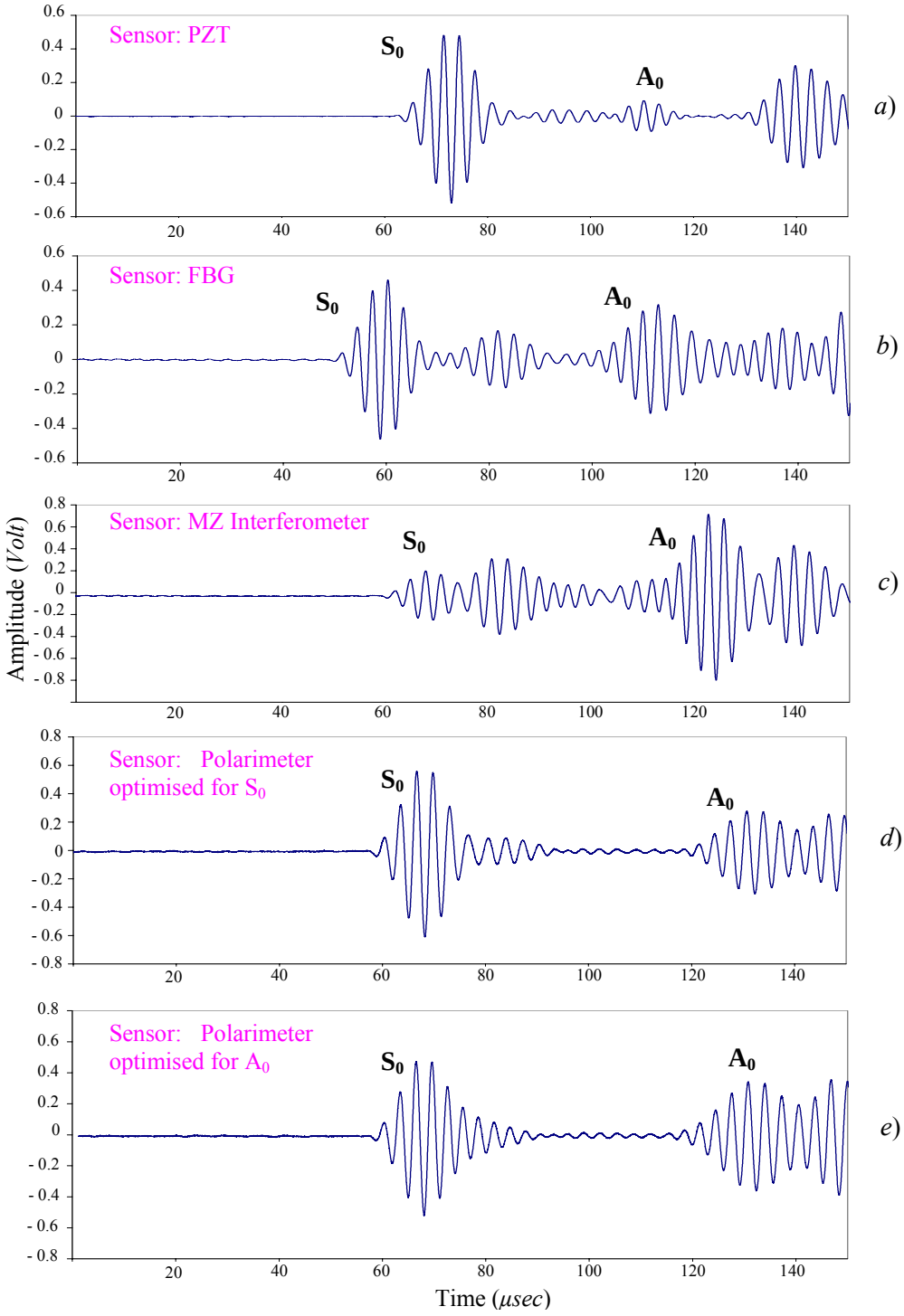

Figure 3.5: Ultrasonic signals from different sensors to a 4.5 cycles toneburst at 270 *kHz*: *a*) PZT, *b*) FBG, *c*) Modified MZ interferometer, *d*) Polarimetric sensor optimised for S_0 mode, and *e*) Polarimetric sensor optimised for A_0 mode.

Generally the S_0 portion of the signal is the easiest to identify since it has a group velocity that is often double that of the A_0. For the 4.5 cycle toneburst excited, the S_0 and A_0 modes will separate over a short distance. How easy the A_0 will be to separate out from the remainder of the signal is dependent not only on how many higher order modes are generated, but also on the arrival times of reflections of the S_0 from edges of the sample. Whilst it is possible to work on large enough sample plate to avoid confusing reflections, in a practical application this may not always be the case. The main reason for being interested in A_0 detection sensitivity is that the antisymmetric mode is generally the more sensitive to delaminations within the plate due to its greater shear strain component [10].

If we compare traces taken from different sensors obtained under identical ultrasound launch conditions, the relative amplitudes of the modes will be different in each case. Theoretical modelling of the S_0 and A_0 modes shows that the relative amplitudes of the in-plane and out-of-plane displacement is very different.

If we compare the trace taken with the interferometer (which detects out-of-plane displacement) to that obtained with the Bragg grating (detects in-plane displacement), we see that the relative S_0 and A_0 mode amplitudes are very different (see figs. 3.5c and 3.5b).

The case of the polarimetric sensor is more complex since the amplitudes of the S_0 and A_0 depend in different ways on the polarisation state in the sensing fibre, therefore the relative amplitude also changes. This is presumably due to the different pressure fields associated with the two modes, but this is more difficult to quantify.

The general trends of the relative sensitivities of the sensors are as expected, i.e. the relative amplitude of the S_0 compared to that of the A_0 is much greater when the FBG is used than is the case with signals from the interferometer, for the reasons discussed above. Precise quantification of this requires further work to take into account various scaling factors. The polarimetric sensor behaves much more like the Bragg grating than like the interferometer, suggesting that it is more sensitive to in-plane displacement, though this may be due to the way in which the sensor is mounted (as previously described) as this determines the way in which the acoustic pressure wave interacts with it.

	S_0/A_0 relative amplitude				
Frequency	*PZT*	*FBG*	*Interferometer*	*Polarimeter max S_0*	*Polarimeter max A_0*
270 *kHz*	1.51	1.46	0.31	2.00	1.44
110 *kHz*	0.69	0.30	0.21	0.77	0.76

Table 3.1: Comparison of the relative S_0 and A_0 amplitudes for the different ultrasonic sensors at frequencies of 270 *kHz* and 110 *kHz*.

3.6 DAMAGE DETECTION IN STRUCTURAL MATERIALS USING POLARIMETRIC SENSOR

Once the ultrasonic signal is detected various signal processing analysis can be applied in order to test for the existence of damage in the propagation path of the ultrasonic wave. When the excited ultrasonic signal is as simple as in the previous case, where only two Lamb modes are generated, then a simple time analysis is enough to identify presence of damage in the plate. Chapter 5 has been dedicated for a more detailed description of this and other processing techniques. Time analysis mainly consists in the comparison of the detected acoustic signature of the structure in a damaged state with a previously obtained signature for a reference undamaged situation or healthy condition. The signature comparison is based on two basic methods; one being to look for changes in the transmitted acoustic signal (e.g. amplitude, phase, etc.) and the other to look for additional reflected and/or scattered signals from the damaged region, which can be considered as a passive acoustic source. Unless the damage is large, the magnitude of the perturbation caused by the damage in comparison to the undamaged signature signal will be very small, which demonstrate the importance of configuring the interrogation scheme in a way that provides optimum sensitivity due to the high directionality characteristic of most optical fibre sensors.

For the damage detection experiment we have chosen to use the polarimetric detection system for its easy operability and great repeatability. However in Chapter 6 we also have applied other detection systems for damage detection applications, such as the non-contact modified MZ interferometer which we have combined with a broadband and also non-contact laser generation of ultrasounds technique. We have also been involved in damage detection using FBGs, based on a single frequency excitation of the low order Lamb modes and applying a time analysis signature comparison technique as here presented for the polarimetric sensor, the results were published in [11].

In order to ascertain the suitability of the polarimetric sensor for damage detection a Perspex plate of 3 *mm* thickness was used onto which the optical fibre sensor was mounted and three PZT disc wafers acting as Lamb wave sources bonded (experimental lay out is shown in fig. 3.6). A hole, which behaves as a passive acoustic source, was made in the plate to simulate damage with a tight fitting plug being produced to enable the damage to be reversed. Silicone grease was used to provide the maximum acoustic continuity between the plug and the sheet. In this way, the detected ultrasonic signal is the combination of the ultrasound following the direct path between source and receiver, with the signal produced by the scattered wave emanating from the damage.

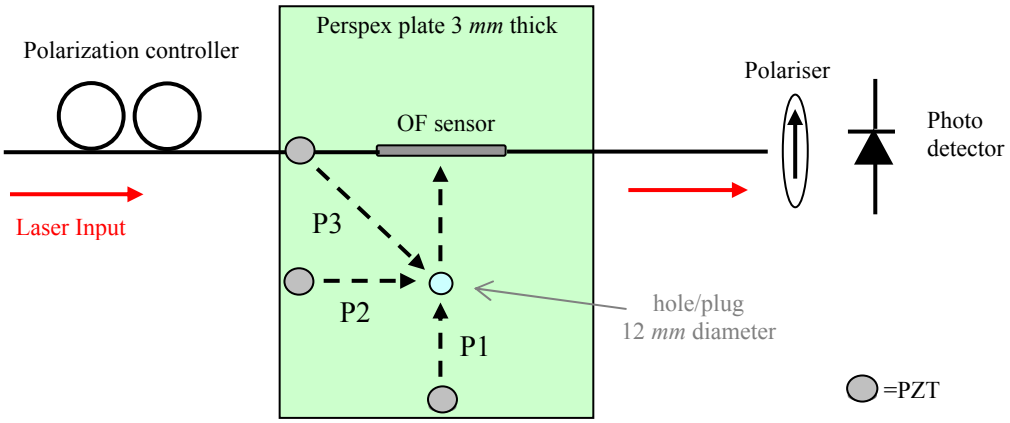

Figure 3.6: Plate layout for damage detection experiment with the polarimetric sensor.

The positioning of the transducers allowed for three paths to be investigated showing different aspects of the interactions between the Lamb waves, the hole and the sensor. The polarimetric sensor for this experimental configuration can best be used in two ways. Firstly, to look for defects in the area between the PZT source and the sensor through observing changes in the transmitted acoustic wave. In this case the source and transducer are aligned such that the incident wave is normal to the fibre (path 1 in our experiment). The second method is to look for reflections from a defect, in which case the transducer is situated such that the direction of the ultrasound wave is along its axis (path 3 in fig. 3.6).

The PZT source was excited with a 5 cycle (see Appendix E) sinusoidal toneburst at a frequency of 150 *kHz* providing the optimum acoustic coupling between the source and the Perspex plate. For the damage detection analysis we have only concentrated on the perturbations occurring to the S_0 mode propagation. Because it is the fastest propagating mode, the interaction with its scattering from the damage can adequately be isolated from the interaction with the reflections of the borders of the plate. In opposition with the A_0 mode that could be affected not only by the interaction with the reflections of the faster propagating S_0 mode but also with the last part of the incident pulse of the S_0 mode.

Analysis of the different paths ultrasonic signals

The detected ultrasonic signals for the three different paths are analysed next. In the figures associated to each path, three plots are presented; the one in black represents the plate without hole, the blue plot is when the hole plug is open and the red plot is the signal difference of the previous two and represents the signal due to the presence of the hole.

- *Path 1*: The source and hole are aligned normal to the sensor giving optimum sensitivity to the signals from both. The signal for the plate with hole is slightly attenuated

with respect to the case without hole (fig. 3.7). This may be thought of as being due to the slight phase difference that the ultrasonic signal scattered by the damage has over the direct propagating one. Hence the cancelling interference between the two slightly out of phase waves causes the amplitude attenuation. The scattered signal due to the presence of hole (in red) is 20% of the original signal amplitude.

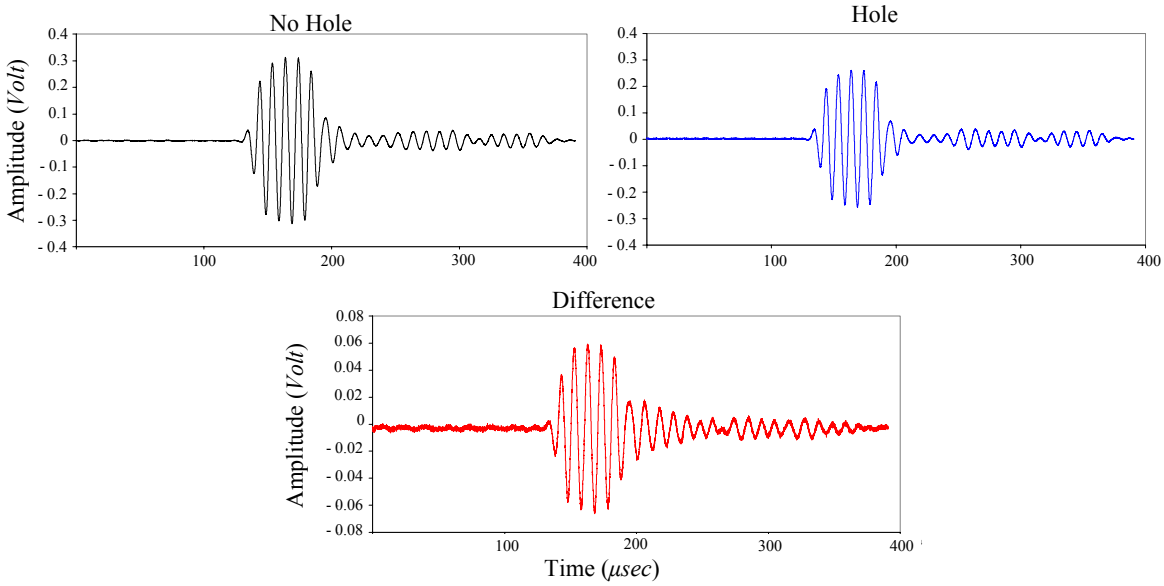

Figure 3.7: Ultrasonic signals for path 1 of fig. 3.6 for damage detection with polarimeter.

- *Path 2*: The PZT source is now at 45 degrees to the sensor resulting in a rather messy signal due to integration effect of the ultrasonic wavefront along the fibre sensor length. The integration effect is the subject of next chapter, where we also calculate the directionality of this type of sensors, which agrees with what we see in these experiments where the sensitivity of the sensor decreases as the source changes from a perpendicular orientation (as for path 1) to a parallel orientation (as for path 3). Hence the smaller amplitude of the signal for the case without hole (fig. 3.8 in black) respect to the previous path case. Comparing the plot with and without hole in fig. 3.8 we notice big differences after 150 *μsec*. The difference is appreciable in the red plot of the same figure which corresponds to the reflection from the hole of the signal excited by the PZT. The signal reflected from the hole is normal to the sensor corresponding with the direction of optimum sensitivity for the sensor. That is why the amplitude of the reflection is of similar amplitude to that the direct signal from the source.

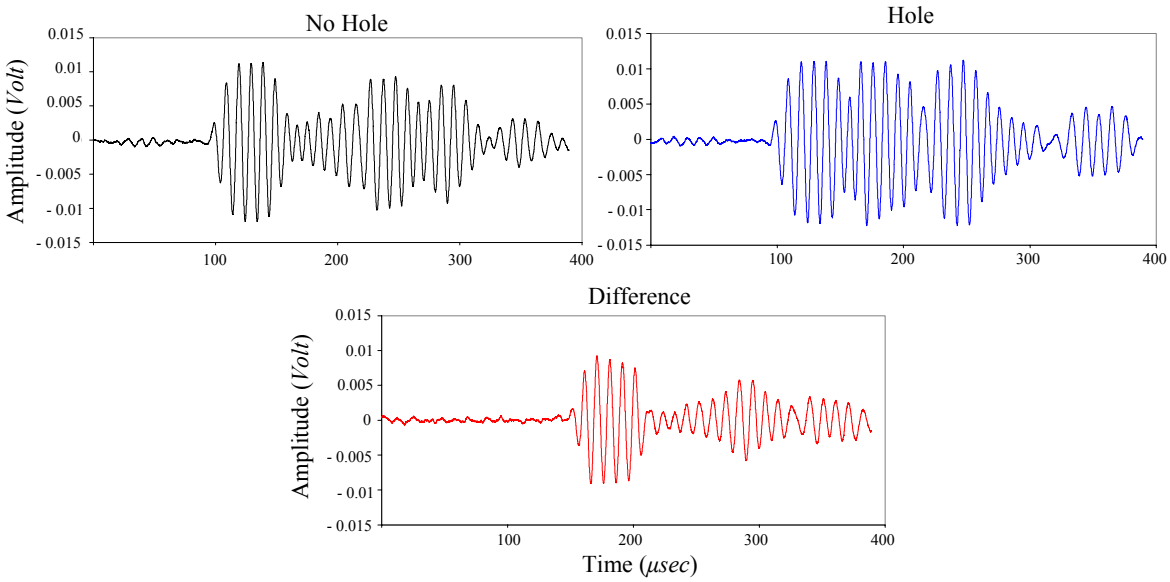

Figure 3.8: Ultrasonic signals for path 2 of fig. 3.6 for damage detection with polarimeter.

➢ *Path 3*: Now the ultrasonic signal from the source to the sensor is along the axis of the sensor which corresponds to the minimum sensitivity of the fibre sensor (as shown in next chapter). However like in the previous case, the signal reflected from the hole propagates in the direction of maximum sensitivity and as seen in fig. 3.9 the difference between the signals detected with and without hole are of higher amplitude than the signal directly from the PZT source with no hole. That difference which now happens at a later time (175 μm) agrees with the position of the hole for a wave propagating at the speed of the S_0 Lamb mode in aluminium at 150 *kHz* when the length of propagation corresponds to that of path 3.

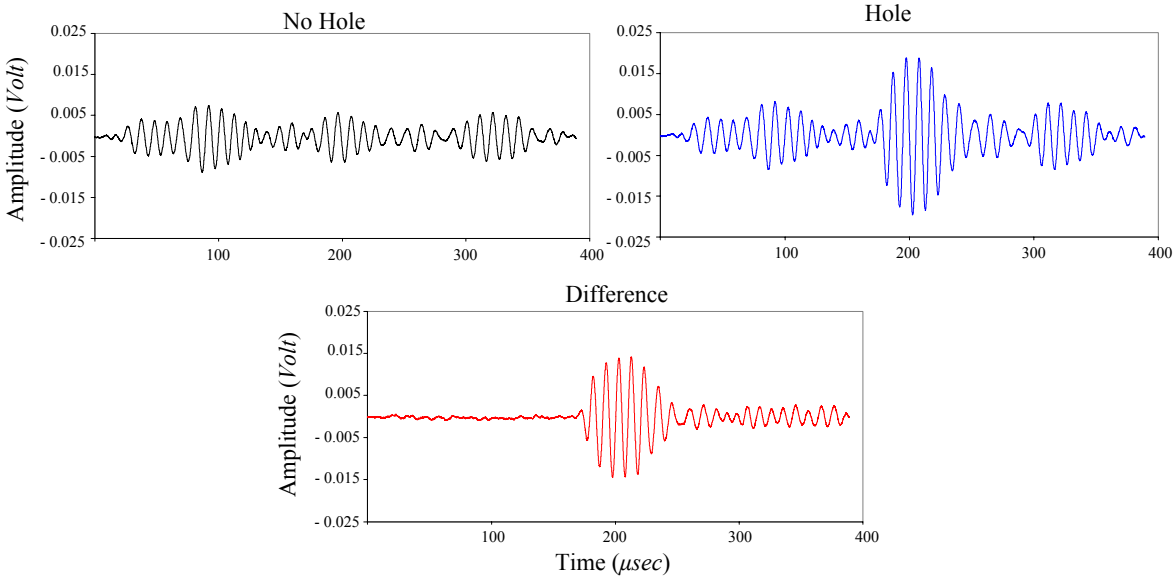

Figure 3.9: Ultrasonic signals for path 3 of fig. 3.6 for damage detection with polarimeter.

As we have seen in these examples, if the damage is in between the direct path source to sensor, then the perturbation in the detected time signal will be due to the slight phase change that the damage scattered signal has over the direct propagating one. The time signal in this case will be very similar to the undamaged situation with certain attenuation due to the cancelling interferences of two signals slightly out of phase. However if the damage is not in the direct path source to sensor then the damage creates a new path for the propagating ultrasound, of a different length to that of the direct path. The time signal in this case will show perturbations in the part of the signal which corresponds to the time delay of the propagating modes through the new path. Furthermore, the ultrasound following the new path approaches the sensor in a different direction than the ultrasound following the direct path. This generates damaged signals of different magnitude depending in the position of the damage when a highly directional sensor is applied (like in our situation).

3.7 ULTRASONIC SOURCE LOCATION USING A FIBRE BRAGG GRATING ROSETTE

An important feature of the optical fibre sensors here presented (apart of the modified Mach-Zehnder interferometer) is their inherent high directionality, which complemented with adequate signal processing can be used for damage location applications.

This example concentrates on FBG sensors for hole-through damage location in an aluminium plate. Nevertheless, the presented technique could also be extended to the other highly directional optical fibre techniques, but because they are not point sensors like the FBG the processing of the detected ultrasonic data is rather more complex due to their ultrasonic wavefront integration effect. Chapter 4 contribute to a better understanding of such complex interaction.

A schematic of the basic principle of operation for the interrogation method used in our damage location application was shown in fig. 3.1. This interrogation methodology is beneficed by the wavelength division multiplex (WDM) characteristics of FBGs, such that a distributed ultrasonic sensor can be made from a single optical fibre with multiple FBGs (of different Bragg wavelength) inscribed within. A low noise, narrow line-width tunable laser diode together with a high sensitivity photodetector are used for interrogating each one of the sensing gratings (connected in the way shown in fig. 3.1).

If the optical wavelength of the tunable laser source is tuned to the point of FWHM (Full Width at Half Maximum) of a grating reflectivity response curve, then any shift of the spectrum by interaction of the grating with the strain field of the ultrasonic wave will as a

result modulate the reflected optical power at the photo-receiver (as already explained in fig. 2.15). The use of a widely tunable laser source allows tuning (therefore interrogating) to the multiple gratings within a single fibre line.

The well-defined cosine-squared directional characteristic of the FBG sensor [12] enables us to configure three or more gratings into a rosette geometry in order to detect the direction from which an incoming ultrasonic wave is arriving. The rosette geometry is well-known from electrical strain gauges and consists of three strain gauges bonded to the sample surface to form an equilateral triangle. In the case of FBGs we use three gratings (whose reflectivity spectrum is shown in fig. 3.10-*right*) written onto a single fibre and bonded, onto the structural surface, symmetrically with their axes oriented 120 degrees respect to each other (as shown in fig. 3.10-*left*).

The cosine-squared sensitivity of the FBGs with respect to the angle between the ultrasound propagation direction and the fibre axis, is a maximum when the incident wave is in the direction of the fibre axis and a minimum when the direction is normal to the fibre.

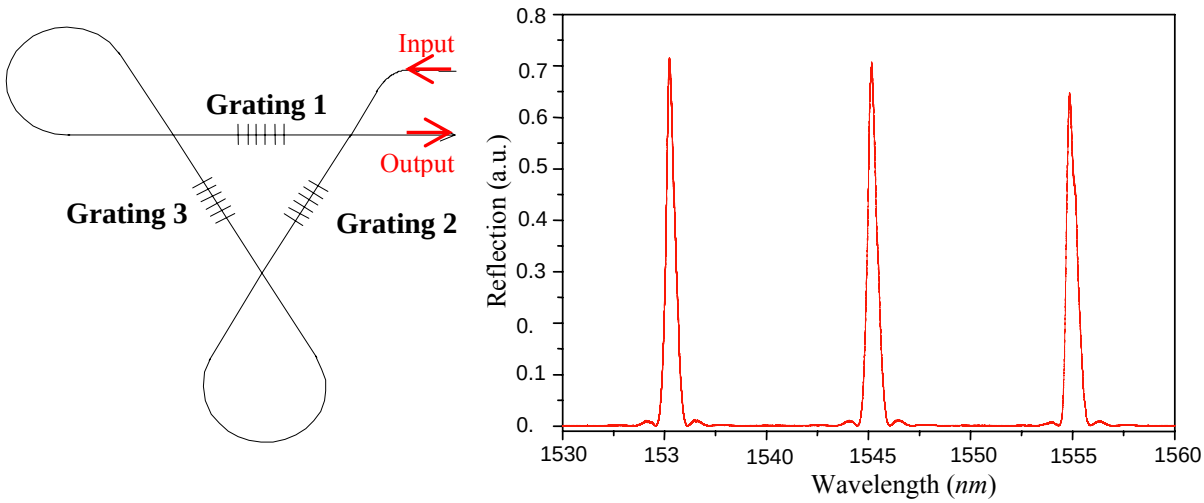

Figure 3.10: (*Left*) FBG rosette configuration for damage location. (*Right*) Reflectivity spectra of the FBGs associated to the rosette used in the experiments.

The direction of an incoming wave may be determined from the relative amplitudes of the signals from each of the three gratings of the rosette, using a suitable algorithm (for a more detailed description of the algorithm see [5]).

The problem when analysing the measured data for one rosette is the periodicity of the squared-sinusoidal amplitude function, because for each amplitude there are four possible corresponding angles giving a total of twelve angles for a rosette consisting of three gratings. Only one angle, α_{R1}, however, will satisfy the values for all of the gratings. The task is to

find this angle that gives the direction to the acoustic source for the first rosette as shown in fig. 3.11. After analysing data from two rosettes one ends up with two directions but four angles, as $\alpha_{R1,2} + 180°$ would also represent the desired direction. The final job is then to find the two angles for which the corresponding straight lines intersect. Calculating the *x*, *y* coordinates of the intersection will give the location of the acoustic source. If a passive source damage is considered then the location of the damage is accomplished.

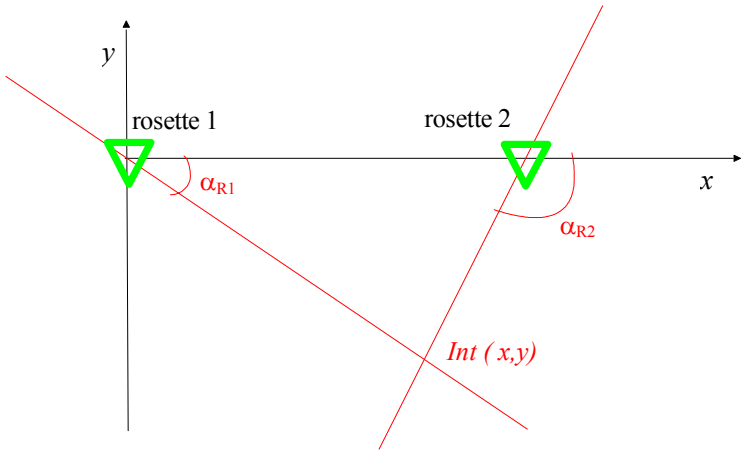

Figure 3.11: Intersection of the directions of two FBG rosettes, associated to the optimized angles α_{R1} and α_{R2}, for acoustic source location.

In order to test the accuracy of this procedure two FBG rosettes were bonded onto the surface of an aluminium plate of 1 *mm* thickness with three PZT sources and two holes-through of 12 *mm* diameter located in between the rosettes as shown in fig. 3.12. In order to distinguish the acoustic signals generated by the holes from those generated by the PZT sources, the holes are created like before with a plug that fits into the hole such that we can simulate reference and damage conditions. Additionally the position of the PZTs in relation to the FBG rosettes was carefully chosen such that transducers A and B were placed normal to one grating for each rosette and the other PZT (C) was located in the centre of the plate. Therefore when the hole is not in the line with the primary acoustic path, the grating will respond to the reflected wave which comes from a direction at which the grating is more sensitive.

The experimental results of the location predicted by the FBG rosette configuration are indicated by red stars in fig. 3.12. The letter associated to each star indicates the PZT source used for each location prediction. In conclusion in order to obtain the most accurate location results, we must avoid using a source aligned along the axis of any of the gratings in the rosettes. Because the ultrasonic signal detected directly from the PZT source is so large that

it is difficult to recover the signal generated by the hole. A more detailed description of the technique and results can be found in [5].

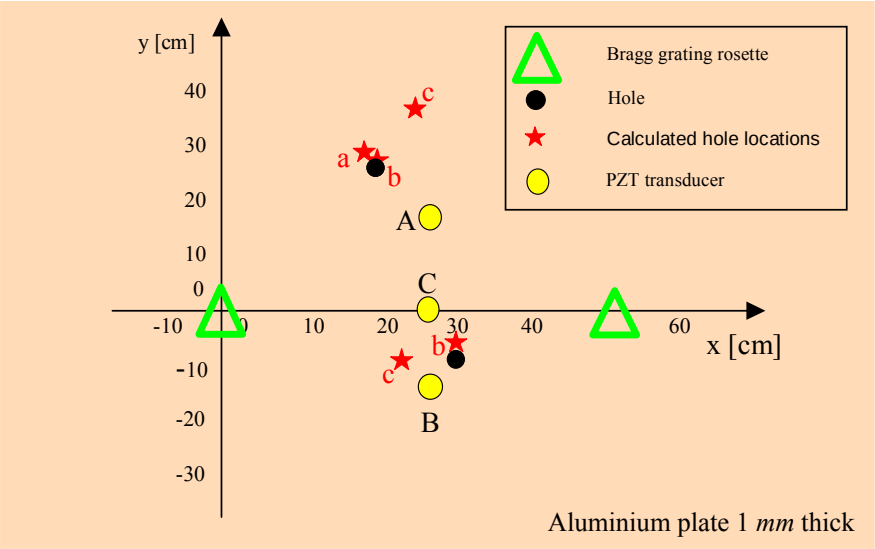

Figure 3.12: Experimental aluminium plate layout for hole location using FBG rosettes.

3.8 CONCLUSIONS

In this chapter we have presented the experimental realization and instrumental description of the four optical fibre systems (FBG, both configurations of the Mach-Zehnder interferometer and the polarimetric sensor) described in previous chapter for the detection of ultrasounds.

We have also described the technique developed for the bonding of the sensing optical fibre onto the surface of the sample under test. This technique which mainly consists in casting the optical fibre into a resin mould prior to attachment to the plate's surface, provided reproducible initial bonding conditions of the sensing fibre. Therefore repeatable and reliable ultrasonic signals under same launching conditions could be detected.

We have experimentally confirmed the suitability of the various optical fibre sensors for ultrasonic wave detection. We compare the ultrasonic traces taken from the different sensors obtained under identical ultrasound launch conditions (at two frequencies 110 *kHz* and 270 *kHz* at which only the low order modes S_0 and A_0 are excited). The relative amplitudes of the detected modes were different for each sensor as predicted theoretically. Because the relative amplitudes of the in-plane and out-of-plane displacement associated to each mode is very different, as well as the sensitivity to the interaction with each of these displacements differs for each sensor.

Finally we applied the optical fibre sensors to damage detection and location.

The polarimetric sensor was used for damage detection and it was shown that its damage sensitivity was very much dependant in the orientation of the damage respect to the ultrasonic source and respect to the sensor's directivity pattern. Time analysis was applied to the processing of the detected ultrasonic data, mainly consisting in the comparison of the detected acoustic signature of the structure in a damaged state with a previously obtained signature for a reference undamaged situation. And we looked for changes in the transmitted acoustic signal (e.g. amplitude, phase, etc.) and for additional reflected and/or scattered signals from the damaged region.

In the damage location application we used FBGs sensors, due to their inherent high directivity and the simplicity of analysis associated to their cosine-squared directional characteristic and their wavelength division multiplexing characteristics. Three FBGs were used in a rosette configuration and two of such rosettes were needed to locate hole-through damages in an aluminium plate. It was found that in order to obtain the most accurate location results, care should be taken not to align the ultrasonic sources along the axis of any of the gratings in the rosettes.

3.9 REFERENCES

[1] Betz D., Thursby G., Culshaw B. and Staszewski W. *Acousto-ultrasonic sensing using fiber Bragg gratings*, Smart materials and structures, vol. **12**, pp. 122-128, 2003.

[2] Atherton K., Dong F., Pierce G. and Culshaw B. *Mach-Zehnder optical fiber interferometers for the detection of ultrasound*, Proc. SPIE Smart Structures and Materials, vol. **SPIE-3986**, pp. 27-34, 2000.

[3] Dong F., Atherton K., Pierce S. G. and Culshaw B. *Measurement of in-plane and out-of-plane displacements for ultrasonic flaw detection*, 5th European Conference on Smart Structures and Materials, Proceeding of SPIE, vol. **4073**, pp. 324-331, 2000.

[4] Thursby G., Dong F., Yong Y., Sorazu B., Betz D. and Culshaw B. *Fibre optic polarimetric detection of lamb waves*, 15th International Conference on Optical Fibre Sensors Portland (USA), 2002.

[5] Betz D. *Application of optical fibre sensors for Structural Health and Usage Monitoring*, PhD Thesis, University of Sheffield, Sheffield, 2004.

[6] Pierce S. G., Philp W. R., Gachagan A., McNab A., Hayward G. and Culshaw B. *Surface-bonded and embedded optical fibers as ultrasonic sensors*, Applied optics, vol. **35(25)**, pp. 5191-5197, 1996.

[7] Yong Y. *Surface-bonded optical fiber works as ultrasonic sensor*, MPhil Thesis, University of Strathclyde, Glasgow, 2002.

[8] http://www.promatech.co.uk

[9] *Damage assessment in smart composite structures: DAMASCOS*, EU Project # BE974213, 2001.

[10] Thursby G., MacLean A., Hogg H. and Culshaw B. *Ultrasound detection of damage in complex carbon fibre/metal structures*, 13th Inter. symposium on Smart Structures and Materials SPIE, San Diego, 2006.

[11] Betz D., Siedler S., Thursby G., Culshaw B. and Staszewski W. *Damage detection using fiber Bragg grating ultrasonic sensors*, Proceeding of the 16th International conference on optical fibre sensors, Japan, 2003.

[12] Betz D., Thursby G., Culshaw B. and Staszewski W. *Lamb wave detection and source location using fibre Bragg gratings rosettes*, Proceedings of the 10th Int. Symp. on Smart Struc. and Materials SPIE, San Diego, 2003.

Chapter 4

WAVEFRONT INTEGRATION TECHNIQUE

4.1 INTRODUCTION

The ultrasonic waves can be detected by a variety of methods (PZTs, FBGs, interferometric sensors, polarimetric sensors, etc.) described in Chapter 2, most of which produce essentially point measurements and therefore necessitate an array of sensors to cover any given area. If we bond an optical fibre onto the surface of the material or embed it within it, a sensor may be formed that is sensitive to the interaction of the acoustic wave along its length, acting as an acoustic wavefront integration sensor. This means that we can potentially interrogate a large area with just one sensor. With the added advantages that in this approach the sensor is fixed in position, therefore causing a minimal variation in the acoustic coupling at the interface with the sample under test. Additionally like any optical fibre sensor it is lightweight and immune to electromagnetic radiation. It possesses multiplexing capabilities and can produce a very high fidelity reception over a wide bandwidth [1]. Furthermore optical fibre sensors can be integrated into composite materials to form smart structures without altering their mechanical properties [2].

The detection of ultrasonic waves by such sensors can be achieved through either measuring the changes in the output phase of the light (Mach-Zehnder interferometric sensor [1]) or by monitoring changes in the polarimetric state (polarimetric detection system [3]). Whichever method is used the response of the sensor is highly directional as described in Chapter 2, a fact that may be used to improve the sensitivity of damage detection and its location [4].

If we consider the damage to be a secondary passive acoustic source, the signal obtained by the sensor will be a combination of that from the acoustic wave directly from the primary source (e.g. a PZT) and that from the damage as shown in fig. 4.1-*right*. The relative magnitudes of these two signals will determine our ability to separate and identify them.

By experience, the polarimetric and modified MZ interferometer system require the length of the sensing bonded/embedded optical fibre to be greater than an acoustic wavelength so that an acceptable signal can be produced. Hence unless the acoustic wavefront is at all times parallel to the fibre (as shown in fig. 4.1-*left*), there may be more than one ultrasonic wavefront crossing it at any given moment (fig. 4.1-*right*). Different parts of the fibre length may be subjected to varying positive and negative pressures. The properties of the output light of the fibre sensor will thus be an integrated value of all these variations. As we will see in this chapter, this integrating effect will lead to some complex periodic sensitivities of this sensors with respect to its length, acoustic wavelength, distance between source and sensor and the orientation of the acoustic wave propagation direction respect to the sensor. This complex response clearly affects their ability to allow the separation and identification of the signals associated to the primary and secondary acoustic sources, thus a better understanding of wavefront integrating sensors response is needed for their useful application into NDT. Until now the integrating characteristic of optical fibre sensors has not been studied in depth, with very few reports published about it. Due to their ultrasonic wavefront-integrating characteristic the obtained signals are difficult to analyse. In this chapter we present my contribution to a better understanding of this kind of sensors by a basic theoretical model of the integration effect and the comparison of the results with experimental data.

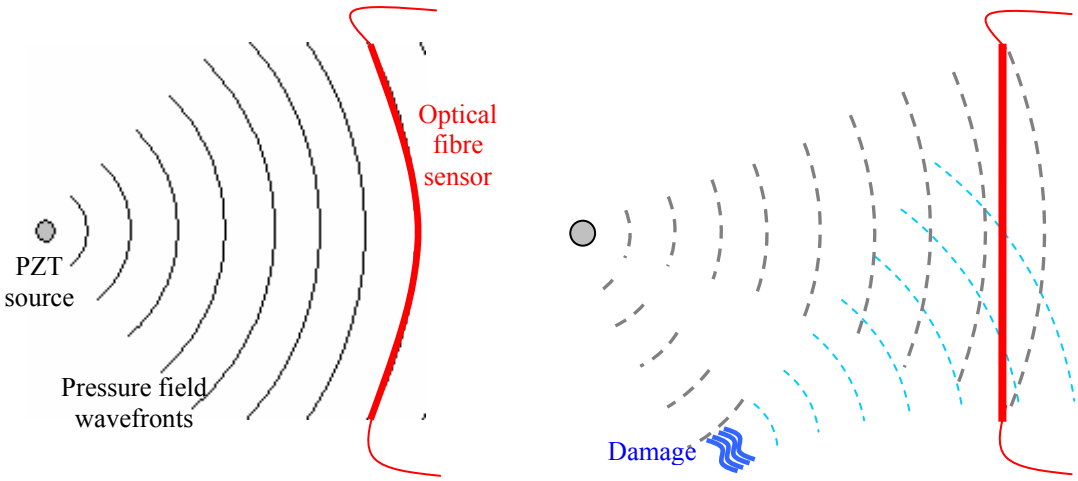

Figure 4.1: (*Left*) When the optical fibre sensor is parallel to the ultrasonic wavefront, the optical phase in the fibre changes equally and its time variation is equal to the wave amplitude. (*Right*) In any other fibre orientation the phase change in the fibre will be an integrated effect along the fibre length of the ultrasonic wavefront. The presence of damage can be considered as a secondary passive source.

4.2 WAVEFRONT INTEGRATION MATHEMATICAL MODEL

The mathematical model for the wavefront integration simulation here presented is based in the operation of the optical fibre Mach-Zehnder interferometer system presented in previous chapters. In this detection system, a finite length L of optical fibre of the interferometer sensing arm is bonded to the surface or embedded into the sample material. The pressure field associated to the propagating ultrasonic waves induces a modulation of the refractive index in the fibre core, causing a difference in the optical phase with respect to the light propagating in the reference arm. When both light beams are combined in the output photo-detector an interference pattern proportional to the phase difference between sensing and reference beams is observed in the detected optical intensity power, as given by eqn. 4.1.

$$I = \frac{I_0}{2} \cdot \left[1 - \cos(\Delta\phi)\right] \tag{4.1}$$

Where I_0 is the input optical intensity to the interferometer and $\Delta\Phi$ is the difference on the optical phase delay of the beams at the end of both arms. As mentioned in previous chapters $\Delta\Phi$ is the combination of a slow varying phase shift Φ_d (due to environmental perturbations and any phase difference between both arms due for instance to a length mismatch) and the term due to the interaction of the ultrasonic wave with the sensing arm $\delta\Phi$. The amplitude of the induced phase difference by the ultrasound can correctly be assumed to be small. Additionally because the environmental perturbation is usually a slow varying signal, by high pass filtering the optical intensity output of the interferometer, we can assume that its modulation is only caused by the ultrasonic wave signal component. Hence we can express the interferometer intensity modulation due to ultrasonic wave perturbation as:

$$\delta I = \left.\frac{\partial I}{\partial \Delta\phi}\right|_{OP} \cdot \delta\Delta\phi = \frac{I_0}{2}\sin\left(\Delta\phi_{OP}\right) \cdot \delta\Delta\phi = \frac{I_0}{2} \cdot \delta\phi \tag{4.2}$$

We have considered that the interferometer is locked in the quadrature operation point, thus $\Delta\phi_{OP} = (2n+1)\cdot\pi/2$, where n is an integer indicating that the interferometer can be locked into any fringe of the interference pattern. Equation 4.2 shows that the intensity modulation at the output of the interferometer is linearly proportional to the ultrasonic phase modulation in the sensing arm.

If we neglect any polarization effect over the phase modulation, then as described in [7] the cause of this modulation is due to a perturbation in the propagation constant $\beta = 2\pi\, n_{eff}/\lambda_0$ (with λ_0 being the wavelength of the used light in vacuum) and/or a change in the physical length of the sensing section of the optical fibre L, as expressed in eqn. 4.3.

$$\delta\Delta\phi = \beta \cdot \delta L + L \cdot \delta\beta \tag{4.3}$$

The change in β could be caused by two principles [7]; *strain-optic effect* which consist mainly in a change of the effective refractive index of the fibre n_{eff} by the ultrasonic wave stress field and the *waveguide mode dispersion effect* caused by a change in the fibre core diameter by the ultrasonic wave strain field. Considering a homogeneous stress through the section of the fibre, based on the fact that the ultrasonic wavelengths in our experiments are >> the fibre diameter [5]. It can be shown [7] that the *waveguide mode dispersion effect* is several orders of magnitude smaller than the *strain-optic effect*, hence it can be neglected. On the other hand the phase modulation caused by the change in the optical fibre length is caused mainly by the strain component in the longitudinal axis. This strain component is negligible unless the direction of propagation of the acoustic wave is parallel to the fibre longitudinal axis, in which case as the length of the bonded/embedded fibre is several times the value of the ultrasonic wavelength, the integration effect of expansions and compressions along the fibre length will cancel each other.

In conclusion we can accurately assume that the phase modulation $\delta\Delta\phi$ is caused by a modulation of n_{eff} in the embedded or bonded fibre of the sensing arm due to the stress field of the acoustic wave. In order to express a relationship between the changes in n_{eff} and the acoustic wave pressure field some simplifying assumptions were considered in our model:

- Propagating Lamb waves are generated by a point source on a sheet of uniform thickness of an isotropic material.
- Ultrasound pressure field is sinusoidal in time and space and follows a cylindrical wavefront in the plate as it propagates from the source as an ultrasonic guided wave (Lamb wave). The magnitude of the pressure field is given by:

$$\mathrm{Pr}\,essure = \frac{A_0}{\sqrt{r}}\sin\left(\omega_s t - k_s r\right) \tag{4.4}$$

  Where r is the distance to the ultrasonic source, A_0 is the amplitude of the wave one meter from the source, ω_s is the temporal frequency of the acoustic wave and k_s is the spatial frequency of the acoustic wave. The radial symmetry of the stress field is assured by the PZT ultrasonic source used [6].

- We consider a linearly proportional change in n_{eff} by the stress field, as given by:

$$n_{eff} = n_{eff\,0} + \xi\frac{A_0}{\sqrt{r}}\sin\left[2\pi\left(f_s t - \frac{r}{\lambda_s}\right)\right] \tag{4.5}$$

Where n_{eff0} is the effective refractive index of the optical fibre without any ultrasonic perturbation, and ξ is an arbitrary proportional constant.

- The effects of acoustic attenuation are assumed to be negligible over the difference in the distances to the source from the points along the length of the fibre sensor, due to the reduced dimensions of the fibre sensors involved.

The refractive index modulation in eqn. 4.5 affects each section of the sensing fibre of infinitesimal length δx. We can then integrate these values to get the change in the effective index of the total length of the sensor and then convert it into an optical phase modulation as shown in eqn. 4.6.

$$\Delta\phi = \frac{2\pi}{\lambda_0}\int_{-L/2}^{L/2}\left(n_{eff}(x) - n_{eff\,0}\right)\cdot dx = \frac{2\pi}{\lambda_0}\cdot\xi\cdot A_0\int_{-L/2}^{L/2}\frac{\sin\left(\omega_s t - \frac{2\pi}{\lambda_s}r\right)}{\sqrt{r}}\cdot dx \tag{4.6}$$

Where x is the axis of the fibre and r is the distance from the source to a section δx on the fibre as shown in fig. 4.2. If we rewrite the vector $\boldsymbol{r}$ as the sum of the vectors $\boldsymbol{r'}$ (distance source to centre of fibre) and $\boldsymbol{x}$ (distance from centre of fibre to the section δx) as defined in fig. 4.2, and normalize their values by the ultrasonic wavelength λ_S (such that $r' = n\lambda_S$, $x = x'\lambda_S$) and the length of the fibre as $L/2 = m\lambda_S$. Then we can express the optical phase modulation normalized respect to $4\pi\xi A_0/\lambda$ as:

$$\Delta\bar{\phi} = \int_{-m}^{m}\frac{\sin\left(\omega_s t - 2\pi\cdot\sqrt{n^2 + x'^2 - 2\cdot n\cdot|x'|\cdot\cos\alpha}\right)}{\sqrt[4]{n^2 + x'^2 - 2\cdot n\cdot|x'|\cdot\cos\alpha}}\cdot dx' \tag{4.7}$$

Where $\alpha = \pi/2 - \theta$. The integral in eqn. 4.7 cannot be solved analytically thus a MATLAB script was written to solve it numerically.

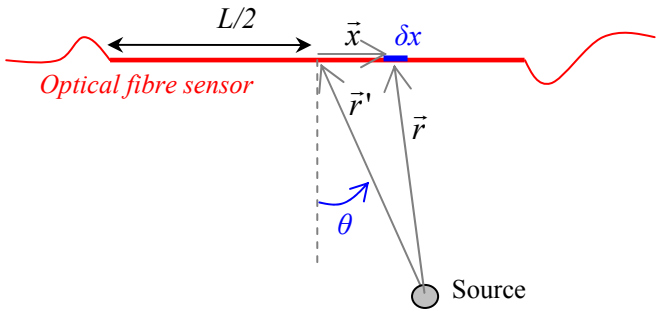

Figure 4.2: Definition of the wavefront integration model variables.

4.3 SIMILARITY BETWEEN POLARIMETER & INTERFEROMETER WAVEFRONT INTEGRATION

The previous theoretical model was developed taking into account only the modulation that the ultrasonic wavefront pressure causes on the effective refractive index of the core of the optical fibre sensor. This model was developed with the idea of applying the Mach-Zehnder interferometer system described in Chapter 2, however a sufficiently stable instrument for this purpose was not available at the time of these experiments. Based in initial experimental analysis we noticed that the polarimetric detection system integrates the signal in much the same way as the interferometric system does but in a more stable way. Therefore we decided to use the polarimetric detection system (described in Chapter 2) instead. Although the interaction principles of both detection systems are quite different in nature, both systems are sensitive to the ultrasonic wave stress field; with the interferometric system based in a refractive index modulation, and the polarimetric system based in the modulation of the polarization state of light due to the birefringence induced by the pressure field into the fibre. Initial analysis and the agreement between the previous model and the experiments based in polarimetric sensor evidences that positive and negative changes are produced in the fibre birefringence of the polarimetric sensor in a similar way to that expected in the fibre effective refractive index for the interferometric system.

In this section we present a more detailed theoretical analysis of the previous affirmations, in order to confirm the similar wavefront integration effect of both detection systems. For this, we have modelled the Lamb wave pressure field interaction with the optical fibre sensors used in the polarimetric detection system. As already described in Chapters 2 and 3, the optical fibre sensors consist of a single mode optical fibre (125 μm cladding diameter) cast into an epoxy resin mould prior to their attachment to the plate, this allows a more reliable and reproducible results than bonding the optical fibre directly to the plate. The plate to which the sensors are bonded to is a Perspex plate 3 *mm* thick, for this model we can consider the dimensions to be long enough as to avoid any reflexion from its borders. A cross section view of the experimental configuration is shown in fig. 4.3-*left*.

The similarity in elastic properties of the Epoxy mould and the Perspex plate, and the small diameter of the optical fibre in comparison with the mould dimensions, the plate thickness and the ultrasonic wavelength (~1 *cm*), allows approximating the whole system as having the optical fibre embedded into a Perspex plate of 4.5 *mm* thick (as shown in fig. 4.3-*right*). Additionally because the fibre coating has also similar acoustic impedance than Perspex then it is acceptable to consider the coating as part of the Perspex plate and that the birefringence

on the optical fibre are induced by the pressure field on the borders of the cladding. This pressure can be obtained by applying the Lamb wave propagation displacement equations (eqn. A.20) in order to calculate the displacement of the material particles around the surface of the fibre cladding.

The birefringence induced in the fibre by the propagating ultrasonic wave, is proportional to the gradient of its pressure field around the section of the fibre and dependent on the direction in which this pressure takes place, as it distinguishes between a compressive pressure and an expansive one. This pressure is proportional to the acceleration of the particles around the cladding, which can be obtained from the second time derivative of the displacement equations given in eqn. A.20.

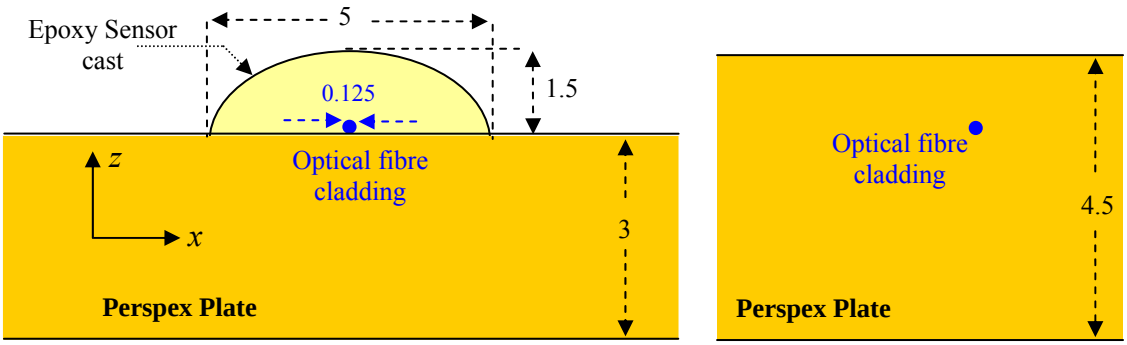

Figure 4.3: (*Left*) Cross section view diagram of the optical fibre sensor used in the polarimetric system. All dimensions are in *mm*. (*Right*) Approximation of the setup in the left to a optical fibre cladding embedded into a 4.5 *mm* Perspex plate.

The obtained expression for the particle acceleration components of a plane wave are given in eqns. 4.8 and 4.9, where the wavefront of the ultrasound is considered parallel to the fibre. Hence the only acceleration components needed are x and z as defined in fig. 4.3-*left*. Because we are only interested in the birefringence distribution induced in the fibre and not in the absolute birefringence changes, then we can express the acceleration components normalized against the vertical displacement in the surface of the plate as:

$$\bar{a}_X(x,z,t) = \mathrm{Re}\left[\frac{-\omega^2\left(\dfrac{\cosh(\bar{q}\cdot\bar{z})}{\sinh(\pi\cdot fd\cdot\bar{q}/c)} - \dfrac{2\bar{q}\cdot\bar{s}}{1+\bar{s}^2}\dfrac{\cosh(\bar{s}\cdot\bar{z})}{\sinh(\pi\cdot fd\cdot\bar{s}/c)} \right)}{\bar{q}\left(1-\dfrac{2}{1+\bar{s}^2}\right)} e^{i\left(\bar{x}-\omega t+\frac{\pi}{2}\right)} \right] \tag{4.8}$$

$$\bar{a}_Z(x,z,t) = \mathrm{Re}\left[\frac{-\omega^2 \left(\frac{\sinh(\bar{q}\cdot\bar{z})}{\sinh(\pi\cdot fd\cdot\bar{q}/c)} - \frac{2}{1+\bar{s}^2}\frac{\sinh(\bar{s}\cdot\bar{z})}{\sinh(\pi\cdot fd\cdot\bar{s}/c)} \right)}{\left(1-\frac{2}{1+\bar{s}^2}\right)} e^{i(\bar{x}-\omega t)} \right] \tag{4.9}$$

Where $\bar{q} = \sqrt{1-(c/c_L)}$, $\bar{s} = \sqrt{1-(c/c_T)}$, $\bar{z}$ and $\bar{x}$ are the plate particles' vertical position and horizontal positions respectively, normalized in ultrasonic wavelengths. Notice that as shown in fig. 4.3-*left* and defined in Appendix A for the definition of eqn. A.20, the origin of z is situated at the middle depth of the plate considered of thickness $2d$, thus the top surface is at $z = d$ and the bottom surface at $z = -d$.

In practice however the propagating ultrasonic Lamb waves are not plane waves but cylindrical ones. Nevertheless, because the optical fibre sensor will always be located in the far field of the ultrasonic source, and because its diameter is much smaller than an ultrasonic wavelength, then we can assume that the arriving Lamb wavefront to each infinitesimal segment of the fibre *dl* is a plane wave as shown in fig. 4.4. In order to include the effect of the length of the fibre as a different distance of each fibre segment to the source ζ, we modify the temporal phase value ωt associated to each fibre segment.

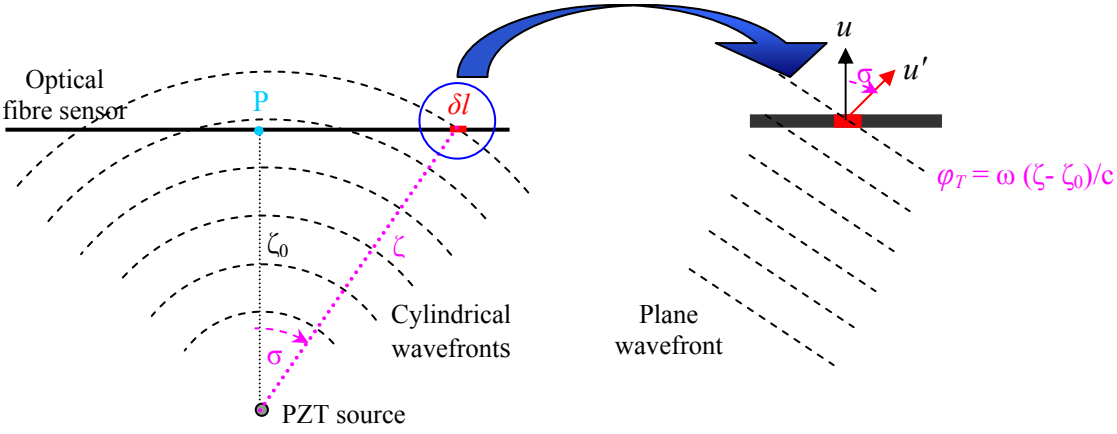

Figure 4.4: (*Left*) The cylindrical propagating Lamb waves can be approximated to a plane wave for each infinitesimal segment length of the fibre sensor (*Right*).

As we can see from the ultrasonic plane wavefront approximation shown in fig. 4.4-*right*, the associated in-plane particle displacement *u*' does not have the same direction for all the fibre segments. In fact *u*' is a function of the angle between the direction source:segment and the normal direction to the fibre (defined in the previous figure as σ). It is the projection of this displacement normal to the fibre *u* that mainly dominates the change in the fibre's refractive index and so in its induced birefringence. As a first approximation we will consider only this

displacement component. We should also neglect the absorption attenuation because the distance of the various fibre segments to the source is not as different as to create a considerable change in the arriving ultrasonic amplitude. In any case as we mentioned, we are not interested in absolute values of the birefringence changes as we saw from the normalization of the particles acceleration distribution along the fibre.

Regarding the induced birefringence into the fibre (which is proportional to the difference in the acceleration vector perpendicular to the fibre in opposite points of the fibre diameter) two different situations can be distinguished as shown in fig. 4.5.

Figure 4.5-*left* shows the situation in which the acceleration vector at the opposite sides of the fibre have opposite direction.

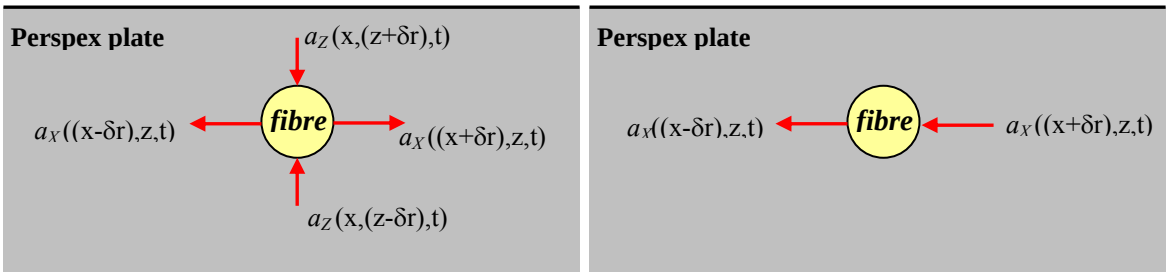

Figure 4.5: Different cases of gradient acceleration vectors in the fibre cladding: (*Left*) Compression and expansion. (*Right*) Displacement.

From one side the situation of the vertical acceleration vectors (a_Z (x,(z+δr),t), a_Z (x,(z-δr),t)), as they point towards the fibre they cause an increment of the pressure over the fibre. On the other hand, the horizontal acceleration vectors (a_X((x-δr),z,t), a_X ((x+δr),z,t)) cause a decrement of the pressure inside the fibre, because they are expanding the fibre diameter. The situation shown in fig. 4.5-*right* has the acceleration vectors at opposite sides of the fibre pointing towards the same direction. Thus in one side the acceleration compress the fibre (a_x ((x+δr),z,t)), meanwhile in the opposite side it is expanding it. The resultant effect is that part of these accelerations is consumed in a displacement of the fibre and not in a birefringence inducing pressure. All this cases are taken into account in our mathematical model.

Finally the Cartesian acceleration components in eqns. 4.8 and 4.9 are converted into cylindrical coordinates for being more adequate in the present analysis, as shown in fig. 4.6-*left* for the unitary vectors of the displacement components. The relationship between both systems of coordinate for the acceleration components are given in eqn. 4.10 and 4.11.

$$\bar{a}_r = \left(\cos\theta \cdot \bar{a}_X + \sin\theta \cdot \bar{a}_Z\right) \cdot \hat{u}_r \tag{4.10}$$

$$\bar{a}_\theta = \left(\cos\theta \cdot \bar{a}_Z - \sin\theta \cdot \bar{a}_X\right) \cdot \hat{u}_\theta \tag{4.11}$$

In the polar coordinates we distinguish between the radial $\hat{u}_r$ and tangential $\hat{u}_\theta$ acceleration components. Although the tangential component has a twist effect over the fibre that will affect its birefringence, we neglect it in the present first approximation. Hence we only take into account the effect of the radial acceleration component as the one that will dominate the induced birefringence. The gradient radial acceleration is calculated as the difference of the radial acceleration components in opposite sides of each fibre section along the length of the fibre. After applying the projection of the radial acceleration component into the direction normal to the fibre (as described previously in fig. 4.4), we get the next expression for the radial acceleration component:

$$\bar{a}_r = \left(\cos\theta \cdot \cos\sigma \cdot \bar{a}_X + \sin\theta \cdot \bar{a}_Z\right) \cdot \hat{u}_r \tag{4.12}$$

Notice that the present analysis considers only the case shown in fig. 4.4, where the ultrasonic source is normal to the centre position of the fibre (point *P* in the figure). An improvement of the present model would include a new variable that would specify different orientations of the source respect to the fibre. The obvious implications of different source orientations are the changes it would cause in the periodicity of the pressure distribution along the fibre (as shown in fig. 4.8 for the here assumed perpendicular orientation).

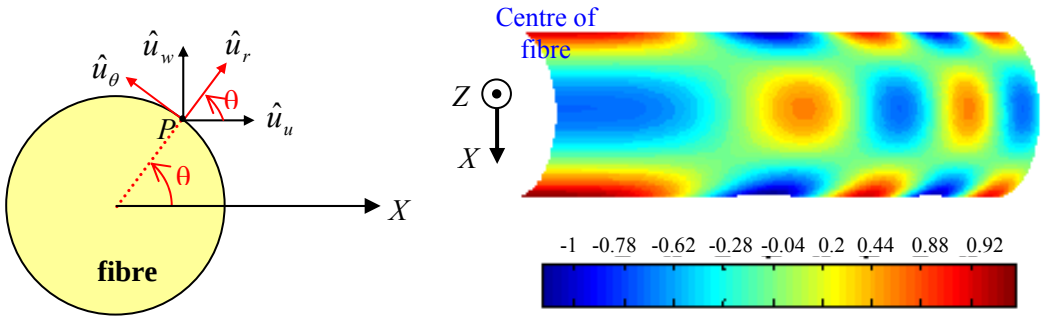

Figure 4.6: (*Left*) Conversion of the unitary vectors from the Cartesian displacement coordinates ($\hat{u}_u$, $\hat{u}_w$) to the polar displacement coordinates ($\hat{u}_r$, $\hat{u}_\theta$). (*Right*) Normalized radial acceleration component for the plate particles around the fibre cladding.

In fig. 4.6-*right* we plot the normalized pressure distribution (or equivalently the radial normalized acceleration difference) along the perimeter of an optical fibre length of 32 *cm* and a distance to the source of 21.6 *cm* perpendicular to the centre of the fibre, with working frequency of 100 *kHz*. The plot shows just half of the fibre length (the other half is symmetric). The red areas are associated to the most intense positive radial acceleration (expansion pressure), and in blue are the most intense negative radial acceleration values

(compression pressure). Noticeable is the fact that the red and blue regions alternate along all the fibre length between in-plane and out-of-plane planes.

To see this more clearly we show in fig. 4.7 only the maximum compressing radial acceleration difference in pink (maximum refractive index increment) and the maximum expanding radial acceleration difference in green (maximum refractive index decrement). The birefringence in the optical fibre is induced by the differential refractive index of these two principal acceleration component axes. It is noticeable that the birefringence axes are parallel to the in-plane and out-of-plane directions of the plate along all the fibre length. The modulated birefringence has a sinusoidal decreasing amplitude distribution in a similar way to the pressure analysis of the wavefront integration model developed for an interferometric detection system (as applied later in this chapter) and with the results shown in fig. 4.8.

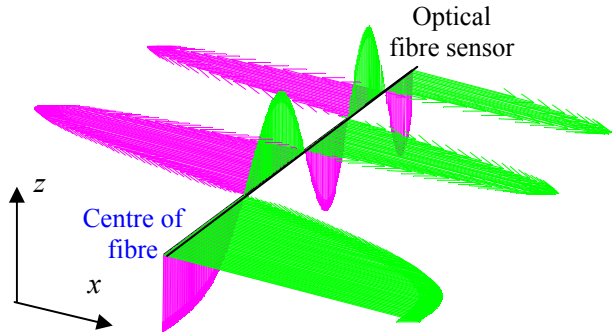

Figure 4.7: Birefringence major (pink) and minor (green) axis radial acceleration components in the section of the fibre along its length. Plotted is half of the fibre sensor of $\sigma_{max} = 0.636$.

A different orientation of the source respect to the fibre sensor would not change the fact that the induced birefringence axes appear parallel to the in-plane and out-of-plane axis of the plate, and it only would affect the periodicity of the birefringence modulation.

Figure 4.8 compares the birefringence axis radial accelerations with the total net radial acceleration in the centre of the fibre. The first case is the one to take into account for the polarimetric detection system as it is the induced birefringence in the fibre core that modifies the polarization state of the light within the fibre. Meanwhile the second case is the one that affects the interferometric system, as it is the total pressure in the fibre core that modulates the effective refractive index of the light propagating within the interferometric sensing arm fibre. It is clear from this figure that the total radial acceleration which modulates the fibre's core effective refractive index follows the positive and negative changes of the fibre in-plane birefringence modulation and symmetrically also follows the chirp modulation behaviour of the out-of-plane birefringence axis.

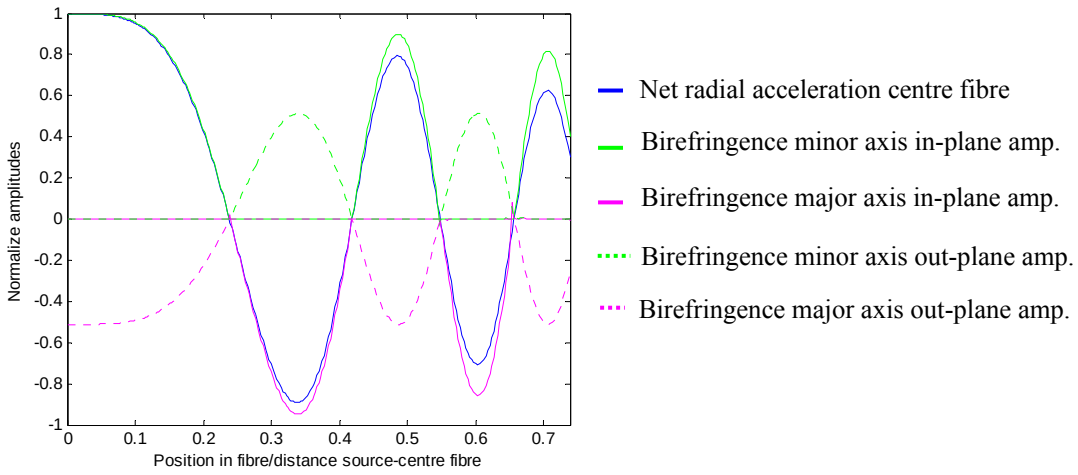

Figure 4.8: Comparison of the normalized birefringence axis radial accelerations (as analysed by polarimetric system) and the normalized total net radial acceleration in centre of fibre (as analysed by interferometric system).

4.4 EXPERIMENTAL VERIFICATION OF MODEL SIMULATIONS

In this section we present the results obtained with the model by simulating the changing response of a wavefront integration fibre ultrasound detector of different lengths to varying distance and orientation from a point ultrasonic source. This is complemented by a series of related experiments developed in order to validate the model results. In the experiments care has been taken to satisfy as accurately as possible the assumptions related with the mathematical model. Therefore the source driving signals are of low frequency so that only the basic Lamb wave modes are excited, and only the signal produced by the fastest and non-dispersive S_0 mode is analysed (in fig. 4.9-*left* we show in blue a typical detected ultrasonic signal where only the low order modes and their reflection from the plate's boundaries are present). The driving signal consists in all cases of a few cycles Hamming windowed sinusoidal tone bursts (like the signal in red in fig. 4.9-*left* for a 4.5 cycles case). The window decreases the frequency components of the ultrasound, reducing the dispersion effect in the propagating waves, which have yet to be incorporated into the model, making the signal closer to a single frequency sinusoidal as simulated in the model. The low frequency of the propagating ultrasonic waves (around 100 *kHz* in Perspex with group velocity for S_0 mode of ~2.44 *km/s* and around 270 *kHz* in aluminium with group velocity for S_0 mode of ~5.44 *km/s*) assures that the ultrasonic wavelength is >> than the fibre core (~10 μm for single mode fibre) thus providing a homogeneous stress through the section of the fibre.

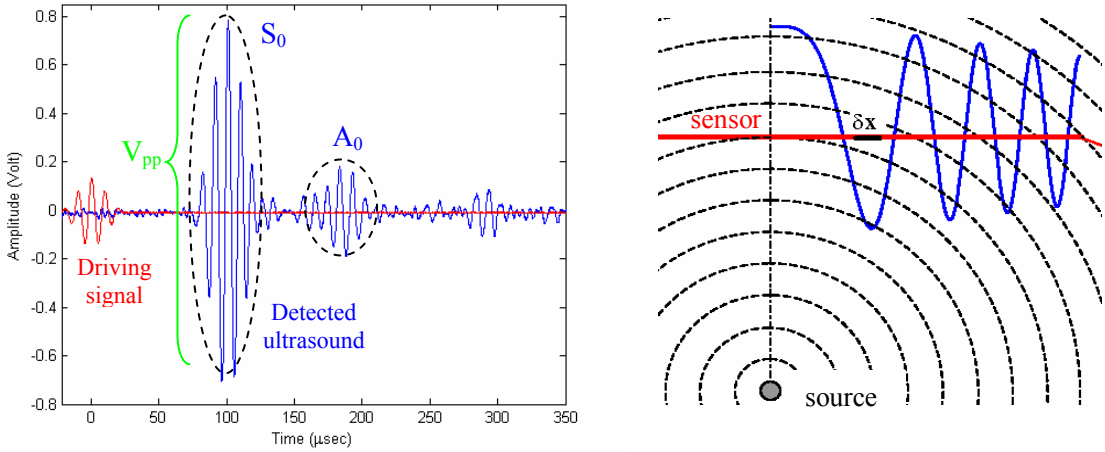

Figure 4.9: (*Left*) Typical wavefront integration fibre sensor detected ultrasonic signal (in blue) for a 4.5 cycles tone burst driving signal (in red) at 100 *kHz*. The first two arriving bursts correspond to the incident S_0 and A_0 mode, and the rest are their reflections. In this section we compare the model optical phase maximum modulation values with the maximum peak to peak variation of the S_0 mode for the detected ultrasonic signals (defined as V_{pp} in the figure). (*Right*) Pressure field distribution along the optical fibre sensor as the wave pass through.

A thin PZT disc of 1 *cm* diameter ultrasonic source is used in all the experiments (its specifications and operation are properly described in Chapter 2). Since the ultrasound originates from a number of points along the transducer face, then the ultrasound intensity along the propagating beam is affected by constructive and destructive wave interference. These are sometimes also referred to as diffraction effects in the NDT world. This wave interference leads to extensive fluctuations in the sound intensity near the source, known as the *near field*. The pressure waves combine to form a relatively uniform front at the end of the near field, in what is called the *far field*. In the far field, the beam spreads out in a pattern originating from the centre of the transducer. The equation for the far field is given in eqn. 6.6, where l is in this case the dimension of the source. Because the simple mathematical model of the wavefront integration effect considers only point ultrasonic sources, the optical fibre sensors are always located at a distance within the far field of the source (for the frequencies used in this chapter and the materials, this is less than 2 *cm* from source).

The simulation from the mathematical model provides normalized values of maximum variation of the optical phase due to the strain-optic effect that the ultrasound causes over the fibre sensor. These values can be compared with the maximum optical intensity modulation of the output of the polarimetric system as justified in previous sections. However because the optical fibre sensors are not entirely non-birefringent before arrival of the ultrasonic wave, due to stresses produced by the embedding/bonding process itself. Then the

unrepeatable nature of the embedding/bonding process causes that the initial birefringence induced in the fibres is not equal for all the sensors. Therefore this may suggest that the maximum changes in the intensity of the different sensors may not be comparable. Fortunately the repeatability of experimental results for different sensors of same length and under same conditions respect to the ultrasonic source, suggest that the comparison between different sensors is acceptable. The reason for this lies in our technique used for obtaining the ultrasonic data from the polarimetric system. That is, we optimize the polarization controller, before the fibre sensor, and the orientation of the polarizer such that maximum sensitivity is achieved in all cases. Hence neglecting the different initial polarization of the fibre sensors, so that only the polarization of the light at the exit of the fibre sensor and before the polarizer matters (as described in Appendix C).

The maximum optical intensity modulation of the polarimetric system is measured in our experiments as the peak to peak voltage value of the S_0 mode burst (defined in fig. 4.9-*left* as V_{pp}) for being the first arriving ultrasonic wave component and so free from interference with other modes or reflections.

4.4.1 Sensor length analysis

In the first of our model analysis, we study how the wavefront integration affects the detected ultrasonic signal by only varying the length of the integrating sensors, meanwhile the orientation and distance to the ultrasonic source is fixed.

The integral of the model (eqn. 4.7) was solved for one period of the ultrasound considered pure sinusoidal for simplification purposes (it was also simulated for a 5 cycles non-windowed sinusoidal toneburst and similar normalized results were obtained). The frequency of simulation was chosen to be 100 *kHz* as it provides best coupling between PZT source and the Perspex plate used in our experiments. The fixed distance between source and centre of the fibre sensor was chosen to be 9.6 ultrasonic wavelengths (or $n = 9.6$) in order to be in the far field. The source is considered perpendicular to the fibre sensor or rather $\theta = 0$ (as defined in fig. 4.2). The range of fibre lengths simulated goes from 0 to 14 ultrasonic wavelengths (or equivalently $0 < m \leq 7$). The result of the simulation is a 3D plot as that shown in fig. 4.10-*right* where the plane of definition is given by the two variables m or length of fibres and time, and the vertical magnitude represents the normalized variation of the fibre optical phase ($\Delta\bar{\phi}$). Because we are only interested in the maximum modulation of the optical phase (or sensitivity) for each sensor length, we can simplify this plot into a 2D one (fig. 4.10-*left*) as a view of the 3D plot along the plane $\Delta\bar{\phi}$ - m.

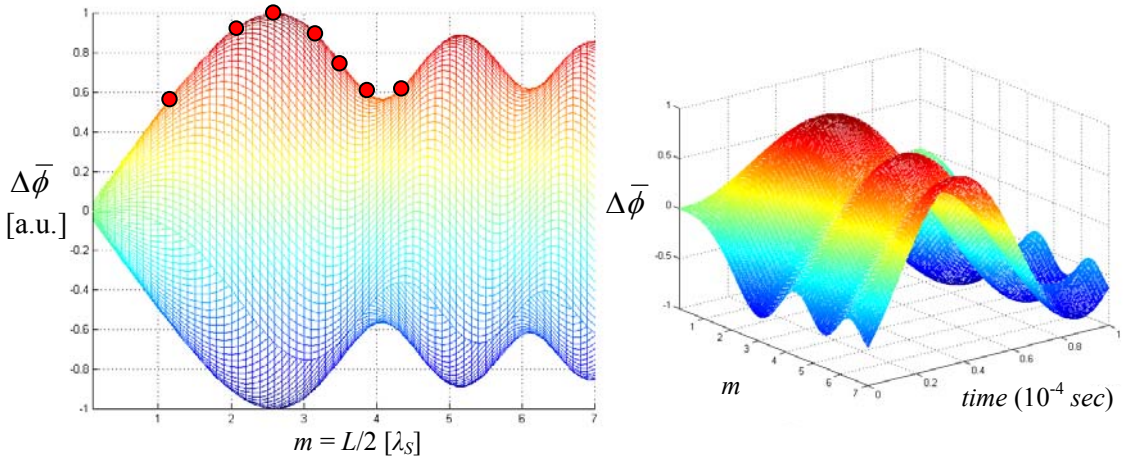

Figure 4.10: Simulation of the numerical integration of eqn. 4.7 for distance sensor–source = n = $9.6\lambda_S$, and ultrasonic frequency f_S = 100 *kHz*, for a changing length of the fibre sensor from 0 to 14 λ_S. (*Left*) Maximum variation of the normalized optical phase during a period time of the sinusoidal ultrasonic wave. (*Right*) Same plot showing the 3rd dimension *time*.

The sensitivity of the wavefront integration given by our model is characterised by a series of oscillations of decreasing amplitude and period (fig. 4.10-*left*). The first oscillation which starts from zero sensitivity for a zero length fibre has the highest peak (and so highest sensitivity). The next oscillations have decreasing sensitivity peaks, with the amplitude of the oscillations tending to zero as m tends to infinity. The physical explanation of this curve is as follows. As we might expect, $\Delta\bar{\phi}$ initially increases as the sensor becomes longer and a larger portion of the wavefront interacts with it. We might intuitively predict that this increment would occur until the sensor length permits a maximum wavefront phase difference of π between the ends and the centre of the sensor so that at a particular time all the fibre length is under compressing pressure (thus maximum positive value of $\Delta\bar{\phi}$) and at another time all the fibre is under expanding pressure (thus maximum negative value of $\Delta\bar{\phi}$). As the length of the fibre is further increased, at any given time the sensor will be affected by a combination of compression and expansion pressure distributions (as shown in fig. 4.9-*right*), causing positive and negative local changes in the effective index of the fibre, thus compensating each other towards the integrated optical phase change. This causes the characteristic oscillating distribution of the $\Delta\bar{\phi}$ curve respect to the sensor length. Therefore if we consider a sensor sufficiently long that a wavefront phase difference of 2π can occur, the first half wavelength (0-π) will exert positive pressure and the second half (π - 2π) negative pressure. If the effects of these two parts were equal they would cancel each other out to give a zero $\Delta\bar{\phi}$. This does not occur in fig. 4.10-*left* because the second part of the

pressure distribution is not equal to the first one, for two reasons. Firstly, the length of the fibre over which the second half acts is shorter (due to the geometry as shown in 4.9-*right*). Secondly the pressure exerted by the wave will be less as the distance from the source to the fibre will be greater, and the pressure field is inversely proportional to the root square of the distance. In consequence, the minima in the $\Delta\bar{\phi}$ - m curve are never zero and each successive maxima is lower than the previous one, as observed.

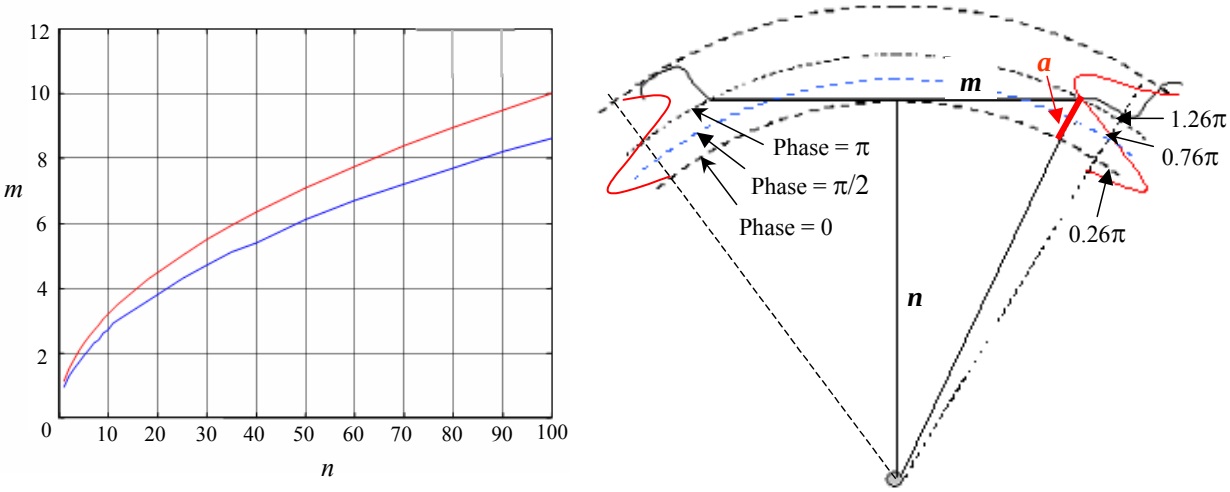

Figure 4.11: (*Left*) Relation between length of sensor (m) and distance source - sensor (n) that provide maximum $\Delta\bar{\phi}$, in blue for our simulation results and in red for the intuitive case in which the sensor length permits a maximum wavefront phase difference of π between the ends and the centre of the sensor. (*Right*) Different distributions of the pressure field along the length of the integrating sensor.

In fig. 4.11-*left* we plot the relation between the length of the integrating sensor and distance to the source that are associated to the first peak of the $\Delta\bar{\phi}$ - m curve. In blue as obtained by our simulation and in red for the intuitive case in which the sensor length permits a maximum wavefront phase difference of π between the ends and the centre of the sensor. We notice that these two cases do not agree. In fact by linear regression of the blue curve, we calcualte that it corresponds to the case in which the ultrasonic wavefront phase difference between the centre and ends of the integrating sensor is $0.74{\cdot}\pi$ (or $a = 0.74{\cdot}\pi$ with a defined in fig. 4.11-*right*). Obviously only one of both situations can be right but which one? we might expect it to be π, but as the phase of the acoustic wave changes from 0 to π, the maximum pressure moves from the centre of the fibre towards the ends. As it does so, its effect on the fibre decreases since it acts on a shorter section of the fibre. We can see this in left hand part of fig. 4.11-*right*, where the wavefront from 0 - $\pi/2$ affects approximately 2/3 length of the sensor but the wavefront from $\pi/2$ - π only affects approximately 1/3. Consider now the case of a sensor having a length such that a maximum of π phase difference could

occur along its length and choose the phase of the wave such that at no point on the sensor is the pressure negative. We would then have the situation of the wave depicted in the left side of fig. 4.11-*right*, where the wavefront phase is 0 (i.e. null pressure) at the centre of the sensor so most of the length of the sensor only is being affected by a small pressure field. The maximum of the pressure field is at a phase of $\pi/2$ which occurs further towards the end of the sensor and thus affects it less. It can be shown that the integrated change in the optical phase of the sensor will be bigger if we have a situation such as that shown in the right hand side of fig. 4.11-*right*, where the pressure peak is almost at the centre of the sensor. To avoid having a negative pressure field in part of the length of the sensor which would reduce the effect of the positive field, the length of the sensor should be restricted such that a maximum phase difference of $0.74 \cdot \pi$ can occur along the sensor.

The mathematical model created has already been of great use in order to correct our intuitive wrong idea of the relation length of sensor and distance to the source that provides maximum sensitivity.

Experimental verification

A set of experiments was developed to check the results of the sensor length analysis given by our model. Seven different length optical fibre sensors were bonded onto the surface of a Perspex plate of 3 *mm* thickness. All the sensors were perpendicularly oriented to a PZT source at a distance of 21.6 *cm* (which corresponds to n = 9.6 at an ultrasonic frequency of 100 *kHz* and measured group velocity of 2.25 *km/s* for the first arriving S_0 mode). The lengths of the sensors were chosen to agree with the values of m indicated by red dots in fig. 4.10-*left* (with an error of 0.2 due to a 0.5 *cm* length error in the fibre sensors associated to the sensors mould in which the fibres are embedded as shown in fig. 4.3-*left*, and to an error in the measured S_0 group velocity of 0.1 *km/s*), their length in *cm* is indicated in fig. 4.12, where a picture of the experimental lay out is also presented. The polarization controller, polarizer, laser and high pass filter are associated to the polarimetric detection system, in the other hand the signal generator and the 50 dB high voltage amplifier are used to excite the two PZTs used as ultrasonic sources (we need 2, in order to have all the fibre sensors oriented perpendicularly to at least one of them). For the sensors of length (15.5, 19.5 and 4.9 cm) the source will be PZT_1, whilst for the sensors (14, 17.2 and 8.8 cm) it will be PZT_2. To normalise the detected ultrasound of all the sensors, since there are 2 different PZT sources, we will use the fibre sensor in the middle between both sources as the reference one (of length 11.3 *cm* which corresponds to a value of m = 2.4 associated to the maximum peak of $\Delta\overline{\phi}$ in fig. 4.10).

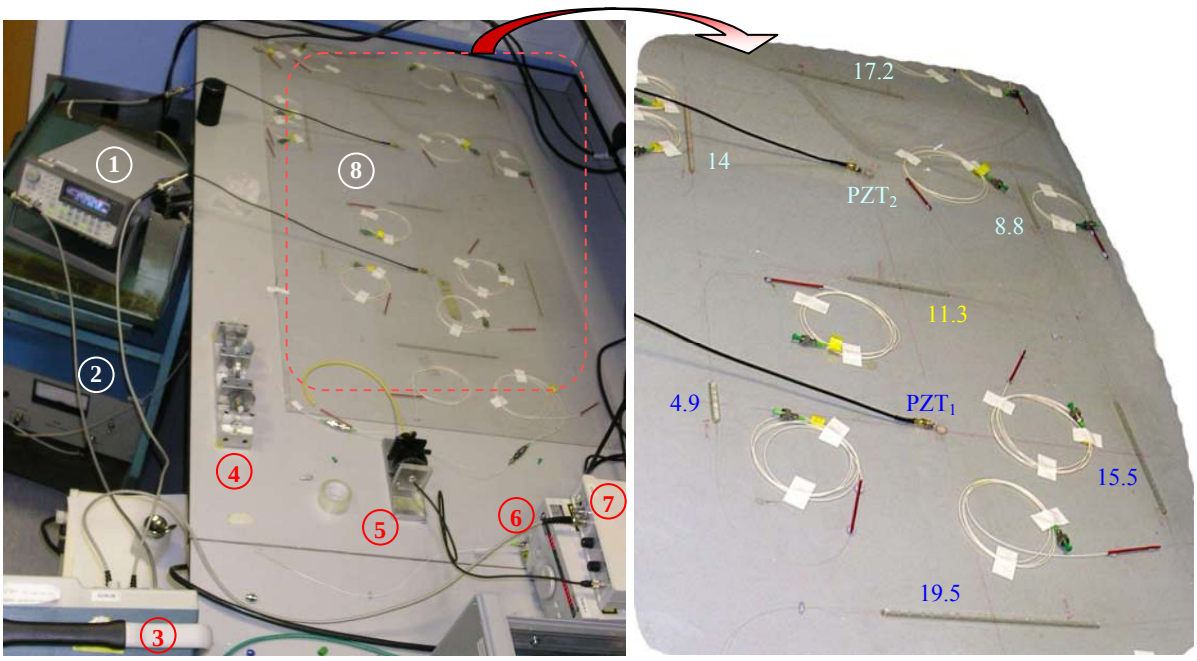

Figure 4.12: Experimental set-up of the wavefront integration sensor length analysis using the polarimetric detection system. The components in the set-up are; 1) Signal generator, 2) 50 *dB* High Voltage amplifier, 3) Oscilloscope, 4) Polarization controller, 5) Linear polarizer and HF InGaAs photodiode, 6) Laser source, 7) HP filter and amplifier, and 8) Perspex plate of 3 *mm* thickness with various length fibre sensors and PZT ultrasonic sources as shown in the right. All the lengths are given in *cm*. The distance from centre of sensors to closest PZT source is 21.6 *cm*.

The generated ultrasound is a 5 cycles tone burst at 100 *kHz* Hamming windowed, as it would be impossible to analyse a pure sinusoidal Lamb wave (as simulated in our model) because the propagating modes will mix with their reflection in the detected signal.

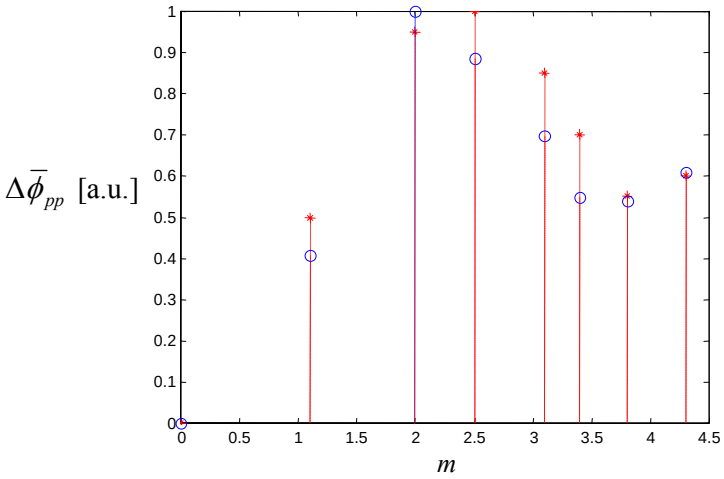

Figure 4.13: Comparison between the normalized maximum peak to peak of the experimentally detected ultrasonic data (as blue circles) and the simulated results of our model (as red dots), for n = 9.6 and f_s = 100 *kHz*.

The normalized peak to peak value of the S_0 mode burst (defined as V_{pp} in fig. 4.9-*left*) detected by each sensor are plotted as blue circles in fig. 4.13 together with the normalized peak to peak values of the simulated $\Delta\overline{\phi}$ as red dots (we call it $\Delta\overline{\phi}_{pp}$).

Although there is not an exact agreement between the experimental results and the model we see that both of them seem to describe a similar shape for the $\Delta\overline{\phi}$ - *m* curve, including a peak and a subsequent minimum. Compared to the predicted curve in fig. 4.10-*left*, the experimental results produce a curve which appears slightly compressed to lower values of *m* and for which we do not have an answer yet. The model has been tested for other frequencies above and below the one of the previous experiment in order to see if effectively our basic integration model can predict the trend of the sensitivity curves.

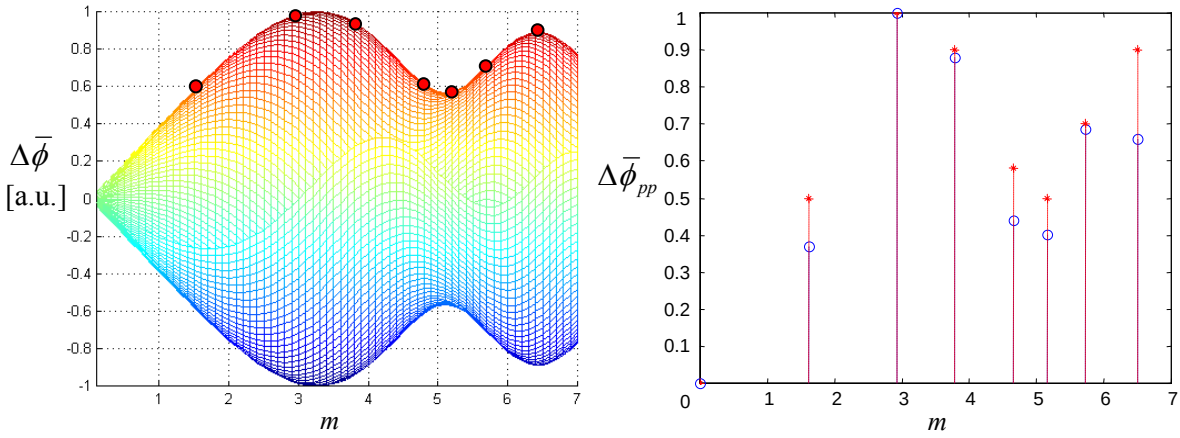

Figure 4.14: (*Left*) Model simulation for $n = 14.4$ and $f_S = 150$ *kHz* changing the length of the sensor from 0 to $14 \cdot \lambda_S$. (*Right*) Comparison between experimental results (circles) and the model (dots).

Figure 4.14 shows the results when the ultrasonic frequency is 150 *kHz*. In this case the model predicts that for the set of sensor lengths previously chosen (shown as red dots in fig. 4.14-*left*) a double oscillation should appear. Effectively that is what we see in the experimental results plotted in 4.14-*right* (as before). However still we can see important discrepancies between the normalized values of the experimental points and the model.

Finally in fig. 4.15 we show the case for an ultrasonic frequency of 60 *kHz*. Now the model predicts a single peak which effectively is confirmed in the experimental results. The increased discrepancies in the normalized values of the experimental and model results of the present case respect to the previous ones may be due to the fact that the amplitude of the detected ultrasound for the optical fibre sensors is at 60 *kHz* between 3 and 10 times (depending in the sensor length) smaller and double noisy than for the other two frequencies. The reason for a worse signal to noise ratio is that 100 *kHz* is the PZT source resonant

frequency for the used Perspex plate and the frequency 150 *kHz* is found to provide the best coupling between Perspex plate and the optical fibre sensor.

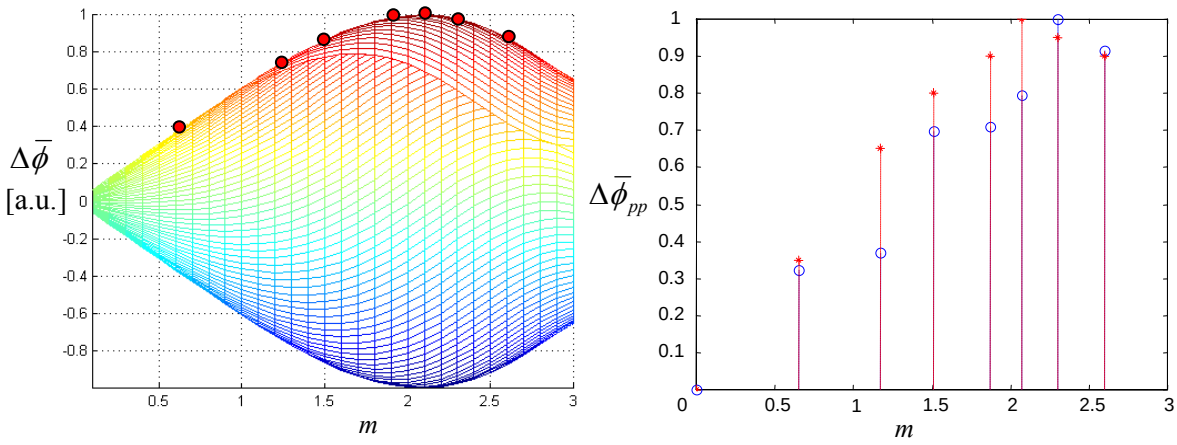

Figure 4.15: (*Left*) Model simulation for $n = 5.76$ and $f_S = 60$ *kHz* changing the length of the sensor from 0 to $14 \cdot \lambda_S$. (*Right*) Comparison between experimental results (circles) and the model (dots).

The presented experimental results satisfy the theoretically predicted trends well enough to demonstrate that the basic premises of our model are correct. The accuracy of the practical results may be compromised by the difficulty in producing repeatable sensors, even using casting techniques. This is because the interaction of the acoustic wave with the fibre is very dependent on the nature of the bond between it and the sample plate. Nevertheless the presented analysis shows that our simple model may be used to determine the optimum length of the fibre sensor for maximum sensitivity of any of the wavefront integration detection systems presented in Chapter 2.

4.4.2 Sensors-source orientation analysis

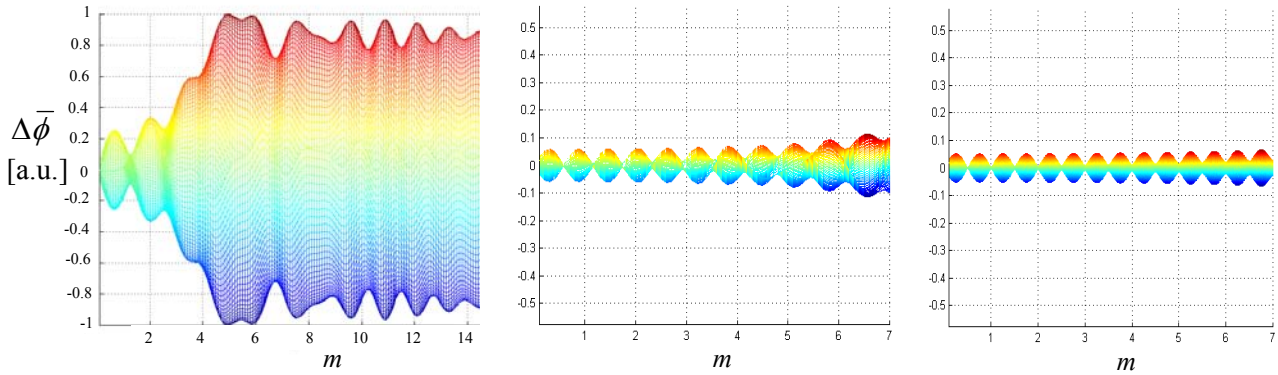

Figure 4.16: Simulated normalized optical phase modulation for varying sensor length from 0 to $14\lambda_S$ (longer in the left figure), a distance centre sensor to source of $9.6\lambda_S$ and different source-sensor orientations: (*Left*) $\theta = 23^0$, (*Centre*) $\theta = 60^0$ and (*Right*) $\theta = 90^0$. In all cases the simulated ultrasonic frequency is 100 *kHz*.

Another interesting analysis of the wavefront integration is what happens when the sources are not symmetrically orientated to the centre of the sensor or equivalently when $\theta \neq 0$ (with θ as defined in fig. 4.2). Figure 4.16 shows the simulation results by solving eqn. 4.7 for three different orientations such that left corresponds to $\theta = 23^0$, centre for $\theta = 60^0$ and right for $\theta = 90^0$. In all cases the simulated ultrasonic frequency is 100 *kHz* and as before the distance from source to centre of the sensors is $n = 9.6$ and the analysis is solved for a varying length of the sensors $0 < m \leq 7$ (longer in the left figure to clearly see the trend).

From fig. 4.16-*left* we can see that as occurred with the case $\theta = 0^0$, the $\Delta\bar{\phi}$ - m curve is characterized by a series of oscillations, however when the angle of source orientation is not perpendicular to the sensor, the peaks of the oscillations increase with the length of the sensor till reaching an absolute maximum (f.i. this maximum occur at $m = 5$ for the case in fig. 4.16-*left*) and then decrease and saturate as with $\theta = 0^0$. As the angle θ increases the number of oscillations also increases although their peak amplitude decreases because the number of ultrasonic wavefronts integrated by the sensor also increase. The closer we get to $\theta = 90^0$, which means the ultrasonic direction of propagation is parallel to the axis of the fibre sensor, then $\Delta\bar{\phi}$ decreases considerably (the sensor becomes less sensitive) because the integrating sensors are stress field sensitive. Opposite to what happens with FBG sensors which are strain sensitive, hence more sensitive to this orientation.

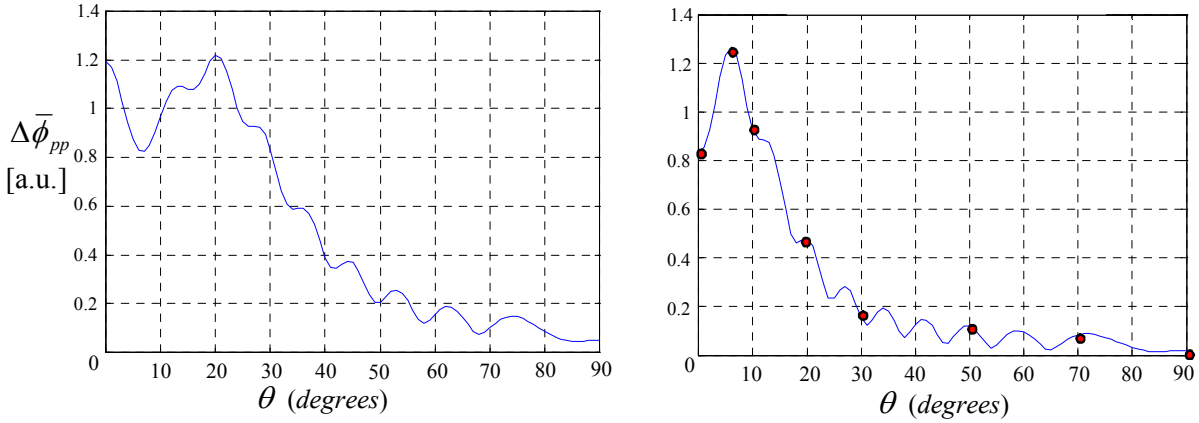

Figure 4.17: Directional sensitivities of the integrating sensors as predicted by our model for a ultrasonic frequency of 270 *kHz*, a fixed length of the sensor of 19.5 *cm* (or $m = 5.024$ in aluminium plate): (*Left*) for distance source-sensor of 16 *cm* (or $n = 8.24$). (*Right*) For distance source-sensor of 31 *cm* (or $n = 16$)

Our model simulation also shows that the absolute maximum of $\Delta\bar{\phi}$ occurs with longer sensor as the angle θ is increased, and for a fixed sensor length the value of the maximum decreases in general with θ as shown in fig. 4.17. These plots represent the peak to peak

change of the maximum peak of $\Delta\bar{\phi}$ for a varying angle θ between 0^0 and 90^0, a fixed length of the sensor of 19.5 *cm* (or m = 5.024 in aluminium plate), simulated ultrasonic frequency of 270 *kHz* and distance from source to centre of sensor of 16 *cm* for the left plot and 31 *cm* for the right plot. The directional sensitivity of the integrating sensors follows a rapid fall off towards a plateau at high angles θ. However at low angles the integrating effect causes a rather complex orientation sensitivity characteristic which is a function of the acoustic wavelength, sensor length and distance source-sensor (as noticed from the big differences between the two plots in fig. 4.17).

Experimental verification

The experiment described next is designed to validate the directional sensitivity of fig. 4.17-*right*. Due to the long distances involved (31 *cm*), we have decided to use an aluminium plate of less attenuation than Perspex. In an aluminium plate of 1 *mm* thickness we bonded a single fibre sensor of length 19.5 *cm*, and in a circle of radius 31 *cm* with centre in the middle of the fibre we glued eight PZTs used as ultrasonic sources (labelled in red with the value of their orientation θ respect to the fibre sensor, in the lay-out of the experiment shown in fig. 4.18-*left*).

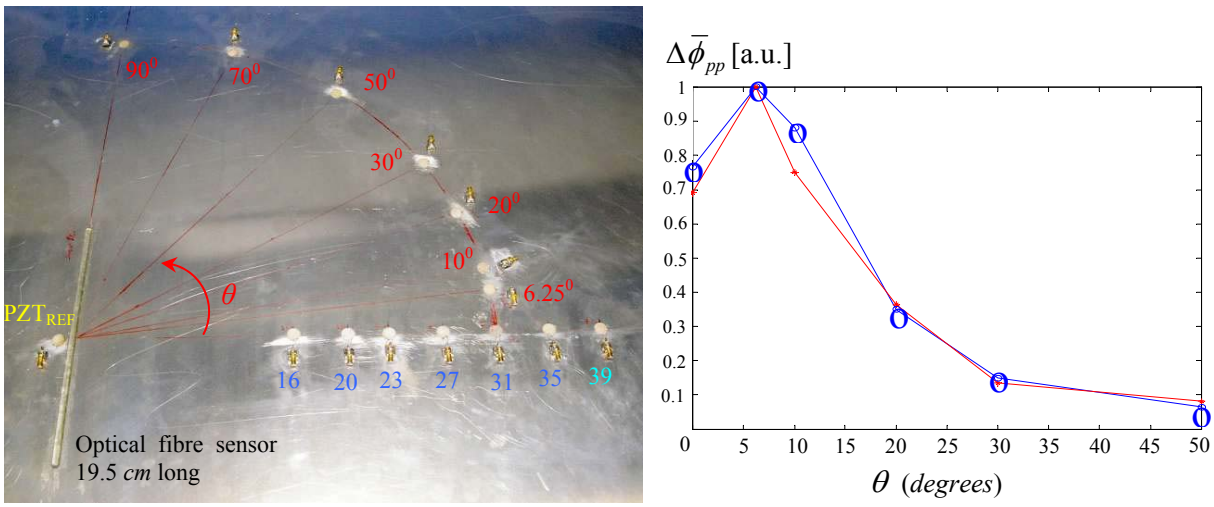

Figure 4.18: (*Left*) Aluminium plate experimental layout of the wavefront integration sensor-source orientation analysis (for PZTs labelled in red with the value of angle θ associated) and distance analysis (for PZTs labelled in blue with distance to centre of fibre sensor in *cm*). The present layout is completed with the same components as in fig. 4.12, associated to the polarimetric detection system. (*Right*) Comparison of directional sensitivity between experiments (blue circles) and model (red dots).

As in the experiments for the sensor length analysis, we use a 5 cycles Hamming windowed tone burst but now at 270 *kHz* as it is the one which provides optimum coupling in the aluminium plate. To normalize and compare the peak to peak ultrasound by the different

sources we use a reference PZT (labelled as PZT_{REF} in fig. 4.18-*left*), situated 1 *cm* from the centre of the fibre sensor. Again we are interested in the peak-to-peak of the S_0 mode signal.

Ideally because all PZT sources are equally far from the PZT_{REF}, its recorded ultrasonic signal should be equal for all the PZT sources. In practice this does not happen because the coupling between the different PZTs and the plate is different as it is impossible to get a perfect exact bonding condition for all of them. It is good approximation to consider the coupling coefficient for each of them constant with the time as they are glued to the plate.

But it will be necessary to normalize the recorded signal by the fibre sensor for all the sources in order to compare them. Next we explain how to do this.

As an example we analyse what happen with an arbitrary PZT. We can express the amplitude of the ultrasonic wave detected by PZT_{REF} as:

$$A_{PZTref} = \phi_{PZTref} \cdot \phi_{PZT} \cdot \frac{A_{PZT}}{\sqrt{r_{PZTref}}} \tag{4.13}$$

Where A_{PZTref} is the amplitude of the ultrasound in the plate near the PZT_{REF}, A_{PZT} is the amplitude of the oscillations in the PZT source, ϕ_{PZTref} is the coupling coefficient between plate and PZT_{REF} source and ϕ_{PZT} is the coupling coefficient between PZT source and plate.

On the other hand the amplitude of the ultrasound detected by the sections of the fibre sensor at a distance *r* from the source (in the far field) is equal to:

$$A_{fibre}(r) = \phi_{fibre}(r) \cdot \phi_{PZT} \cdot \frac{A_{PZT}}{\sqrt{r}} \tag{4.14}$$

Where $A_{fibre}(r)$ is the amplitude of the ultrasound in those points of the fibre at a distance *r* from PZT source and $\phi_{fibre}(r)$ is the coupling coefficient between plate and those points of the fibre at a distance *r* from PZT source.

Therefore if we want to normalize $A_{fibre}(r)$ so that it can be compared with the amplitude of the other PZTs we have to compensate the term that depends in the PZT source (ϕ_{PZT}). To do this we just need to divide eqn. 4.14 by eqn. 4. 13 so that we get:

$$\overline{A}_{fibre}(r) = \frac{A_{fibre}(r)}{A_{PZTref}} = \frac{\phi_{fibre}(r) \cdot \sqrt{r_{PZTref}}}{\phi_{PZTref} \cdot \sqrt{r}} \tag{4.15}$$

In conclusion to normalize the detected signal by the optical fibre sensor for the different PZT sources we divide the fibre detected peak to peak ultrasonic signal by the one detected with PZT_{REF}, for each of the PZT sources.

The measured normalized peak to peak values of the ultrasound by the fibre sensor for the different PZT sources orientation are plotted in fig. 4.18-*right* as blue circles and compared with the simulation results as red dots (as taken from the red dots in fig. 4.17-right which correspond to the experimental orientation of the sources). The experiments follow very well the simulations with the discrepancies being within the experimental error (due to an angle error of the PZT sources of 1.5^0 due to their diameter of 1 *cm* and the error associated to the measured group velocity values of around 0.1 *km/s*). Notice how the maximum sensitivity effectively occurs at the angle of 6.25^0 as predicted by our model. We have not plotted the result associated with the PZTs at angles 70^0 and 90^0 because the detected signal was of same order as the noise.

4.4.3 Sensors-source distance analysis

The last of the wavefront integration analysis is related to the changes in the sensor sensitivity due to the variation of the distance from the centre of the sensor to the source. Now the length of the integrating sensor is fixed, as well as the orientation which we have chosen perpendicular ($\theta = 0^0$).

For the experimental realization we have used the same fibre sensor and plate than the previous case and we have glued seven PZT sources along the line perpendicular to the axis of the fibre at distances varying from 16 *cm* to 39 *cm* as shown in fig. 4.18-*left* (the PZT sources in this case are labelled in blue with the value of their distance to the centre of the fibre sensor).

The same ultrasonic frequency as before (270 *kHz*) and an experimental ultrasonic signal consisting on 5 cycles Hamming windowed tone burst were used.

The model simulation for a pure sinusoidal ultrasound is shown in fig. 4.19-*left*. We notice that for the range of values of n associated with our experimental distances source:sensor (it goes from $n = 8.25$ for closer PZT source at 16 *cm* to $n = 20$ for the farthest PZT source at 39 *cm*) the trend of the sensor sensitivity follows a single valley.

The experimental peak to peak values of the detected ultrasonic signals should also be normalized in order to compensate for the different coupling coefficient due to a non-repeatable bonding of the various PZT sources (as explained before). Additionally because the sources are at different distances from the sensor, we also need to normalize the experimental data to compensate the spreading attenuation associated to the propagating cylindrical Lamb waves. The total normalization consists in dividing the peak to peak signal values detected by the fibre sensor with the source being PZT_j by the term:

$$\frac{A_{PZTref\_j}}{A_{PZTref\_1}}\sqrt{\frac{r_{PZT\_j}}{r_{PZT\_1}}} \tag{4.16}$$

Where A_{PZT_1} and A_{PZT_j} are the peak to peak values of the signal detected by PZT_{REF} when the source is PZT_1 and PZT_j respectively (with PZT_1 chosen to be the closest one to the sensor). The values r_{PZT_1} and r_{PZT_j} are the distance of each source to the PZT_{REF}.

The experimental normalized data is shown as red dots in fig. 4.19-*right*, and it is compared with the results from the simulation in blue circles. Notice that we have plotted two different simulation results; the straight line one is associated to the case in which the simulated ultrasound is a pure sinusoidal, meanwhile the dashed line is obtained when the simulated ultrasound is a 5 cycles non-windowed toneburst.

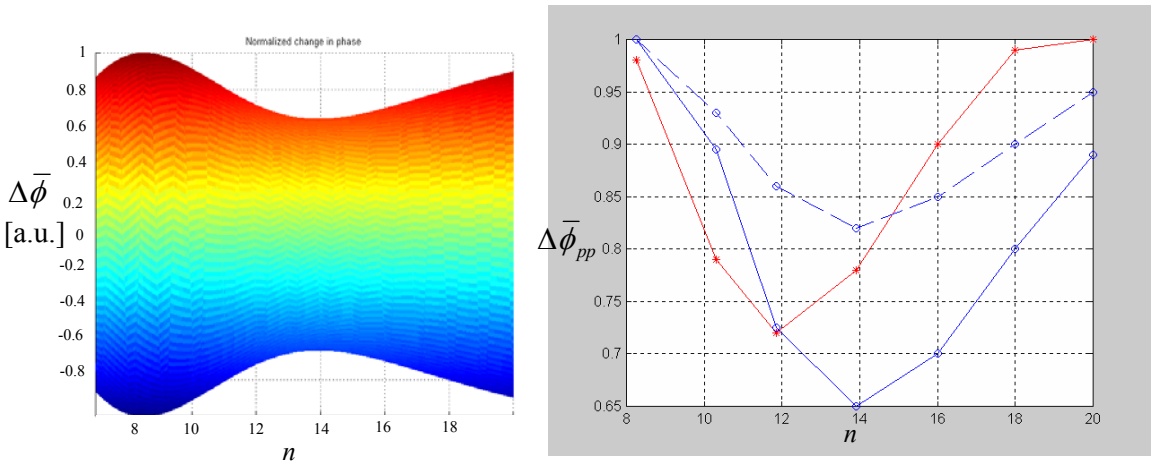

Figure 4.19: (*Left*) Simulated normalized optical phase modulation for varying distance source-sensor with perpendicular orientation and fixed length of the sensor 19.5 cm (or m = 5.024 in aluminium), for an ultrasonic frequency of 270 *kHz*. (*Right*) Comparison between experimental results (red dots) as the normalized peak to peak values of detected signals, and simulation (in blue circles) as peak to peak change in $\Delta\bar{\phi}$, using a 5 cycles tone burst signal (dashed line), and a sinusoidal signal (straight line).

The experimental results follow again the trend of the simulation where a single valley was predicted. However the valley in the experimental results seems to be compressed towards decreasing values of n. In addition the experimental curve is in between the ones obtained for a simulated pure sinusoidal ultrasound and the one obtained for a simulated 5 cycles non-windowed toneburst. We remember that the ultrasound excited in the experiments is a Hamming windowed 5 cycles toneburst, which can be considered to be in between the two simulated cases. The higher discrepancies between experiments and simulation in the present analysis respect to the previous ones, may be related to the fact that in the previous two analysis the distance source to sensor was fixed meanwhile not in this case. Hence

meanwhile the dispersion effect of the propagating ultrasounds was not important in the previous analysis, it is relevant in the present one. The dispersion effect is not considered in our model. Nonetheless further analysis has not been done and this effect has to be quantified yet. Another reason for the discrepancies is associated to the unconsidered situation of having important reflexions of the propagating ultrasound from the rest of the PZT sources bonded in the path to the sensor. These reflections as they are in the direct path source-sensor will arrive within the time interval of the arrival of the S_0 mode burst causing a perturbation in the measured peak to peak values which has not been simulated.

In the other hand the general discrepancies between the simulation and the experiments for all previous cases could mainly be dominated by the changing phase and amplitude response of the PZT as a resonant system which generates a real ultrasonic signal in the sample slightly different from the excited one. Also the non-repeatable bonding process of the fibre sensors and the PZT sources may have an important effect. Further research has yet to be done to fully understand the discrepancies and further improve the model.

4.5 CONCLUSIONS

The changing response of an integrated fibre ultrasound detector to varying distance and orientation from the source has been analysed theoretically, and simulated in the MATLAB environment, for sensors of differing lengths. A periodic response to both changing distance and orientation of the source was seen and explained in terms of the ability of an acoustic wave to produce both positive and negative changes in the effective index of a fibre. For a sensor whose length is crossed by several acoustic waves at any given instant, these positive and negative effects may cancel each other out to varying degrees. This integration effect gives the sensor its characteristic response.

The integration model has also corrected the wrong intuitive idea that for an ultrasonic wave propagating perpendicular to the fibre axis, the maximum fibre sensor response is achieved when its length permits a maximum wavefront phase difference of π between the ends and the centre of the sensor. Instead the model predicts that the maximum response should occur when the maximum permitted phase difference is of $0.74 \cdot \pi$. We have successfully explained how this is possible.

The basic trends, of the modulation that the acoustic wave pressure field induces over the sensing property of an OFS, predicted by the model as a change in the sensor length, distance to the source and orientation have been experimentally confirmed. The model also characterizes the directivity pattern of these integrating optical fibre sensors with obvious

implications in damage location. The unintuitive model prediction of maximum sensitivity for an orientation of the fibre axis non perpendicular to the propagation direction of the ultrasound contrasts with the sensitivity typical of pressure sensors. This prediction was positively verified experimentally.

We have also demonstrated theoretically, as we observed experimentally, that a polarimetric sensor exhibits similar integration behaviour to that predicted for an interferometric system. Suggesting that positive and negative changes are produced in the fibre birefringence in a similar way to that expected in the fibre refractive index.

The results indicate that optimum ultrasonic detection may be achieved through careful positioning and orientation of the optical fibre. These results may be applied, for example in NDT, where scattered ultrasound from defects introduces new effective sources that may be characterized by arrays of these integrating sensors.

We have identified areas for improvement in the theoretical analysis; to include a more precise modelling of specific propagating ultrasonic waves and the addition of the propagating wave dispersion effect. Improved models are currently in development.

4.6 REFERENCES

[1] Pierce, S. G., Philp, W. R., Culshaw, B., Gachagan, A., McNab, A., Hayward, G., Lecuyer, P. *Surface bonded optical fibre sensors for the inspection of CFRP plates using ultrasonic Lamb waves*. Smart Mater. Struct. **5**, pp. 776–787, 1996.

[2] Michie W. C., Culshaw B. and Uttamchandani D. *Optical fibre techniques for structural monitoring in composites*, S*mart Structures for Aircraft and Spacecraft*, 75th meeting of AGARD (Lindau, Germany), Conf. Proc. 531, SPS, pp 1-8, 1992.

[3] Thursby G., Dong F., Yong Y., Sorazu B., Betz D. and Culshaw B. *Fibre optic polarimetric detection of Lamb waves*, 15th Optical Fiber Sensors Conference Technical Digest, pp 321-324, (Portland, USA), 6-10 May 2002.

[4] Thursby G., Sorazu B., Dong F., Betz D. and Culshaw B. *Damage Detection in Structural Materials using a Polarimetric Fibre Optic Sensor*, Proceedings of SPIE SS/NDT, San Diego-CA (USA), 2003.

[5] Flax L., Cole J. H., De Paula R. P. and Bucaro J. A. *Acoustically induced birefringence in optical fibers*, Journal of the Optical Society of America, vol. **72(9)**, pp 1159-1162, 1982.

[6] Giurgiutiu V., Bao J. and Zhao W. *Active sensor wave propagation health monitoring of beam and plate structures*, Proceedings of the SPIE's 8th International Symposium on Smart Structures and Materials, Newport Beach, CA (USA), 4-8 March 2001.

[7] Hocker G. B. *Fiber-optic sensing of pressure and temperature*, Applied Optics, vol. **18(9)**, pp. 1445-1448, 1979.

Chapter 5

SIGNAL PROCESSING

5.1 INTRODUCTION

A SHM and NDT system requires a proper analysis of the data collected by the sensor system in order to be effective. This analysis should provide information related with the structural integrity, and the presence, location and characterization of damage.

The *processing system* is the component of the SHM/NDT system in charge of the data analysis. It may consist of a *centralized* processing unit or a *distributed* group of more local processing units. The processing system is the brain of the SHM system, it deciphers and interprets the data collected by the sensor system, and in most cases it is build over four levels as described in Chapter 1; *Pre-processing*, *Feature extraction*, *Pattern processing* and *Decision/Intervention*.

In this thesis the pre-processing of the data is done by averaging, digital filtering and smoothing, and by the use of wavelet de-noising techniques. The feature extraction is mainly manual by previous knowledge of the propagating ultrasonic wave patterns and the geometrical boundaries of the structure. Most of the signal processing applied in this work is concerned with pattern processing, where time-domain and frequency-domain techniques are used for damage detection, characterization and location. Also time-frequency analysis and two dimensional Fourier transform techniques are applied to assess structural condition by analysis of the changes in the propagation dispersion characteristic of the induced ultrasonic guided waves into the sample under test. Finally optimization techniques like Genetic Algorithms are used for the extraction of the material elastic and geometrical properties from the dispersion propagation information, which can infer the presence of structural loading or defects within the material, presenting a very accurate reflection of the integrity of the structure.

Signal processing does not create more information than that presented in the transient signal, but it can provide a different perspective on the same information, highlighting aspects that otherwise would go unnoticed.

In the next sections we present the mathematical tools that constitute the analysis techniques applied thoroughly in Chapters 3, 4, 6 and 7.

5.2 TIME DOMAIN ANALYSIS

The experimental data directly recorded not only on this thesis but also in most ultrasonic based monitoring systems, consist of the temporal variation that the wave's propagating stress and/or strain field causes in the measuring parameter of a detection system.

Time domain analysis is the most simple of the possible signal processing techniques. It does not require any transformation of the original detected data signal and only simple conditioning of the temporal signals is necessary; for instance compression, filtering and noise reduction.

We have already seen some examples of time-domain analysis in the conventional ultrasonic techniques described in section 1.3.1 of Chapter 1. The *through-transmission technique* looks into the changes of the detected pulse amplitude in order to locate and characterize the size of any damage located between the ultrasonic source and receiver. The flaw scatters part of the incident ultrasonic signal, more the bigger the size of the flaw, limiting the amount arriving to the receiver. In the other hand, the *reflection technique* is based on the appearance of new pulses arriving to the detector after the incident pulse, and before its reflection from the far side of the sample. The arrival time of these new pulses can be used to locate the damage within the plate and the pulse amplitude to characterize its dimensions. Because conventional ultrasonic techniques use bulk waves, characterized for being single mode and non dispersive, a time analysis should provide most of the monitoring information.

When dealing with ultrasonic guided waves a high level of complexity is added to the time analysis due to their dispersive and multimode propagating nature. The dispersion causes the inspection ultrasonic pulse to spread with propagating distance and time, decreasing the amplitude of the received pulse signal and as a result worsening the SNR and sensitivity of the system. The increment in the signal duration caused by the dispersion effect also decreases the spatial resolution, meaning that the reflections from two flaws in close proximity could not be separately identified, or equally from a flaw close to the geometrical borders of the structure [1]. In the other hand, the presence of multi modes causes the shape of the propagating pulse to change with propagated distance as a consequence of the interference of the propagating modes at different speeds, with their reflections from the geometrical borders of the sample and from the damages and with new generated modes by

mode conversion. When the number of propagating modes is too high, the time signal is so complex that other signal processing techniques are required, as shown in the next sections.

The time analysis is in most cases developed around a sinusoidal Hamming windowed tone burst driving signal, due to its localization in time and narrow frequency bandwidth characteristics. A detailed explanation and description of this signal is given in Appendix E.

The frequency of the tone burst is chosen based in the particular source transducer (for instance if a PZT is used then a frequency close to its resonance frequency must be chosen) and in the acoustic coupling characteristics between source and plate and plate and receiver. Nonetheless this frequency is chosen so that only the fundamental Lamb wave modes A_0 and S_0 exist. The S_0 mode is characterized by its practically non-dispersion properties at low frequency thickness products, as shown in fig. A.8 for aluminium. In the other hand, the A_0 mode is highly dispersive at very low frequencies, but it becomes one of the most non-dispersive modes at frequency:thickness products over the frequency at which the S_0 mode starts becoming dispersive, for instance in fig. A.8 this point is around 1 *MHz mm*. The time analysis is in this way highly simplified, such that the non-dispersion and double mode propagation allows applying time analysis in a similar way as in conventional ultrasonic techniques as previously described. This analysis is based in the recognition and examination of the differences observed by direct comparison of sample records at different times with a reference signal obtained for a known undamaged condition, usually referred as *pattern recognition*. The presence of any difference can be interpreted as caused by damage, which behaves as a secondary source when the incidental ultrasonic waves reflect on it.

5.2.1 Application to NDT

Next we list the most common time analysis approaches to the differences observed in the recorded signal in order to extract damage information:

- *Amplitude attenuation of the propagating pulses without time delay*; this is commonly associated to presence of damage in the direct path between source and receiver. The ultrasonic signal scattered by the damage has a slight phase change over the direct propagating one. The cancelling interference between the two slightly out of phase waves causes the amplitude attenuation (see Chapter 3 for some examples). The magnitude of the attenuation may be used to characterize the damage dimensions. However as mentioned in [2] the use of only amplitude attenuation for a single Lamb wave mode is not always a good indicator of damage. Perturbations in the coupling characteristics between transducer and structure due to temperature or additional vibration excitation may also be the cause.

➢ *Appearance of new pulses or amplitude perturbations in the pulses of the slower propagating modes*; this may indicate presence of damage outside the direct path source-sensor. The damage creates a new path for the propagating ultrasound, with a different length to that of the direct path. Perturbations appear in the time record at instants corresponding to the time delay of the fastest modes propagating through the new path (some examples of this are also shown in Chapter 3). Furthermore, the scattered ultrasound following the new path approaches the sensor in a different direction than the ultrasound following the direct path. If a highly directional sensor is used for the detection stage (i.e. wavefront integration optical fibre sensors or FBGs) then damage signals of different magnitude will appear regarding the position orientation of the damage. This information can be used for damage location as explained in Chapter 3 for the FBG rosette configuration.

➢ *Time phase delay of the fastest propagating mode*; as caused by the presence of big size damage (in comparison with the ultrasonic wavelength). The ultrasonic wave is deviated into a different path of noticeable length difference in comparison with the undamaged situation. An example of this is shown in fig. 5.1 for a carbon fibre composite plate with increasing delaminations damage *on path* and *on axis* of plate fibres.

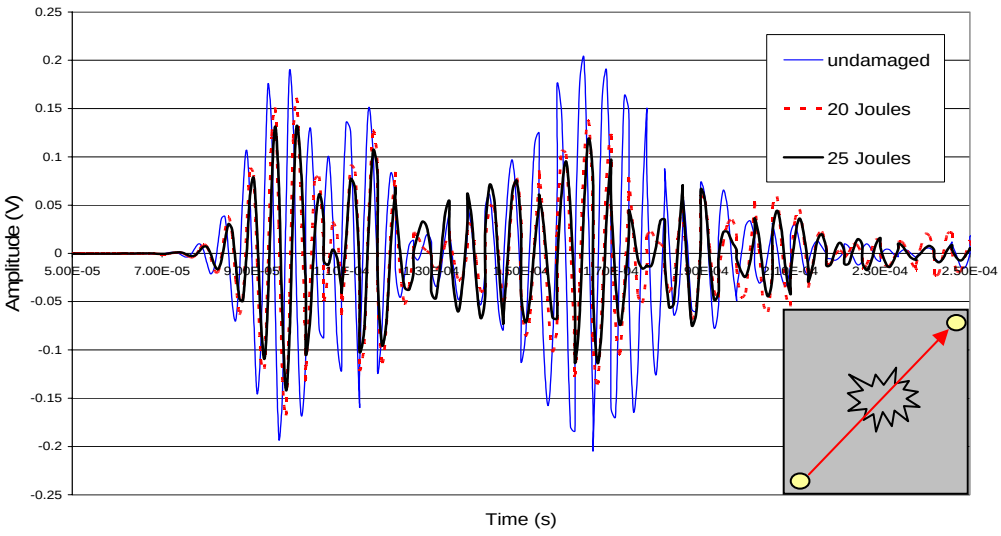

Figure 5.1: Signal traces for the undamaged case and for two damaged cases of increasing impact energy in between source and receiver and in the direction of the plate fibres.

The time delay can be used for sizing the *on path* damage, as it increases with the damage size, as shown in [3]. This analysis must be carefully done as the phase information of the propagating ultrasound is very sensitive to changes of the environmental temperature that causes time phase delays.

- *Presence of non excited modes or of pulses originated by mode conversion*; mode conversion occurs when a Lamb mode wave interact with a non symmetric boundary [4]. The result is the generation in the damage of new modes at the same frequency as the incidental mode wave. In most inspection applications an ultrasonic signal of single mode is excited, the presence in the received signal of additional pulses with different group velocities of those for the excited mode, indicates obvious mode conversion. In [5] we can see an example of this technique.

- *Average energy of the detected signal*; the presence of damage scatters part of the energy of the incident ultrasound, into different directions within the plate, reducing the amount of energy arriving to the detector. The energy is usually given by the RMS of the detected discrete time signal x[k] as:

$$x_{RMS} = \sqrt{\frac{1}{N}\sum_{k=0}^{N-1} x^2[k]} \tag{5.1}$$

Where N is the number of samples and $k = 0, 1,\ldots,N-1$.

An analysis of the changes in the received average energy can provide information of the size of the damage as shown in [3]. Again careful consideration of the effect of temperature must be taken, because the plate attenuation is temperature dependant, as well as the acoustic coupling characteristics between source and plate and plate and receiver.

5.3 FREQUENCY DOMAIN ANALYSIS

In most situations it is useful to characterize the raw time signal into other signal domains, a different point of view to the same information may highlight aspects that otherwise would appear unnoticed. Another reason for transformation to other domain is the possible data reduction and simplification that could be achieved.

The frequency representation is a powerful way of looking into signal information because it characterizes the presence of periodic events. Meanwhile the time analysis tell us how the signal changes in time, the frequency analysis characterizes those changes.

The transformation of a signal from the time domain into the frequency domain is done by the *Fourier transform*, named after the French scientist J. Fourier who in 1822 published an interesting work that allowed representing any continuous periodic signal as an infinite sum of periodic complex exponential functions.

5.3.1 Fourier Transform

The Fourier transform describes the continuous spectrum of a non-periodic and continuous time signal $x(t)$ as given by:

$$F[x(t)] = X(f) = \int_{-\infty}^{\infty} x(t) e^{-j2\pi ft} dt \tag{5.2}$$

As we can see the Fourier transform is a complex function that expands the signal *x(t)* into an infinite family of sinusoidal waves ($e^{-j2\pi ft}$) completely unlocalized in time. The Fourier analysis provides amplitude and phase information of the signal frequency content, but it does not tell us when these frequencies appear.

The Fourier transform presents a broad set of well known properties that most books about signal processing list (see for instance [6]). Nevertheless, we consider interesting to mention particularly two:

- $X(f)^* = X(-f)$, which can be rewritten as $|X(f)| = |X(-f)|$. The amplitude of the negative frequency components is equal to the amplitude of the positive ones, so that the spectrum amplitude is reproduced twice and symmetrically with respect to the spectrum origin, as shown in fig. 5.2-*left*.

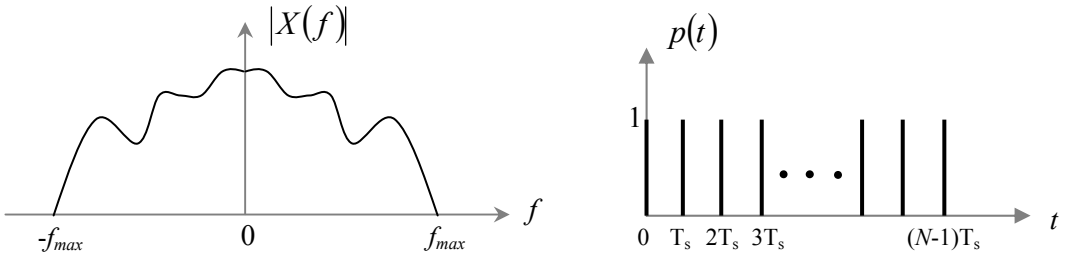

Figure 5.2: (*Left*) Spectrum amplitude of a continuous signal $x(t)$. (*Right*) Time definition of a sampling function $p(t)$ with spacing T_s

- Given two continuous functions; $x(t)$ and $y(t)$ then $F[x(t)\cdot y(t)] = X(f) \otimes Y(f)$. The Fourier transform of the product of two functions is the convolution of their respective Fourier transforms.

The time signals that we obtain in the experiments are discrete in opposition to the previously analysed continuous functions. A discrete signal is defined by a sequence of sampled points $x[n]$ obtained from the analogous signal at intervals given by the sampling period T_s. The discrete signal can be interpreted as the product of the continuous analogous signal and a sampling function $p(t)$ defined as a combination of Dirac deltas delayed in time, by T_s from each other (as shown in fig. 5.2-*right*). The Fourier transform of $p(t)$ is another combination of Dirac deltas delayed in frequency by $1/T_s$ and of amplitude $1/T_s$. If we apply

the convolution property of the Fourier transform, the frequency spectrum of the discrete signal is given by the convolution of the Fourier transforms of the individual functions *x(t)* and *y(t)* as shown in fig. 5.3. Thus the frequency spectrum of the continuous function *x(t)* is reproduced in each frequency multiple of $1/T_s$. Only the reproduction of the frequency spectrum at zero frequency is relevant, because the other reproductions only provide redundant information.

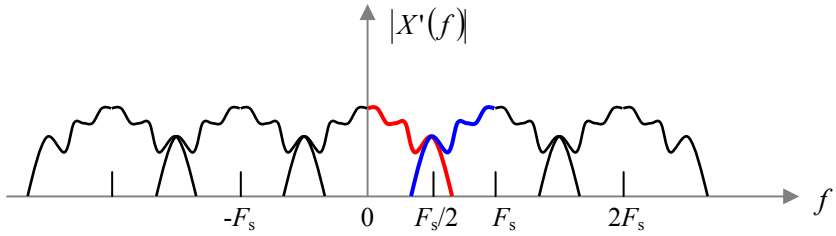

Figure 5.3: The frequency spectrum of a sequence of sampled values from an analogous signal is formed by repetition of the analogous signal spectrum at each multiple of the sampling frequency F_s.

In fig. 5.3 we notice an overlapping of adjacent spectrums (in red and blue), this happens when the maximum frequency component f_{max} of the analogous signal is bigger than half the sampling frequency. This effect is known as *aliasing* and it has a very negative effect in the frequency information of the sampled signal, so that the frequency spectrum provides erroneous information in this region.

The Fourier transform can also be discretized for computational implementation over discrete data sequences, being known then as discrete Fourier transform or DFT, given by:

$$X[k] = \sum_{n=0}^{N-1} x[n] e^{-j2\pi nk/N} \tag{5.3}$$

Where N is the number of samples in the sequence $x[n]$, with n being related to the continuous time variable such that $t = nT_s$ and k related with the frequency such that $f = k/T_s$. Both n and k are integers defined between 0 and N-1. The computation of the DFT is usually done by application of the Fast Fourier Transform (FFT) algorithm, which take advantage of the periodicity and symmetry of the complex exponent in eqn. 5.3 so that a more efficient calculation can be achieved by reducing the number of operations [7].

5.3.2 Application to NDT

The frequency analysis provides information of structural perturbation by comparison of the amplitude and phase information of the Fourier transform with the reference state of a known undamaged situation.

- *Frequency spectrum changes*; The main effect of the presence of damage is a general reduction of the spectral amplitude [2,3], caused by scattering of the ultrasonic energy by the damage. This effect appears as a low pass filtering of the ultrasonic waves, as the smaller the ultrasonic wavelength the bigger its scattering for a given size damage.

The spectral amplitude attenuation can also be mode selective due to different interaction characteristics of the different modes with different kind of damages. Or in a similar way a mode conversion will also affect the frequency spectrum. Because the energy associated to a given frequency will now be distributed into different modes that have different displacement and stress distributions and so they will interact differently with the receiver. Changing the response of that particular frequency.

Additionally the effect that the different damages cause over the local loss of stiffness and other mechanical parameter of the structure is translated into changes of the structure's natural frequency [8]. This may affect the frequency distribution of the propagating wave, including the generation of new frequency components [9].

- *Phase diagram changes*; as previously mentioned different damages interact differently with the different propagating modes, this may cause different phase delays to the different propagating modes that will show as perturbations in the phase diagram of the detected signal.

A temperature change is also a very common cause of phase perturbations. An increment in the temperature decreases the stiffness of the structure and so the ultrasonic waves propagate slower affecting differently to the different frequency components and generating a phase delay between them.

5.4 TIME-FREQUENCY ANALYSIS

When a time signal is transformed into the frequency domain the time information of its events is lost. This is not a problem when dealing with *stationary* signals (those whose spectral content do not change over time). But it is a big drawback for physical signals that contain numerous non-stationary or transitory characteristics such as; dispersion, drift, trends, abrupt changes, and beginnings and ends of events. For non-stationary signals nor the time neither the frequency domain alone is enough to properly describe them, but a combination of both domains are needed, this is the time-frequency analysis.

The number of applications in which a time-frequency analysis is required is so big and so diversified that a large number of time-frequency representations have been developed within the years. These can be divided in two classes [10]; the first class or *atomic*

decompositions decomposes the signal into elementary components or *atoms* well localized in time and frequency, some examples are; Short time Fourier transform and Wavelet transform. The second class or *energy distributions* distributes the energy of the signal along the two variables time and frequency, some examples are; Wigner-Ville distribution, Cohen's class and the reassignment method. A detailed review and applications of the different time-frequency distributions can be found in [11]. Remarkable is the fact that time-frequency analysis can show the appearance of mode conversion effect as a consequence of the presence of non-symmetric damage in the sample as shown in [12,13].

The study of the broadband ultrasonic signals in Chapter 6, for the extraction of the propagation dispersion characteristics of multiple Lamb wave modes, is a clear example of time-frequency analysis. For this application the STFT and the reassignment method were chosen because of their advantages in comparison with other time-frequency representations, as pointed in reference [14], and they are explained next.

5.4.1 Short Time Fourier Transform (STFT)

The idea behind the STFT is as old as 1946, due to Dennis Gabor [15] who adapted the Fourier transform to analyze only a small section of the signal at a time - a technique called windowing the signal.

Mathematically the continuous STFT of a time signal *x(t)* is defined as:

$$STFT_h(x;f,t) = \int_{-\infty}^{\infty} x(\tau)\, h(\tau - t) e^{-j2\pi f\tau} d\tau \tag{5.4}$$

The window function *h(τ-t)* breaks the original signal *x(τ)* in segments around each time instant *t*, and each segment is analyzed by the conventional Fourier transform, to finally summing up all the results in the frequency domain.

The discrete STFT is more intuitive to understand and because the time signals experimentally obtained are discretized it makes more sense to concentrate in its description as given by eqn. 5.5.

$$STFT_h[x;k,l] = \sum_{n=0}^{N-1} h[n] \cdot x[n + l \cdot H] \cdot e^{-j2\pi kn/N} \quad \text{where } l = 0,1,2,\ldots \tag{5.5}$$

In the discrete STFT the time sequence $x[n]$ is divided into segments of equal number of points M, which are individually windowed by a window sequence h[n] of similar length (notice that h[n] = 0 for $n > M$) as shown in fig. 5.4. Finally a DFT of length $N \geq M$ is applied to each segment, so that the segment may be extended with zeros if $N > M$, known as

zero padding. The added zeros help to increase fidelity of the estimated spectrum by the DFT (as the bins are closer) to the true spectrum of the signal, but a real improvement of resolution can only be achieved if a longer time signal intervals are taken. If no zero padding is applied then a very coarse visual display of the spectrum can be obtained that may lead to misinterpretation of the data.

The length of the segments characterizes the time and frequency resolutions of the transformation, being inversely related to each other. A long segment means low time resolution, and because a longer time is Fourier analysed then a higher frequency resolution is achieved. Opposite occurs if a shorter segment is taken. Clearly the STFT suffers from what is known as *Heisenberg uncertainty* [11], it is not possible to have simultaneously perfect resolution in both time and frequency. The Heisenberg uncertainty is mathematically described by the Heisenberg-Gabor inequality where $\sigma_t^2 \cdot \sigma_\omega^2 \geq ¼$ must be satisfied, with σ_t being the time deviation and σ_ω being the frequency deviation.

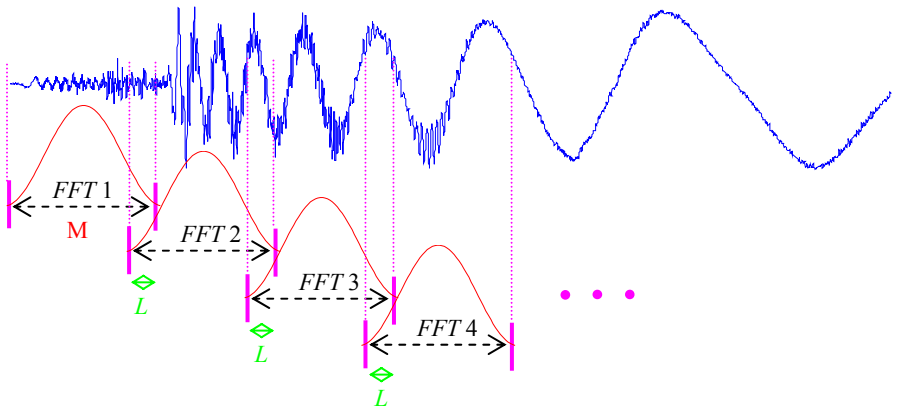

Figure 5.4: The STFT divides the time signal into overlapping windowed sections and FFT them.

The value of the inequality is associated to the spread of the spectrogram, and it is determined by the window function applied. For instance a Gaussian window satisfies the equality $\sigma_t^2 \cdot \sigma_\omega^2 = ¼$, becoming the optimal window from a resolution point of view. However a Hanning ($\sigma_t^2 \cdot \sigma_\omega^2 = 0.2635$) or Hamming window is preferable because although they provide a slightly worse resolution to that of the Gaussian window, their effect over the time signal shape modification is much smaller [16]. The selection of window is a trade-off between frequency resolution and side-lobe attenuation. More about applications and description of window functions is given in Appendix E.

The segments in which is divided the time sequence may overlap when $H < M$ (as shown in fig. 5.4 for $M - H = L$), where H represents the time advance of the window and the time resolution of the STFT (the higher H then less overlap and worse time resolution). The reason to overlap adjacent windows lies in the loss of information due to the fact that the

ends of the windows, as smoothly go to zero, hugely attenuate the original time signal. Short duration events taking place in these regions would be lost unless overlapping takes place. Selecting how big should be the overlapping is application dependant, where if as in our case, the main goal is to create a visual representation of the signal, then the overlapping should be chosen by simply trading off temporal resolution for computation time and looking to how the time-frequency representation looks. If perfect reconstruction of the input signal is required then the overlapping should be such that all data is weighted equally or that the overlapped window functions sum to a constant over all n, $A_h[n] = \sum_m h[n - l \cdot H] = c$. For Hamming and Hanning windows this occurs when $L = M/2j$, for j being an integer [17].

The common way to plot the STFT of a time signal is by its *spectrogram*, defined as the squared modulus of the STFT. It represents the energy distribution of the signal in the time-frequency domain.

5.4.2 Reassigned Spectrogram

Looking to the group velocity dispersion curves obtained by the STFT and plotted in Chapter 6, it is clear that the resolution provided is not more than slightly acceptable. Which is not a surprise as the STFT is without any doubts the simplest of the existing time-frequency analysis.

In 1995 Auger and Flandrin presented a technique named *reassignment method* in an attempt to improve the spectrogram [18]. This technique can considerably improve the time-frequency resolution of the spectrogram, by means of the STFT's phase information that the spectrogram neglects. In this method the energy distribution of the spectrogram is moved away from its original location (t, f) to a new location given by the reassigned coordinates $(\hat{t}, \hat{f})$ as defined in eqn. 5.6. Thus improving the sharpness of the localization of the signal components by concentrating the energy of the spectrogram at the centre of energy rather than at the geometrical centre as the STFT does.

$$\begin{aligned} \hat{t} &= t - \Re\left(\frac{STFT_{Th}(x;t,f) \cdot STFT_h^{*}(x;t,f)}{\left|STFT_h(x;t,f)\right|^2} \right) \\ \hat{f} &= f - \Im\left(\frac{STFT_{Dh}(x;t,f) \cdot STFT_h^{*}(x;t,f)}{2\pi \cdot \left|STFT_h(x;t,f)\right|^2} \right) \end{aligned} \tag{5.6}$$

This is better understood if we rewrite the continuous STFT equation 5.4 as a 2D convolution of the Wigner-Ville distributions of the time signal (given by $W_x(t, f)$) and of the

used window function (given by $W_h(t, f)$). This is done in eqn. 5.7, and we recommend [18] for a more detailed implementation.

$$STFT_h(x; f, t) = \int_{-\infty}^{\infty}\int_{-\infty}^{\infty} W_x(s, \xi) W_h(t - s, f - \xi) ds\, d\xi \tag{5.7}$$

This equation shows that the value of a time-frequency representation at any point (t, f) is the sum of all the terms $W_x(s, \xi) \cdot W_h(t - s, f - \xi)$, which can be interpreted as the contributions of the Wigner-Ville distribution values of $x(t)$ at the neighbouring points $(t - s, \omega - \xi)$, weighted by the Wigner-Ville distribution values of the window function.

A graphical representation of the reassignment method operation is shown in fig. 5.5. The spectrogram calculates the average weighted intersection between W_x and W_h, assigning it to the geometrical centre of W_h (situated at coordinates (t, f)). Even if the Wigner-Ville distribution of the signal W_x indicates no energy in this point, the averaging effect of the spectrogram assigns a nonzero value to that coordinate as long as there are some nonzero W_x values around, as shown in fig. 5.5. The smoothing window function makes energy appearing where the original signal does not have it, broadening the signal components. The reassignment method avoids this energy broadening by assigning the intersection value to the centre of energy $(\hat{t}, \hat{f})$ of this domain rather than to the geometrical centre (t, f). Some examples of the resolution improvement in the group velocity dispersion curves are shown on the plots in the associated section of Chapter 6.

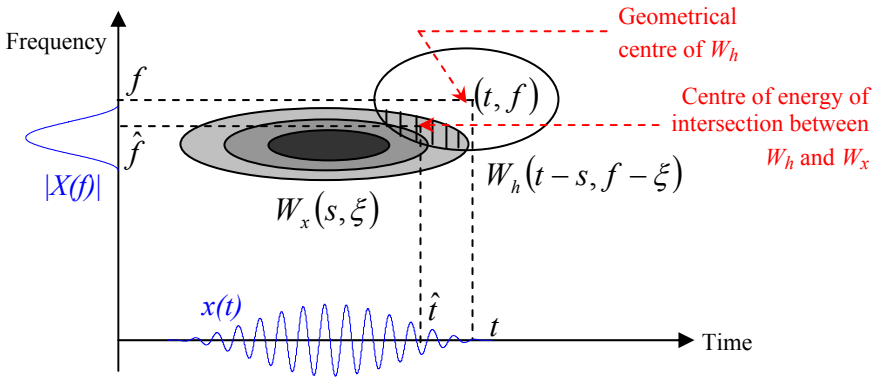

Figure 5.5: Principles of the reassignment method from the points of view of a 2D convolution of the Wigner-Ville distributions of the time signal W_x and used window function W_h. $|X(f)|$ is the spectrum of the time signal $x(t)$. The coordinates (t,f) are the geometrical centre of W_h, and $(\hat{t}, \hat{f})$ are the reassigned coordinates.

5.5 TWO-DIMENSIONAL FOURIER TRANSFORM (2D-FT)

The 2D-FT is an extension of the 1D case previously presented. When applied to a function of two independent variables $u(x, t)$ it decomposes the function into a combination of 2D complex exponentials function of both variables, as shown in eqn. 5.8. In this section we consider the two variables to be time and space as it applies to our particular application in Chapter 6.

$$H(f,k) = \int_{-\infty}^{\infty}\int_{-\infty}^{\infty} u(x,t)\cdot e^{-i2\pi(kx+ft)}dx\,dt \tag{5.8}$$

In order the argument of the complex exponentials to be dimensionless, in the 1D-FT the time domain was transformed into its inverse, the frequency domain ($f = 1/T$, with T being the time period). In the 2D-FT the space is also converted into its inverse, the wavenumber domain ($k = 1/\lambda$, with λ being the spatial wavelength).

The application of the 2D-FT for the analysis of propagating multimode Lamb wave signals was first due to Alleyne and Cawley [19] in 1991, based on that Lamb waves are sinusoidal in both the frequency and the spatial domain (see eqn. A.20). Then a 2D-FT is a natural conversion of the Lamb wave time signals, measured at different distances source-sensor, to the frequency-wavenumber domain, which describe the dispersion propagation characteristics of the different excited Lamb modes.

In practice the two dimensional function to which we apply the 2D-FT is a discrete matrix, in comparison to the vector or sequence of sampled data in the 1D-FT. This matrix $u[\bar{x},\bar{t}]$ consist of a time sampling of the detected time signals, such that $t = \bar{t}\cdot T_s$, with $\bar{t}$ integer and T_s being the time sampling period. And of a spatial sampling given by equally spaced distance source-sensor Δx, such that $x = \bar{x}\cdot\Delta x$, with $\bar{x}$ integer and Δx the space sampling period. The discrete 2D-FT is given in eqn. 5.9.

$$H[\bar{f},\bar{k}] = \sum_{\bar{x}=0}^{M-1}\sum_{\bar{t}=0}^{N-1} u[\bar{x},\bar{t}]\cdot e^{-i2\pi\left(\frac{\bar{k}\bar{x}}{M}+\frac{\bar{f}\bar{t}}{N}\right)} \tag{5.9}$$

The evaluation of the 2D-FT can be implemented by calculating the two successive one dimensional transforms as described in fig. 5.6, this allows applying the FFT algorithm for a very high efficiency estimation of the 2D-FT. In fig. 5.6 first a time Fourier transform is applied and then a space Fourier transform, however notice that the 1D Fourier transform could be applied in any order.

The 2D-FT rewrite the time and space broadband pulse sources propagation information, as a combination of the sinusoidal waves $e^{-i2\pi(kx+ft)}$ components of this pulse source, and it tells us how this mono-frequency waves propagate. This is why the curves that we obtain in $|H(f, k)|$ are the phase velocity dispersion curves, in comparison with the group velocity dispersion curves we obtained with the time-frequency analysis.

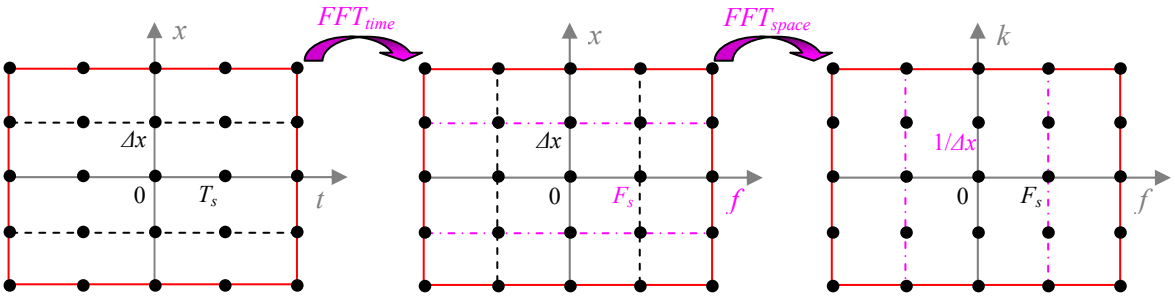

Figure 5.6: Separability of the 2D-FT into two 1D-FT.

The properties of the continuous 1D-FT case can be extrapolated to the 2D case as; $H(f,k)^* = H(-f,-k)$ and $H(-f,k)^* = H(f,-k)$ or equivalently $|H(-f,-k)| = |H(f,k)|$ and $|H(f,-k)| = |H(-f,k)|$, shown in fig. 5.7-*left*, where the domain of definition of the 2D-FT for a continuous set of data $u(t, x)$ is shown. Here f_{max} and k_{max} are the maximum frequency and wavenumber components respectively. Four sections are distinguished in the domain of definition of the continuous 2D-FT; the darker sections have the same $|H(f, k)|$ value and the lighter sections have also the same $|H(f, k)|$ values but different from the darker sections.

In a similar way to the 1D case, the discrete data matrix $u[\bar{x},\bar{t}]$ can be expressed as the product of the continuous 2D data function $u(x,t)$ and a 2D sampling function $p(x,t)$ defined as a combination of 2D Dirac deltas delayed in time by T_s and in space by Δx from each other. Like in the 1D case previously studied, the 2D Fourier transform of $p(x,t)$ is another combination of Dirac deltas delayed in frequency by $1/T_s$ and in wavenumber by $1/\Delta x$. The property of convolution is rewritten for the 2D-FT of a product of 2D functions as the 2D convolution of their associated 2D-FT. This means that the 2D-FT domain of definition of the discrete data $u[\bar{x},\bar{t}]$ correspond to the reproduction of the domain of definition of the continuous function $u(x,t)$ shown in 5.7-*left*, in both dimensions for each multiple combination of $1/T_s$ and $1/\Delta x$, as shown in 5.7-*right*. The two main dark and light sections are now reproduced infinitely. These two sections have all the 2D-FT spectra information, thus it is enough to concentrate only in one of these section pairs (red squared in 5.7-*right*).

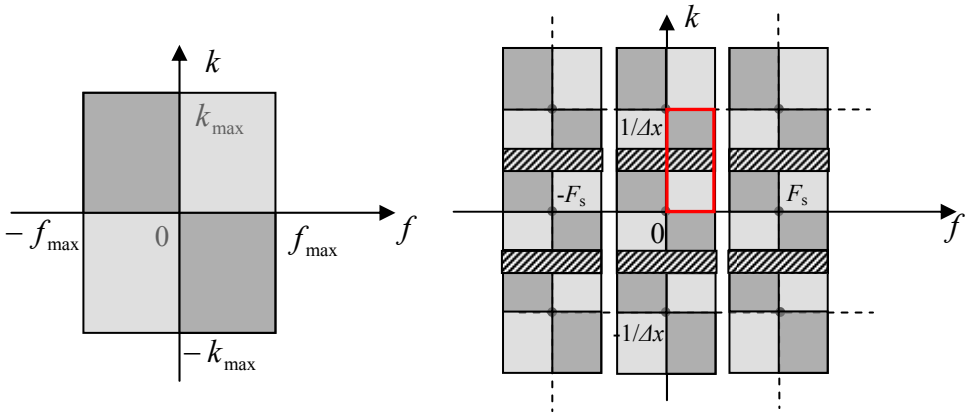

Figure 5.7: Domain of definition of the 2D-FT: (*Left*) for the continuous set of data *u(t, x)*. (*Right*) for a discrete set of data.

Aliasing

The selected sections in fig. 5.7-*right* are shown to overlap in the *k* direction or wavenumber domain, which happens when $k_{max} > 1/(2\cdot\Delta x)$, this is called *aliasing*, similar to what we saw in the 1D-FT case. However whereas in the 1D-FT once we have aliasing no useful information can be extracted from the overlapping area. In the 2D-FT we do can extract some information, due to the physical meaning that the second dimension gives to the negative frequencies (opposite to the 1D case, where negative frequencies has no physical meaning). Let us look at this more carefully.

The 2D-FT domain of definition associated to low wavenumber values (light grey square) corresponds to positive values of *k* and *f* of the original domain for the continuous set of data (fig. 5.7-*left*). This section corresponds to the projection of the continuous data *u(x,t)* to complex exponential functions of the type $e^{-i2\pi(kx+ft)}$. In the other hand, the domain of definition associated to the high wavenumbers values (dark grey square) corresponds to positive *f* but negative *k* in the domain of definition for the continuous 2D-FT and so a projection to complex exponential functions of the type $e^{-i2\pi(-|k|x+ft)}$. Because the practical application of the current processing technique deals with ultrasonic wave data, then the 2D-FT decomposes the propagation characteristics of the ultrasound in sinusoidal waves as given by the previous complex exponentials.

As it will be defined in Chapter 6, the 2D matrix of ultrasound sampled data $u[\bar{x},\bar{t}]$ relates the magnitude *x* with the distance source-sensor, increasing *x* means increasing this distance. Thus a sinusoidal wave given by $e^{-i2\pi(-kx+ft)}$ means that to keep the phase $2\pi\cdot(-|k|x+ft)$ constant as the distance source-sensor is increased, the propagation time *t* must also be increased. In the other hand, waves given by the exponential $e^{-i2\pi(kx+ft)}$ propagate in

opposite direction to the previous ones and so if the former were incident waves, then the latter type are reflected waves.

In consequence the overlapping sections in the analysed domain of definition (dashed region in fig. 5.7-*right*) due to spatial aliasing, involves waves propagating in opposite direction for each intersecting square. Their associated dispersion curves have opposite slope sign, so in the overlapping area they only intersect in theory in 1 point. In practice the experimental dispersion curves are not perfect lines, but they have some width, thus intersecting between themselves in a finite section as shown in next chapter. Nonetheless the perturbation between the overlapping dispersion curves is very reduced and most of the dispersion information can be easily extracted at aliasing conditions. This is a great advantage because it allows us to work with smaller spatial sampling frequencies ($1/\Delta x$), thus increasing the wavenumber resolution of the dispersion curves ($= 1/(M \cdot \Delta x)$, for M being the number of spatial samples).

The 2D-FT dispersion curves are in the wavenumber – frequency domain, but they can easily be transformed to the more common phase velocity – frequency domain by $v_{ph} = f/k$.

The separation between incident and reflected waves that characterized the 2D-FT can be used for determining the presence of damage [20,21]. If the geometrical borders of the structure can be excluded from the analysed data, then the presence of reflected waves is due to damage. The amplitude of these reflections can help to the damage characterization. Additionally the 2D_FT technique can also be applied for damage detection and characterization based in the comparison with a reference undamaged 2D-FT dispersion curves signature. As mentioned in Chapter 6 the damage has a low pass filter effect if it is in the way between source and receiver and this can be detected in the 2D-FT plot. The damage can also be detected and characterized by studying the presence of broken ridges of the wavenumber-frequency dispersion curves modes for the damaged 2D_FT case in comparison with the undamaged signature and a decrement of the magnitude of the modes curves amplitude. These effects are more intensive the bigger the damage and they are caused by the interference of the propagating Lamb wavefield with the scattered wavefield generated in the damage [22].

5.6 WAVELETS ANALYSIS

Similarly to the time frequency analysis in section 5.4, the wavelet analysis was created as a way of representing the frequency evolution of non-stationary data. However in contrast to the uniform resolution given by the STFT, the wavelet analysis is characterised for its multiresolution approach, giving good time resolution and poor frequency resolution at high

frequencies and good frequency resolution and poor time resolution at low frequencies, as shown in fig. 5.8-*right*. This is a good approach when the analysed signal has high frequency components for short durations and low frequency components for long durations, as it is usually the case in physical signals. However this attributes are not suitable for resolving broadband multimode Lamb waves, which is the application for which we require time-frequency representations (as shown in Chapter 6). As pointed in [14] the wavelet transform does not provide enough frequency resolution at high frequency meanwhile it gives a very high time resolution. A reassignment spectrogram is a more suitable time-frequency representation for our application.

The wavelet analysis has other important applications, de-noising of signals is one of them. As shown in [9] filtering de-noising (such as low pass, high pass or bandpass and bandstop filters) are not as effective as wavelet de-noising.

Wavelet analysis is a very modern signal processing subject and the number of books, journals and conferences dedicated to it is vast. For any interested reader we would suggest [23], here I limit myself to only give a basic description to understand how we used it as a de-noising tool.

The wavelet analysis is based in the *wavelet transform* shown in eqn. 5.10, that decomposes a time signal $f(t)$ into a series of waveforms of effectively limited duration called *wavelets* $\frac{1}{\sqrt{s}}\psi\left(\frac{t-u}{s}\right)$. These waveforms are created by dilating (scaling by parameter s) and translating in time (by parameter u) a mother wavelet. Because the wavelets are localized in time and frequency then it is the dilatation and translation what allows them to provide a multiresolution time-frequency analysis.

$$W_{\psi}(s,u) = \frac{1}{\sqrt{s}} \int_{-\infty}^{\infty} f(t) \cdot \psi^{*}\left(\frac{t-u}{s}\right) dt \tag{5.10}$$

The wavelet transform is not a pure time-frequency analysis but a time-scale. Like in a map, high scales are associated to a global view of the analysed signal (low detail) meanwhile low scales represent the most detailed part of it. In contrast, in terms of frequency, low frequencies correspond to global information of a signal, whereas high frequencies correspond to detailed information.

- Low scale → High frequency
- High scale → Low frequency

A more detailed relationship between scale and frequency can be obtained in [24,25].

The expression in eqn. 5.10 transforms a time signal into a continuous time-scale domain, thus it is called continuous wavelet transform. This representation is very redundant because for each infinitesimal translation in time, the time signal is transformed to all possible scales continuum. A more efficient version is the Discrete Wavelet Transform (DWT), where only a subset of possible discrete scales and translations are allowed.

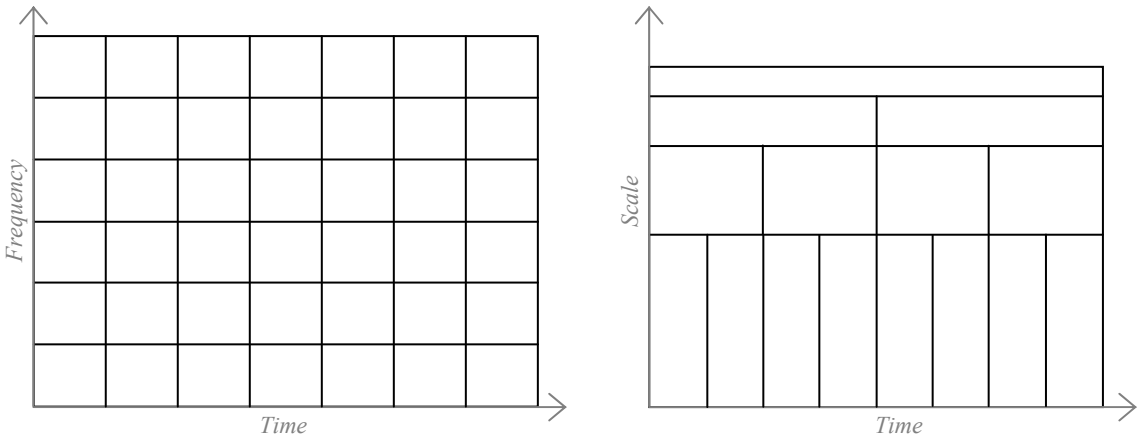

Figure 5.8: (*Left*) Time-frequency resolution of the STFT. (*Right*) Time-scale multiresolution of the wavelet transform. The scale has an inverse relationship with frequency.

The most commonly used discretization is the dyadic one, where the time-scale grid components are expressed based on powers of two. Equivalently, this means that the possible scale values to be chosen are $s = 2^m$, and the possible time values are $u = n \cdot 2^m$, with m and n integers. The discrete wavelets are now rewritten in a dyadic way as:

$$\psi_{m,n}(t) = \frac{1}{\sqrt{2^m}} \psi\left(\frac{t - n \cdot 2^m}{2^m} \right) \tag{5.11}$$

Between all the possible wavelets that satisfy eqn. 5.11, those that form an orthogonal basis are used as they are concise and decompose time functions without any redundancy. The DWT can be expressed as:

$$c_{m,n} = \int_{-\infty}^{\infty} f(t) \cdot \psi_{m,n}{}^{*}(t) dt \tag{5.12}$$

The reconstruction of the original time signal is given by:

$$f(t) = \sum_m \sum_n c_{m,n} \cdot \psi_{m,n}(t) \tag{5.13}$$

Following this definition of the reconstructed original time signal we will try to show how the Discrete Wavelet Transform can be used as a de-noising tool. In order to understand this,

first we need to define what it is called the *details* components of the signal *f(t)*, $D_m(t) = \sum_n c_{m,n} \cdot \psi_{m,n}(t)$. The details D_m represent the time behaviour of the signal *f*(*t*) within different frequency bands because they are related by $f(t) = \sum_m D_m(t)$, where *m* was defined as the discrezation of the scale magnitude *s*, and so it is related with the frequency components of the time signal. If we look to a given scale (or frequency) level *M* then we can divide the details into two sorts; *fine details* being those with $m \leq M$, that correspond to associated scale values $s = 2^m \leq 2^M$, and *coarse details* or *approximation* given by the rest of detail component, expressed as $A_M = \sum_{m>M} D_m(t)$. The fine details are associated to the smallest scale values or equivalently highest frequency components. In the other hand the approximation is associated to the low frequency components. This relationship between the fine details and approximation with the frequency is what give their names. It is important to realize that the original time signal *f*(*t*) is the sum of its approximation and its fine details at any given level *M*, so that $f(t) = A_M + \sum_{m \leq M} D_m(t)$, and that the approximation at a lower level *M*-1 is given by the sum of the approximation and the fine detail at the next level or $A_{M-1} = A_M + D_M$.

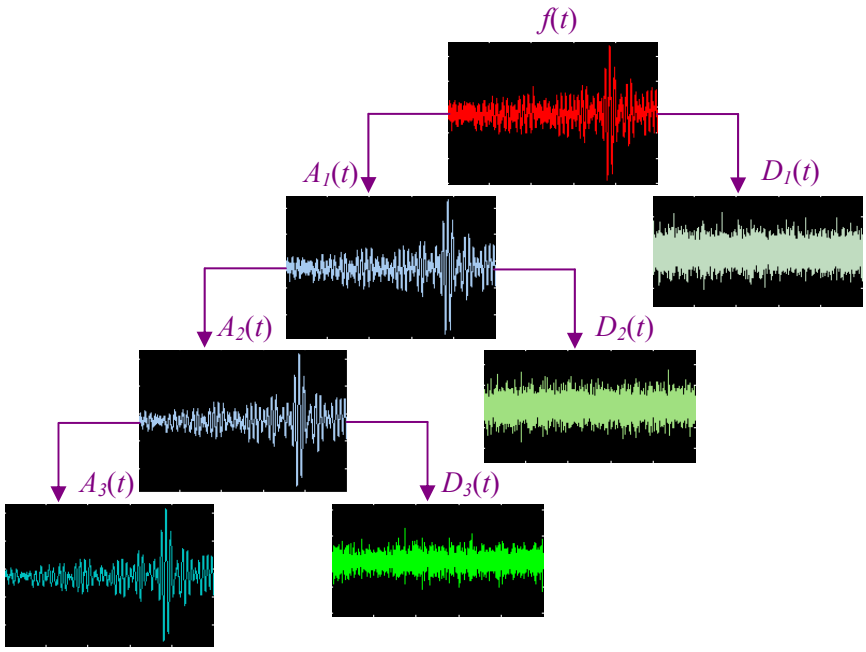

Figure 5.9: Wavelet decomposition of a time signal *f*(*t*) into three levels of approximations A_M and details D_M. The lower the level of the detail, the higher its frequency content of the original time signal, meanwhile the higher the level of the approximation, the lower its frequency content of *f(t)*.

In conclusion, a signal can be decomposed to any level M as a combination of an approximation at that level and as many fine details as the value of the chosen level M. For instance, in fig. 5.9 we have decomposed the original time signal at the top in three levels, with the level $M = 3$ at the bottom of that figure

The original time signal of fig. 5.9 is a real example of an ultrasonic signal of 4.5 cycles toneburst detected with an optical fibre sensor bonded onto the surface of an aluminium plate as shown on fig. 4.18. If we look to the decomposition of the $f(t)$ in level 2, then $f(t) = A_2 + D_1 + D_2$, but if we look to its decomposition at level three then $f(t) = A_3 + D_1 + D_2 + D_3$. The approximations at lower levels appear less and less noisy, but in detriment of losing progressively the high frequency information, passed to the details in which the approximation at lower levels are decomposed.

The lower the level associated to a detail, then the higher its frequency content from the original time signal. Such that D_1 is taking the highest frequency components meanwhile D_3 takes the lowest high frequency components of $f(t)$.

Wavelet de-noising does not consist in taking off all the details until a certain level, but into reducing them according to different thresholding techniques. For instance a *soft-thresholding* as used in this thesis, cancels the details with amplitude smaller than a certain threshold value, meanwhile those details with amplitude above this threshold are just shrink. The advantage of wavelet de-noising respect to filtering de-noising is that the de-noised signal still keeps high frequency information of the original signal but its noise is adequately filtered out.

5.7 OPTIMIZATION ALGORITHMS

This section describes a signal processing approach very different to the ones before. Meanwhile in the previous cases, the signal processing methods were applied to the detected ultrasonic time signals, in the present cases the technique is applied to already processed data. In particular, they are applied to the ultrasonic wave modes dispersion propagation information extracted through the 2D-FT and the reassigned spectrogram from the time signals.

These techniques are solely applied in Chapter 7, for the optimization of the error function developed in order to extract the elastic properties of the materials as described in the inversion process. Although what matters at this point is that the optimization is the process of finding the values of the variables $\boldsymbol{x} = [x_1, x_2,\ldots,x_n]$ of a function $f(\boldsymbol{x})$ that minimize (or maximize) it, the function is usually called the *objective function*. The obtained extremum of

the objective function (maximum or minimum) can be either *global*, effectively being the highest or lowest value of the function. Or *local*, in which case it is the highest or lowest value but only in a finite neighbourhood around the initial estimation of the variables.

Next we briefly describe the three optimization techniques used in this thesis, a more detailed explanation can be found in [26,27]. Because the objective function is, in the problem that interests us (see Chapter 7), a nonlinear function of the design variables, then all the optimization techniques here presented are nonlinear. We start with the most commonly used nonlinear optimization technique known as *downhill simplex algorithm*, later we present a more powerful algorithm that uses line search procedures in conjunction with a quasi-Newton method and it is optimized for least-squares problems as it is our case. These two methods can handle discontinuities but they might only give local minimums. That is why we also use a technique well suited for finding global solutions, the *Genetic algorithm*.

5.7.1 Downhill simplex algorithm

This method was originally developed by Nelder and Mead [28], and it should not be confused (as many times seen in literature) with the simplex method of linear programming where the function to be optimized is a linear combination of the independent variables.

This optimization function is characterized by requiring only function evaluations without the need of numerical or analytic derivatives. Although it is not very effective in terms of the number of function evaluations that it requires [26], it can be extremely robust and fast, what make of it one of the most used optimization techniques.

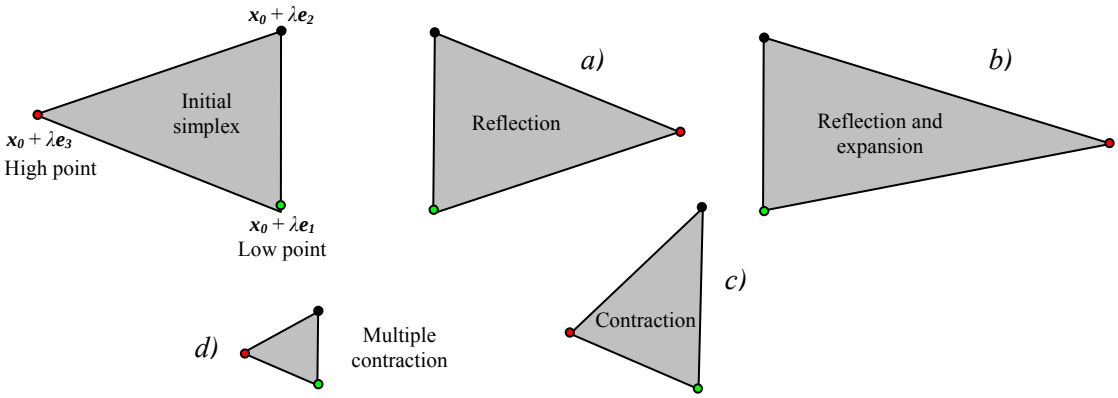

Figure 5.10: Possible changes of a simplex in the downhill simplex algorithm, starting from the initial estimation at $\boldsymbol{x_0}$: *a)* Reflection away from the point of higher function value. *b)* If possible reflection and expansion to take larger steps. *c)* Contraction in from the high point in 1D. *d)* Contraction from all dimensions towards the low point.

This method makes use of the geometrical concept of a *simplex*, which in two dimensions (as it is our case of two variables) is a triangle (see fig. 5.10). This triangle encloses an area of the definition region of the function variables (x_1, x_2) that is defined by the three points that are its vertices. The downhill simplex method starts by creating a simplex from the initial estimation point $\boldsymbol{x_0} = (x_{10}, x_{20})$.

For each iteration of the search of the values of the variables that optimize the objective function, the point of the simplex with largest function value is moved through the opposite face of the simplex to a point with a lower value. This step is called *reflection* and it gives a new simplex. Whenever possible the algorithm expands the simplex in one or other direction to take larger steps and when it is close to a *valley floor* then it contracts the simplex in the transverse direction and tries to go down the valley. In some cases it may also contract itself in all directions towards the best vertex point. These different operations are shown in fig. 5.10.

These steps are repeated until the termination criteria is met. Various termination criteria can be taken with the most common being; the diameter of the simplex is less than the specified tolerance or that the distance moved by the vertex in that step or the decrease in the function value is smaller than a given tolerance.

This method can handle discontinuities but it might only give local solutions.

5.7.2 Gradient method and line search algorithm for nonlinear least-squares problem

Search methods that use only function evaluations, as the downhill simplex algorithm, are most suitable for problems that are very nonlinear or have a number of discontinuities [27]. In fact gradient methods are generally more efficient when the function to be minimized is continuous in its first derivative, as it is generally the case in our optimization application in Chapter 7. Gradient methods use information about the slope of the function to dictate a direction of search where the minimum is thought to lie. Of the methods that use gradient information, the most favoured are the quasi-Newton methods and of this family is the one used in our algorithm. These methods use the curvature information of the function at each iteration to reformulate the optimization problem as a quadratic model problem of the form:

$$\min_{\boldsymbol{x}} \frac{1}{2} x^T H \cdot x + c^T x + b \tag{5.14}$$

Where H is the Hessian matrix [29], c is a constant vector and b is a constant. The optimal solution for this problem $\boldsymbol{x_{opt}}$ occurs when the partial derivatives of x go to zero:

$$\nabla f\left(x_{opt}\right) = H \cdot x_{opt} + c = 0 \tag{5.15}$$

Once the direction of search is known, the algorithm uses a line search procedure to know how far to move in that direction towards the minimum. For a more detailed explanation consult [27].

When the optimization problem is a nonlinear least-squares problem such as in eqn. 5.16 then the special structure that the gradient and Hessian matrices have can often be exploited to improve the iterative efficiency of the solution procedure.

$$\min_{\boldsymbol{x}} \; f(x) = \min_{\boldsymbol{x}} \sum_i f_i(x)^2 \tag{5.16}$$

This method is more powerful than the downhill simplex algorithm, because it uses not only function evaluation but also gradient information, therefore providing more accurate results. Additionally as this function is optimized for least-squares problems, then it is proven to be iteratively also more efficient, as shown in our application in Chapter 7. However the function to be minimized must be continuous, and as in the previous method it might only give local solutions.

5.7.3 Genetic Algorithm

Genetic algorithms are a method for solving optimization problems, modelled based on the principles of evolutionary biology via natural selection. Genetic algorithms were originated by John Holland for his studies of cellular automata [30]. One of the best references in the subject is [31] and here we just give a general overview of how it works.

First the algorithm starts creating a random *initial population* of solutions, this population can cover the entire range of possible solutions of the optimization problem, or it may concentrate in areas where optimal solutions are likely to be found. Then in each iteration a new improved population (*children*) of possible solutions is generated based on the vectors (*genes*) of the current population members (*parents*) that have better *fitness* values (minimum values of the function to be optimized). The *reproduction* creates four types of children for each iteration:

- *Elite children* are copies of the parent's vectors with the best fitness values.
- *Crossover children* are created by combining the vectors of a pair of parents.
- *Mutation children* are created by introducing random changes (*mutations*) to the vector of a single parent.
- *New blood* are new entirely random individuals (new vectors).

The reproduced new population also includes a small proportion of members that are less fit and with random solutions. This is done to keep the diversity of the population large, preventing premature convergence on poor or local solutions. Genetic algorithms derives the optimal solution not by producing optimal populations in each iteration, but by continuous improvement of each generation creating individuals that are superior to the others (the elite).

The algorithm stops the reproduction of new generations, when one of the terminating criteria is satisfied:

- The fitness value of the best point in the present population is better than a limit.
- A given number of generations have been produced.
- Successive generations no longer produce better fitness results.

The main differences of genetic algorithms with the previously described optimization algorithms is that for each iteration a population of points is generated instead of a single point, and that the improvement of populations in each iteration is based in computations that involve random choices, opposite to the deterministic computation in which are based the previous algorithms.

Genetic algorithms are less susceptible to give a local minima than the previous methods, and they highly improve the chances of finding a global solution [32]. But they tend to be computationally expensive. It is precisely this better tendency to provide global minima what makes of it a choice for the inversion process of Chapter 7 in order to compare with the optimized solutions obtained with the computationally faster previous methods.

5.8 REFERENCES

[1] Wilcox P., Lowe M. and Cawley P. *Long range Lamb wave inspection: The effect of dispersion and modal selectivity*, Review of Progress in Quantitative Nondestructive Evaluation, vol. **18**, pp. 151-158, 1999.

[2] Lee B. C. and Staszewski W. J. *Modelling of Lamb waves for damage detection in metallic structures: Part II. Wave interactions with damage*, Smart Materials and Structures, vol. **12**, pp. 815-824, 2003.

[3] Pierce S. G., Dong F., et. al. *Damage assessment in smart composite structures: the DAMASCOS programme*, Air & Space Europe, vol. **3(3)**, pp. 132-138, 2001.

[4] Diligent O. *Interaction Between Fundamental Lamb Modes And Defects in Plates*, PhD Thesis, Imperial College, London, 2003.

[5] Lowe M. J. S., Cawley P., Kao J-Y. and Diligent O. *The low frequency reflection characteristics of the fundamental antisymmetric Lamb wave A_0 from a rectangular notch in a plate*, J. Acoust. Soc. Am., vol. **112(6)**, pp. 2612-2622, 2002.

[6] Ifeachor E. C. and Jervis B. W. *Digital signal processing: A practical approach*, Addison-Wesley, 1996.

[7] Posadas Yague J. L. and Benet Gilabert G. *Transformada rápida de Fourier (FFT) e interpolación en tiempo real: Algoritmos y aplicaciones*, Dep. de Informática de sistemas y computadores, Universidad Politécnica de Valencia, 1998.
[8] Kessler S., Spearing S., Atalla M., Cesnik C. and Soutis C. *Structural health monitoring in composite materials using frequency response methods*, Composites Part B, vol. **33**, pp. 87-95, 2002.
[9] Giurgiutiu V. and Yu L. *Comparison of STFT and Wavelet transform of transient and tone burst wave propagation signals for SHM*, Proceedings of the 4th International Workshop on SHM, pp. 1267-1274, 2003.
[10] Auger F., Flandrin P., Goncalvès and Lemoine O. *Time frequency Toolbox: for use in MATLAB – tutorial*, CNRS, 1996.
[11] Cohen L. *Time frequency analysis*: theory and applications, Prentice Hall, 1994.
[12] Hurlebaus S., Niethammer M., Jacobs J. L. and Valle C. *Automated methodology to locate notches with Lamb waves*, Journal of the Acous. Soc. of Am., vol. ARLO 2(4), pp. 97-102, 2001.
[13] Benz R., Niethammer M., Hurlebaus S. and Jacobs L. J. *Localization of notches with Lamb waves*, Journal of the Acous. Soc. of Am., vol. 114(2), pp. 677-685, 2003.
[14] Niethammer M. and Jacobs L. J. *Time frequency representations of Lamb waves*, Journal of the Acoustical Society of America **109 (5)**, pp 1841-1847, 2001.
[15] Gabor D. *Theory of Communication*, J. IEE, vol. **93(3)**, pp. 429-457, 1946.
[16] M. Niethammer, L. J. Jacobs, J. Qu and J. Jarzynski *Time-frequency representation of Lamb waves using the reassigned spectrogram* Journal of the Acoustical Society of America, vol. **107(5)**, pp. L19-L24, 2000.
[17] Serra X. *A System for Sound Analysis/Transformation/Synthesis Based on a Deterministic Plus Stochastic Decomposition*, PhD Dissertation, Department of Music, Stanford University, 1989.
[18] Auger F. and Flandrin P. *Improving the readability of time-frequency and time-scale representations by the reassignment method*, IEEE Trans. Signal Processing, **43**, pp. 1068-1089, 1995.
[19] Alleyne D. and Cawley P. *A two-dimensional Fourier transform method for the measurement of propagating multimode signals*, J. Acoust. Soc. Am., **89(3)**, pp. 1159-1168, 1991.
[20] Alleyne D. and Cawley P. *The interaction of Lamb waves with defects*, IEEE Trans. On ultrasonics, ferroelectrics and freq. control, vol. **39(3)**, pp. 381-397, 1992.
[21] Diligent O., Lowe M. J. S. and Cawley P. *Reflection and scattering of the S_0 Lamb mode from circular defects in plates*, Review of prog. In Qauntitative NDE, vol. **20**, pp. 134-141, 2001.
[22] Eisenhardt C., Jacobs L. J. and Qu J. *Experimental lamb wave spectra of cracked plates*, Review of Progress in QNDE, vol. **19A**, pp. 343-349, 2000.
[23] Chui C. K. *Wavelets analysis and its applications-Vol 1&2*, Academic Press, 1992.
[24] Niethammer M. *Application of time frequency representations to characterize ultrasonic signals*, MSc thesis, Georgia Institute of Technology, 2001.
[25] MATLAB Wavelet Toolbox User's Guide.
[26] Press W. H., Flannery B. P., Teukolsky S. A. and Vetterling W. T. *Numerical Recipes in C : The Art of Scientific Computing*, Cambridge University Press, 1992.
[27] MATLAB Optimization Toolbox User's Guide.
[28] Nelder J. A. and Mead R. *A simplex method for function minimization'* Computer J. **7**, pp. 308-313, 1965.
[29] Eric W. Weisstein. "Hessian." From *MathWorld*--A Wolfram Web Resource. http://mathworld.wolfram.com/Hessian.html
[30] Holland J. H. *Adaptation in Natural and Artificial Systems*, University of Michigan Press, Ann Arbor, 1975.
[31] Goldberg D. E. *Genetic Algorithms in Search, Optimization and Machine Learning,* Addison-Wesley, 1989.
[32] MATLAB Genetic Algorithm and Direct search Toolbox User's Guide.

Chapter 6

OPTICAL EXTRACTION OF LAMB WAVES DISPERSION FEATURES

6.1 INTRODUCTION

This chapter presents a SHM application of ultrasonic guided waves very different to those described in Chapter 3 that mainly involved damage detection, location and characterization. For those applications, PZT actuators for ultrasonic generation were always used. The narrow bandwidth frequency excitation characteristic of this type of contact actuators was not only adequate for the time and frequency analysis typical of those applications. But in fact it was beneficial when dealing with the dispersive and multimode propagating nature of Lamb waves, as it allowed a simplified analysis based on single frequency excitation of the low order Lamb wave modes.

The application presented in this chapter consists in generating the structure's Lamb waves transfer function to be used as an extremely sensitive indicator of the material condition and/or structural loading. For this, a short harmonically rich mechanical pulse excitation is launched into the structure thus generating a wide spectrum of both spatial and temporal ultrasonic frequencies. This impulse response allows obtaining a multiplicity of transfer function measurements simultaneously. Which can be represented as the structure's Lamb wave dispersion curves by means of the processing techniques thoroughly described here.

Appendix A shows that the dispersion curves are sensitive to the structure material throughout the thickness of the plate, and also sensitive to the boundary conditions above and below the plate itself. Thus monitoring their changes can be used as a sensitive indicator of the structural conditions. In particular, in Chapter 7 we are able to assess, from the following obtained dispersion curves, the most important mechanical and geometrical properties of structural materials –namely Young's modulus, Poisson's ratio and thickness.

The broad temporal and spatial spectrum bandwidth ultrasonic excitation and detection requirements of the current application has not a better suited system than that obtained

through the combination of the non-contact optical ultrasonic detection system and the non-contact optical ultrasonic generation system presented in Chapter 2 as shown in fig. 6.1. Although a more detailed description of the operation of this tool is presented in section 6.5 of this chapter, it is basically composed by a Q-switched high power pulse laser source for the ultrasonic generation stage and a modified Mach-Zehnder surface displacement interferometer for the detection stage. This active interrogation system has the benefit of not requiring physical contact with the structure itself to either excite or interrogate the system response, as both of these functions are executed remotely.

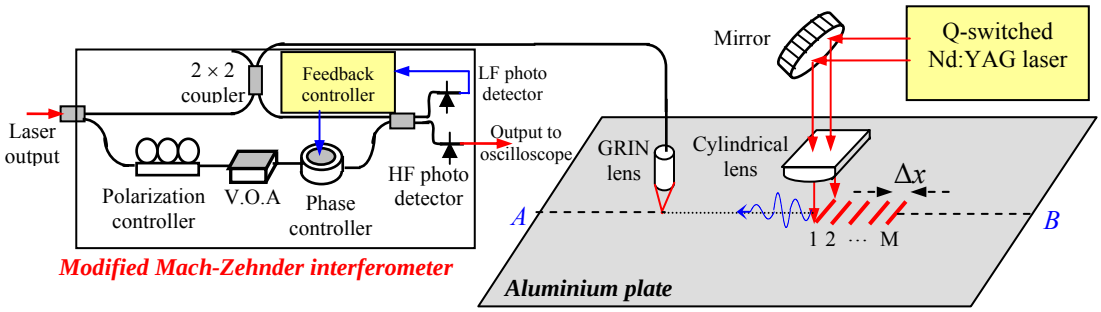

Figure 6.1: Set up of the experimental equipment for the all optical remote inspection tool. The ultrasounds are optically generated by a Q-switch (Nd:YAG) laser, and optically detected by a modified Mach-Zehnder interferometer. V.O.A. is a variable optical attenuator.

The chapter is outlined as follows; we start by presenting the equipment description of the non-contact all optical material characterization tool which will be later used for the experimental extraction of the Lamb wave dispersion curves of different materials. Afterwards we present and compare from an experimental point of view and restricted to the present application, the two signal processing techniques used to extract the Lamb waves dispersion information stored in the generated and detected ultrasonic wave data. These techniques being the reassigned spectrogram and the two dimensional Fourier transform, were described theoretically in Chapter 5. Here we analyze the radically different properties and applications of both approaches. Later we apply the two data interpretation procedures and the developed inspection system to two NDT experimental situations; temperature change sensitivity and damage detection.

We end this chapter by commenting the potential extension of the present structural characterization technique directed to micrometers dimensions structures. This can be achieved by the combination of the very high frequency ultrasonic detection capabilities of a fibre Fabry-Perot interferometer with the non-destructive low power ultrasonic generation characteristics of a high frequency modulated semiconductor laser source.

6.2 ALL-OPTICAL & REMOTE INSPECTION TOOL FOR MATERIAL CHARACTERIZATION

Being an important part of this thesis the monitoring of the elastic properties of solid plate-like structural material, has required a huge amount of work in the development of computational programs to implement the different signal processing techniques required and described in the previous chapter. Complementarily, in order to test their validation and to orientate this thesis into a practical and commercial approach, we have also designed and physically build the all-optical remote inspection tool as it is presented in fig. 6.2. In this section we describe its various components, classified into three groups; ultrasonic generation optical system, ultrasonic detection optical system and laser source beam pulse steering, positioning and confinement element.

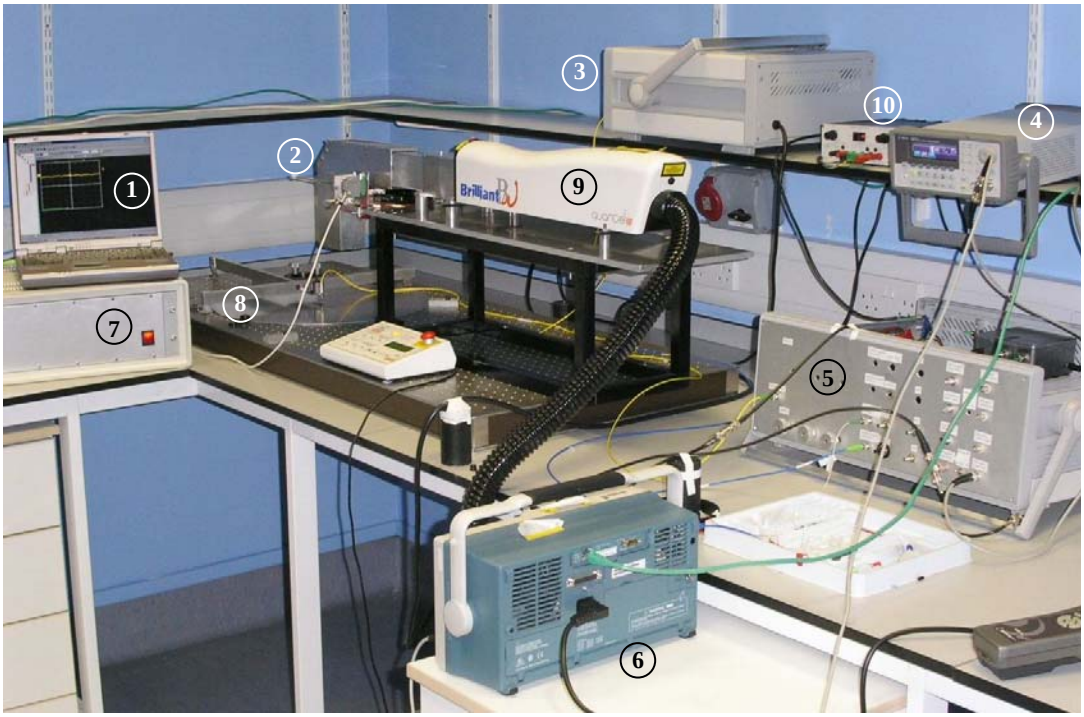

Figure 6.2: Set up of the experimental equipment for the all optical remote inspection tool. The different components are: 1) Signal processing and inspection automation, 2) Source beam steering arm, 3) Interferometric laser source (1310*nm*), 4) Signal generator, 5) Interferometer, 6) Oscilloscope (data acquisition), 7) Steering arm motor controller, 8) Aluminium sample plate, 9) Q-switched laser source and 10) Interferometric DC power supply.

6.2.1 Brilliant B (Quantel) Q-switched Nd:YAG high power laser source

A Q-switched narrow pulse high power laser source has been chosen for the ultrasonic wave generation. This source as discussed in Chapter 2 is very adequate for the present application. Its extreme narrow pulse (*nsec* temporal width) is capable of exciting a very

wide temporal frequency range varying from DC to hundred of *MHz*. Additionally the source laser beam can be focused to very small spatial spot dimensions, providing a spatial impulse source that allows the excitation of a wide variety of spatial modes.

The high power energy involved in this ultrasonic source is capable of generating ultrasonic waves of detectable amplitude at the macroscopic dimensions involved in our experiments. The laser was operated within the ablation regime conditions, enhancing the interferometric detectability of the propagating waves due to their complementary out-of-plane displacement generation and detection characteristics. Furthermore, changing the focussing properties of the laser beam could also provide some beam forming that further enhances the amplitude of the detected waves. In particular a line focus encourages propagation perpendicular to the axis along which the line focus is generated and where the modified Mach-Zehnder interferometer sensing beam spot is focused. The directionality of the line-source with plane waveforms generated parallel to the line decreases the spreading attenuation in comparison with an omnidirectional circular spot source.

A commercial Brilliant B series high power, solid state Nd:YAG Q-switched laser, manufactured by Quantel was used. This compact laser is constituted of three main parts as shown in fig. 6.3; the laser head, the cooling, power supply and control unit box and a remote control device for remote operation. This laser also allows external full control capabilities through RS232 interface, being of great advantage for the automatic operation of the monitoring application.

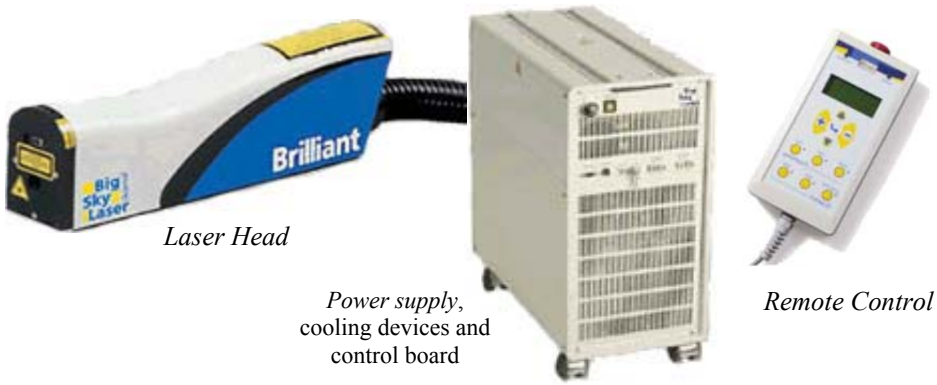

Figure 6.3: Brilliant B (Quantel) Q-switch Nd:YAG high power laser components.

The Brilliant B laser is capable of delivering a maximum pulse energy of 850 *mJoules* at 1064 *nm* wavelength, in a pulse width duration of ~ 5 *nsec* and pulse repetition rate of 10 *Hz*. This provides a peak power of 160 *MWatt* and an average power of 8.5 *Watt*. The unfocused beam spot diameter is ~ 7 *mm*, however a cylindrical lens is used in order to focus the beam into a line-source 7 *mm* long and 1 *mm* width.

The energy per pulse can be controlled by varying the delay between the activation of the flash lamp and the Q-switching. We have measured with a *Gentec EO* power meter the average power delivered as a function of this delay and the results are plotted in fig. 6.4. Notice that the maximum power is not reached when the delay is zero but for this particular laser it occurs at ~ 275 *μsec*. This is due to the time required after the gain medium is pumped with the flash lamp, in order to reach the maximum attainable population inversion and to avoid prelasing undesirable effect that would destabilize the laser pulse beam profile.

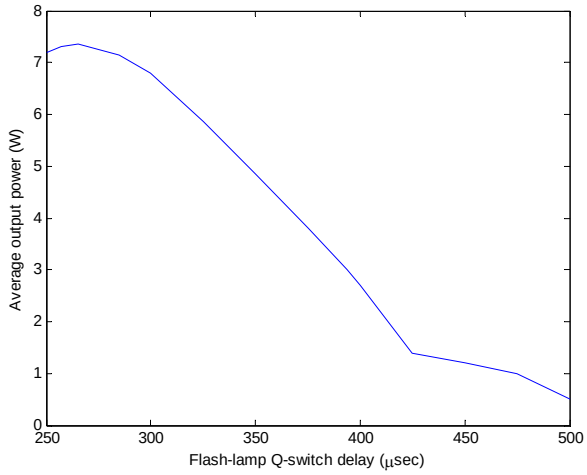

Figure 6.4: Experimentally measured relationship between the Brilliant B Q-switched laser source average output power and the delay between the activation of the flash-lamp and the Q-switching.

Even for the lowest provided average power of 0.3 *Watt* (for a delay of 500 *μsec*), which corresponds to a pulse energy of 30 *mJ*, and a peak power of 5.8 *MW*att, the power density after focused into a line-source is 82.4 $MWcm^{-2}$ considerably exceeding the ablation threshold for aluminium (10 $MWcm^{-2}$). Hence all the experimental work has been done in the ablation regime, and in order to minimize surface damage of the sample a delay close to the maximum value of 500 *μsec* was always chosen.

6.2.2 Surface displacement modified Mach-Zehnder optical fibre interferometer

The optical system used for broadband and remote ultrasonic detection was fully described previously; the system working principles and the function of its different components was fully treated in Chapter 2, meanwhile Chapter 3 offered the parameters characterization of the used components.

6.2.3 Laser source beam pulse steering, positioning and confinement element

Despite the compact dimensions of the Brilliant B high power laser, its 7 *kg* and 57.5 *cm* long head make of it difficult to move for an accurately directionality of its output beam towards the desired target. A more satisfactory approach is to steer the beam by a mirror properly coated for the laser wavelength and peak powers. The hazardous operability of such powerful beam also requires the development of an articulated cage that not only confines the beam but also allows its free and highly accurate steering for the present application.

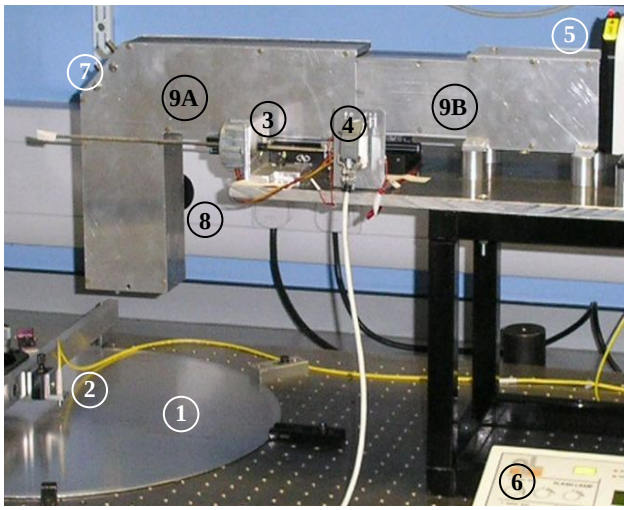

Figure 6.5: Source beam pulse steering and confinement arm: 1) Aluminium sample plate, 2) GRIN lens of the interferometer sensing arm, 3) Stepper motor, 4) motor connection to the programmable control board, 5) Q-switched laser head and 6) remote control, 7) laser beam steering mirror orientation screws, 8) cylindrical lens focusing screw, 9A and 9B) Laser beam enclosing cage.

Such device has been designed and created during the present thesis and it is shown in fig. 6.5. The confinement cage consists of two hollow components; one component, identified as 9B, is a straight long tube fixed into the table that holds the laser head just touching the side from where the beam exits it. The second component, identified as 9A, is an elbow shaped tube that is hold from one side of the elbow to a moving platform fixed into the same table that holds the laser head. This component has a bigger diameter than the former and as it moves towards or from the laser head it allows the straight fixed tube (9B) to slide inside decreasing or increasing respectively the length of the beam confining space as the elbow is moved. The curved region of the elbow tube has an steering mirror fixed to its inside wall and it can be orientated with two degrees of freedom by two steering screws from outside the tube (labelled as 7 in fig. 6.5). At the end of the vertical part of the elbow shaped tube a cylindrical lens is attached into a vertically moving structure displaced by a wheel outside the tube (labelled as 8) in order to focus the line-source into the surface of the sample plate.

This configuration allows the delivery of the laser beam to a horizontal plate placed over an optical table, for an easier and more stable experimental condition.

The high accuracy for the laser beam positioning, within a fraction of a millimetre, is achieved by having the moving platform, over which is fixed the horizontal part of the elbow tube, moved by a digital linear actuator DLA (labelled as 3 in previous figure). The DLA is based on a four phase permanent magnet stepper motor and utilises a rotor with an internal thread to provide linear motion via a leadscrew. In particular a McLennan L92211 series DLA was used, capable of providing a maximum linear force of 21 *N* and a linear distance travelled per step of 0.0254 *mm*. The length of the used leadscrew allowed a maximum linear displacement of 21.5 *cm*. The motor was connected via a RS232 serial link to a bipolar stepper motor drive board controlled by a programmable control board designed to control one or two stepper motors, thus allowing a two dimensional positioning of the line-source over the sample surface. However in our experiments only one motor was used because a linear displacement of the source was enough. The drive and control boards together with the adequate power supply were assembled in a box for portability (labelled 7 in fig. 6.2).

6.2.4 Automatic remote operation potential of the inspection tool

We want to highlight the remarkable potential of the automatic operation of the developed monitoring tool. Starting from the Q-switched laser source that can be fully operated by RS232 interface, and continuing with the remotely controlled positioning of the laser beam by a similar interface. In addition, the ultrasonic signal detected by the modified Mach-Zehnder interferometer is acquired by a TDS3014 Tektronix digital oscilloscope remotely connected to a computer through an Ethernet link and fully controlled by the WaveStar software. The connection of all the components to a single processing unit (labelled 1 in fig. 6.2) and remote operation was tested and validated during our experiments. However not yet a full automation of the ultrasonic generation and data acquisition process has been achieved. Mainly because of the high magnitude of unpredictable perturbations that surrounds the experimental environment (such as underground circulation near to the lab, or nearby door slams). These high magnitude perturbations overrun the range of operation of the interferometric control loop so under these circumstances the interferometer becomes unstable and the detected data perturbed. A future improvement for the automation monitoring tool would consist in developing a program that would look to the interferometer low frequency signal, identifying these cases and hold the automatic data acquisition until the interferometer stabilizes back again.

6.3 ULTRASONIC DATA OBTAINED BY EXPERIMENTAL APPLICATION OF THE INSPECTION TOOL

Most of the experiments here presented were made over aluminium plates of square and circular shapes and 1.18 *mm* thickness. Aluminium is a low cost, isotropic material with low attenuation and enough stiffness as to generate good detectable amplitude ultrasonic waves at long distances. The small thickness allows studying the small ultrasonic Lamb wavelengths that the broadband optical excitation provides (as explained in Appendix A only Lamb waves with wavelengths of the order of the plate thickness or bigger may propagate). In this section we look into the ultrasonic waveforms experimentally obtained with this inspection tool and identify ways of improving them for later processing in order to extract the materials dispersion curves.

In all experiments the aluminium plate sample was rested on an optical table in order to minimize the low frequency environmental noise (for instance, people walking around the sample). We have always avoided physical contact between the metallic surface of sample and table, so that the propagating ultrasound would not be affected by leakage to the optical table or even presence of other type of ultrasonic waves, such us surface waves in the optical table or interface Stoneley waves (as described in Appendix A).

The quality of the ultrasonic signals obtained very much depended on the adequate operation of the modified Mach-Zehnder interferometric system. Where first a proper bonding of the reflective film was required followed by an accurate alignment of the interferometric sensing arm's GRIN lens. Later we feed the interferometric optical phase modulator with a low frequency electric signal and optimized the polarization controller and variable optical attenuator of its reference arm in order to set up its operation point to deliver maximum fringe visibility. Once this was done, the input to the PZT phase modulator was substituted by the output of the low frequency feedback controller, which keeps the interferometer working in the optimum operation point, compensating the low frequency environmental perturbations. The ultrasonic data was then provided by the output of the HF photodetector which was fed to a digital oscilloscope and averaged in order to improve the data signal to noise ratio.

Figure 6.6–*left* shows the first of the experimental ultrasonic data obtained (top) together with the low frequency feedback control signal (bottom). The ultrasound was generated with a flash lamp:Q-switch delay of 375 μsec, corresponding to an average optical power of around 4 W (as shown in fig. 6.4). The power to the sample from the interferometric GRIN lens was 1.7 mW. The signals have been averaged 64 times as they provide good enough

signal to noise ratios without compromising the time length required to measure the ultrasound if a higher averaging would had been chosen.

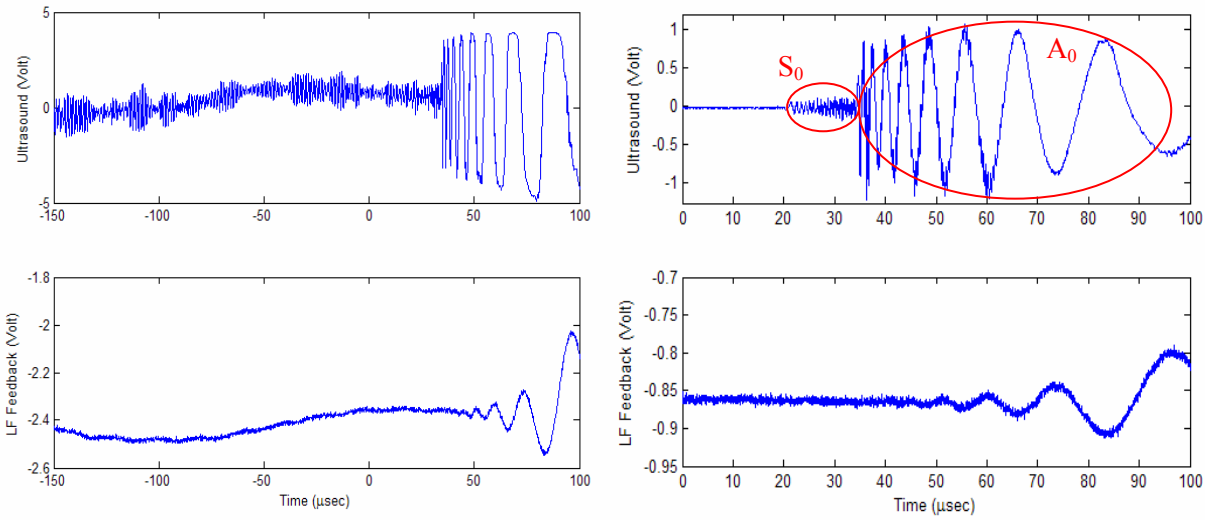

Figure 6.6: Typical detected ultrasonic waveforms in aluminium (*top*) and interferometric LF feedback control signal (*bottom*): (*Left*) Optical source of average pulse power 4 *W* and interferometric laser power to sample of 1.7 *mW*, 1*MΩ* coupling oscilloscope:HF photodetector. (*Right*) Average pulse power of 1.2 *W* and interferometric laser power to sample of 1 *mW*, 50*Ω* coupling oscilloscope:HF photodetector and 15 *MHz* low pass filter of the signal.

The first noticeable characteristic of this signal is the presence of saturation, due to the fact that the HF photodetector saturates for input optical powers around 1 *mW* giving a maximum optical peak to peak voltage of 8 *V* (as it is the case in this saturation). The reason for the saturation may be double, from one side the optical power source is too high generating high amplitude ultrasonic waves and in the other hand the interferometric laser input power is also too high. The presence of ultrasonic information before the trigger time reference (0 *sec*) shows that effectively the excited ultrasonic waves are of high amplitude, as they have not yet be totally attenuated between consecutive laser pulses (pulse rate 10 *Hz*). Part of this information contains also low frequency oscillation noise of high amplitude as well as high frequency noise. Additionally the HF photodetector should be coupled to the oscilloscope at 50 *Ω* for impedance matching purposes, but in the previous experiments it was coupled at 1 *M Ω* in order to avoid the high pass filtering effect that the oscilloscope add when dealing with an AC input signal.

After careful manipulation of these parameters a much improved ultrasonic signal was obtained (fig. 6.6–*right*). The flash lamp:Q-switch delay was now chosen to be 450 *µsec* (or equivalently an average pulse power of 1.2 *W*) and the power to the sample from the interferometric GRIN lens was almost half (~ 0.1 *mW*). This seems to fix the saturation

problem and allows the ultrasonic waves to attenuate between pulses. Later an RF low pass filter at 15 *MHz* was added to the output of the HF photodetector, which reduced enormously the high frequency noise. The 50 *Ω* coupling of the HF photodetector to the oscilloscope not only improved the signal to noise ratio, but additionally the high pass filter (with cut-off frequency at 200 *kHz*) introduced by the oscilloscope improved the contrast of the high order modes of higher frequency and small amplitude. Due to the attenuation suffered by the very large, low frequency A_0 and S_0 mode components, typical of the ultrasonic signals generated with ultrasonic sources with main component normal to the plate's surface [2].

The improved ultrasonic waveform of fig. 6.6–*right* clearly shows some signatures; it appears dominated by the S_0 and A_0 modes (circled in red), modulated by high frequency components of smaller amplitude, corresponding to high order symmetric and antisymmetric modes. It is noticeable the pronounced dispersion of the A_0 mode, meanwhile the S_0 mode propagate non-dispersively. The much higher amplitude of the A_0 region is due to its more dominant out-of-plane displacement characteristics in comparison with the S_0 mode at the low frequency:thickness product associated (below 2 *MHz*).

Another improvement of the ultrasonic signal was achieved when the source beam pulse was focused into a region where previous long period repeated ablation had caused a line hole through the aluminium plate. Only in this case was it possible to get an ultrasonic signal as that shown in figure 6.7-*left*, where the S_0 mode amplitude is increased, meanwhile the A_0 mode amplitude decreases, allowing a better detection of the modulating high order modes.

Our interpretation of this improved signal is as follow. When the laser beam is focused to the surface of the plate where the hole is present, the beam ablates the hole's lateral surfaces, as shown in fig. 6.7-*right*, generating reactive forces with a big component parallel to the surface of the plate. In fact this force component may be bigger than the reaction component normal to the plate's surface. Because the energy of the beam pulse is same as in previous cases, then by conservation of energy, the new ultrasonic source has a higher in-plane ultrasonic component coupling efficiency and a worse out-of-plane coupling efficiency than before. Since the relationship between out-of-plane and in-plane displacement for each modes in a given depth is constant then by improving the in-plane displacement component of the S_0 mode, also its out-of-plane displacement is considerably increased. In the other hand, the A_0 mode which has mainly an out-of-plane displacement component will be attenuated because the out-of-plane coupling efficiency of the source has decreased. This interpretation has been verified in the ANSYS model presented in the next section. Where the ultrasonic wave generation and propagation characteristics of a source similar to those

described has been simulated in a plate-like structure. We will see that when the simulated ultrasonic source has only a normal to the sample's surface reaction then the ultrasonic wave simulated has the same characteristics of that shown in fig. 6.6–*right*, however when a noticeable in-plane displacement component is added to the ultrasonic source, then the ultrasonic waveform acquires the characteristics of the one presented in fig. 6.7-*left*.

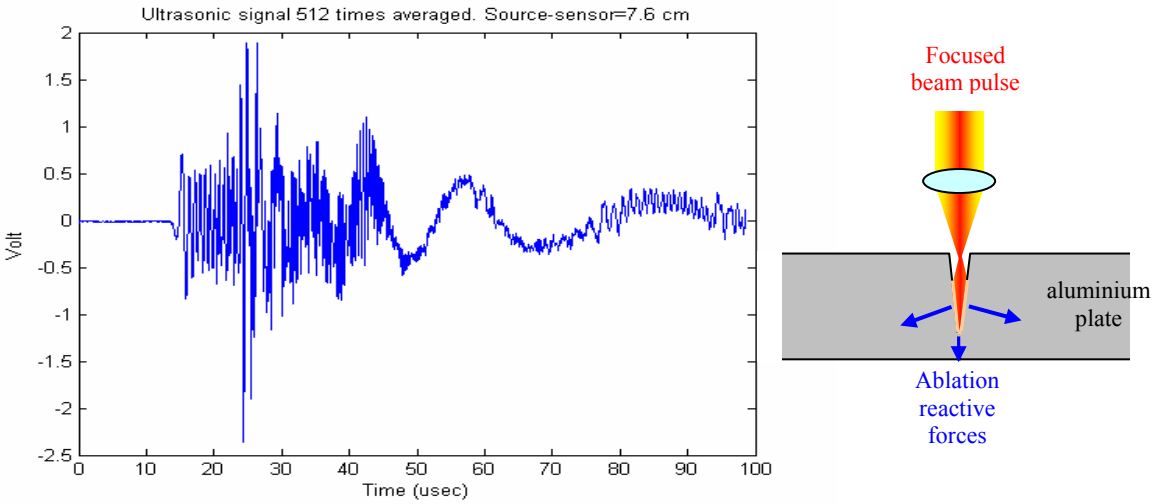

Figure 6.7: (*Left*) Improved ultrasonic signal with a high S_0 mode component and an attenuated A_0 mode, the modulating high order modes are now more apparent. (*Right*) Diagram for the interpretation of the improved ultrasonic signal in the left.

The later improved ultrasonic signal can not be used for NDT analysis in the experimental conditions in which it was obtained here, because it implies a serious damage of the sample under test. Nevertheless, the properties associated to the ultrasonic source capable of generating ultrasonic signals with improved S_0 mode component and weakened A_0 mode component, is nothing else than having a considerable in-plane reaction component. We saw in Chapter 2 that the thermoelastic regime provides precisely this characteristic. Unfortunately at the time at which these experiments were developed we did not have the capabilities of exciting such a source with good enough ultrasonic wave amplitude at the distances source:sensor involved.

6.4 FINITE ELEMENT MODELING OF ELASTIC WAVES PROPAGATION IN A PLATE

Before dealing with the experimental complexities of the previously presented monitoring tool, and due to the geometrical simplicity of the plate-like structures. We considered it advantageous to start by simulating the propagation characteristics of the ultrasonic waves under similar generation and detection conditions as those in the experimental tool. This

simulation is developed using the ANSYS commercial finite element (FE) software following ideas presented in [3]. The results of the simulation will give us an idea of the expected experimental data and validity of the processing methods, ruling out the effect of experimental perturbations.

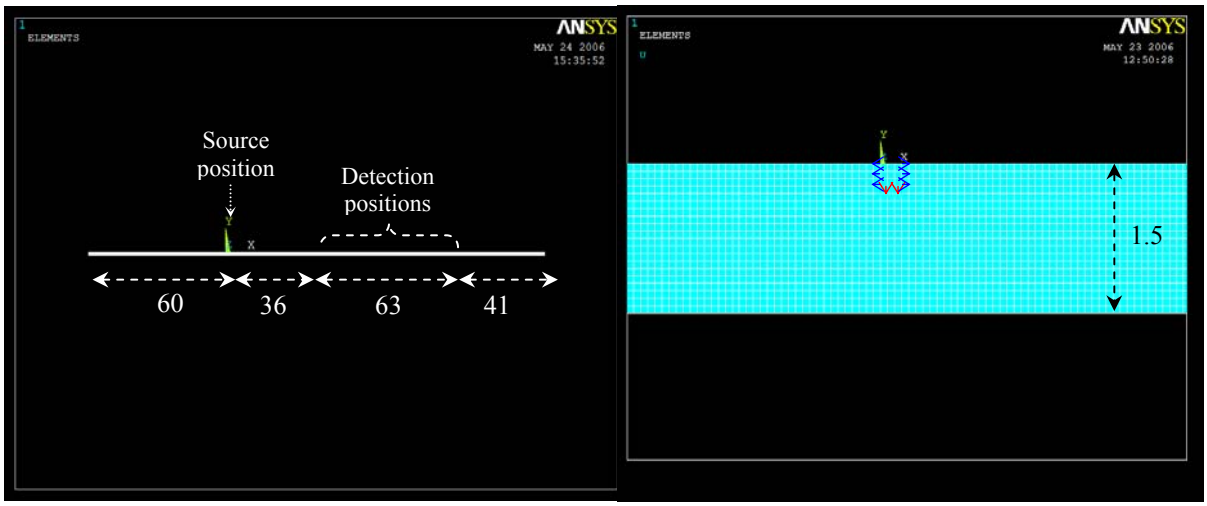

Figure 6.8: ANSYS model of a 2D aluminium plate with all the dimensions given in mm. (Left) Plate lateral view showing the position of the ultrasonic sources and detectors. (Right) Zoom where the sources are located. Additionally the mesh of the model is appreciated.

The plate-like structure was modelled as a 2D rectangle of 1.5 *mm* thickness and 20 *cm* long. The coordinates were chosen; *Y*-dimension as out-of-plane coordinate and *X*-dimension for the in-plane coordinate (as shown in fig. 6.8-*right*). Notice that the plate geometrical model does not include the third dimension *Z* for simplification purposes. The analytical equation of motion of Lamb waves, in which it is based the theoretically obtained dispersion curves, is obtained in Appendix A under the conditions of plane wave propagating ultrasound. Hence we have chosen the particle movement of the plane waves to be restricted to the *X*-*Y* plain, so that the *Z*-dimension is not relevant. This situation very much resemble our experiments, because the ultrasonic source is a line-source perpendicular to the ultrasonic detection points situated within a line perpendicular to the source line and intersecting it in its centre. Notice that the accuracy of the Rayleigh-Lamb wave equation of motion very much depends in the satisfaction of the infinite plate condition. Thus although our model is finite in dimensions we have made it long enough and positioned source and sensors far from the lateral borders (see fig. 6.8-*left*) of the plate to avoid reflections, but always under the limitation that higher dimension implies higher computational power for the simulation.

The structures material properties were those for aluminium; $E = 70.7584\ GPa$, $\nu = 0.3375$, $\rho = 2.7\ gr/cm^3$.

The structure was meshed using a *PLANE42* element type as shown in fig. 6.8-*right*, defined by four nodes with two degrees of freedom at each node; translations *UX* and *UY* in the (nodal) *X* and *Y*-directions. The element length is an important parameter to define, it should be small enough so that the model is able to accurately represent the short wavelengths of the broadband optically generated ultrasounds. With the drawback that a too small length would imply a larger number of elements in the mesh of the structure, thus a larger system of differential equations to be resolved and processing time and power required. In [4] is recommended to use more than 10 nodes per smallest wavelength, however in [3] it is shown that this limitation is not so critical. In our model we have taken an element length of 0.1 *mm* as the best compromise for the smallest wavelengths on the order of 1 *mm* to be expected.

The ultrasonic driving mechanism is simulated as a vertical pulse displacement applied to a few nodes in the source position as shown by the red arrows in fig. 6.8-*right*. This source very much resembles the experimentally applied optical generation in the ablation regime (as described in Chapter 2). Figure 6.9 shows the time function profile of the driving pulse displacements. The shape of this pulse has no practical purpose, apart of being able of exciting ultrasonic waves of broad frequency spectrum components, in this case from DC to a few tends of *MHz*. The temporal resolution or integration time step Δt of the finite element analysis is another critical parameter for the correct simulation of the transitory behaviour. Thus the accuracy of the solution is increased by using increasingly smaller time steps, with the disadvantage that too small values would increase enormously the processing time of the simulation. For the *Newmark* time integration scheme used in our ANSYS analysis a good compromise is achieved if the time step satisfies eqn. 6.1 [5].

$$\Delta t < \frac{1}{20 \cdot f_{\max}} \tag{6.1}$$

Satisfying the condition in previous equation for the time step would imply that in order to accurately resolve frequencies on the order of 10 *MHz* we would need a time step smaller than 5 *nsec*. For the model here presented of a rectangle of the 200 x 1.5 mm^2 and meshing element length of 0.1 *mm*, the number of elements required is 30000, with 2 degrees of freedom each so the differential equation matrix to be solve has 60000 elements. In addition, this equation has to be solved for each time step, which for the distances source:sensors considered in our model (to be in far field) a simulating time of 40 μsec would require 8000 solution steps to be calculated. This simulation would require a very high processing time and power, which we do not consider to be necessary for the purpose of the basic verification here intended. Hence a Δt = 18 *nsec* has been assumed to be a good enough compromise.

The excited ultrasonic waves are detected by measuring the vertical displacement component of point nodes in the surface of the plate far enough from the source as to be in the far field being 36 *mm* in this case (as shown in fig. 6.8-*left*). This resembles the operation of the modified Mach-Zehnder interferometer used in our experiments.

Figure 6.9: Time profile of the vertical displacement applied over the source nodes in the direction shown by the red arrows in fig. 6.8-*right*.

The propagation dispersive characteristic of the generated ultrasound is extracted by the 2D-FT technique presented in Chapter 5. The spatial scanning required to generate the data used by this processing technique can be realised through moving either the source or the detector by equally spaced distances Δx. In the ANSYS model we chose to move the detection position.

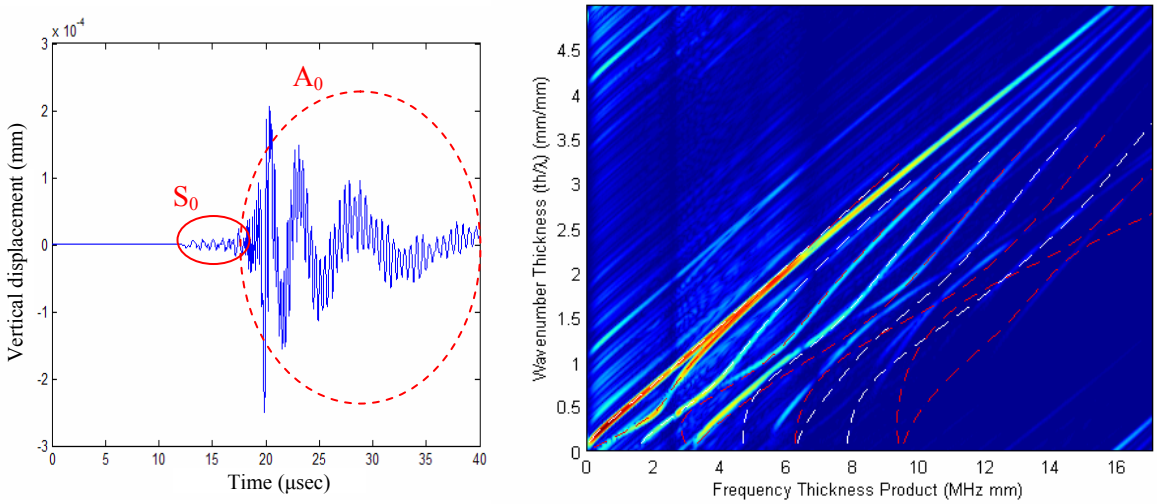

Figure 6.10: (*Left*) Typical vertical displacement in the surface of the plate for the propagating ultrasonic in the ANSYS simulation (for a distance source:sensor of 68 *mm*). Red circled are the dominating S_0 and A_0 modes at low frequency values. (*Right*) Wavenumber domain dispersion curves obtained by 2D-FT analysis over a set of detection positions equally spaced (0.3 *mm*) on the ANSYS model. Red light colour for the highest spectra values and dark blue for the lowest. The spectral amplitude is given in logarithmic scale. Superimposed in dashed lines are the theoretical dispersion curves (white for symmetric modes and red for antisymmetric ones).

A typical detected ultrasonic signal is presented in fig. 6.10-*left*. The similarity of this signal with the experimentally obtained ones (fig. 6.6–*right*) in previous section is evident. Again it appears dominated by the S_0 and A_0 modes, with the latter much bigger than the former, modulated by high frequency components of smaller amplitude, corresponding to high order symmetric and antisymmetric modes.

Figure 6.10-*right* shows the wavenumber domain phase velocity dispersion curves obtained with the 2D-FT processing of the set of vertical displacement data (similar to that in 6.10-*left*) obtained at equally spaced positions in the surface of the plate. It is clearly shown that only certain wavenumber:frequency combinations have considerable amplitude values (notice that the colour is plotted based in a logarithmic scale of the 2D-FT magnitude values, with red representing the highest values and dark blue the lowest). In dashed white and red lines we have superimposed the theoretically predicted dispersion curves obtained with the MATLAB program by me developed that solves the highly unstable and non-linear Rayleigh-Lamb wave equations. In most of the plotted region the agreement between theoretical model and ANSYS simulated model is considerable.

We may notice that at high normalized wavenumber values (over 3 *mm/mm*) a noticeable disagreement is appreciable. This is obviously due to the limitations of the model's mesh elements finite length. In the other hand we notice that for frequency:thickness products above 4 *MHz mm* the agreement is quite bad at low wavenumber values, but not at high values. This means that the restriction of the time steps given by eqn. 6.1 is not that critical, however what really limits the time step values is that this must be smaller than the time taken by the fastest possible wave to propagate between successive nodes in the mesh. The dispersion curves region in the bottom right corner of fig. 6.10-*right* (high frequencies and high wavenumbers) is associated to the fastest phase velocity values and so they are not very well simulated, hence the bad agreement. In the other hand the top right corner of the curves even though it is associated to small wavelengths and high frequencies, above the limitations of the elements size and time step chosen for the simulation, it agrees perfectly with the theory because they have associated very small phase velocities.

Finally, we have used the ANSYS model also to validate the previous interpretation of the improved experimental ultrasonic data seen in fig. 6.7-*left*. For this we have added in-plane displacement components into the ultrasonic source (shown by blue horizontal arrows pointing in both directions in fig. 6.8-*right*). The time profile of the horizontal displacement sources is identical to the vertical ones presented in fig. 6.9. The detected ultrasonic waveform's vertical displacement at the same distance source:sensor to that of fig. 6.10-*left*

is shown in fig. 6.11. We see the similar characteristics of the improved experimental ultrasonic waveform of previous section, where the S_0 mode component has increased amplitude considerably to a similar magnitude of that of the A_0 mode component. The high order mode signals appear now clearer, modulating both the S_0 and A_0 mode components. This simulation confirms that effectively ultrasonic sources with considerable in-plane component reaction, improves the generated ultrasonic data.

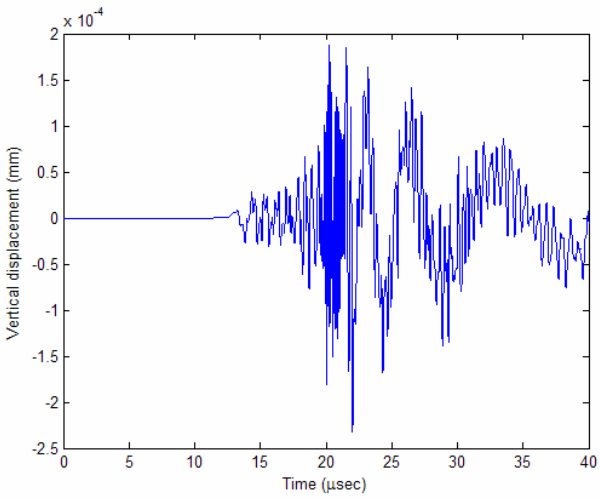

Figure 6.11: Improved ultrasonic signal by adding in-plane displacement components in the ultrasonic source for the ANSYS simulation, like in fig. 6.10-*left* the distance source:sensor is 68 *mm*.

As we will see later, the results of the 2D-FT dispersion curves for the FE model presents multiple similitudes with the experimentally obtained ones. For instance, the presence of same gaps in the magnitude of various modes dispersion curves, and the vertically reproduction of the high magnitude A_0 and S_0 modes. The fact that these effects are common for both the experiments and the simulation, warranties that they are specific of the waves propagation characteristics or of the data processing technique and not due to experimental limitations or perturbations. We will see more about this in the next section.

The present results clearly illustrate the effectiveness of using FE analysis for modelling ultrasonic wave propagation characteristics. Although here it has only been applied to very simple plate-like structures however it gives an idea of the potential of this technique to simulate more complex structural geometries for which analytical solution of the equation of motion may not exist (for instance modified ring structures as studied in [3]) or it may be difficult to obtain (for instance anisotropic materials). The FE method can potentially provide a solution for any given geometry, as long as the geometry and its boundary conditions can be modelled [3].

6.5 EXPERIMENTAL EXTRACTION OF THE DISPERSION CURVES

In this section we apply the two signal processing techniques described in Chapter 5 to the set of ultrasonic waveforms rich in spatial and temporal spectrum information obtained with the all-optical, non-contact inspection tool developed. This gives us the ultrasonic Lamb waves dispersion propagation characteristics for aluminium plate-like samples. Meanwhile the 2D-FT provides the dispersion information as phase velocity dispersion curves in a wavenumber - frequency:thickness product domain, the time-frequency analysis provides the same information as group velocity dispersion curves. However the two approaches have radically different properties and applications. We show later that the dispersion curves obtained by the time-frequency analysis are sensitive to the properties of the material path between source and detector. In contrast, the dispersion curves obtained with the 2D-FT are sensitive to the properties of the material between the minimum and maximum separations of the source and the detector.

6.5.1 Two-dimensional Fourier transform (2D-FT): Phase velocity dispersion curves

The two dimensional discrete Fourier transform operating in both space and time domains requires of two dimensional ultrasonic data periodically sampled both in time and space. The time domain sampling is done by the A/D conversion of the digital oscilloscope to which the output of the interferometer's HF photodetector is connected. The spatial domain periodic sampling is achieved by detecting a multiplicity of surface displacement measurements corresponding to source:sensor separations incremented through a constant interval Δx up to a total length L. The value of L determines the minimum spatial frequency (or wavenumber) increment which can be resolved in the transformed data whilst the increment Δx determines maximum spatial frequency which can be resolved (or minimum ultrasonic wavelength).

The increment in the source:sensor separation can be done by moving either the detection point for a fixed source location (as we did in the ANSYS model simulation), or by moving the ultrasonic source, keeping the position of the detection optics fixed. In the diagram of the experimental arrangement shown in fig. 6.1, we see that the later is the realisation approach chosen here. Because the line-focused laser source does not require the precise focusing stability of the interferometric detection beam. The laser source is periodically shifted by the action of a motor, as it moves the beam confinement arm that includes in its farther end the beam's steering mirror and the cylindrical lens (as described in fig. 6.5).

The two dimensional discrete ultrasonic data obtained experimentally, is represented by a matrix $U[m,n]$ of dimensions M x N (as shown in eqn. 6.2), where N is the number of time

samples taken for each ultrasonic waveform and M the number of ultrasonic waveforms measured (one for each position of the source).

$$\begin{array}{c} t \longrightarrow \\ x \downarrow \end{array} \begin{pmatrix} u_{11} & u_{12} & u_{13} & * & * & * & u_{1N} \\ u_{21} & u_{22} & u_{23} & * & * & * & u_{2N} \\ * & * & * & * & * & * & * \\ * & * & * & * & * & * & * \\ * & * & * & * & * & * & * \\ u_{M1} & u_{M2} & u_{M3} & * & * & * & u_{MN} \end{pmatrix} \tag{6.2}$$

The discrete 2D-FT algorithm applied over the data matrix considers the top left corner as the origin for both space and time dimensions. Thus the time domain is considered increasing from left to right and the space domain from top to bottom. The time domain consideration corresponds to the experimental propagation time, with higher time corresponding with longer ultrasonic wave propagation duration. In the other hand, the rows in the matrix are filled by the data associated to the closest distance source:sensor in the top and with the farthest distance in the bottom, which means that the x dimension of the 2D-FT corresponds to the magnitude distance source:sensor, such that increasing distance is defined as positive x domain direction.

We saw in Chapter 5 that the 2D-FT converts the 2D continuous ultrasonic data into a combination of complex exponential functions $e^{-i2\pi(kx+ft)}$ and that the associated spectra is divided into four redundant sections as shown in fig. 6.12-*left*. The dark quadrants providing identical spectra information and being associated to exponentials of the type $e^{-i2\pi(|k|x-|f|t)}$ and with the light coloured quadrants providing complimentary spectra information but identical information between themselves, being associated to exponentials of the type $e^{-i2\pi(|k|x+|f|t)}$. Therefore, from the four quadrants only two (one dark and one light coloured) contain all the necessary spectra information. Opposite to what happens in 1D-FT, where not all the domain of definition has physical meaning (this is the case of the spectra associated to negative frequency values), in 2D-FT every section of the domain of definition is associated to single frequency waves propagating in a particular direction. This physical meaning is even more relevant when as in the present case the 2D-FT is applied to propagating ultrasonic wave data. Thus based in the previous definition of the experimental coordinates x and t, the 2D-FT domain of definition associated to the exponential type $e^{-i2\pi(|k|x-|f|t)}$ represents waves that take a longer propagation time for an increasing distance source:sensor, this is the case of incident waves propagating directly from source to sensor,

and of waves that reflect in the border of the plate at the other side of the sensor, point *A* in fig. 6.1. In the other hand the domain associated to the exponential type $e^{-i2\pi(|k|x+|f|t)}$ represents waves for which the propagation time decreases for increasing distance source:sensor. This is the case of waves reflected at the border in the same side of the sources, point *B* in fig. 6.1.

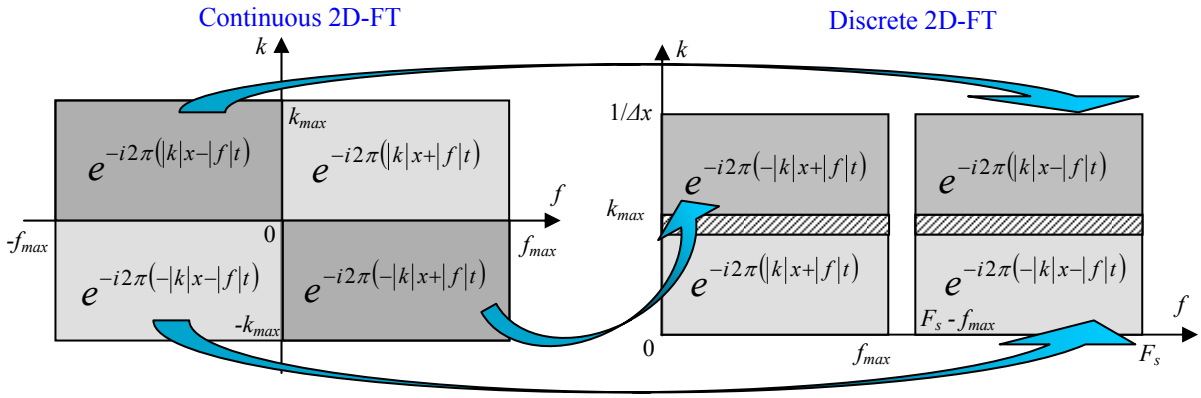

Figure 6.12: Conversion of the domain of definition for the continuous (*left*) 2D-FT to the discrete (*right*) 2D-FT and their associated complex exponential type.

When the 2D-FT is discretized, the domain of definition of the continuous 2D-FT is infinitely reproduced in both dimensions (frequency and wavenumber) with the centre situated at each multiple combination of $1/T_s$ and $1/\Delta x$, as described in Chapter 5. In fig. 6.12 we show this conversion concentrating only on the positive low frequency and low wavenumber values domain of definition of the discrete 2D-FT. Remember that all the spectra information of the 2D-FT is stored in the combination of just one dark and one light coloured quadrants, thus in order to extract the full propagating waves dispersion information on the discrete 2D-FT we only need to look at positive frequency values until the maximum excited ultrasonic frequency f_{max} and at positive wavenumber values until $1/\Delta x$. The quadrant at low wavenumber values is associated to waves reflected in point B in fig. 6.1 (called *reflected waves quadrant* from now on), meanwhile the quadrant at high wavenumber values is associated to incident waves directly from source to sensor or reflected in point A in fig. 6.1 (called *incident waves quadrant*).

The discrete 2D-FT part of fig. 6.12 also shows a common phenomena in our experimental dispersion curves. This is the presence of spatial aliasing shown as dashed intersection of dark and light coloured quadrants in the region where $k = 1/2\Delta x$. However no temporal aliasing occurs because the sampling frequency of 100 *MHz* is much higher than double the maximum detected ultrasonic frequency, given by the 15 *MHz* low pass filter applied. We already explained in Chapter 5 that the spatial aliasing occurring in the 2D-FT does not have

such damaging effects as when it happens in 1D-FT, and as we will see in the next sections most of the dispersion information of this intersection region can accurately be extracted.

Example of the simulated operation of the 2D-FT technique

In order to understand how the 2D-FT applied to a set of ultrasonic data (as previously described) can provide the phase velocity information of the propagating ultrasound, we start here with a simplified set of 'ultrasonic' data. These 'ultrasonic' waveforms are considered to be non-dispersive and single mode. Let us define the continuous waveform associated to the closest distance source:sensor as *u(t)*, and for all the set of data we consider the time interval of definition being long enough as to have all the ultrasonic information included, even at the farthest distance source:sensor (as shown in fig. 6.13-*left* for a simulated ultrasound given by several cycles toneburst). In this case the time waveforms for the different distances source:sensor can be given as a time delay of *u(t)*, so that the waveform at *n-th* source would be given by: $u_n(t) = u(t-t_n)$, where $t_n = n \cdot \Delta x / c_{ph}$ is the time delay respect to the closest source to the sensor. Δx is the distance between sources and c_{ph} is the phase velocity of the propagating non-dispersive 'ultrasound'.

If we call *U(f)* the time Fourier transform of *u(t)*, then by the Fourier transform properties of a time delayed signal we get that the time Fourier transform of $u_n(t)$ is given by:

$$F_t[u(t-t_n)] = U(f) \cdot e^{-i2\pi f t_n} = U(f) \cdot e^{-i2\pi f n \Delta x / c_{ph}} \tag{6.3}$$

The absolute value of the temporal Fourier transform for all the set of data is the same $|F[u(t-t_n)]| = |U(f)|$, thus independent of the position of the sources. The phase velocity information as shown in eqn. 6.3 is stored in the phase of the temporal Fourier transform, this is why a second 1D Fourier transform, in the displacement domain *x*, is needed in order to extract it. As mentioned in Chapter 5, a 2D-FT can be implemented by calculating the two successive one dimensional transforms. Thus the spatial domain Fourier transform is applied over the time domain Fourier transform for each frequency component. In eqn. 6.4 the spatial Fourier transform is applied over the time Fourier transform at the frequency f_0 and a continuous source distribution has been considered.

$$F_x[U(f_0) \cdot e^{-i2\pi f_0 x / c_{ph}}] = \int_{-\infty}^{\infty} U(f_0) \cdot e^{-i2\pi f_0 x / c_{ph}} \cdot e^{-i2\pi k x} dx = U(f_0) \int_{-\infty}^{\infty} e^{-i2\pi x \left(\frac{f_0}{c_{ph}} + k\right)} dx = U(f_0) \cdot \delta(f_0 / c_{ph} + k) \tag{6.4}$$

Where $\delta(f_0 / c_{ph} + k)$ is a Dirac Delta function, being 0 for all values of $k \neq - f_0 / c_{ph}$ and being equal to 1 when the wavenumber $k = - f_0 / c_{ph}$. Hence the 2D-FT applied to the non-dispersive, single mode set of data here described, is only different from zero at the frequency:wavenumber combinations that satisfy $k = - f / c_{ph}$, which in the frequency :

wavenumber domain corresponds to a line with negative slope equal to $-1/c_{ph}$ and defined in the quadrant of negative wavenumber values.

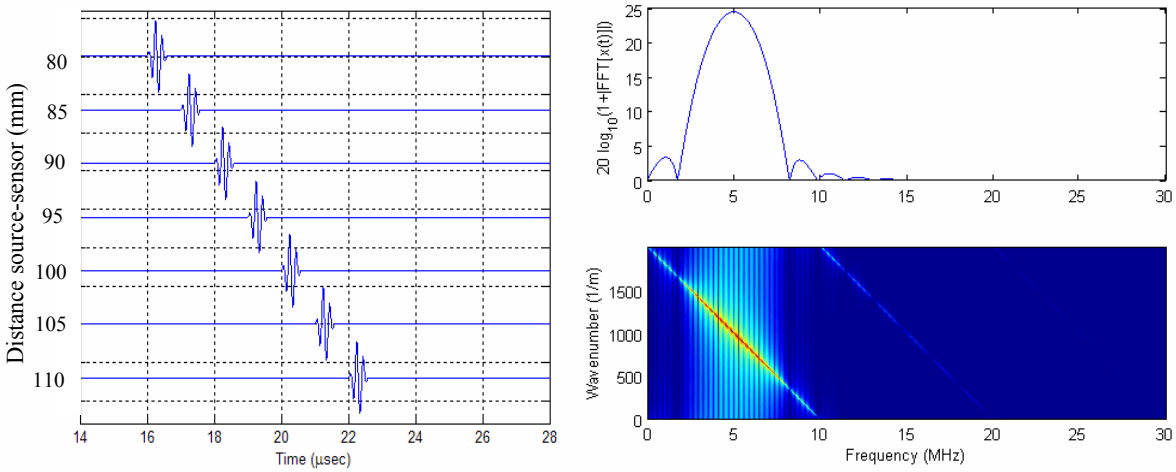

Figure 6.13: (*Left*) Set of time data for the simulated 2D-FT application. The 'ultrasound' is considered a several cycles toneburst non-dispersive and single mode. (*Right*) Modulus of the time Fourier transform of the toneburst signals (*top*), and 2D-FT spectrum of the set of data (*bottom*).

We already described in Chapter 5 that the region of negative wavenumber and positive frequency is associated to waves propagating toward increasing values of the *x* dimension (or distance source:sensor), and this is the condition imposed previously in the current set of data when we decided that as the distance source:sensor increases also the time delay increases. If the position of the sources is discrete then spatial leakage takes place, so that the dispersion curve line appears broadened in the wavenumber domain direction as shown in bottom of fig. 6.13-*right*, due to the discontinuity in the spatial domain data. No temporal leakage is shown in previous figure, because the propagating 'ultrasound' is a time windowed toneburst so no discontinuity appears in the periodic extension associated to the time domain DFT (as described in Appendix E). Notice the presence of spatial aliasing in this figure for frequencies over 10 *MHz*, and the negative slope of the line as predicted. The wavenumber values (vertical axis) are not negative because this plot is obtained for a discrete 2D-FT where the spectrum associated to negative wavenumbers is reproduced at positive wavenumber values below the inverse of the spatial sampling period (being 0.5 *mm* in the example of fig. 6.13-*right*), as explained in Chapter 5.

Application of the 2D-FT over experimental data

The first experimental extraction of the phase velocity dispersion curves has been carried out over a rectangular aluminium plate of 1.18 *mm* thickness and dimensions 45x30 cm^2, with a similar configuration to that in fig. 6.1. The distance from border point A to sensor is 16.2 *cm*, closest distance source:sensor is 7.35 *cm*, total length of source locations is 3.45 *cm* and

the distance from the farthest source to the border point B of the plate is 18 *cm*. The perpendicular direction to the line-sources that pass through the sensor is symmetrically centred to the plate, at a distance to the borders of the plate of 15 *cm* each side.

For the first presented dispersion curves (fig. 6.14) obtained with a MATLAB algorithm by me developed, we used a spatial sampling period of Δx = 0.254 *mm* (or 10 motor steps), taking 137 ultrasonic waveform samples (one for each source location) in order to cover the 3.45 *cm* of length of the source locations. The oscilloscope sampling period is 10 *nsec* and the ultrasonic waveforms are sampled for 100 μ*sec* in order to avoid reflections from the borders of the plate. The obtained data matrix $U[m,n]$ is always zero padded in time and space to the closest power of 2 to speed the calculation of the 2D fast Fourier transform algorithm and increase fidelity of the estimated spectrum to the true spectrum of the signal.

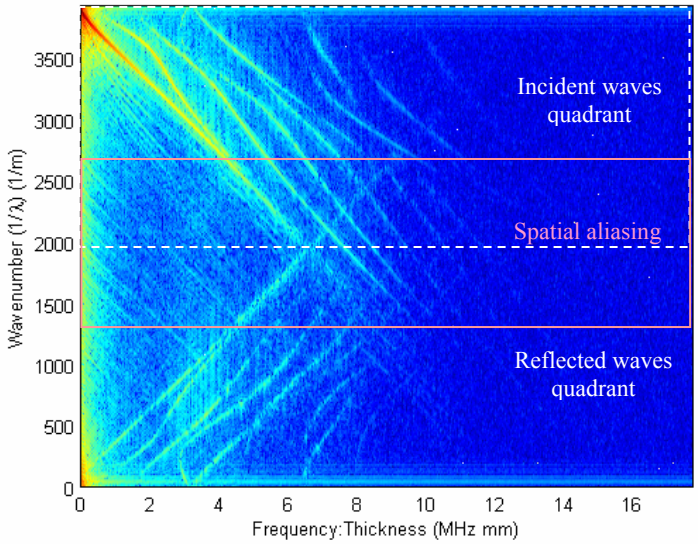

Figure 6.14: 2D-FT spectra representing the Lamb waves phase velocity dispersion for an aluminium plate in the wavenumber domain. The red light colour represents the highest spectra values and dark blue the lowest. The spectral amplitude is given in logarithmic scale. Thickness of the plate 1.18 *mm*, Δx = 0.254 *mm* and total displacement length of the sources is 3.45 *cm*.

Only the spectra of the 2D-FT associated to the incident wave and reflected wave quadrants is plotted, because they contain all the available dispersion information. Thus the wavenumber is plotted between 0 and $1/\Delta x$ ($1/m$) and the frequency is plotted between 0 and 15 *MHz* (or equivalently maximum frequency:thickness product value is 17.7 *MHz mm*). The spectra information given by the 2D_FT is a 3D plot. The complexity of the shapes and multiplicity of the dispersion curves configuration makes difficult to interpret anything in a 3D plot. Hence a 2D plot of the top view of the frequency – wavenumber plane is more adequate, with the amplitude of the 2D-FT spectra at each point being colour coded; red light

indicating highest values of the ultrasonic spectra components and dark blue lowest. The amplitude has been represented in logarithmic scale due to the enormous amplitude difference between the excited A_0 and S_0 modes at low frequencies and the high order modes at higher frequencies as shown in the typically detected ultrasonic waveform of fig 6.6–*right*.

The first thing to notice in the 2D-FT spectra of fig. 6.14 is that although the ultrasonic laser source excites waves of all frequency:wavenumber combinations, only a few well defined curves present a significant amplitude (given by light colours in contrast with the dark blue background). Hence only waves with those frequency:wavenumber combinations can propagate in the structure. The perfect agreement of these curves with the theoretically obtained phase velocity dispersion curves for aluminium (as seen in later plots), prove the Lamb wave nature of these waves.

Three sections have been identified in fig. 6.14, of which we have previously discussed about; incident waves quadrant (white dashed squared) in the top half of the spectra, reflected waves quadrant in the bottom half and the spatial aliasing in the centre. The Lamb waves dispersion curves in the incident waves quadrant have much higher amplitude (as shown by the more lighter and red colour levels) than those in the reflected waves quadrant, as it would be expected because the closest lateral border of the plate is chosen far enough as to minimize the reflected waves during the recording interval of time of the ultrasonic waveforms (100 μsec). For instance the reflection of the fastest propagating mode (S_0 mode at low frequencies, with group velocity ~5.44 *km/s*) generated by the closest source to the sensor, would be detected at around 92 μsec from the launched laser pulse. Obviously slower propagating modes would not arrive within the detection interval of time, however we still see them in the reflected waves dispersion curves. This is the case, for instance, of the A_0 and S_0 mode over 2 *MHz mm* where their group velocity value is under 3.1 *km/s*. The reason for these reflected waves to appear is because they do not come from reflections of the waves generated in the current laser pulse but from waves that were generated in previous pulses and that still are not totally attenuated. Remember that the ultrasonic waveforms are averaged 64 times and that the repetition rate of the Q-switched laser is quite high (10 *Hz*). In the dispersion curves of the ANSYS model (fig. 6.10-*right*), where the incident and reflected wave quadrant were swapped, we do not see waves in the reflected wave quadrant (now top half) because in this case the ultrasonic waveforms are not averaged and a source of a single pulse was modelled.

The reflected waves dispersion curves has been used in the literature for damage detection and characterization applications [6,7]. However in the work of this thesis where we are only

interested in the incident waves dispersion curves, their effect are only harmful, due to the spatial aliasing suffered in our experimental realizations. Causing intersection between the reflected wave dispersion curves and the incident wave curves in a few points within the area of aliasing. Fortunately, as already addressed in Chapter 5 and previously in this chapter, still most of the dispersion curves information can be correctly extracted from the aliasing region (as we can see in fig. 6.14).

Meanwhile the phase velocity associated to any point of the continuous 2D-FT dispersion curves is given by f/k, this expression does not apply to the negative slope dispersion curve in the incident wave quadrant (high wavenumber values k) of the discrete 2D-FT. Where in order to take into account the incident wave quadrant projection (shown in fig. 6.12) due to the discretization of the 2D-FT, the correct phase velocity would be given if the wavenumber is rewritten as $|k' |= |k – 1/\Delta x|$, or if the incident and reflected wave quadrants of the discrete 2D-FT spectra are swapped as done in fig. 6.10-*right* for the ANSYS model. During the rest of this chapter we will plot the incident wave quadrant as positive slope in the low wavenumber half of the 2D-FT spectra, because this is the quadrant we are interested about.

Enhancement of the 2D-FT processing algorithm

The 2D-FT spectra plotted in fig. 6.14 confirms the correct operation of the developed inspection tool and the adequacy of the processing technique applied. However it is obvious that further optimization are required in order to be able to extract an accurate set of the dispersion curves values of the material. The main points requiring improvement are listed next with the solution applied:

1. *1D leakage*: This effect is due to the discontinuities at the boundaries of the spatial and temporal finite length data. As explained in Appendix E, this causes the existence of frequency values that do not correspond with the FFT bin values (both in wavenumber and frequency) and their energy is spread over all the frequency and wavenumber range. The temporal data discontinuity is obvious in fig. 6.6–*right*, where the high amplitude of the A_0 mode at low frequencies contrasts hugely with the null amplitude of the beginning of the waveform. The effect of this discontinuity can be seen in the intense horizontal leakage at low wavenumber values for the reflected wave quadrant and at high wavenumber values for the incident wave quadrant in fig. 6.14.

The spatial data discontinuity can be seen in fig. 6.15–*left* where we plot the detected ultrasonic amplitude as a function of the distance source:sensor at a common time instant of 33 μsec.

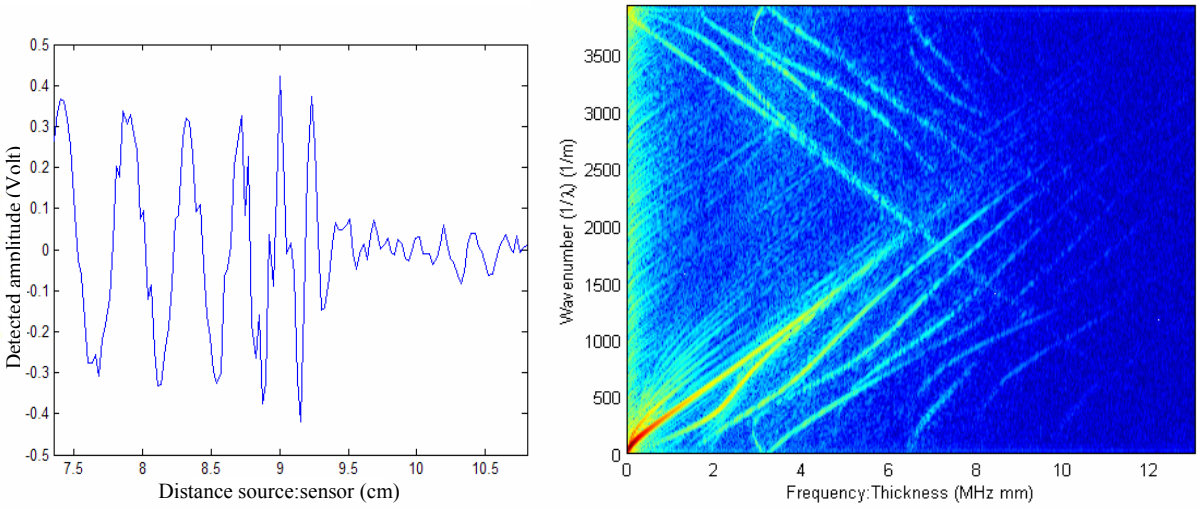

Figure 6.15: Correction of the 1D leakage in both frequency and wavenumber: (*Left*) Space data for the ultrasonic detected amplitude as a function of the distance source:sensor at a common time instant 33 μsec. (*Right*) 2D-FT spectra after applying spatial and time Kaiser window functions with β=3.

The solution to this problem is to apply window functions, both in space and time, to the ultrasonic data matrix $U[m,n]$. The developed algorithm in MATLAB allows choosing between different windows by defining the parameter β of a Kaiser window function [8], such that; β = 0 represents no window, β = 5 is the Hamming window and β = 6 is the Hanning window. The higher the value of β the bigger the attenuation of the temporal and spatial data at the boundaries of the window, thus less energy will appear in the 2D-FT spectra dispersion curves. Fig. 6.15–*right* shows the corrected dispersion curves for a β = 3 and fig. 6.16-*left* for a β = 6. In contrast to the dispersion curves in fig. 6.14, now we have swapped the incident and reflected wave quadrants (as previously mentioned) and decrease the maximum frequency:thickness plotted as no observable signal appears over 13 *MHz mm*. The 1D leakage has been corrected. The lower β window dispersion curves not only show the high order modes dispersion curves at high frequency values better (these modes arrive at the beginning and end of the time data, hence being more attenuated with increasing β windows), but also the higher β dispersion curves appear more spread.

2. *DC offset of the ultrasonic waveforms*: this causes the appearance of the high energy DC frequency component at all wavenumber values, intensified by the 1D spatial leakage of the highest amplitude A_0 mode at low frequencies. This can be corrected by applying a high pass (HP) filter to the time data. We have analysed the effect of various filters (Bessel, Chebyshev and Butterworth) and observed that the latter gave better dispersion curves. Where an order 1 and cut-off frequency of 350 *kHz* provided good correction of the DC

offset without perturbing too much the dispersion curves of A_0 and S_0 at low frequency values.

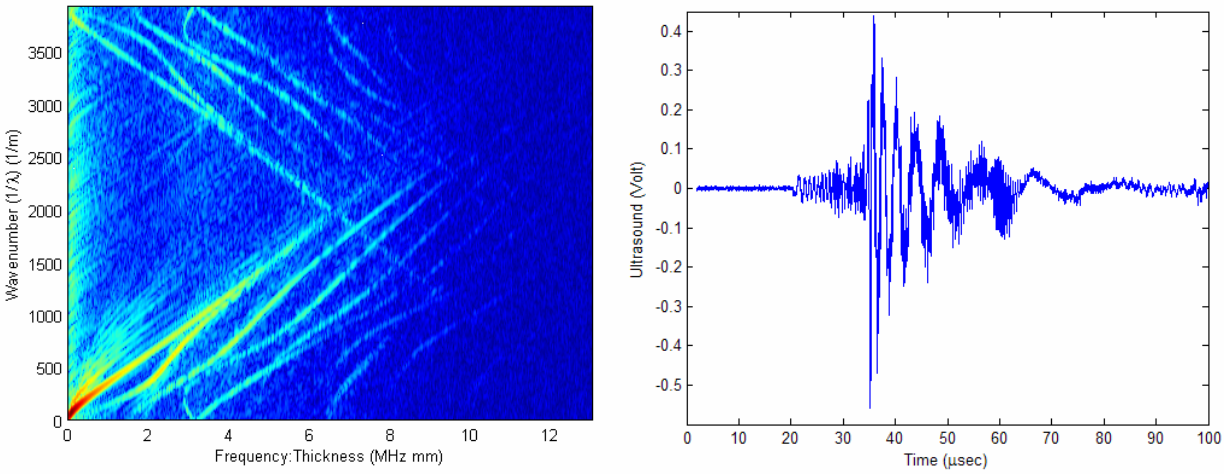

Figure 6.16: (*Left*) 2D-FT spectra after applying spatial and time Kaiser window functions β=6. (*Right*) Ultrasonic waveform of fig. 6.6–*right* after applying 1st order HP Butterworth filter at 350*kHz*.

The benefits of applying such a HP filters are more than only cancelling the DC offset. Figure 6.16-*right* shows the ultrasonic waveform of fig. 6.6–*right* after applying the Butterworth HP filter. The amplitude of the A_0 mode at the middle end of the time signal has been highly attenuated as it corresponded to low frequency values. In consequence the higher order modes of higher frequency values that modulate A_0 mode (unaffected by the filter) are now clearer in the time signal. In addition the HP filter decreases the discontinuity in the boundaries of the time signal in a similar way to the time window function. However in contrast with the window function, the HP filter has the advantage of not decreasing the small amplitude high order modes arriving at the beginning and end of the time signal (modulating the S_0 mode). Figure 6.17–*left* shows the 2D-FT spectra over the same ultrasonic data as before but now we HP filter it with the previous Butterworth filter and only space window function with β= 3 is used. The improvement as a much better presence of the high order modes (circled region) is obvious. The disadvantages are that the high frequency components of the reflected waves, which arrive at the end of the time data are not attenuated either (in contrast with the application of the time window that attenuates everything at the end and beginning) so a bigger interaction between reflected and incidental wave dispersion curves occurs in the spatial aliasing section. Additionally, as the high amplitude of the low order modes and the DC offset has been reduced, also the contrast of the dispersion curves with the noise has decreased, thus the 2D-FT spectra appear more 'dirty'. To correct this problem we need first to understand what exactly this noise is, my interpretation is given next.

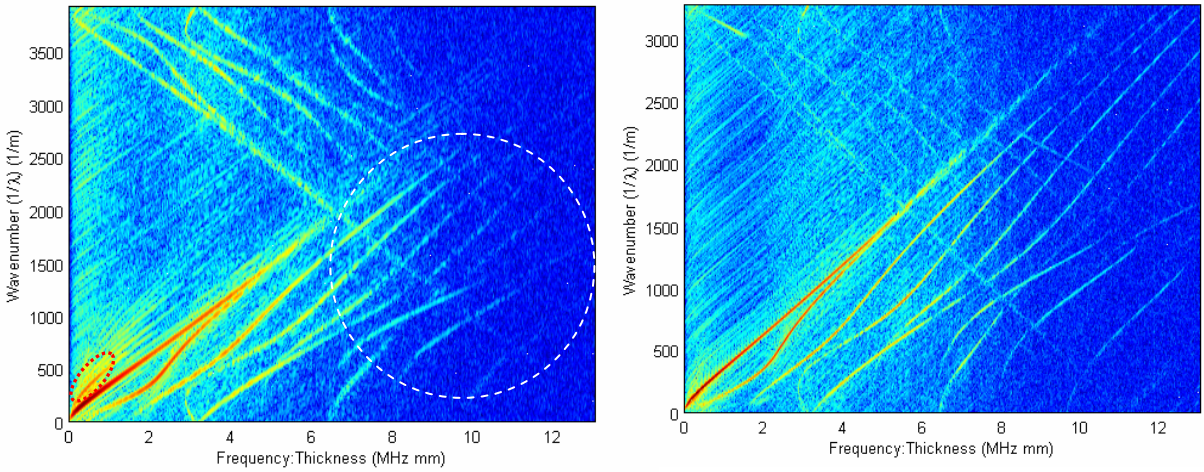

Figure 6.17: (*Left*) 2D-FT spectra after applying a 1st order HP Butterworth filter at 350 *kHz* and a Kaiser spatial window function β=3. Improvement of the high order modes (white circled) to previous cases. (*Right*) As in the left but duplicating temporal sampling period and with Δx = 0.3048 *mm*.

3. 2D leakage: A careful look of the noise in the 2D-FT spectra of fig. 6.17–*left* shows that it consist in curves of positive slope parallel to the high amplitude (red coloured) part of the dispersion curves associated to A_0 and S_0 modes. In a similar way as happened with the 2D-FT of the ANSYS model in fig. 6.10-*right* which points to its data processing origin rather than experimental perturbation.

The only meaningful explanation we can think about for the origin of this vertical repetition of the A_0 and S_0 modes dispersion curves, is that it is the result of a 2D leakage projected in the wavenumber domain. In contrast with the 1D leakage previously explained, the 2D leakage is caused by the discontinuity within the spatial data (not in its boundaries of definition) as it can be seen in the irregular shape of fig. 6.15–*left*. The fact that the temporal data does not present these discontinuities explains why the projection of this 2D leakage only take place in the wavenumber direction (vertically).

Changes in the time sampling period will change the irregularities in the space data, thus this leakage is affected by both dimensions, hence its name 2D leakage.

The only way of decreasing the 2D leakage effects is by increasing both the spatial and temporal sampling periods, meanwhile maintaining the number of total samples, as this will make the bins of the 2D-FT spectra to be closer, increasing the resolution of the dispersion curves. In figure 6.17–*right* we show the improvement by doubling the time sampling period to 20 *nsec* (still small enough to avoid temporal aliasing) and a spatial sampling period of Δx = 0.3048 *mm* (12 motor steps). Because we already have spatial aliasing, we cannot increase

as much as we want the spatial sampling period as this increases the intersection area between incident and reflected wave quadrants and it could worse the spectra rather than improve it. We observed that the chosen spatial sampling period of 0.3048 *mm* was the best compromise for our application.

A great improvement in the dispersion curves can be observed in figure 6.17–*right*, but the 2D leakage has only been attenuated very slightly. The higher resolution of the spectra makes more evident that it consists in a repetition of the A_0 and S_0 mode curves.

A final improvement has been added to the MATLAB algorithm to enhance the contrast of the dispersion curves with the 2D leakage noise by directly acting in the 2D-FT spectra matrix and decrease the average of the peaks associated to this noise. Figure 6.18-*left* shows the final improved spectra normalized also in the wavenumber axis (by multiplying with the thickness of the plate) so that the dispersion curves can be compared with the superimposed theoretical Lamb waves dispersion curves for aluminium. A great agreement between theory and practice is observed, with slight discrepancies at high order modes. These errors are associated to the small differences between the elastic constant values (E, ν and ρ) used for estimating the theoretical dispersion curves and the actual ones for the sample. In fact in the next chapter we will use these discrepancies in the dispersion curves to evaluate the elastic property values of the material.

It is remarkable that the presented technique can perfectly obtain and display the dispersion curves until order modes as high as 5 (for both symmetric and antisymmetric modes).

Lamb waves negative group velocity

Finally we want to call the attention to the reflected waves quadrant of this figure. The amplitude of the reflected wave dispersion curves is very much attenuated apart of the two regions circled. The pink circled region is associated with the fastest propagating Lamb waves (the S_0 mode in the non-dispersive region) as previously explained. These are the only waves which after reflecting in the border B of the plate (see fig. 6.1) arrive within the sampled 100 μsec for each laser pulse. The other high amplitude region of the dispersion curves is circled in green and it corresponds to the S_1 mode in the region of frequency:wavenumber values at which this modes presents a negative group velocity. As explained in Appendix D, the negative group velocity can be understood as the energy of the generated pulse wave propagating in opposite direction to the waves phase velocity. Thus the incident wave from source to sensor propagates as $e^{-i2\pi(|k|x+|f|t)}$ so it appears in the reflected wave quadrant, meanwhile the reflected component in the border B of the plate will appear

in the incident wave quadrant, that is why only in this case of negative group velocity the reflected wave quadrant has bigger amplitude than the incident wave quadrant.

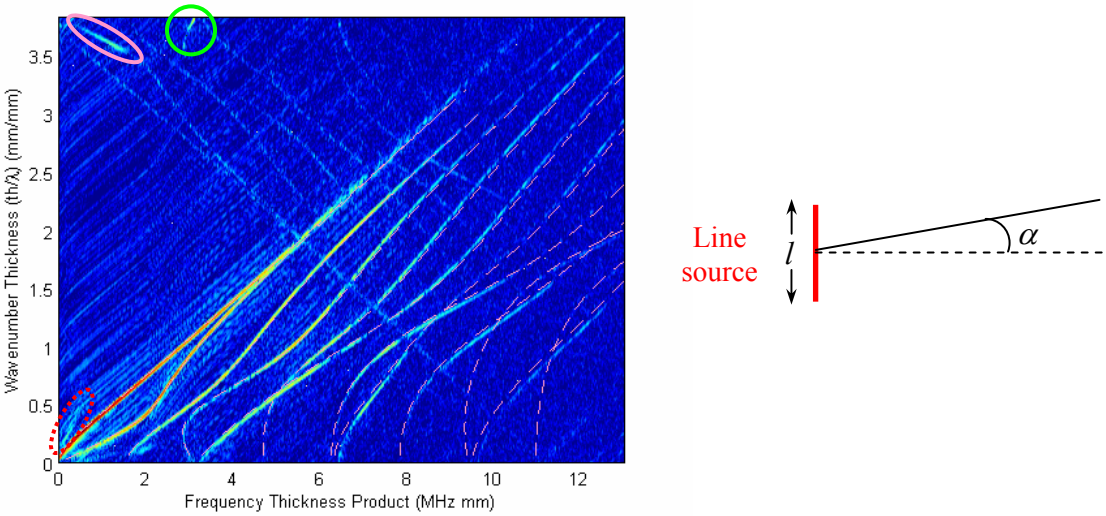

Figure 6.18: (*Left*) Same 2D-FT spectra as fig. 6.17–*left* after applying the noise reduction algorithm. Superimposed in dashed pink lines appear the theoretical dispersion curves for aluminium. Pink circled is the fastest propagating S_0 mode reflected waves and in green the S_1 mode with negative group velocities. In red dashed circle a non-theoretical dispersion curve. (*Right*) Definition of variables for line-source radiation directivity.

4. *Extraneous dispersion curve*: The last aspect of the experimental dispersion curves that require further understanding is the non theoretical dispersion curve shown as dashed red circled in figs. 6.17–*left* and 6.18-*left*. This curve is not presented in the 2D spectra of the ANSYS model, thus its origin is experimental. In fact as we will see next it is related with the radiation directivity of a line-source.

The theoretical expression for the radiation directivity $R(\alpha)$ of a line source of constant amplitude along its length l is given in the far field by eqn. 6.5 [9]. Where α is the angle with the normal to the line-source as shown in fig. 6.18-*right* and λ the wavelength of the generated wave.

$$R(\alpha) = \left| \frac{\sin\left[(\pi l / \lambda)\sin\alpha\right]}{(\pi l / \lambda)\sin\alpha} \right| \tag{6.5}$$

The concept of *far field* was introduced in Chapter 4. Here we concentrate on its definition related to a line source, such as in [9] it is the distance to the point of observation that is large compared to the length of the source. The far field is characterized by the pressure level decreasing 6*dB* for every doubling distance with the generated ultrasonic beam spreading out in a pattern originating from the centre of the source. The equation for the far field is [9]:

$$r_{far\_field} = \frac{l^2}{2\lambda} - \frac{\lambda}{8} \text{ with } l \geq \frac{\lambda}{2} \tag{6.6}$$

Where r is the distance to the observation point from the centre of the line source. The second term of eqn. 6.6 can be neglected for $l > 2\lambda$, which for the experimental laser source length of ~1 *cm* corresponds to values of *wavenumber*th* > 0.23 (*mm*/*mm*). This is true for most of the excited dispersion curves as seen in fig. 6.18-*left*. Thus the far field in our experiments would be given by the smallest excited λ (or highest wavenumber) of considerable amplitude, which from previous dispersion curves we can say to be λ_{min} ~ 0.45 *mm*, giving a far field value in our experiments of ~7*cm*. Our closest distance source:sensor has always been bigger than this value, hence satisfying the far field condition.

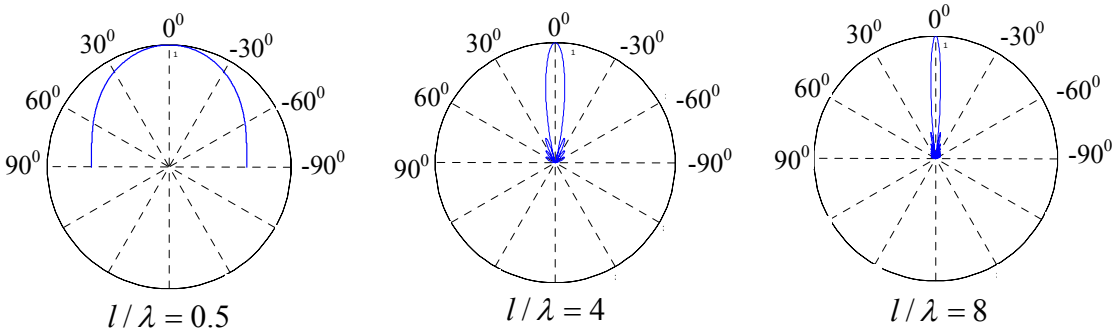

Figure 6.19: Line-source radiation directionality $R(\alpha)$ with the source considered horizontal, for three different values of l/λ.

Figure 6.19 shows in a polar diagram the radiation directivity as given by eqn. 6.5 for three values of l/λ, with the source considered horizontal. The line-source is omnidirectional for ultrasonic waves of wavelengths of the order o bigger than its length, however it becomes very directional when the wavelength is a fraction of the line length. It can be shown [9] that when the amplitude of the line source has a Gaussian distribution (as it is the case of a laser generated line-source) then it becomes more directional for higher wavelengths and more omnidirectional for smaller wavelengths.

Thus for our experimental line source of 0.8 *cm* length, we could consider to be omnidirectional for the ultrasonic waves associated to points in the dispersion curves with k < ~300 (1/*m*). For all the high order modes and also for the S_0 mode the amplitude of the waves excited at these wavelengths is very small as it can be seen from the 2D-FT spectra of figs. 6.17–*left* and 6.18-*left*. However the A_0 mode has its maximum amplitude in this region. The path difference of the A_0 mode omnidirectional waves generated by adjacent line-source and reflected in the closest point of the lateral borders perpendicular to the direction source:sensors (indicated as A and B in fig 6.29-*left*) is bigger than the path difference for

the direct path source:sensor (given by the spatial sampling period Δx). Hence they have a longer propagation time associated, but the 2D-FT considers that the path difference is Δx. Therefore they appear in the 2D-FT spectra with a smaller phase velocity or bigger k, agreeing with the extraneous dispersion curve of fig. 6.17–*left* and 6.18-*left*. This reflection, similarly to the reflection in point A of fig. 6.1, only appear in the incident wave quadrant because as the distance source:sensor increases then also the propagation time does.

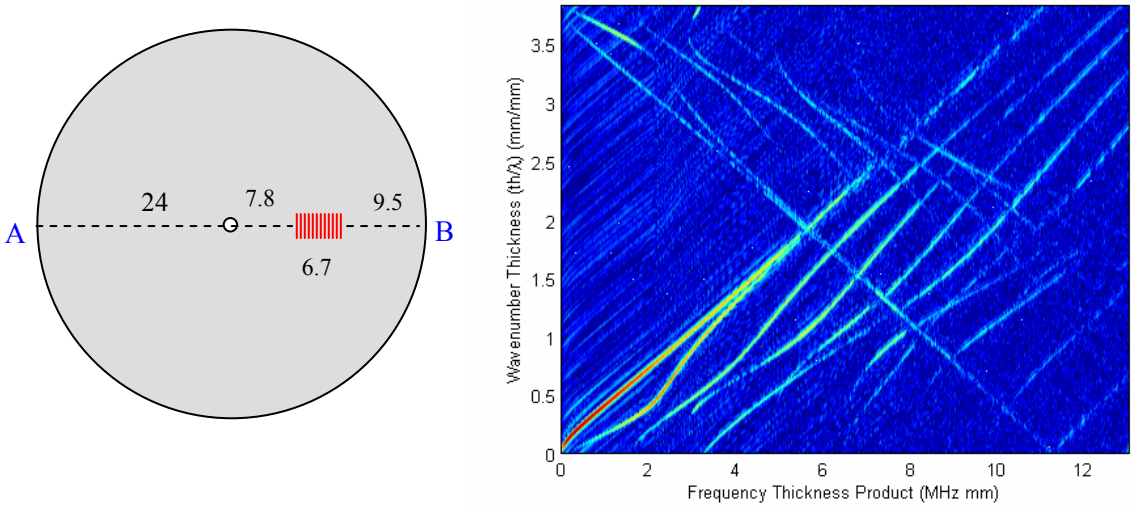

Figure 6.20: Verification of the interpretation of the extraneous mode in the experimental dispersion curves: (*Left*) Experimental realization on a cylindrical aluminium plate, all dimensions in *cm*. (*Right*) 2D-FT spectra of the circular plate experiments obtained in a similar way as fig. 6.18-*left* including the noise reduction algorithm.

An experimental confirmation of this origin of the extraneous mode was developed by situating the sensor in the centre of an aluminium circular plate of 1.18 *mm* thickness and 48 *cm* diameter. The sources are launched in the centre of one of the plate's radius as shown in fig. 6.20–*left*. In this realization the only waves reaching the sensor are those directly incident or reflected in the borders of the plate in the direction source:sensor (points A and B in fig. 6.20–*left*). Any other reflection cannot reach the centre of the plate were the sensor is located. Thus the 2D-FT spectra for this case should not include the described extraneous dispersion curves if the previous interpretation is correct. Effectively no presence of this extraneous mode can be seen in the experimental dispersion curves plotted in fig. 6.20–*right*.

Conversion of the dispersion curves from the wavenumber domain to the phase velocity domain

The experimental dispersion curves by the 2D-FT are directly obtained in the wavenumber – frequency domain, however they can easily be converted to the most common phase velocity – frequency representation (as seen in Appendix A) by taking into account that $c_{ph} = f/k$.

Figure 6.21 shows this transformation for the incident wave quadrant dispersion curves of fig. 6.18-*left*. More about this conversion will be seen in the next chapter.

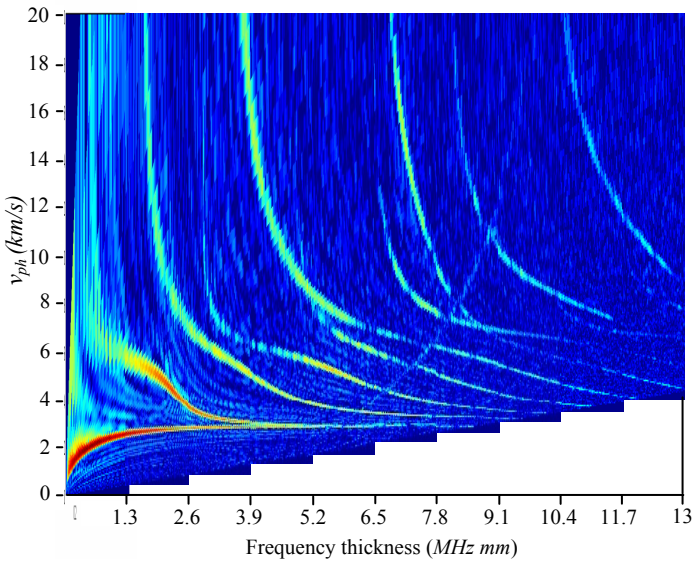

Figure 6.21: Conversion of the incident wave quadrant dispersion curves of fig. 6.18-*left* into the phase velocity –frequency:thickness product domain.

A final addition to the developed algorithm for the 2D-FT processing technique has include a semiautomatic function that analyse the obtained 2D-FT spectra matrix in the wavenumber domain and localize the specific peaks associated to the incident wave quadrant dispersion curves. Hence the experimental dispersion curves are given as a combination of points (wavenumber, frequency:thickness) for each mode. In fig. 6.22 we plot the resultant dispersion curves lines obtained from the spectra in fig. 6.18-*left* which will be used in the inversion process application of the next chapter.

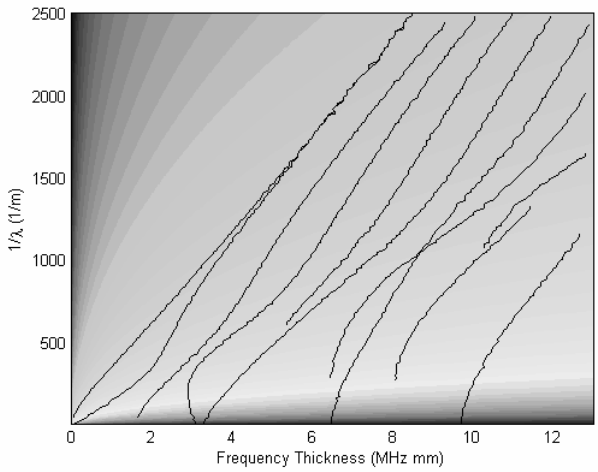

Figure 6.22: Experimental dispersion curves lines obtained from peaks of the spectra in fig. 6.18-*left*.

6.5.2 Time-frequency analysis: Group velocity dispersion curves

The second of the signal processing techniques applied to the experimental ultrasonic data is able to extract the Lamb wave propagation dispersion information looking just to a single shot measurement with one source:detector separation. This technique identifies the temporal frequency components within the single pulse as a function of time delay between the launch of the pulse and its arrival. In general the signal components of the response shown in fig. 6.6-*right* at a particular time delay, correspond to a number of different frequencies with the same propagation velocity. The dispersion information provided by this technique is through the group velocity dispersion curves rather than the phase velocity dispersion curves given by the 2D-FT. However both dispersion information are related by eqn. A.26. Although both processing techniques provide equally the propagating Lamb waves dispersion information, however as described in next section both techniques has an important difference as how this information relates with the monitoring of the sample structural condition.

Two different ways of obtaining the frequency:delay characteristics of the propagating ultrasound have been exploited; the short time Fourier transform and the reassigned spectrogram.

Short time Fourier transform (STFT)

This is the simplest and most effective way of obtaining the frequency:delay characteristics. It consists of dividing the ultrasonic time data in overlapping sections that are windowed and to which an FFT is applied in order to obtain their frequency content. A more extensive operation of this technique has been presented in Chapter 5, thus here we only deal with its practical application to the previously obtained experimental data.

A Hanning window was considered for this application, as justified in Chapter 5. The length of this window is equal to the length of the sections in which the ultrasonic time data is divided and it characterizes the time and frequency resolution. Thus a big window provides better frequency resolution but worse time resolution and vice versa. After analysing the effect of different window lengths over the obtained spectrograms, it was decided that a length of 384 provided a good compromise for multimode ultrasonic signals, agreeing with the analysis done in [10]. The time data of each segment was latter zero padded until a length of 512 (closest power of 2) in order to speed the FFT algorithm and to increase fidelity of the estimated spectrum.

The effect of window overlapping was also studied. Overlapping adjacent windowed sections of the time signal compensate the loss of information caused by the ends of the windows, as smoothly go to zero and hugely attenuating the original time signal.

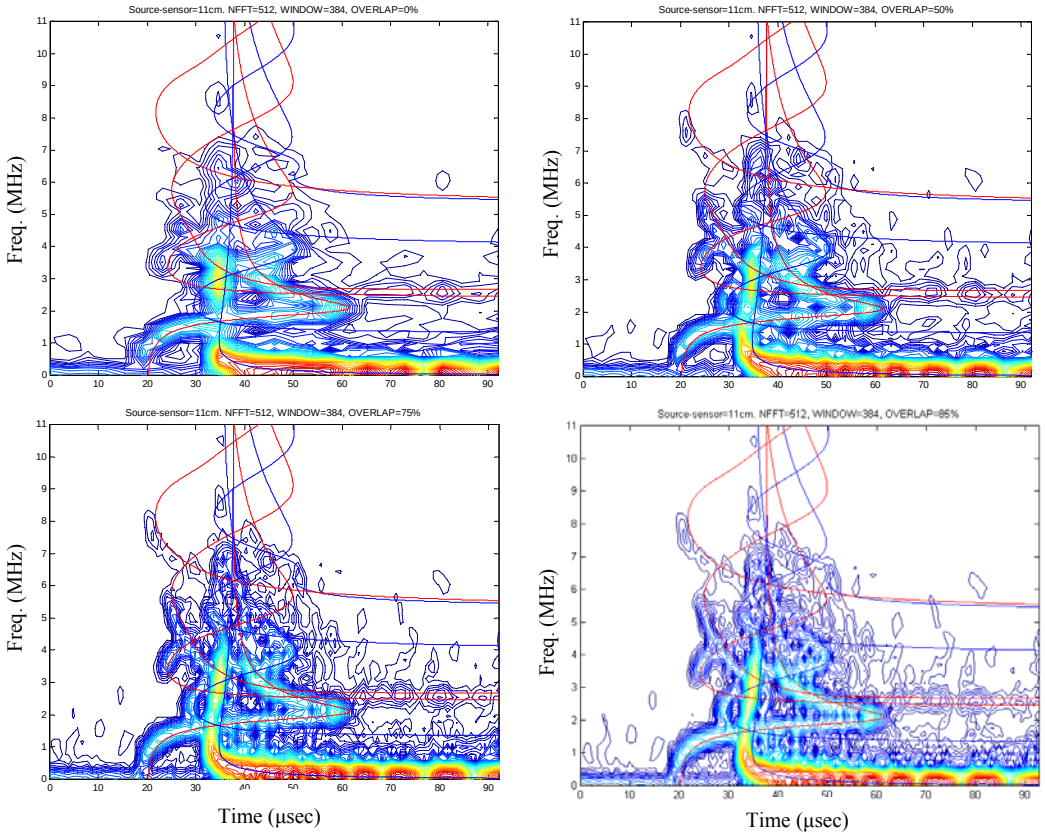

Figure 6.23: Spectrogram (as logarithmic scale contour plot with red light colour for highest values and dark blue for lowest) of ultrasonic signal obtained at distance source:sensor = 11 *cm*. STFT applied for window size = 384 and each segment zero padded to 512 length. The window overlap is increased from top left to bottom right: (*Top left*) Overlap 0%. (*Top right*) Overlap 50%. (*Bottom left*) Overlap 75%. (*Bottom right*) Overlap 85%. Superimposed are the theoretical group velocity dispersion curves; red for symmetric modes and blue for antisymmetric.

Overlapping also improves the time resolution of the spectrogram. In fig. 6.23 we show such improvement by comparison of the spectrogram (as a contour representation with red light colour for highest spectra values and dark blue for lowest, in a logarithmic scale) obtained for the same ultrasonic signal (as shown in fig. 6.6-*right*), and a window size of 384 sample points but the percentage of window overlapped is increased. As the overlapping percentage increases, the dispersion curves appear sharper and with more detail (look for instance to the improved difference between 50% and 75% overlap), at the expenses of a higher computing power requirement. Although no additional dispersion information is obtained when increasing from 75% to 85% overlap.

In the spectrograms of fig. 6.23 we have also superimposed in red and blue lines the theoretical symmetric and antisymmetric modes group velocity dispersion curves for aluminium (until order 3). The experimental dispersion curves appear slightly shifted

towards smaller time values in comparison with the theoretical ones. This is an effect of the *specgram* function by MATLAB which we used to calculate the STFT. Because this algorithm assigns the spectra obtained in each segment to the starting time value of the segment.

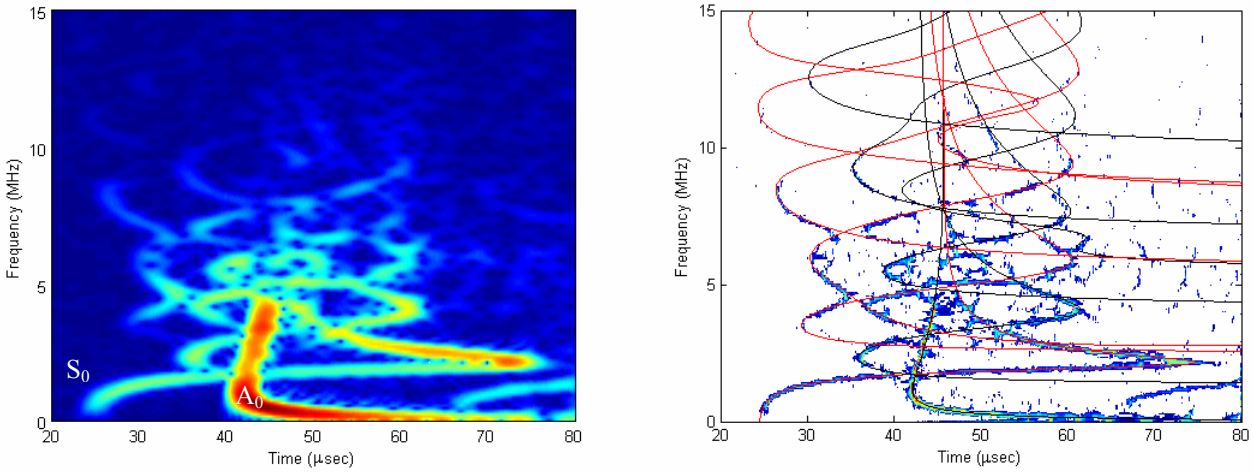

Figure 6.24: (*Left*) Spectrogram obtained with an overlap=window_length-1. Plotted using the *pcolor* MATLAB function. (*Right*) Contour plot of the reassigned spectrogram of the same ultrasonic signal as that in the left. Superimposed are the theoretical group velocity dispersion curves for aluminium (red for symmetric modes and black for antisymmetric ones).

An alternative approach was to use an algorithm based on eqn. 5.5 provided in [11]. This algorithm uses an *overlap=window_length*-1 but it does not suffer from time shift. A spectrogram obtained by this algorithm is plotted in fig. 6.24. This spectrogram is plotted in a similar way as the 2D-FT spectra in previous sections and in fact it is easier to distinguish the dispersion curves than in the contour plots of fig. 6.23. The improved representation of the group velocity dispersion curves is achieved after applying a 1st order high pass Butterworth filter at 350 *kHz* (as we did with the 2D-FT analysis). The spectrogram clearly shows how two curves are dominating from an energy point of view, associated to the A_0 and S_0 modes as indicated in fig. 6.24. We can clearly see that the earliest arriving mode is the S_0 (at 25 *μsec*) and that before the arrival of the high amplitude A_0 mode (at 40 *μsec*) there are multiple high order modes that modulate the higher amplitude signal component of the S_0 mode as previously shown in fig. 6.16-*right*. Same happen with the high order modes arriving during the interval of the dominating A_0 mode.

Reassigned spectrogram

The main disadvantage of the simple STFT technique is its time-frequency resolution limitations, evident in the spread of the dispersion curves of fig. 6.24-*left*. Although some dispersion information can be extracted from this figure, it is not of high precision. The

technique named *reassignment method* developed by Auger and Flandrin can improve considerably this resolution by means of the STFT's phase information that the spectrogram does not use. This technique was extensively explained in Chapter 5. Figure 6.24-*right* shows the amazing potential of this technique through the clear improvement of the spectrogram in fig. 6.24-*left*. We have also superimposed the theoretical group velocity dispersion curves for aluminium and a perfect agreement is achieved. Notice that we do not have the time shift of the experimental dispersion curves towards lower time values as previously in fig. 6.23.

The algorithm used for the reassigned spectrogram is an improved version of that provided in [11].

6.6 COMPARISON OF THE SIGNAL PROCESSING METHODS

The two signal processing approaches have radically different properties and applications. The time-frequency analysis is experimentally advantageous as it only requires a single ultrasonic data set, in contrast to the large series of equally spaced data that the 2D-FT requires. In principle the mechanics of the propagating waves dispersion behaviour is contained in any measured waveform (as long as the waveform is long enough and sufficient frequencies are excited), hence both techniques provide similar dispersion information. Why then do we apply the 2D-FT? It can be argued that the reassignment method has problems to properly resolve the intersections that commonly occur in the group velocity dispersion curves. This problem is not present in the 2D-FT. Nonetheless this effect will only be a real problem depending on the actual application. We can also argue that the more measurements taken by the 2D-FT would give a more averaged result, thus probably its results are less affected by experimental error and also has better resolution. Still they provide same information or do they really? A more detailed analysis of both techniques has lead to our conclusions (never seen before) that the dispersion information these two signal processing techniques provide is in fact quite different.

The time-frequency analysis takes a single trace and plots the frequency content within that trace along the time axis. Since the time axis refers to the delay between the launch of the laser generated ultrasound pulse and the arrival of the ultrasound at the optical detector then clearly all the material between the source launching point and the detector influences in an averaging way the characteristics of its dispersion curves.

The situation with the two dimensional Fourier transform is very different. In this case the propagation characteristics of the multiple waveforms at the detector corresponding to equally spaced launch positions are compared, and it is through the differences in the

waveform propagation that the 2D-FT extracts the dispersion information. Because the path of the sample between the closest source and sensor is common to all the waveforms, it does not affect the shape (dispersion information) of the obtained dispersion curves. However this common path will filter the waveforms frequency content and so affect the domains of definition of the dispersion curves as well as the magnitude of the mode's curve amplitude. This approach is sensitive to the properties of the material between the minimum and maximum separations of the source and detector and it is not influenced at all by the properties of the material in the common path.

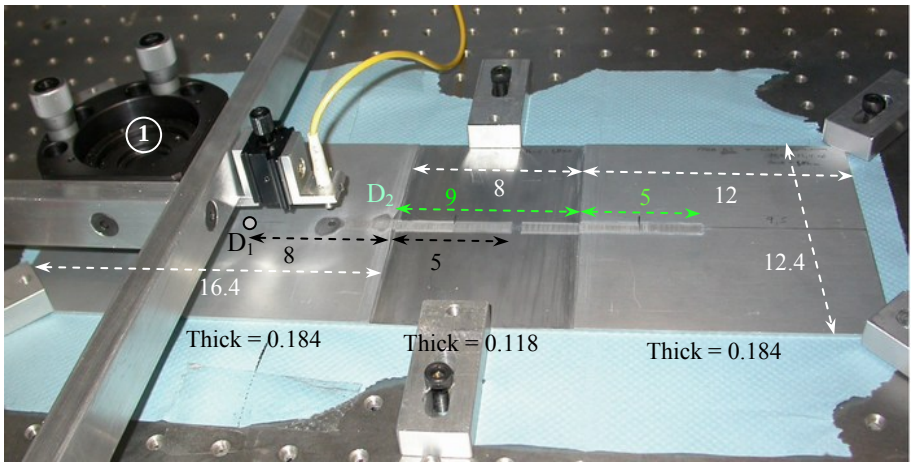

Figure 6.25: Dimensions and experimental setup of the cast aluminium plate for the verification of the area selectivity characteristic of the 2D-FT processing technique. All dimensions are in *cm*.

An experiment has been developed to prove these conclusions based on the fact that the dispersion curves are affected strongly by the thickness of the plate where the ultrasounds propagate (as mentioned in Appendix A).

First we have taken a cast aluminium plate of 1.84 *mm* thickness with dimensions as shown in fig. 6.25 (given in *cm*), and the obtained wavenumber dispersion curves by the 2D-FT technique are plotted in fig. 6.26-*left*. In comparison with the previously presented experiments for aluminium plates, in the present case a bigger region of the dispersion curves is excited. With a much bigger number of very well defined high order modes present. This is due not only to a thicker plate being used (aluminium plates were 1.18 *mm* thick) even though the maximum detected temporal frequency is again low pass filtered at 15 *MHz*, but also because the cast aluminium is a stiffer material than just rolled aluminium so higher ultrasonic amplitudes can be generated without damaging so much the plate's surface.

The excitation of so many high order modes evidences an interesting property of the symmetric high order modes mentioned in Appendix A. Their phase velocity flattens toward

the value of the longitudinal mode just after their cut-off frequency:thickness values, the longer the frequency:thickness product interval the higher the mode's order. In the wavenumber domain this flat region converts into a diagonal line with positive slope, as circled in red in fig. 6.26-*left*. In these regions the symmetric modes behave much as a longitudinal mode, thus their out-of-plane displacement is negligible, the more the higher the mode order.

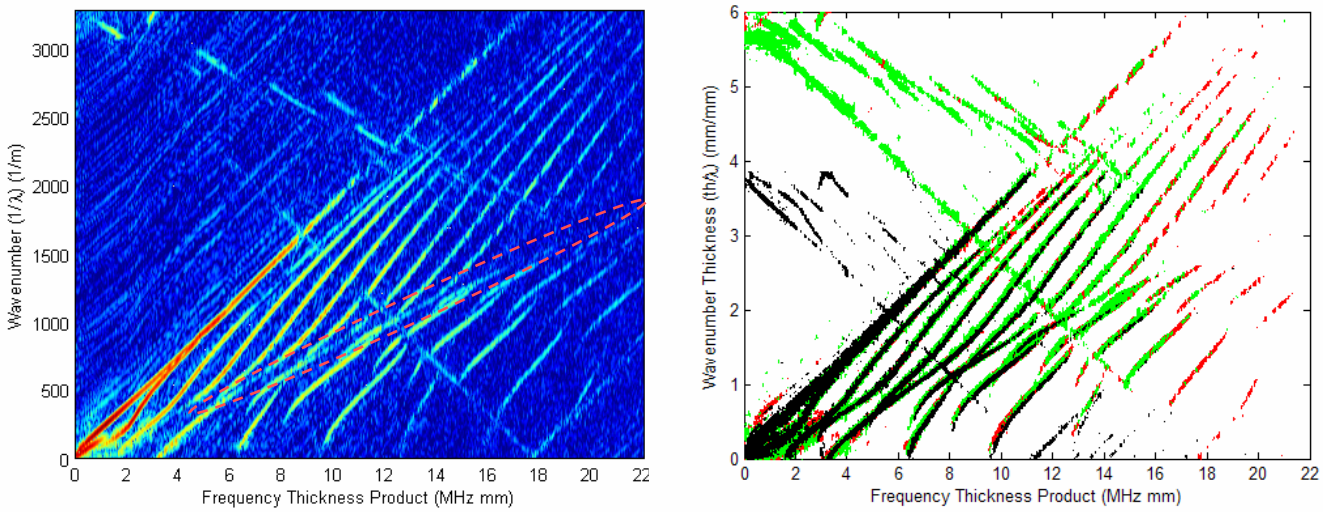

Figure 6.26: Cast aluminium plate dispersion curves by the 2D-FT technique: (*Left*) 2D-FT spectra in logarithmic scale, for homogeneous plate of thickness 1.84 *mm*. Circled region where high order symmetric modes are pure longitudinal. (*Right*) Superposition of the contour plots for the cases; _ **(***red***)** Plate without notch (thickness 1.84 *mm*), _ (*green*) Sources and sensor in both sides of the notch (thickness 1.84 *mm*), and _ **(***black***)** Sources inside the notch with sensor outside (thickness 1.18 *mm*).

Because the interferometric detection system is mainly out-of-plane displacement sensitive the high order modes experimental dispersion curves disappear in that region, more the higher the mode's order.

The experimental dispersion curves in fig. 6.26-*left* have been re-plotted in fig. 6.26-*right* as a red coloured contour plot of normalized vertical and horizontal axis, in order to be able to compare them with the dispersion curves obtained for the same plate but under different thickness conditions as explained next.

We have decreased the thickness in the centre of the plate to 1.18 *mm*, seen as a darker region in fig. 6.25. Under this new specification we have taken two sets of measurements. We have measured the dispersion curves for a case where the sources and the sensor are at both sides of the notch and for a case where the sources are within the notch while the sensor is outside the notch.

In the three analyzed cases the sources area length is 5 *cm*, meanwhile the distance between the closest source to the sensor is 8 *cm*. The normalized dispersion curves of these three cases are superimposed in fig. 6.26-*right* with different colours as described in the figure's caption. A superposition of the incident waves dispersion curves is achieved (the dispersion curves associated to the reflected waves, as described in Chapter 5, do not agree because they were obtained for different spatial sampling period) only when the dispersion curves are normalized taking the thickness value in the last two cases as the thickness of the area where the sources are launched. That is 1.84 *mm* when sources being in the other side of the notch and 1.18 *mm* when sources are inside the notch. The agreement of the normalized dispersion curves means that the thickness of the path between the sensor and the closest source does not have any effect in the dispersion curves shape as we predicted. Even with the length of the path between the sensor and the closest source being almost twice the length of the sources area region.

The 2D-FT provides the flexibility in isolating microscopic type region of the sample for examination that the time-frequency analysis cannot achieve, but at the expenses of requiring more processing power and higher experimental complexity. Thus the 2D-FT analysis can focus the material property analysis to specific areas of the sample rather than the full area between source and receiver.

6.7 EXPERIMENTAL DETECTION OF STRUCTURAL CHANGES

We illustrate the operation of the non-contact, all-optical inspection tool to two different applications; temperature changes detectability and damage detection. Each application is suitable for each of the two signal processing techniques presented.

6.7.1 Temperature experiments

These experiments examine the influence of temperature changes on the dispersion curves for an aluminium sample plate of 1.18 *mm* thick and dimensions 40 x 17 cm^2. To simplify the experimental process we have performed the experiments by suspending the aluminium sample sheet over a circular hotplate of 18 *cm* diameter and adjustable temperature controller. The temperature was monitored using a thermocoupler attached to the plate, with two different values chosen for comparison; 23 ℃ (laboratory conditions) and 112 ± 2 ℃.

Because the temperature changes could only affect a specific region of the plate, this application clearly requires the isolation flexibility of the 2D-FT processing technique. Thus the area where the ultrasonic sources are launched will be monitored to temperature variation by changes in the shape of the wavenumber domain phase velocity dispersion curves.

The contour plot of the dispersion curves for both temperature experiments are superimposed in fig. 6.27-*left* (with darker colour for the higher temperature). Unfortunately the dispersion curves obtained in these experiments were not very well defined probably because the experimental plate could not be firmly held. Nevertheless we still can see clear differences between both cases. But before drawing any conclusion let us first analyze what changes we would be expecting.

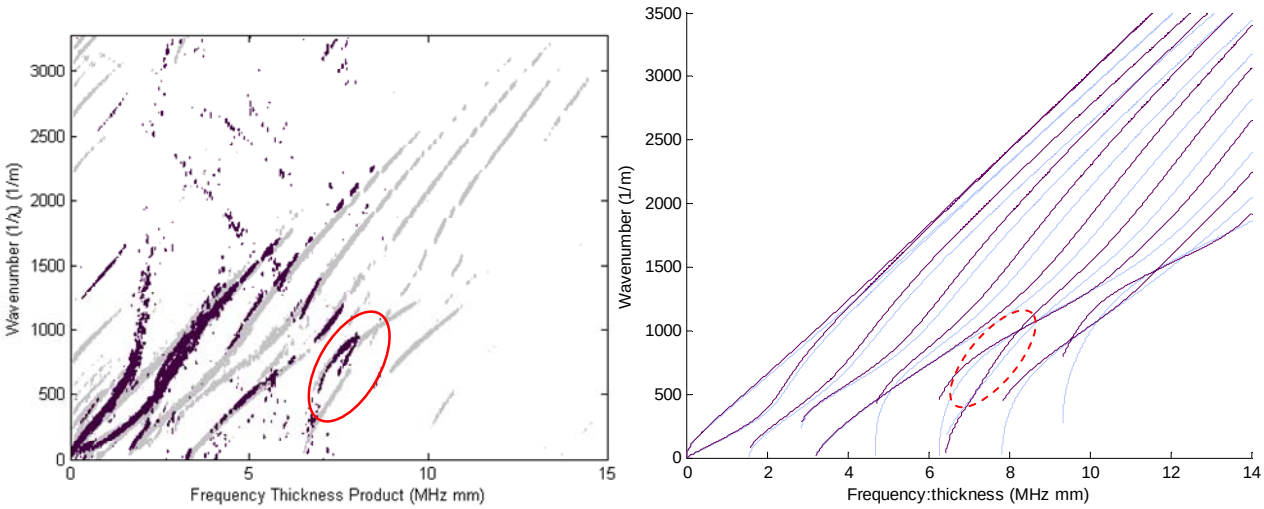

Figure 6.27: 2D-FT dispersion curves comparison for 23^{0}C (light colour) and 112^{0}C (dark colour): (*Left*) Experimentally obtained. (*Right*) Theoretically obtained, for an estimated decrement of 7% on *E* and similar increment on *v*. Red circled shows a similar perturbation of the S_3 and A_3 modes.

Increasing the temperature influences the propagation characteristics predominantly through "softening" the plate, that is through reducing the Young's modulus. Consequently we would expect a lower propagation velocity for a given frequency at the higher temperature, with lower propagation velocities comes a shorter wavelength or higher wavenumber.

The experiment shows effectively this perturbation or shift of the dispersion curves towards higher wavenumber values. It is remarkable the sensitivity of the technique to the relatively small changes in material properties. We have been unable to obtain concrete values of the temperature dependence of the Young's modulus *E* or Poisson's ratio *v*, but [12] says that for aluminium alloys the value of *E* changes regularly with temperature from 76-78 *GPa* at 70 *°K* to 60 *GPa* at 500 *°K*. Considering that *E* is 71 *GPa* at room temperature then we could estimate that *E* is around 65 *GPa* at 112 *°C*. That means a change of only 7% which can easily be detected by our technique. On the other hand *v* increases with temperature, but we don't have an idea of how much. However as demonstrated in Chapter 7, it is the changes on *E* that dominates the changes on the dispersion curves. Using the algorithm I developed, we were able to obtain the theoretical wavenumber domain dispersion curves of high order

Lamb modes, given the elastic property values for isotropic materials. We have plotted in fig. 6.27-*right* what we would expect theoretically by a decrement of 7% in E and a decrement of 7% in v (plotted in dark colour) and the theoretical dispersion curves for aluminium (in light colour). We see a similar shift of the dispersion curves towards higher wavenumber values as the temperature increases. In particular we highlight the intersection of the modes S_3 and A_3 (red circled), as in both cases one of the modes do not change much meanwhile the other has a big shift to the left, again experiments and theory are in general agreement.

6.7.2 Damage detection experiments

As a second demonstration we have examined the impact of damage on the behaviour of the transfer characteristic by inserting a hole between the sensor and the sources using the geometry shown in fig. 6.29-*left*. An aluminium plate of 1.18 *mm* thickness and dimensions 40 x 17 cm^2 is analyzed first under no damage condition so that the plate undamaged signature can be obtained. Later a hole-though damage of increasing diameter is introduced in the plate between the closest source and the sensor. The Lamb wave propagation characteristic are studied to look for any perturbation that would indicate the presence of the damage.

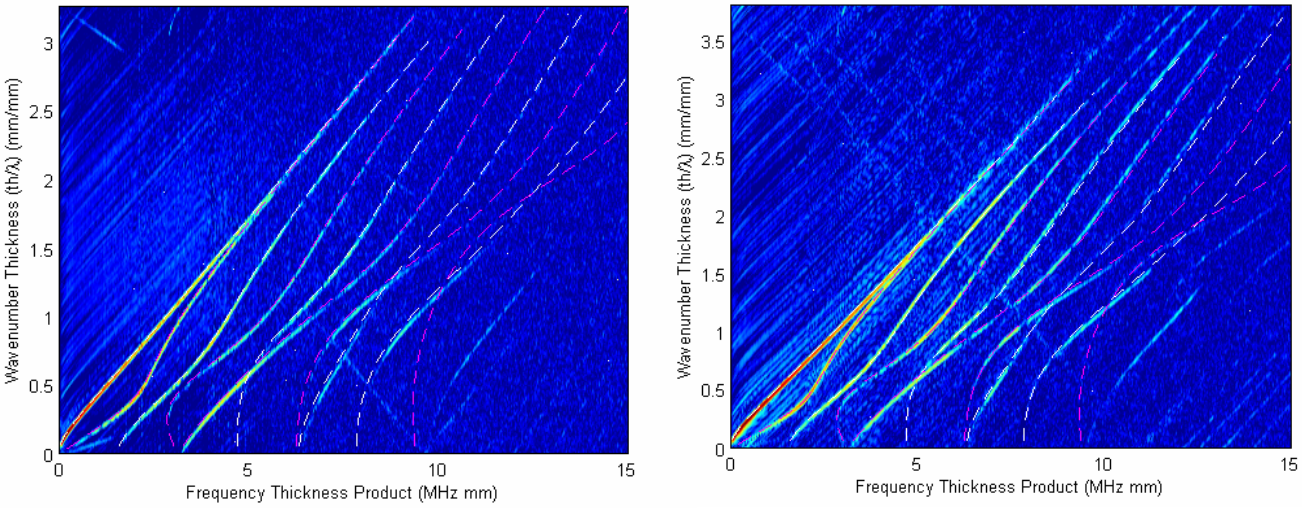

Figure 6.28: 2D-FT dispersion curves analysis for the hole damage experiments: (*Left*) For plate with 1 *cm* diameter hole and spatial sampling distance Δx = 0.3556 *mm*. (*Right*) For undamaged plate and spatial sampling distance Δx = 0.3048 *mm*. In both cases the theoretical dispersion curves are superimposed for comparison purposes.

First we have studied the Lamb waves propagation characteristics from the 2D-FT technique point of view. Hence we have plotted in fig. 6.28 the phase velocity dispersion curves in the

normalized wavenumber domain for the undamaged plate (*right*) and the plate with a 1 *cm* diameter hole (*left*). In both cases we have superimposed the theoretically obtained dispersion curves for aluminium. The comparison between the theoretical and experimental dispersion curves for both show no change of their shape due to the hole. This incapacity of the 2D-FT technique to identify the damage was expected because the damage is located in the common path of the ultrasonic sources. As previously mentioned the effect caused by the damage will appear only as a perturbation of the curves intensity distribution. In this way it is obvious that the dispersion curves in fig. 6.28-*left* are highly attenuated for high wavenumber values, in comparison with the undamaged plate case of fig. 6.28-*right*. The presence of the hole in the path between sensor and the sources scatters the small wavelength ultrasonic waves, causing this wavenumber lowpass filtering effect.

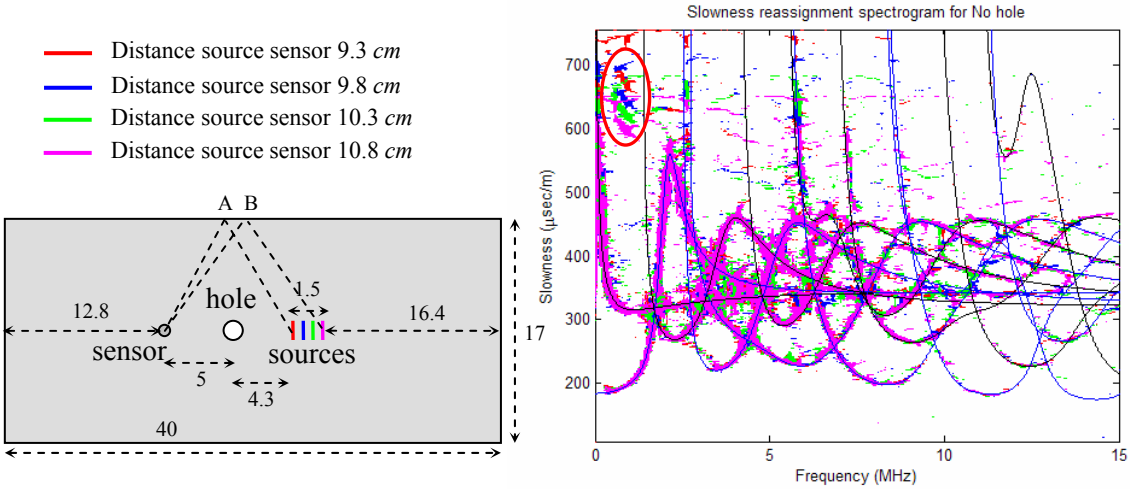

Figure 6.29: (*Left*) Geometry for hole damage demonstration experiments and colour codification of the various distance source-sensor plots. (*Right*) Frequency:slowness curves for the initial calibration with no holes in the sample. Reflected signals circled at top left.

To emphasise the points made earlier, the reassigned spectrogram approach is necessary in this application, since this is sensitive to the source:detector path and changes therein. In this case a single ultrasonic signal would be needed for each case; undamaged plate, 1 *cm* diameter hole and 2 *cm* hole. However for verification and comparison purposes we have taken for each case 4 measurements at different positions of the source as shown in fig. 6.29-*left*. Later for each hole size we calculate the reassigned spectrogram associated to each of the source-sensor distances and we plot them together as contour plots following the colour code defined in previous figure. In order to compare the reassigned spectrograms of sources situated at different distances to the sensor the time-frequency is not the best representation. For this discussion we have found that mapping slowness (the reciprocal of group velocity) against frequency gives the most straightforward representation of what is happening. The

reason not to choose the group velocity representation is because it is not a linear conversion of the time domain representation.

In fig. 6.29-*right* we show the first of these slowness representations, associated to the non-damaged plate. This figure shows an overlap of experimental group velocity dispersion curves associated to the different distance source-sensor cases, and an agreement between these and the theoretical curves superposed in black and blue lines.

There is a region (circled in red) in which the experimental dispersion curves do not overlap. To understand why we must realize that the geometry of the plate is such that there are two principal paths for the ultrasonic waves propagating between the sources and detector; one direct (and through the hole when there is one) and one reflected at the plate side (identified as point A or B). If, for the slowness representation, we take as the source detector distance the direct path, then any indirect paths through the reflected route will manifest themselves as routes with much higher wave number values at a particular frequency. In other words they will appear to progress much more slowly. The red circled non overlapped dispersion curves are associated to the reflection of the A_0 mode in the lateral of the plate.

We must notice that these non-overlapping curves are defined in a very narrow frequency band because of the high pass filtering applied to the detected ultrasonic signals and because at higher frequencies, as previously mentioned, a linear-source becomes highly directional so that no ultrasound is directed to the laterals of the plate.

Note also that the experimental dispersion curve data for the direct route extends to frequencies up to 10 *MHz* and beyond.

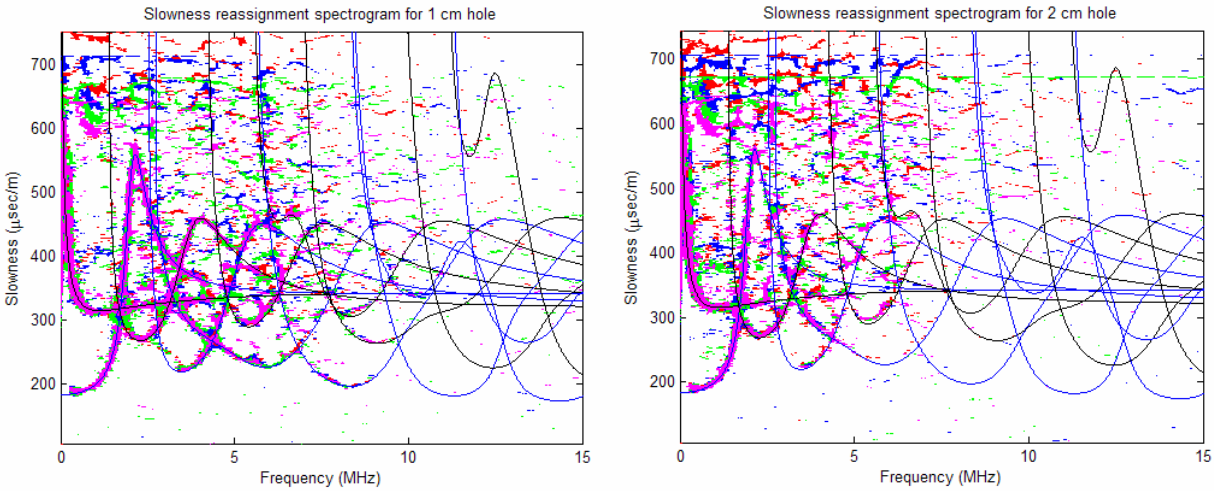

Figure 6.30: Slowness curves with 1 *cm* (*left*) and 2 *cm* (*right*) diameter holes in the sample shown in figure 6.29. Note the high frequency direct signal attenuation as the hole size increases and the onset of much increased multipath scatter with increasing hole size.

The effect of the holes on these curves is shown in fig. 6.30, with the left plot associated to the smaller hole. Two major factors are evident and become more so as the size of the hole increases. The first is that the manifestation of multipath reflections due to miscellaneous routes between sources and detector around the hole becomes more evident as the hole size increases, in other words the apparent noise at high slowness values has become much more obvious. We should not confuse the origin of these non direct path transmission curves, as mode conversion, because as proved in [13] in a symmetric boundary (such as this case's hole-through) there is not mode conversion.

The second evident major factor is that as the frequency increases the through path data reduces significantly with greater hole diameters. For the 1 *cm* hole we see evidence of direct path transmission up to around 5 to 7 *MHz*. For the 2 *cm* hole the evidence of direct path transmission stops at around 3 *MHz*.

Both described effects have their origin in the scattering of the ultrasonic waves of small wavelength (or high frequency) from the direct path source:sensor. These waves only can reach the receiver by reflections in the boundaries of the plate and that is why they appear at high slowness value curves

There is very substantial information content in these curves and to date we have only begun to learn how to interpret this information in a useful manner. The most obvious features concern the increase in the scatter to high slowness values due to the presence of defects and damage. Our signal processing, for both this example and the previous one discussing temperature changes, has been very simply explored upon observed and obvious changes to the dispersion curves in whichever representation we wish to use. With appropriate mathematical processing the discrimination between "unperturbed" and "perturbed" structures can be considerably improved.

6.8 HIGH FREQUENCY ULTRASONIC MONITORING TOOL FOR CHARACTERIZATION OF MICRO-SAMPLES

The developed non-contact inspection tool has a promising prospect in the application of evaluating micro and even nano scale structures, areas where very few, if any, suitable measurement techniques are available. The focusable laser beam associated to both optical ultrasonic generation and detection systems of the macro scale inspection tool can easily be adapted to a micro scale dimension structure. However, in order to adequately characterize microstructures (smaller than 10 μm), ultrasonic waves with frequencies in the range of hundred *MHz* and few *GHz* are required [14,15]. This requisite is feasible in the generation

stage by the Q-switching technique used in the macro scale dimension tool presented, or even much higher frequencies can be achieved if a modelocking technique is used for pulse width generation in the order of 10^{-12} or even 10^{-15} *sec*. Damage in the micro structures can be avoided by the use of low power and high frequency modulated semiconductor laser source for ultrasonic generation.

On the other hand the detection of such high frequencies is not achievable by means of a modified Mach-Zehnder interferometer as previously presented. In collaboration with other members in the group, leaded by Dr. Hee Su Park, we have developed an interferometric detection system that very well adapt to this range of frequencies, based on a Fabry-Perot interferometer configuration. This work has been published in [16] and an extensive treatment has been done in [17].

6.9 CONCLUSIONS

In this chapter we have presented the experimental realization of the all-optical non-contact tool for the extraction of the Lamb wave propagation dispersion characteristics. This system uses a Q-switch Nd:YAG short pulse high power laser to generate a broadband source of Lamb waves, which propagate along a sample plate interacting with its entire volume. Then they are remotely detected by means of a modified Mach-Zehnder surface displacement optical fibre interferometer.

A Finite Element model of the operation of this tool was simulated and its results confirmed the various analyses done over the experimental results.

The two signal processing techniques (reassigned spectrogram and the 2D-FT) presented in Chapter 5 were applied to the experimental data in order to extract the structural information stored in the ultrasonic wave dispersion features. This information is presented as phase and group velocity dispersion curves. A detailed analysis of the different features of their solutions and with the help of the ANSYS model simulation of the system we were able to identify the main areas for improvement of the extracted dispersion curves resolution, contrast and region of definition (1D and 2D leakage, DC offset, radiation directivity of the line-source, etc). For instance in aluminium plate like samples we were able to identify symmetric and antisymmetric Lamb modes until order 5 and in a region within 0 to 4 *mm/mm* wavenumber:thickness product and from 0 to 14 *MHz mm* frequency:thickness product.

Although both techniques provide the Lamb waves dispersion propagation characteristics, this information presents important differences as how it relates with the monitoring of the

sample structural condition. Meanwhile the dispersion information provided by the 2D-FT can focus the material property analysis to specific areas of the sample, the time-frequency analysis analyse the full area between source and receiver. This makes a technique more suitable than the other depending in the application. Thus each processing technique has been applied to a different application, as we analyzed temperature changes sensitivity by the 2D-FT technique, with detectable perturbations caused by changes of 100 degrees. This temperature changes implies modifications of less than 7% in the Young's modulus and Poisson's ratio.

And hole-damage detection by the reassignment spectrogram, clearly showing the increment of a hole-through of diameter varying from 0 to 2 *cm*. The results of these two applications have proved this inspection tool adequate.

6.10 REFERENCES

[1] Dong F., Atherton K., Pierce S. G. and Culshaw B. *Measurement of in-plane and out-of-plane displacements for ultrasonic flaw detection*, 5th European Conference on Smart Structures and Materials, Proceeding of SPIE, vol. **4073**, pp. 324-331, 2000.

[2] Prosser W. H., Seale M. D. and Smith B. T. *Time-frequency analysis of the dispersion of Lamb modes*, JASA, vol. **105(5)**, pp. 2669-2676, 1999.

[3] Moser F., Jacobs L. J. and Qu J. *Modeling elastic wave propagation in waveguides with the finite element method*, NDT&E International, vol. **32**, pp. 225-234, 1999.

[4] Alleyne D. and Cawley P. *A two-dimensional Fourier transform method for the measurement of propagating multimode signals*, J. Acoust. Soc. Am., **89(3)**, pp. 1159-1168, 1991.

[5] ANSYS user's manual version 9.0.

[6] Alleyne D. and Cawley P. *The interaction of Lamb waves with defects*, IEEE Trans. On ultrasonics, ferroelectrics and freq. control, vol. **39(3)**, pp. 381-397, 1992.

[7] Diligent O., Lowe M. J. S. and Cawley P. *Reflection and scattering of the S_0 Lamb mode from circular defects in plates*, Review of prog. In Qauntitative NDE, vol. **20**, pp. 134-141, 2001.

[8] Oppenheim A.V. and Schafer R.W. *Discrete-Time Signal Processing*, Prentice-Hall, 1989.

[9] Ureda M. S. *Line Arrays: Theory and applications*, Audio Engineering Society, 110th Convention paper, Amsterdam (The Netherlands), 2001.

[10] Niethammer M. *Application of time-frequency representations to characterize ultrasonic signals*, M.S. thesis, Georgia Institute of Technology, Atlanta, 1999.

[11] Auger F., Flandrin P., Gonzalves P. and Lemoine O. *Time-frequency toolbox: for use with MATLAB*, 1995-1996.

[12] www.key-to-metals.com/Article73.htm

[13] Diligent O. *Interaction Between Fundamental Lamb Modes And Defects in Plates*, PhD Thesis, Imperial College, London, 2003.

[14] Culshaw B., Pierce G. and Jun P. *Non contact measurement of the mechanical properties materials using an all optical technique*, IEEE Sensors J., vol. **3**, pp. 62-70, 2003.

[15] Shen Y. and Hess P. Real-*time detection of laser-induced transient gratings and surface acoustic wave pulses with a Michelson interferometer*, J. Appl. Phys., vol. **82**, pp. 4758-4762, 1997.

[16] Park H. S., Thursby G. and Culshaw B. *High-frequency acoustic detector based on fiber Fabry-Perot interferometer*, 2nd European workshop on Optical fibre sensors, Spain, 2004.

[17] Hogg H. K. *An optical method for the broadband detection of ultrasound*, Final year project 2004/2005.

Chapter 7

INVERSION PROCESS:MEASURING ELASTIC PROPERTIES

7.1 INTRODUCTION

The use of ultrasonic waves for the measurement of elastic properties of materials date as long as the late 1960's [1]. The need for their measurement and monitoring for a vast number of applications has caused the development of a great diversity of ultrasonic techniques with this sole purpose. These techniques vary from the simplicity of a conventional pulse-echo-overlap ultrasonic method for the measurement of bulk waves velocity [2], to more advanced techniques such as; synthetic aperture scan technique that uses highly focused transducers fluid-coupled to the plate in order to extract the transmission coefficients for anisotropic materials through inversion procedure over carefully selected data [3]. Non-contact techniques are also available, for instance a close proximity technique based in piezoelectric air-transducers that measures the transmission coefficients of A_0 and S_0 mode for direct estimation of the elastic properties [4]. More remote non-contact techniques are based on all-optical generation and detection of the ultrasonic waves, where a wavelet transform is applied over the low frequency A_0 group velocity dispersion curve, that combined with non-linear curve fitting is able to estimate the elastic property values [5]. This thesis has taken the later approach of a non-contact all-optical laser ultrasound generation and detection, because its extremely broad spatial and temporal bandwidth excitation and remote inspection characteristics are unmatched by more conventional ultrasonic techniques. These characteristics are essential for the elastic properties estimation technique approach that we use. Combined with an improved version of the optimization inversion method described in [6], the present system provides a highly accurate and reproducible estimation of not only the elastic but also geometrical properties of the material.

In the previous chapter we applied various signal processing techniques based on the 2D-FT and in the reassigned spectrogram that provided the dispersion characteristics of a broadband multimode ultrasonic Lamb wave propagating pulse.

This chapter makes use of those curves to extract the material's elastic and geometrical properties. This is done by minimizing the differences between the experimental dispersion curves and the theoretically predicted ones (error function) as we change the elastic property values such as Young's modulus, Poisson's ratio and the thickness of the plate specimen.

The monitoring of the changes in the estimated material properties could be a useful indicator of the presence of structural condition perturbations or presence of defects, providing a very accurate reflection of the integrity of the material.

7.2 THE INVERSION PROBLEM AND THE ERROR FUNCTION

The governing equations of motion for Lamb waves are presented in eqn. A.21. However a more appropriate version for numerical computation which avoids the instability of the tangent function is shown in eqn. 7.1. Where SYM is associated with the symmetric Lamb modes and ASYM with the antisymmetric modes. Here f is the temporal frequency of the propagating wave, c is the Lamb wave phase velocity, c_T and c_L are the phase velocity of the transversal and longitudinal bulk modes as described in eqns. A.9 and A.10, given as a function of the material density ρ and the elastic properties E and v. d is the thickness of the plate, and $a = \sqrt{\frac{1}{c_L^{\,2}} - \frac{1}{c^2}}$ and $b = \sqrt{\frac{1}{c_T^{\,2}} - \frac{1}{c^2}}$.

$$\begin{aligned} SYM(f,c,c_L,c_T) &= \omega^4\left(\frac{2}{c^2} - \frac{1}{c_T^{\,2}}\right)^2 \cos(\pi f d a)\cdot\sin(\pi f d b) + 4\frac{\omega^4}{c^2}ab\cdot\sin(\pi f d a)\cdot\cos(\pi f d b) = 0 \\ ASYM(f,c,c_L,c_T) &= \omega^4\left(\frac{2}{c^2} - \frac{1}{c_T^{\,2}}\right)^2 \sin(\pi f d a)\cdot\cos(\pi f d b) + 4\frac{\omega^4}{c^2}ab\cdot\cos(\pi f d a)\cdot\sin(\pi f d b) = 0 \end{aligned} \tag{7.1}$$

Equation 7.1 shows a clear dependency of the Lamb waves propagation characteristic to the principal material elastic properties (Poisson's ratio v and Young's modulus E) and to the structural thickness as given by the variable frequency:thickness product.

As mentioned in Appendix A, the Lamb waves characteristic equation determines the range of phase velocity values for which the different Lamb wave modes exist in a material for a given interval of frequency:thickness product values. The relationship between the ultrasonic phase velocity and the frequency:thickness product values describes the Lamb waves dispersive propagation characteristics and it is graphically represented by the phase or group velocity dispersion curves.

The theoretical calculation of the dispersion curves, by numerical solution of the Lamb wave equation, once the elastic property values and the plate's thickness are known, is generally known as the *forward problem*. Solutions to eqn 7.1 are highly unstable so a powerful and

complex algorithm was developed in MATLAB for this purpose. The *inversion process* deals with the opposite situation, where the values of the elastic properties and the thickness of the specimen are determined through the experimentally obtained dispersion curves.

Rogers analyzed various inversion procedures in [6], with his main conclusion summarized next:

1. The simplest inversion procedure would consist in obtaining at least two pairs of values (c, f) from the experimental dispersion curves and insert them in eqn. 7.1. This pair of values would provide a system of two independent equations with two independent unknowns (E and v). The simultaneous solution of these equations would, in principle, provide the value of the elastic constants. However due to the highly nonlinear nature of the dispersion equations with respect to the variables (E, v), it makes it very difficult and sometimes impossible to find the numerical roots of the equations. Additionally because only two experimental data pairs are used, the solutions would be highly sensitive to experimental errors.

$$G\left(m, f_i, c_i, \rho, E_0, \nu_0\right) = \begin{cases} SYM\left(f, c, c_L, c_T\right) \\ ASYM\left(f, c, c_L, c_T\right) \end{cases} \tag{7.2}$$

2. A more effective inversion procedure consist on minimizing the sum of the evaluations of the *dispersion function* G as defined in eqn. 7.2, at each of a group of N experimental pairs (f_i, c_i). This procedure is mathematically represented in eqn. 7.3, where G^* is the complex conjugate of G (notice that G may be imaginary through a and b) and m identifies if either the SYM or the ASYM mode equation is applied in the definition of G.

$$\sum_{i=1}^{N} G\left(m, f_i, c_i, \rho, E_0, \nu_0\right) \cdot G^*\left(m, f_i, c_i, \rho, E_0, \nu_0\right) \tag{7.3}$$

(E_0, v_0) are the initial estimation of the elastic properties.

This inversion procedure is less sensitive to experimental error estimation of the dispersion curves than the previous one, because it uses more than just two experimental data points. Nevertheless this technique still has the same problem that the previous one regarding the high nonlinearity of the dispersion function with respect to (E, v). In consequence, a unique minimum of the optimization algorithm may not be found and depending on the chosen data region of the experimental dispersion curves, eqn. 7.3 could be very sensitive to small experimental errors and to the initial estimation for the optimization algorithm.

3. The last of the presented inversion procedures is an improved version of the previous one. Like the former, the current inversion procedure uses multiple experimental data points

(f_i, c_i), but it exploits the high linearity observed in the dependency of Lamb waves phase velocity with respect to the elastic property values (as seen in next sections of this chapter).

The present inversion procedure is based in the comparison and minimization of the differences between the experimentally measured phase velocity data and the data values predicted using a theoretical model. To quantify these differences, first an *error function* has to be defined.

The error function is in this case a nonlinear least square function of those differences at the selected experimental frequency:thickness product points, as shown in eqn. 7.4.

$$\sum_{i=1}^{N} \left(c\left(f_i, c_i, \rho, E_0, \nu_0\right) - c_i \right)^2 \tag{7.4}$$

The theoretical value of the Lamb wave phase velocity c can be obtained as the root of the dispersion function G (as defined in eqn. 7.2) as long as an initial estimation of the variables (f, c, E, v) is provided. This is mathematically expressed as:

$$c\left(f_i, c_i, \rho, E_0, \nu_0\right) = root\left[G\left(m, f_i, c_i, \rho, E_0, \nu_0\right)\right] \tag{7.5}$$

A good initial guess for the variables given to the root finding algorithm is to choose the experimental phase velocity c_i at the experimental frequency f_i and the elastic property values as $E_0 = 24 \cdot \rho$ and $v_0 = 1/3$ (as for most metals).

This inversion procedure is superior to the others not only because it uses a large number of experimental data points thus decreasing the experimental uncertainty in the estimation of the parameters, but also because of the linearity that the phase velocity has with respect to E and v in contrast to the high nonlinearity of G. This is the inversion procedure chosen in this thesis. Eqn. 7.4 assumes that all of the data points selected for the inversion process are equally weighted, but as we will see later not all the experimental points are equally good for determining the elastic properties so they should not contribute equally to the error function. In the next sections we will analyse different weighting factors, to solve this problem.

Once the error function is defined with an adequate weighting factor, an optimization algorithm must be applied to the data that will provide the optimum set of material property values that minimize the given error function.

7.3 DISPERSION CURVES CONVERSION FROM WAVENUMBER TO PHASE VELOCITY DOMAIN

The experimental data points (c_i, f_i) selected to be applied in the chosen error function must be given in the phase velocity domain as defined in eqn. 7.4. But the experimentally obtained

dispersion curves in Chapter 6 are naturally given in the wavenumber domain. The conversion from wavenumber to phase velocity is relatively simple and is given by $c_i = f_i/k_i$, with $k_i = 1/\lambda_i$. However because of the non-linearity of the conversion, the uniform spatial frequency grid of the wavenumber domain plot (given by the distances between consecutive wavenumber bins (Δk)) is converted into a non-uniform grid in the phase velocity domain (Δc), as shown in fig. 7.1. We define the distance between adjacent bins as *irresolvable error*, because any value between the bins cannot be properly resolved. The conversion from wavenumber domain into phase velocity domain changes the constant wavenumber irresolvable error into a non-constant phase velocity irresolvable error.

The experimental dispersion curves are obtained by a discrete 2D-FT, so that the frequency values are multiples of the frequency tone $f[1] = 1/(N \cdot T_s)$, where N is the number of points in the ultrasonic time signals after zero padding and T_s is the sampling period. The wavenumber values are multiples of the wavenumber tone $k[1] = 1/(M \cdot \Delta x)$, where M is the number of spatial points taken after zero padding and Δx is the sampling distance for the positioning of the source. The conversion equation from wavenumber to phase velocity is discretized as:

$$c(km/s) = \frac{10^{-3} \cdot n \cdot f[1]}{m \cdot k[1]} \tag{7.6}$$

Where $f[1]$ is given in *MHz* and $k[1]$ in $1/m$, the frequency index n goes from 1 to N and the wavenumber index m goes from 1 to M.

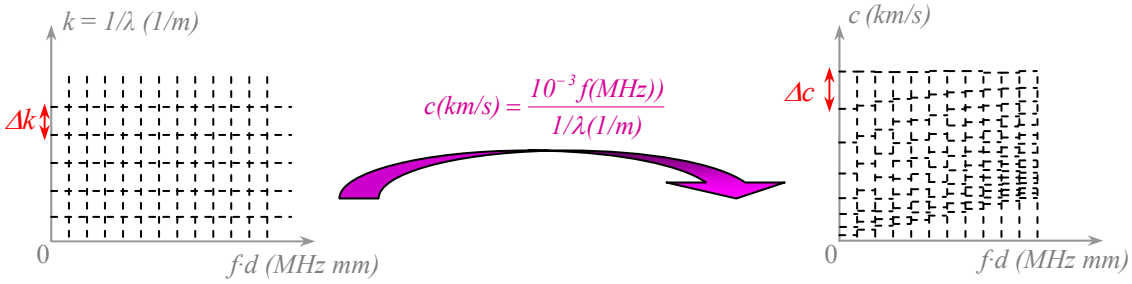

Figure 7.1: Conversion of the sampling frequency bins grid from wavenumber to phase velocity dispersion curves domain.

The phase velocity irresolvable error Δc is given by the difference between adjacent converted wavenumber bins:

$$\Delta c = c(n \cdot f[1], (m+1) \cdot k[1]) - c(n \cdot f[1], m \cdot k[1]) = \frac{10^{-3} \cdot f[1]}{k[1]} \frac{n}{m^2 + m} \tag{7.7}$$

We see in eqn. 7.7 that for a given frequency (represented by n), the irresolvable phase velocity error decreases as the wavenumber increases (represented by m). Opposite occurs

for a given wavenumber (m), if we increase the frequency (n) then Δc increases. Figure 7.2-*left* shows the contour levels of the Δc error given by eqn. 7.7 superimposed to the experimental dispersion curves after conversion to the phase velocity domain (obtained in previous chapter for the rectangular aluminium plate). In this figure we see that the vertical asymptotic regions of the dispersion curves and the non-dispersive region of the S_0 mode have associated the highest irresolvable errors. This explains the oscillations of the S_0 mode's experimental dispersion curve at low frequencies.

More indicative information of the effect that the phase velocity irresolvable error has over the quality of the measured phase velocity data is given by the relative irresolvable error $\Delta c/c$ as shown in eqn. 7.8. Points of high phase velocity values may have big irresolvable errors Δc but they may be better defined than smaller values of c with smaller errors Δc.

$$\frac{\Delta c}{c} = \frac{1}{m} \tag{7.8}$$

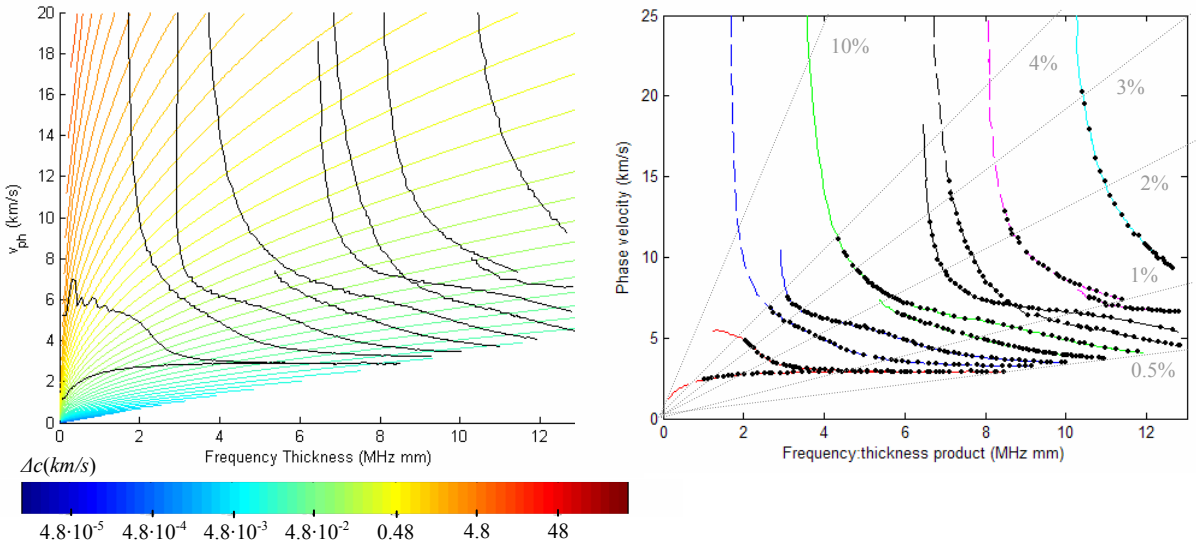

Figure 7.2: Experimental dispersion curves in phase velocity domain: (*Left*) Contour plot of the absolute irresolvable error Δc with red colour associated to higher error and blue to lower. (*Right*) relative irresolvable phase velocity error $\Delta c/c$ constant lines with values between 0.5% and 10%. The dots are the experimental points chosen for applying inversion process in section 7.7.4

The relative irresolvable error is only dependant on the wavenumber value associated to the phase velocity, hence independent of the frequency. Lines that are horizontal in the wavenumber domain are converted to the phase velocity domain into lines that cross the origin point ((c,f)=(0,0)) with positive slope proportional to the wavelength value. In fig. 7.2-*right* we plot a few of these relative irresolvable phase velocity error lines with constant

values between 0.5% and 10%, over the experimental phase velocity dispersion curves. Clearly we see that the vertical asymptotic regions of the high order modes have also a high relative phase velocity error associated, therefore points taken in these regions are not of good quality for the inversion process. The inverse of the relative irresolvable error appears as a good weighting factor to be included in the error function. We can do this by rewriting eqn. 7.8 as a function of c_i and f_i, as given by eqn. 7.9 where l is the total propagated length of the laser source in the 2D-FT experiments.

$$W_{i1} = \frac{1}{\Delta c / c} = \frac{l \cdot f_i}{c_i} \tag{7.9}$$

It is worth mentioning that the irresolvable error associated with the discreet definition of the spatial and temporal frequency bins, dominates over the experimental errors (as shown in Appendix F); where the time errors are related to the oscilloscope inaccuracy for the value of the number of samples per second taken, and the space error is related with the inaccuracy of the laser beam displacement and the Q-switch laser trigger jitter.

We could have considered rewriting the error function to be applied over the wavenumber domain, so that the additional work of doing the experimental dispersion curves domain conversion could be avoided. Nevertheless the benefits of applying the inversion process over the phase velocity domain hugely justify the work investment. These benefits are; linearity of the phase velocity with respect to the elastic properties in contrast with the high non-linearity of the wavenumber, and possibility of selecting those experimental points with the smallest phase velocity errors for the inversion process, in contrast with the uniform error in the wavenumber domain.

7.4 ANALYSIS OF THE PHASE VELOCITY SENSITIVITY CURVES TO CHANGES IN *E* AND *v*

The central idea inside the inversion technique is based in the changes that the variations of the material elastic property values causes over the dispersion curves shape. Figure 7.3 shows the variations of the first five symmetric and antisymmetric modes for changes of 5% in the Young's modulus (in the left), and for changes of 5% in the Poisson's ratio (in the right). Looking to these figures various remarkable points that affect the inversion technique can be highlighted. First, the changes related to a shift of the phase velocity curves for each Lamb mode is reasonably constant to changes in E, in contrast to the high frequency dependency of these shifts when v is changed. In various frequency:thickness product values

some Lamb mode dispersion curves present immunity to changes of ν (for instance S_1 at around 5*MHz mm*), however this never occurs under changes in E.

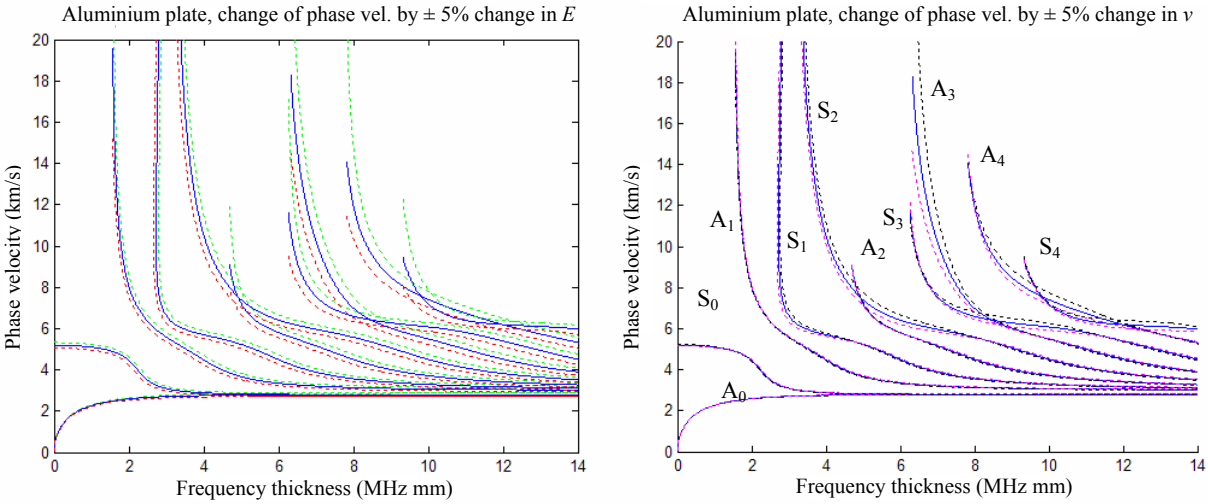

Figure 7.3: Phase velocity curves changes (from a reference case, in blue, with elastic property values $\rho = 2.7\ gr/cm^3$, $E_0 = 24 \cdot \rho = 64.8\ GPa$, $\nu_0 = 0.33$) by variation in 5% of the elastic property values; (*Left*) In green for incremental change of E ($E = 1.05 \cdot E_0$) and in red for decremented change of E ($E = 0.95 \cdot E_0$). (*Right*) In black for incremental change of ν ($\nu = 1.05 \cdot \nu_0$) and in magenta for decremented change of ν ($\nu = 0.95 \cdot \nu_0$).

Second, the changes in the dispersion curve are different for different modes and within a given mode these changes are different at different frequency:thickness product values. For instance the high order modes are in general more sensitive to changes in any of the elastic property values than the low order modes, and for any high order mode the sensitivity is higher in the region of vertical asymptotic behaviour (or cut-off region) than in the region of horizontal asymptotic behaviour. In consequence not all experimental data points (f_i, c_i) are equally suitable for the extraction of the material elastic properties, as they will not contribute equally to the minimization of the error function. This effect should be taken into account as a new improved weighting factor W_{i2} for the error function. To do this we first have to properly define the sensitivity of the Lamb modes phase velocity to small changes of the elastic properties as given by eqn. 7.10, where a linear sensitivity approximation was considered and where $\Delta \rightarrow 0$ (representing small changes).

$$
\begin{aligned}
s_E\left(E^*,\nu^*\right) &= \frac{c\left(E^*+\Delta\cdot E^*,\nu^*\right)-c\left(E^*-\Delta\cdot E^*,\nu^*\right)}{\Delta\cdot c\left(E^*,\nu^*\right)} = \frac{2E^*}{c\left(E^*,\nu^*\right)}\left(\left.\frac{\Delta c}{\Delta E}\right|_{\nu}\right)_{(E^*,\nu^*)} = \frac{2E^*}{c\left(E^*,\nu^*\right)}\cdot\left(\left.\frac{\partial c}{\partial E}\right|_{\nu}\right)_{(E^*,\nu^*)} \\
s_\nu\left(E^*,\nu^*\right) &= \frac{c\left(E^*,\nu^*+\Delta\cdot\nu^*\right)-c\left(E^*,\nu^*-\Delta\cdot\nu^*\right)}{\Delta\cdot c\left(E^*,\nu^*\right)} = \frac{2\nu^*}{c\left(E^*,\nu^*\right)}\left(\left.\frac{\Delta c}{\Delta \nu}\right|_{E}\right)_{(E^*,\nu^*)} = \frac{2\nu^*}{c\left(E^*,\nu^*\right)}\cdot\left(\left.\frac{\partial c}{\partial \nu}\right|_{E}\right)_{(E^*,\nu^*)}
\end{aligned}
\tag{7.10}
$$

At each frequency:thickness product value and for each Lamb wave mode, the defined sensitivity functions s_E and s_ν are the difference between the phase velocities associated to a small increment and to a small decrement of the respective elastic property, normalized with respect to the phase velocity value under no perturbation. In reference to fig. 7.3, s_E is the difference between green and red curves, normalized by the blue one and by analogy s_ν is the difference between the black and magenta curves.

7.4.1 Comparison of sensitivity curves for various elastic property values

An inspection and analysis of the curves associated to the sensitivity functions is more effective and informative than the previous simple visual inspection of the changes in phase velocity dispersion curves. The next analysis shows how the sensitivity curves change for four different modifications of the elastic property values based on those for aluminium (ρ = 2.7 gr/cm^3). Fig. 7.4 shows the five first symmetric and antisymmetric modes for each of these cases with the top being the s_E curves and the bottom the s_ν curves. In the top left corner we have a referential case given by a good initial approximation of elastic properties for most metals; $E = 24 \cdot \rho = 64.8$ GPa and $\nu = 1/3$. The other cases involve an increment of 9% in E as shown in top right, an increment of 9% in ν in the bottom left corner and a combined increment of 9% in both elastic properties as shown in the bottom right corner of fig. 7.4.

Probably the most evident conclusion of looking to any of these sensitivity curves is that the sensitivity to changes in E is much higher than to changes in ν, therefore estimates of E should be expected to be more accurate than estimates of ν. Thus, meanwhile the s_E curves of all the modes for most of the defined frequency:thickness product region have values within [0.1, 0.2], the values of the s_ν curves lie mostly within [-0.01, -0.05] (s_E is around five times bigger than s_ν). Again it is clear that the sensitivity of the Lamb waves dispersion curves are different for the different modes and different frequency:thickness product values within each mode.

More conclusions can be deduced from a comparison of the sensitivity curves of the different cases studied. First, changes only in E does not cause noticeable shape changes of the sensitivity curves, being the only observable effect a displacement of the sensitivity curves towards higher frequency:thickness products values as E increases. Second, changes only in ν causes important change in the shape of the high order modes sensitivity curves (over order 2), being more considerable in the s_ν curve than it is in the s_E curves. However, the changes in ν do not cause any big shift of the sensitivity curves in the horizontal axis.

When we look to the effects associated to the combined changes in both E and ν, then a combination of both previous effects occur; a similar change in shape of the high order modes together with a considerable shift in the horizontal direction.

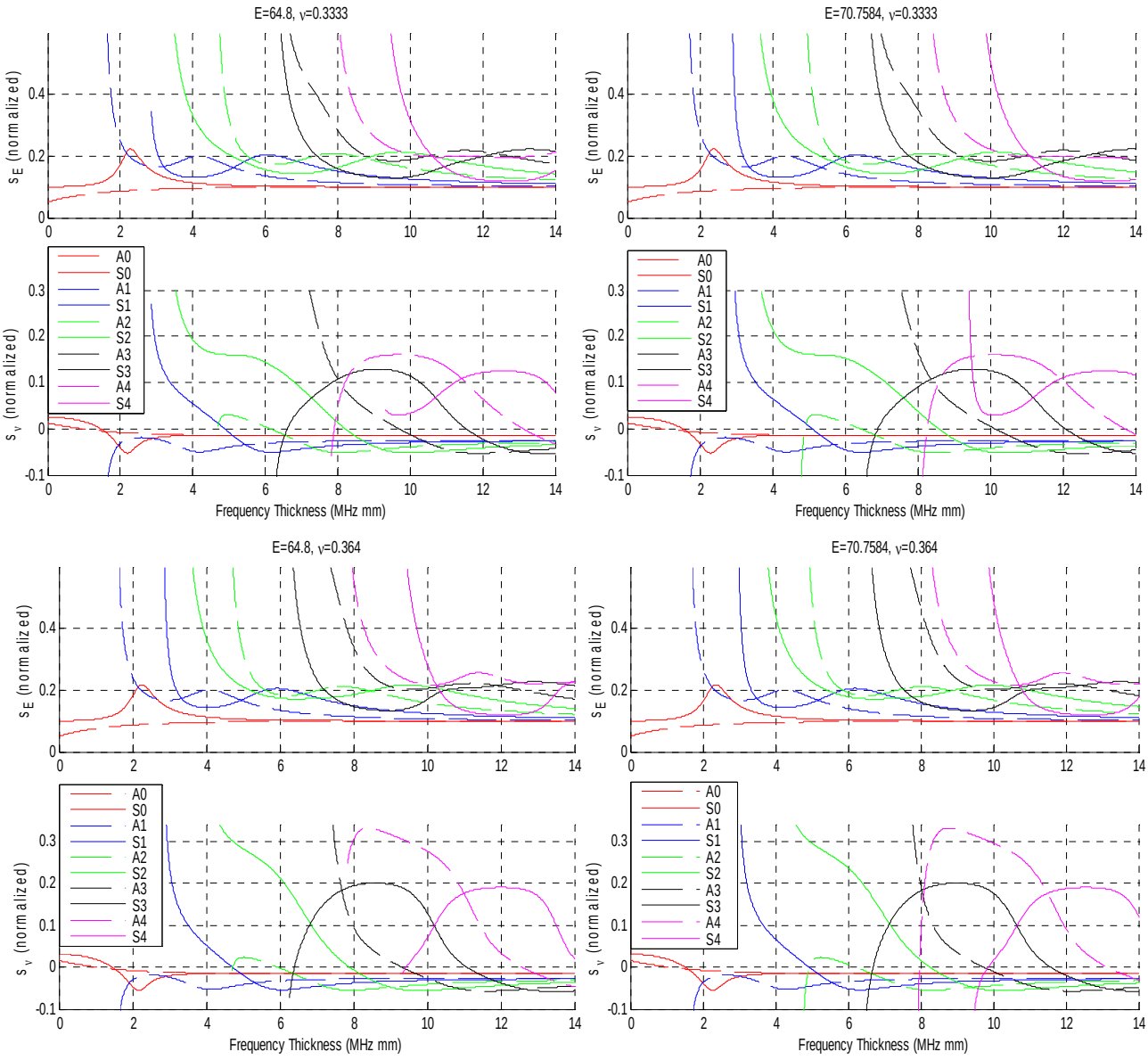

Figure 7.4: Comparison of the sensitivity curves of the phase velocity dispersion curves with changes in E and ν (differential changes of 0.1%). (*Top Left*) Reference case with $E = 64.8\ GPa$, $\nu = 1/3$, (*Top right*) Increment of 9% in E with respect to reference case. (*Bottom left*) Increment of 9 % in ν with respect to reference case. (*Bottom right*) Increment of 9 % in E and ν respect to reference case.

The horizontal shift of the sensitivity curves can easily be explained looking into the changes that the variations of the elastic property values causes over the cut-off frequencies for the

modes associated to each sensitivity curve. This analysis is done extensively in Appendix G and we highly recommend its reading.

It is remarkable that the sensitivity curves associated to Lamb modes of order below three almost do not change in shape. This is true even between the extreme differences in elastic property values of figs. 7.4-*top left* and *bottom right*. The fact that the sensitivity values keep almost constant confirms the linearity of the change in the phase velocity with E and v. However this is not entirely true for the higher order modes, at least not in certain frequency:thickness product regions where the sensitivity curves changes dramatically as the elastic property values change. For instance modes S_3 and A_4 below 12 *MHz mm*, or mode S_4 at all frequencies, also A_3 sensitivity curves changes considerably below 9.5 *MHz mm*.

The changes seen in the sensitivity curves as the elastic property values change could have a negative effect in the inversion process algorithm. As mentioned before the sensitivity values for the selected points are an important weighting factor in the inversion process, but because the optimization algorithm of the inversion process changes the value of the elastic properties in each iteration, then the sensitivity curves also change. This implies that for each iteration we would need to calculate the new sensitivity curves for all the modes, which requires a great amount of processing time.

Fortunately, we notice that the sensitivity curves changes in fig. 7.4 are associated with variations of 9% in the elastic property values. The initial estimation technique presented later in this chapter provides values of the elastic properties very close to the optimized ones, with only a difference of 2.3% in E and 1.2% in v. Therefore the changes in the sensitivity curves caused by these small changes in the elastic property values can be neglected.

7.4.2 Weighting factor and negativity of s_E

At this point it is sensible to define the weighting factor that characterizes the suitability of the chosen experimental points to be applied in the inversion process, regarding their associated sensitivities to the changes in the elastic properties. This weighting factor is defined in eqn. 7.11 and takes into account that the sensitivity to changes in v can be both positive and negative depending in the frequency:thickness product and the Lamb mode, meanwhile the sensitivity curves to changes in E is always positive [6].

$$W_{i2} = s_{Ei} + \left| s_{vi} \right| \tag{7.11}$$

Yet care has to be taken in the previous affirmation, because it is erroneous. Figure 7.5-*left* shows the S_1 mode phase velocity perturbation by changes in E, zoomed into the region where its group velocity becomes negative. The squared area shows that the red phase

velocity curve, associated to E being reduced, is over the green phase velocity curve associated to E being increased. In consequence s_E, as previously defined, is negative. The transition between positive and negative values of s_E is discontinuous, because s_E is never zero, this is due to the fact that the phase velocity dispersion curves associated to changes in only E never intersect between them.

The negative values of s_E are associated only to those regions and modes with negative group velocities. As discussed in Appendix D, only the regions with vertical asymptotic behaviour of the high order modes (both symmetric and antisymmetric) can have a negative group velocity. We have already seen that these points have the highest irresolvable errors and thus they are not of interest in our inversion process. Because of this we can practically consider that effectively s_E is always positive.

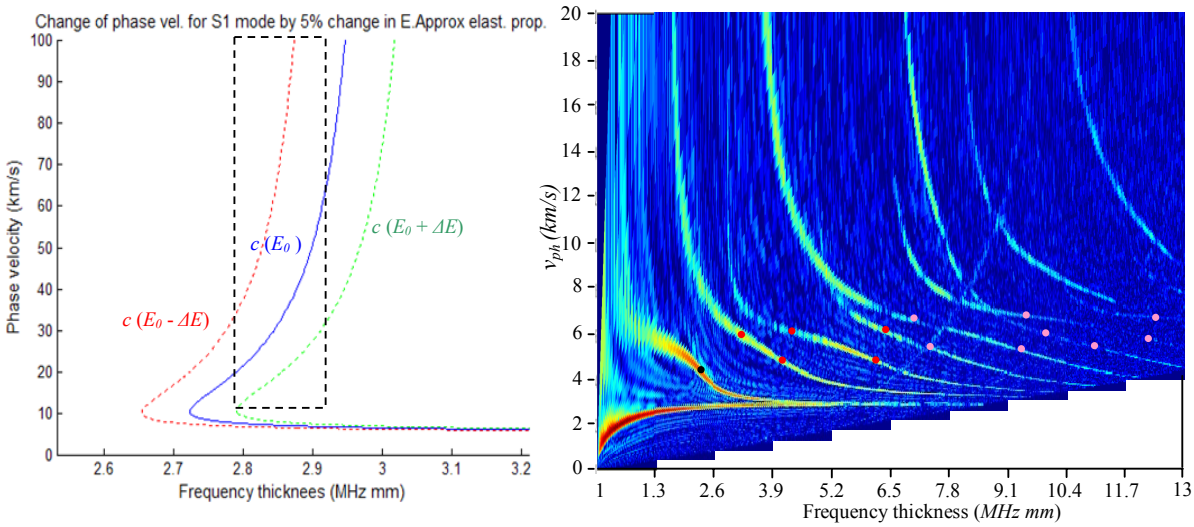

Figure 7.5: (*Left*) S_1 mode dispersion curves variations by changes in 5% on E in the region of negative group velocity. (*Right*) Experimental dispersion curves in the phase velocity domain with the inflection points as coloured dots.

7.4.3 Analysis of the sensitivity curves' inflection points

An analysis of the inflection points of both curves s_E and s_v provide an interesting result depicted in fig. 7.6 (following the same curves colour criteria as in fig. 7.4). The maxima peaks on the s_E curves for each mode occur at very similar frequency:thickness products values as the minima peaks or inflection points in s_v curves for the same mode. The minima peaks in the s_E curves occur at very similar frequency:thickness product values as the maxima peaks or inflection points in the s_v curves, for the same mode curves.

The peaks and inflection points given in fig. 7.6 were obtained by numerical differentiation of the sensitivity curves in fig. 7.4-*top left*. These peaks are given by the frequency:thickness

product values at which the first derivative of the sensitivity curves is zero and the second derivative is different than zero. Meanwhile the inflection points are those at which the second derivative is also equal to zero.

Furthermore, the peaks in s_E (both maxima and minima) are very close in frequency:thickness product values to the inflection points of the phase velocity dispersion curves for the different modes. Fortunately these inflection points are located in an area of high definition in the experimentally obtained phase velocity dispersion curves (see colour dots in fig. 7.5-*right*), therefore these points, which as we will see in the next section are the most adequate for the inversion process, have associated very small experimental errors.

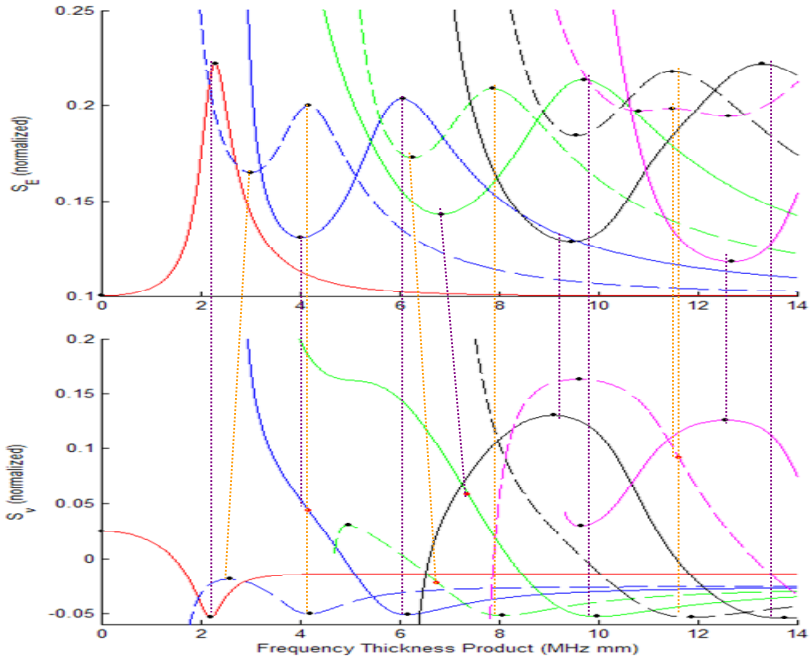

Figure 7.6: Comparison of the maxima and minima peaks of the sensitivity curves for the elastic property values $E = 24 \cdot \rho = 64.8$ *GPa* and $\nu = 1/3$: the symmetric mode peaks are compared by a vertical purple *dashed line* and the antisymmetric mode peaks by a vertical brown *dashed line*.

The inversion process analysis developed so far has been particularized to materials with elastic properties of metals similar to aluminium. However it can also be extended to other materials. For instance, fig. 7.7 shows the sensitivity curves for Perspex (which is a non metallic material) with elastic property values $E = 6.3265$ *GPa*, $\nu = 0.3109$ and $\rho = 1.18$ *gr/cm*^{3}. We clearly see that the peaks and inflection point analysis previously developed for aluminium is also valid for Perspex.

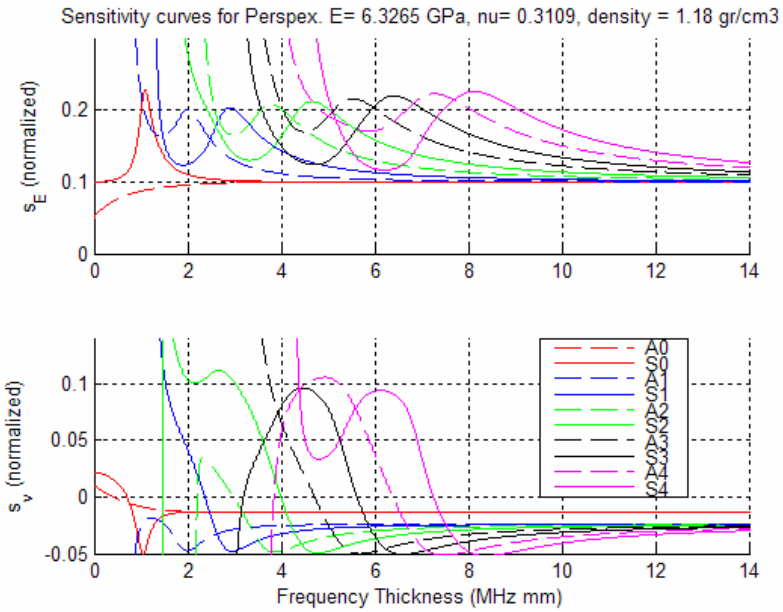

Figure 7.7: Comparison of the maxima and minima peaks of the sensitivity curves for the elastic property values $E = 6.3265$ *GPa* and $\nu = 0.3109$ (Perspex): the symmetric mode peaks are compared by a vertical purple *dashed line* and the antisymmetric mode peaks by a vertical brown *dashed line*.

7.5 SELECTION OF THE POINTS - ANALYSIS OF THE ERROR FUNCTION

Further insight into choosing the most appropriate experimental points for the inversion process can be achieved by an analysis of the error function itself (eqn. 7.4). The optimal experimental points are those that generate one and only one minimum on the error function's 3D surface and that create the sharpest possible surface around that minimum in order to improve the convergence of the optimization algorithm.

The analysis of the error function is subsequently carried out over theoretically obtained phase velocity values. For a given set of points defined by their frequency:thickness product values and associated Lamb mode, we study the sum of the square of the differences between their theoretical phase velocities obtained for the known elastic property values ($E^* = 70.7584$ GPa, $\nu^* = 0.3375$), and the theoretical phase velocity associated to the elastic property values in a region around (E^*, ν^*). This is basically what the optimization algorithm of the inversion process does but rather than calculate the theoretical phase velocity associated to the selected points, it includes the experimental phase velocity values. The result is a surface in a 3D plot, with the domain of definition given by the selected domain of values (E, ν), and the theoretical error function values being the 3rd dimension of the plot. These 3D plots have been represented as contour plots in the next sections and the definition

region has been normalized against (E_0 = *64.8 GPa*, ν_0 = 1/3) for being the most common first approximation for most metals. The minima of the 3D plot surface represents the solution for the optimum values of the elastic properties, which in the mentioned theoretical case will obviously correspond to (E^*, ν^*). Next, we apply the analysis over different Lamb modes and for a different number of points. Important conclusions will be deduced.

7.5.1 S_0 mode

Figure 7.8 shows the contour plot of the error function associated to a single point in the S_0 mode. This point is chosen to be the one that provides maximum s_E and minimum s_v (*fd* = 2.39 *MHz mm*, *c* = 4.05 *km/s*), as shown in fig. 7.4-*top right*.

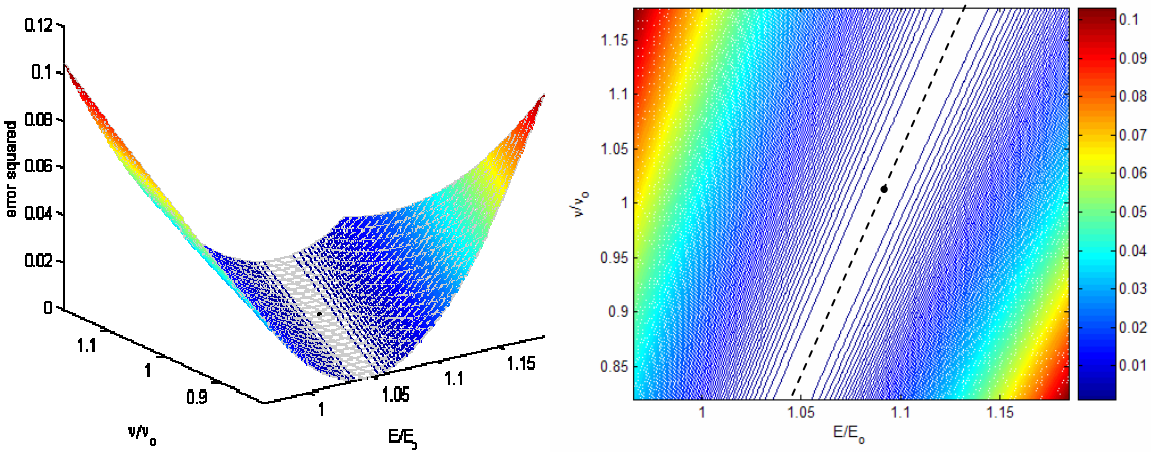

Figure 7.8: Contour plot of the theoretical error function for 1 point in the S_0 mode at (*fd* = 2.39 *MHz mm*, *c* = 4.05 *km/s*): (*Left*) Represented in 3D. (*Right*) Represented in 2D.

The minimum of the theoretical error function is in this case not a point, but a line (dashed line in the figure) in the elastic property values domain. By definition the contour values at fig. 7.8 is the difference between the theoretical phase velocities at the different elastic property values of the domain of definition and the phase velocity at (E^*, ν^*). This difference will be zero at (E, v) = (E^*, ν^*), highlighted as a black dot in previous figures. As the elastic property values changes, the phase velocity also changes because the sensitivity curves s_E and s_v are not always zero. If the change in the phase velocity, caused by a change in one of the elastic properties (say E') can be compensate by the change in the phase velocity caused by a change in the other elastic property (say v') then the new set of values (E', v') will still be a minimum. For instance, in fig. 7.8, the selected point of S_0 mode has associated a positive value of s_E and a negative value of s_v (see fig. 7.4-*top right*). Then as E increases the phase velocity also increases, because s_E is positive. In order to keep $c(E, v) = c(E^*, v^*)$ we need to compensate this increment in the phase velocity by a similar reduction caused by the

change in ν. This implies to increase also ν as $s_\nu < 0$. In consequence the slope of the minima valley is positive as we can see in fig. 7.8. In conclusion when only a point of the dispersion curves is chosen for the error function, then infinite combinations of (E, ν) are solutions of the error function.

The linearity of the minima line is a consequence of the linearity of c with the elastic property values, for changes of the order of a few percent. Its slope in the (E, ν) domain, indicates the relative sensitivity of the dispersion curves to both E and ν at the point at which the error function is calculated. Mathematically the minima line, and any of the contour lines, in fig. 7.8 can be represented as $\partial\nu / \partial E\big|_c$. If we apply to the sensitivity equations 7.10 the mathematical property:

$$\frac{\partial f}{\partial x}\bigg|_y \Big/ \frac{\partial f}{\partial y}\bigg|_x = -\frac{\partial y}{\partial x}\bigg|_f \tag{7.12}$$

We can express the minima line slope as a function of the quotient of the sensitivity values:

$$\left(\frac{\partial \nu}{\partial E}\bigg|_c\right)_{c(E^*,\nu^*)} = -\frac{\nu^*}{E^*}\cdot\frac{s_E}{s_\nu}(E^*,\nu^*) \tag{7.13}$$

Because the minima line is defined by the quotient s_E/s_ν, then interesting properties of the error function can be learned from the differences in these curves for different elastic property values cases, in a similar way as we did in fig. 7.4. However now we only look into the two extreme cases; reference case with E = 64.8 GPa, ν = 1/3 and extreme case with a 9% increment in both elastic properties. Figure 7.9 shows the curves s_E/s_ν associated to the first five symmetric and antisymmetric modes with the same colour code as in fig. 7.4. The comparison of the curves for both cases shows almost no difference, only being considerable in the region of vertical asymptotic discontinuity for the high order modes. These regions are associated to the frequency:thickness product values at which $s_\nu = 0$ for each Lamb mode and these points are affected by the horizontal shift previously discussed as the cut-off frequencies of the high order modes changes when the elastic property values also change. Because the low order modes do not have cut-off frequency, they are not affected by this shift and that is why the curves s_E/s_ν for these modes do not change neither in this region. In the rest of the frequency:thickness product values the s_E/s_ν curves are very horizontal, with mainly four different values being distinguished; two positive and two negative.

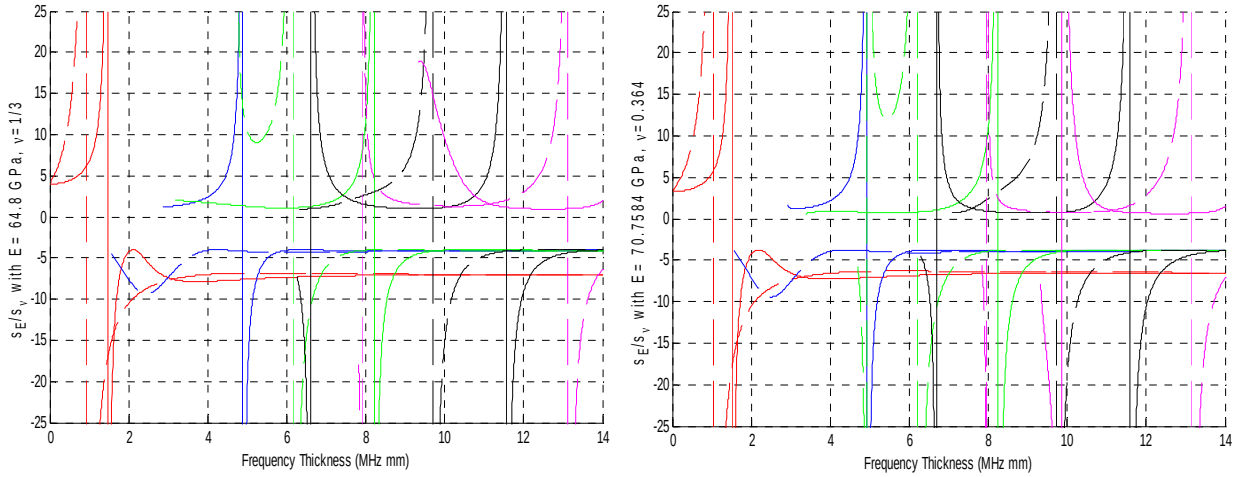

Figure 7.9: s_E/s_v curves for first five symmetric and antisymmetric modes as in fig. 7.4, for elastic property values: (*Left*) $\rho = 2.7\ gr/cm^3$, $E = 64.8\ GPa$, $\nu = 1/3$. (*Right*) $E = 70.7584\ GPa$, $\nu = 0.364$.

The minima line slope is different for the different selected experimental points, however if these points are chosen where s_E/s_v have a horizontal behaviour, then only four slopes are distinguished being very constant during a long interval of the elastic property values. In the other hand if the selected point has a frequency:thickness product values near to a case of $s_v = 0$, then the slope changes even for small changes of the elastic properties, as we see in fig. 7.10 for mode S_1. In this case the minimum of the error function is not a line but a curve with a tangent equal to s_E/s_v at each pair of values (E, v).

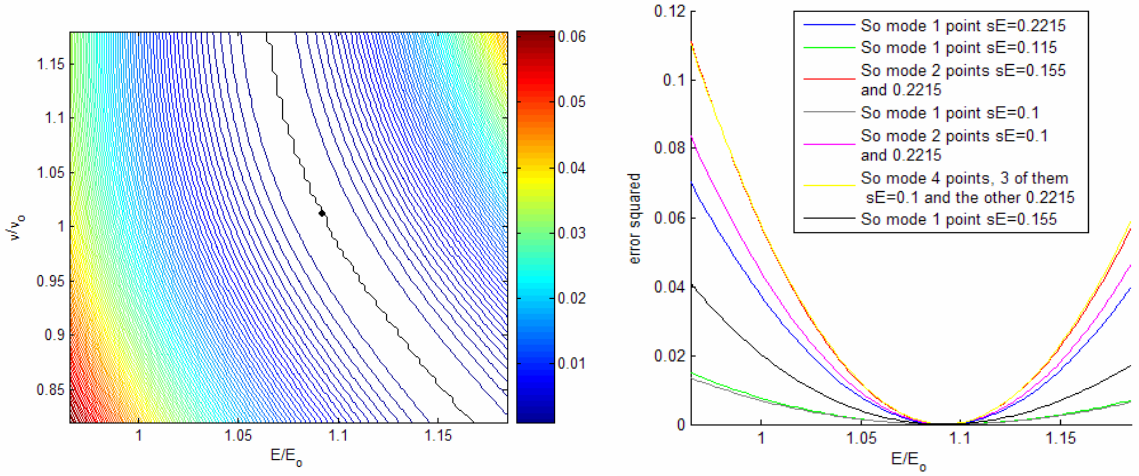

Figure 7.10: (*Left*) Contour plot of the theoretical error function for one point in the S_1 mode at ($fd = 4.53\ MHz\ mm$, $c = 5.83\ km/s$). (*Right*) Sharpness of the minimum against E for different points.

In order to get a unique solution for the error function, more than one point must be chosen. The solution for the elastic property values is given by the intersection of the minima lines associated to each of the points. The less parallel is the slope of the minima lines associated to the selected points, the more accentuated the convergence of the error function to the

unique solution will be, as shown in fig. 7.11. The left part of this figure represents the theoretical error function for two points in the S_0 mode with a very similar negative value of s_E/s_v (being -4 for the lower frequency point and -5 for the higher one). The minimum has a very smooth convergence, and although a unique solution exist, the contour plot shows it as a minima line, this being a proof of its poor convergence. The right part of fig. 7.11 shows the opposite situation, where the two selected points have opposite sign of s_E/s_v (being +4 for the lower frequency point and -4 for the higher one). Notice the clear appearance of a unique minimum evidencing the much better convergence of this case.

The bigger the value of s_E and s_v, the more accentuated the valley of the error function will be. Because this causes a faster change in the phase velocity for the same changes of the elastic properties. As we mentioned, s_E is in general much bigger than s_v, hence it is the s_E that controls the value of the sharpness of the minimum point, and this sharpness will be bigger with respect to the variable E than with respect to v.

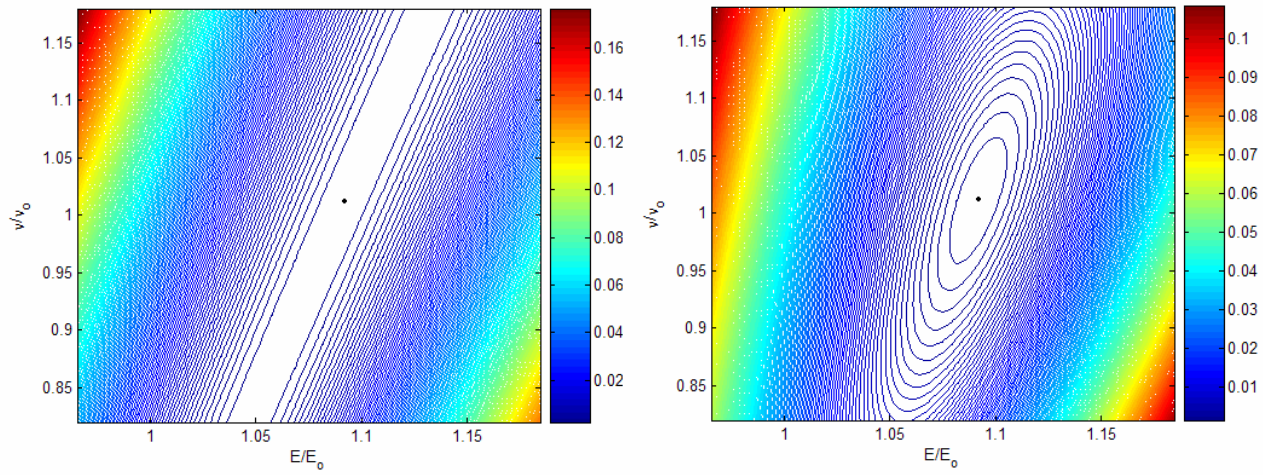

Figure 7.11: Contour plot of the theoretical error function for two points in the S_0 mode. (*Left*) Same sign minima line slopes at (fd = 2 *MHz mm*, c = 4.78 *km/s*) and (fd = 2.39 *MHz mm*, c = 4.05 *km/s*). (*Right*) Opposite sign minima line slopes at (fd = 0 *MHz mm*, c = 5.44 *km/s*) and (fd = 2.39 *MHz mm*, c = 4.05 *km/s*).

As an example fig. 7.10-*right* shows the values of the theoretical error function in the minimum point respect to the variable E for different selected points in the S_0 mode. When only one point is selected then it is clear that the higher the value of s_E associated with it, the sharper the curvature towards the minimum (see curves green, black and blue). However when more than one point is used then the sharpness is also affect by other factors such as; their respective minima slope relationship and the angle of these minima slopes respect to

the E variable axis. However the dominating factor is given by the average of the s_E value for the different points.

In conclusion, the convergence of the inversion process is highly improved by selecting those points with bigger sensitivity values and combining points with positive and negative values of s_v. As shown in the previous section, the inversion process is greatly benefited by the fact that the maxima peaks on the s_E curves for each mode occur at very similar frequency:thickness products values as the minima peaks of s_v for the same mode, and even more important, these peaks are associated to the inflection points in the phase velocity dispersion curves, corresponding to point of low experimental error values.

7.5.2 A_0 mode

The conclusions for the analysis of the S_0 mode are general and they can be extrapolated to any order mode, both symmetric and antisymmetric.

The antisymmetric modes in general are less suitable for the measurement of the elastic properties than the symmetric modes, mainly because the quotient s_E/s_v for antisymmetric modes does not have horizontal sections of both signs as the symmetric modes do. Then the linear slopes associated to the antisymmetric modes points are not only of the same sign, but also very parallel, because as we mentioned and as we can see in fig. 7.9 the horizontal region does not change significantly. In consequence, points selected only in the horizontal region of the curves s_E/s_v for just antisymmetric modes lead to weak minima of the error function. Even though, these antisymmetric points can provide a solution of the inversion process, in contradiction to the affirmation by Rogers in [6] that the A_1 mode alone failed to provide any solution. Our optimization algorithm not only provided a solution for two points of just the A_1 mode (the points associated to the minimum and maximum of the curve s_E/s_v at frequency:thickness products 2.5 *MHz mm* and 4.5 *MHz mm*), but in fact the provided solution is more accurate than the one provided by only two points in the S_0 mode (the two points of fig. 7.11). A better solution is achieved because the selected points in the A_1 mode have higher s_E than the points chosen in the S_0 mode.

The analysis of the error function for points on the A_0 mode gives us an idea for the last weighting factor to be included in the error function presented in eqn. 7.4. The phase velocity difference is bigger, for a same given change in the elastic property values, at those points with higher phase velocity values associated. Even if they have same sensitivity to changes in E and/or v. Therefore the error function will be dominated by the vertical asymptotic points of the high order modes in the cut-off frequencies, because they are the highest phase velocity values in any dispersion curve. These points, as previously mentioned,

are the ones with the highest experimental error associated and so the ones to be avoided, instead of being favoured. The most obvious correction would be to add a weighting factor that normalizes the phase velocity difference in the error function, as given in eqn. 7.14.

$$\sum_{i=1}^{N}\left(\frac{c\left(f_i,c_i,\rho,E_0,\nu_0\right)-c_i}{c_i}\right)^2 \tag{7.14}$$

The beneficial effect of this improvement in the error function can be seen in fig. 7.12 where we have compared the old and new error function applied to two points in A_0 mode (*fd* = 0.0057 *MHz mm*, *c* = 0.24 *km/s* and *fd* = 2 *MHz mm*, *c* = 2.68 *km/s*), with similar s_E (around 0.1) but one order of magnitude different in the phase velocity. To the left we have applied the old error function and it is evident the bad convergence to a unique solution even though they are points with opposite sign for the quotient s_E/s_ν. The minimum is dominated by the much higher phase velocity of the point at 2 *MHz mm* so the error function resembles its minima line. To the right of fig. 7.12 we apply the new error function to the same points, where a clear unique minimum is detected as it should be expected from points with opposite sign minima line slope and equal values of s_E.

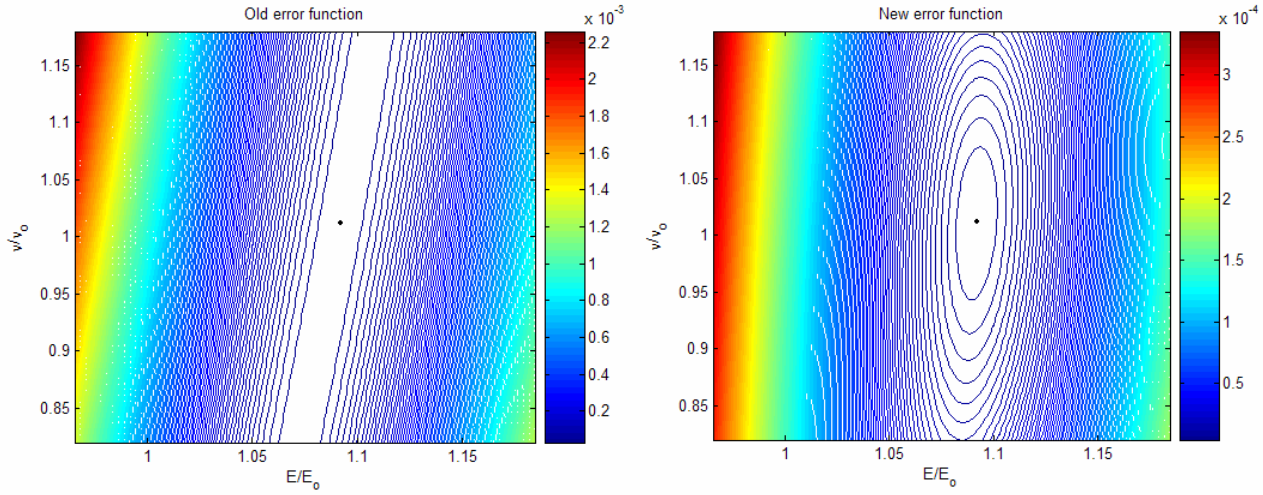

Figure 7.12: Comparison of the old error functions (*Left*) and the new error function (*Right*) for two points of the A_0 mode with similar s_E and s_ν. Elastic property values E_0 = 64.8 GPa, ν_0 = 1/3.

If we combine all the previous weighting factors as described in eqn. 7.11 and eqn. 7.9 we can finally write the definitive error function (eqn. 7.15), which will be applied in the rest of this chapter.

$$\sum_{i=1}^{N}\left(\frac{s_{Ei}+\left|s_{\nu i}\right|}{c_i/(f_i\cdot l)}\right)\cdot\left(\frac{c\left(f_i,c_i,\rho,E_0,\nu_0\right)-c_i}{c_i}\right)^2 \tag{7.15}$$

The benefits provided by the possibility of choosing a few points of the dispersion curves that are highly optimized for the convergence of the error function, are obvious. First, a faster execution and less computer power requirements of the inversion process. Second, the less the number of points chosen then the less likely to lead to failure of the numerical methods used, plus there is less sensitivity to poor initial estimation of the elastic properties. However increasing the number of experimental points used in the inversion process will decrease the effect of the experimental errors over the estimation of the elastic properties, by means of averaging its effect with a bigger number of experimental points. Rogers suggest in his paper [6] that adding new points with lower sensitivities could have bad influence in the estimation of the elastic properties because the minimization calculation could select the wrong mode. The inversion process algorithm we have developed avoids this problem by a clever verification technique of the solved mode. Additionally as we saw in fig. 7.9 the points in the different Lamb modes have their minima line slope uniformly distributed within five different values, combining positive and negative slopes. This obviously helps in a nice convergence of the error function. On the other hand the highly accurate initial estimation of the elastic properties presented in the next section compensates some of the benefits of using less number of points. Adding more points has not caused any appreciable failure of the numerical methods.

We have executed the same numerical analysis done by Rogers in [6] but applied to our algorithm. He compares the elastic properties estimated for three different cases, taking points only from the S_0 mode theoretical dispersion curves with an added random error of normal distribution equal to 1%. First case, only the two optimized points of fig. 7.11 are chosen. Second case, ten points evenly distributed in the frequency:thickness product region between 0 and 14 *MHz mm*. Third case, one hundred evenly distributed points are taken. Next we show the estimated elastic properties in each case:

	Two optimum points	*10 evenly distributed points*	*100 evenly distributed points*
E (*GPa*)	71.0559	70.4407	70.6995
v	0.3574	0.3325	0.3364

Table 7.1: Estimated elastic property values by applying inversion process to different number of experimental points.

Taking into account that the generally accepted elastic property values for aluminium are; E = 70.7584 *GPa* and v = 0.3375, then we can see that the more number of points we take, the more accurate the estimated elastic properties are. This is in contrast with the results given in [6] where the case of only two optimized points was the most accurate. It is important to notice however that the case of 10 points takes four times more processing time than the two

points case, and the one hundred points case takes thirty times more processing time than the two points case.

In the section in which we apply the inversion process to the experimental dispersion curves a uniform distribution of points for all the modes has been used. Nevertheless the important conclusions obtained in this section for selecting the most suitable points can be a great and powerful improvement for future inversion process algorithms.

7.5.3 High order modes

The high order modes require also an analysis of their effect over the error function. We have already mentioned and seen in fig. 7.4 that the points in the dispersion curves with highest sensitivity values to the changes in the elastic properties are those in the frequency:thickness product region around their cut-off frequencies. However the high sensitivity associated with these points is an effect of their vertical asymptotic behaviour. Such that the small horizontal displacement that the changes in the elastic properties causes over the position of the cut-off frequency values will, by definition of a vertical asymptotic point, hugely affect the phase velocity value in this region. The uncertainty in the frequency:thickness product associated to the FFT of the experimental data causes, in the same way as the small horizontal displacements of the dispersion curves, a big phase velocity error. In addition, we also know that the experimental points related to these regions have associated the highest irresolvable error, as previously defined in this chapter, due to the conversion of the dispersion curves from the wavenumber domain to the phase velocity domain. Therefore in contrast with other publications [7,8] we have avoided during the inversion process the points associated to the vertical asymptotic regions. Nonetheless, it is interesting to look at the effect that these points have over the error function.

The phase velocity numerical calculation in the frequency:thickness product values near the cut-off frequencies of the high order modes, can be highly complicated during the inversion process. Small changes on the elastic properties can move the cut-off frequency to higher frequency:thickness values so that the frequency:thickness value of the chosen experimental point does not have solution. The algorithm we have developed wisely and in an optimized way deals with this problem, allowing us to study what happen with the error function in these regions.

Figure 7.13-*left* shows the theoretical contour plot of a point of the A_1 mode near to the cut-off frequency (fd = 1.61 *MHz mm*, c = 25.5 *km/s*). In black we show the minima line slope, which once again perfectly agrees with the minima line associated to the slope in eqn. 7.13 (in red). We must notice that the minima line is very parallel to the border that limits the

elastic property values region for which the phase velocity exists. This region is situated to the right of the dark red contour values (highest theoretical error values). In this region, the values of the elastic properties are such that the cut-off frequency has been shift to frequency:thickness products bigger than fd = 1.61 *MHz mm* so no solution of the dispersion curves can be found. In a similar way we show in fig. 7.13-*right* the contour plot for the S_2 mode at a point near the cut-off frequency (fd = 3.3 *MHz mm*, c = 49.4 *km/s*). In this case we see how the minima line curves follows the curvature of the border of existence of the phase velocity and its slope at (E^*, v^*) is as predicted by eqn. 7.13.

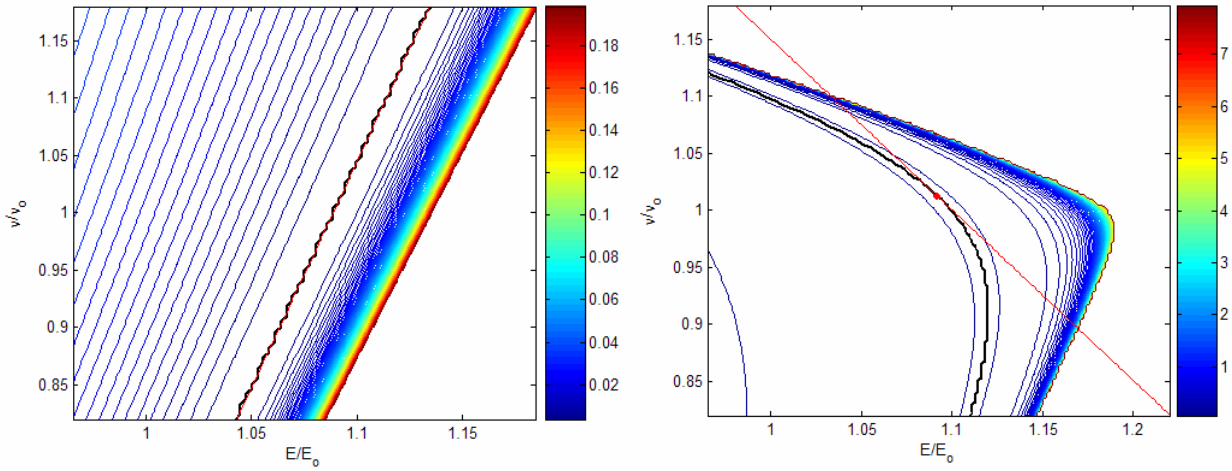

Figure 7.13: Contour plot for high order modes at a frequency:thickness product close to their cut-off frequencies: (*Left*) For A_1 mode at (fd = 1.61 *MHz mm*, c = 25.5 *km/s*). (*Right*) For S_2 mode at (fd = 3.3 *MHz mm*, c = 49.4 *km/s*).

The shape of the border of existence of the phase velocity is defined by the bulk wave phase velocity associated to the mode's cut-off frequency value, in a similar way to the horizontal shift of the sensitivity curves explained in Appendix G. For instance the high order mode A_1 has a cut-off frequency:thickness product equal to c_T / 2. We saw in fig. G.1-*left* of Appendix G how c_T changes as the elastic properties (E, v) change. Its contour values are lines with positive slope with the bulk wave phase velocity increasing as E increases and v decreases. The border of existence is defined by the combination of the elastic property values that makes the cut-off frequency:thickness product be equal to the frequency:thickness product of the point being used in the error function fd_{A1}. When this is applied to the A_1 mode and by the relationship between bulk waves phase velocity and elastic properties given in eqn. A.9 and A.10, it can be easily calculated that the border of existence for the A_1 mode is given by:

$$\bar{v} = \frac{1}{v_0}\left(\frac{E_0}{8 \cdot \rho \cdot fd\_{A1}^{\,2}} \cdot \bar{E} - 1\right) \tag{7.16}$$

Where $\overline{E}$ = E/E0, $\overline{\nu}$ = ν/ν0, ρ = 2.7 *gr/cm*^{3} and for the case in fig. 7.13-left we have *fd_A*$_1$ = 1.61 *MHz mm*, it exactly corresponds to the border of existence that we see in that figure.

In a similar way we can interpret the more complicated shape of the border of existence for the S_2 mode in fig. 7.13-*right*. In this case the bulk wave phase velocity associated to its cut-off frequency can be c_T or c_L / 2 regarding the value of the elastic property ν, thus for:

- $\nu < 1/3$, the cut-off frequency = c_T, then the border of existence is similar to the A_1 mode case as a positive slope line, given by:

$$\overline{\nu} = \frac{1}{\nu_0}\left(\frac{E_0}{2 \cdot \rho \cdot fd\_{S2}^{\,2}} \cdot \overline{E} - 1\right) \tag{7.17}$$

- $\nu > 1/3$, the cut-off frequency = c_L / 2. In this case the cut-off is equal to the other bulk wave phase velocity. We have to look to fig. G.1-*right* of Appendix G in order to see how c_L changes as the elastic properties (E, ν) change, where now the contour are slightly curved lines of negative slope. Very much what we see in the border of existence on fig. 7.13-*right*. The border of existence can be written as:

$$E = \frac{4 \cdot \rho \cdot fd\_{S2}^{\,2} \cdot (1+\nu)(1-2\nu)}{(1-\nu)} \tag{7.18}$$

- $\nu = 1/3 = \nu_0$, then c_L / 2 = c_T, this corresponds to the intersection of both previous borders of existence in fig 7.13-*right*.

All cases perfectly match the border of existence that we see in fig. 7.13-*right*.

The powerful inversion process algorithm developed also deal effectively with the frequency:thickness product region associated to negative group velocities (the concept of group velocity is described in Appendix D). One of the main effects of the modes with negative group velocity is that they have phase velocity values defined at frequency:thickness products below their cut-off frequency as seen in fig. 7.5-*left*. We have already seen that the S_1 mode for elastic property values similar to those of aluminium present negative group velocity. We show in fig. 7.14-*left* the theoretical error function associated to a point of this mode near to its cut-off frequency (*fd* = 2.89 *MHz mm*, *c* = 8.84 *km/s*). The cut-off frequency of the S_1 mode varies between c_T and c_L / *2* regarding the value of ν as it happens with the S_2 mode. In fact these two modes swap these cut-off frequencies, so that the smaller value between c_T and c_L / *2* is the cut-off frequency of S_1 and the bigger is associated to S_2. As we saw in Appendix D the negative group velocity only appears in situations like this one, when two consecutive high order modes of the same type (symmetric

or antisymmetric) share cut-off frequencies proportional to different bulk wave phase velocities. The negative group velocity is always associated to the lower high order mode between them, and only when the value of the elastic properties causes these two cut-off frequencies to be close enough. The border of existence for the contour plot of the theoretical error function is then complementary to that of fig. 7.13-*right*, so that the positive slope border is now at $v > 1/3$ (because at this value of the Poisson's ratio the cut-off frequency associated to S_1 mode is c_T) and the negative slope border (where the cut-off frequency is $c_L / 2$) is defined for $v < 1/3$. However as we plot the adapted versions of equations 7.17 and 7.18 into the S_1 mode contour plot (green dashed lines) we see that only for high values of the Poisson's ration $v > 1.3$ there is an agreement with the border of existence. In the rest of the domain of definition the border of existence is less restrictive by having the cut-off frequency equal to the frequency:thickness value of the chosen point. The reason for a smaller restriction is due to the fact that this mode has associated negative group velocity for this region of elastic property values so that phase velocity values are defined below its cut-off frequency. When $v > 1.3$ the difference between the cut-off frequencies associated to S_1 and S_2 is big enough as to avoid interaction of their dispersion curves such that no negative group velocity exist for the S_1 mode. This is why in this region the cut-off frequency limit agrees with the border of existence.

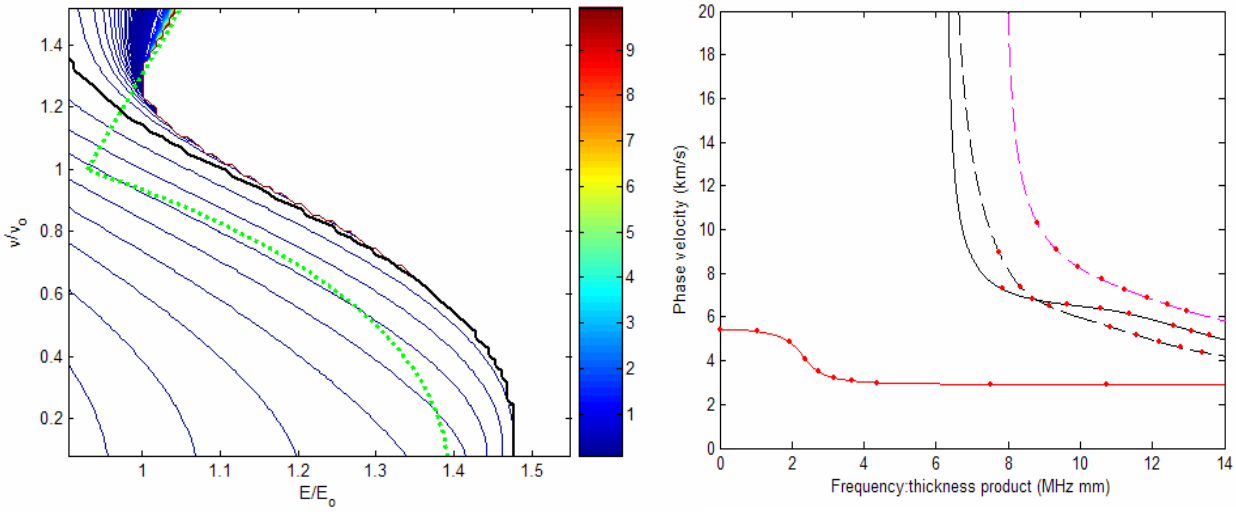

Figure 7.14: (*Left*) Contour plot for S_1 modes at a frequency:thickness product with negative group velocity ($fd = 2.89$ *MHz mm*, $c = 8.84$ *km/s*). (*Right*) Uniformly selected points of the modes S_0, S_3, A_3 and A_4.

The analysis of the error function presented in this section has never been published before. Most of the interesting conclusion here deducted may be included in a future version of the inversion procedure in order to further optimize and automate it.

We finish this analysis of the error function by looking into the effect of the phase velocity values experimental error. Some qualitative idea of this effect can be achieved by adding a normal distributed noise of amplitude 4% in the theoretical phase velocity values for the points selected. Figure 7.15 shows this analysis for different experimental points situations. The contour error function diagrams in the top of this figure are associated to a set of two points selected from the mode S_0 (*fd* = 0 *MHz mm*, *c*= 5.44 *km/s*) and the mode S_3 (*fd* = 11.37 *MHz mm*, *c*= 6.14 *km/s*). These points have been carefully selected so that an interesting phenomena can be displayed. For some combinations of the selected points, the curvature of their minima lines allow intersection in more than one point, thus multiple local minima exist (see fig. 7.15-*top left*).

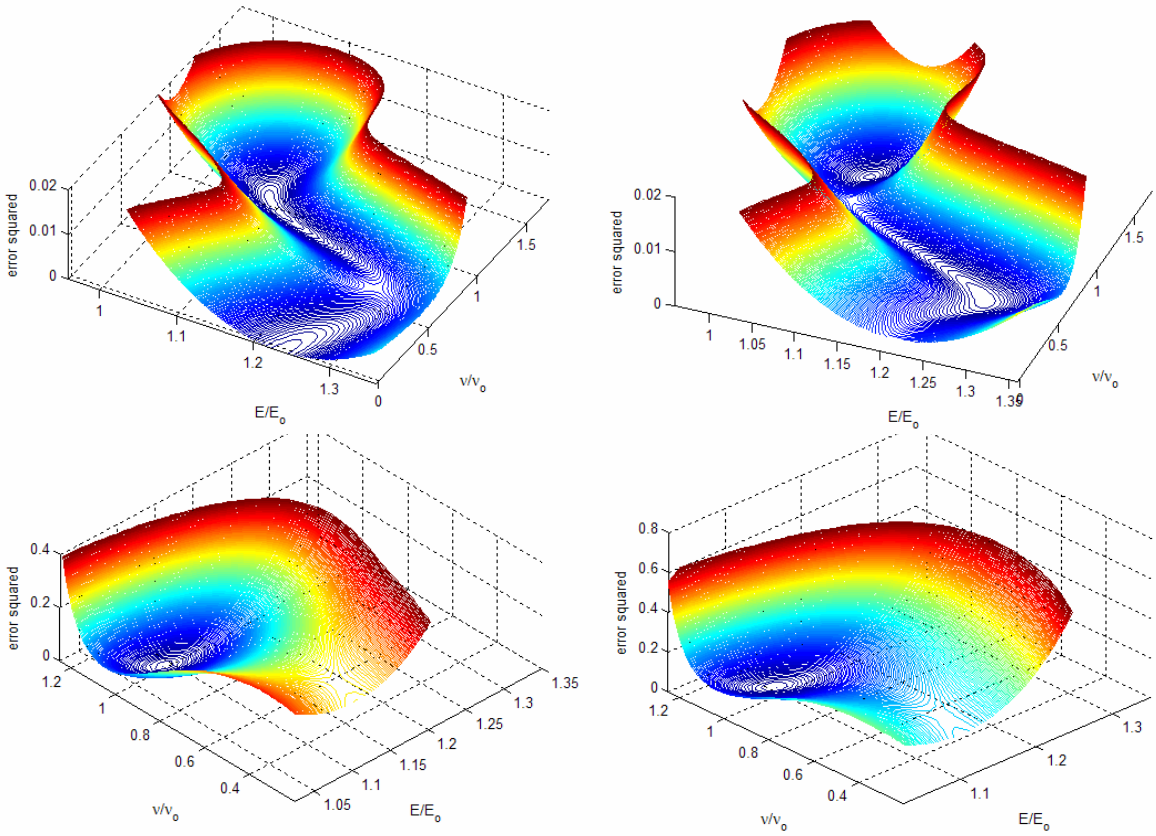

Figure 7.15: Effect of a normal distributed error in the phase velocity of amplitude 4%, over the contour plot of the theoretical error function: (*Top*) Two selected points; (*fd* = 0 *MHz mm*, *c*= 5.44 *km/s*) in the S_0 mode and (*fd* = 11.37 *MHz mm*, *c*= 6.14 *km/s*) S_3 mode. (*Bottom*) Uniformly selected points of the modes S_0, S_3, A_3 and A_4. No error and added error at left and right respectively.

The global minimum corresponds to the correct solution of the elastic property values. Usually, as in the depicted case, the multiple local minima are far enough so that a good initial estimation of the elastic property values should make the inversion algorithm to

converge to the correct solution. However if we add a normal distributed error of 4% in the phase velocity value of the selected points then the local minimums could get close to each other as shown in fig. 7.15-*top right*.

This problem will be addressed in section 7.7 by applying global optimization techniques to the inversion process, like for instance a genetic algorithm. Nonetheless the previous multiple local minima effect was a worse case scenario, in most situations this is not a problem. In fact the multiple solutions effect decreases when a higher number of points from different modes are selecting for the inversion process. Because the experimental error tends to average out, and because the multiple shapes of the minima lines associated to the different points also cancel out the additional local minima, as shown in the figures 7.15-*bottom*. These figures include the previous points and some others from four different modes (S_0, S_3, A_3 and A_4) as shown in fig. 7.14-*right*. With the left figure showing just the theoretical phase velocity values, and the right figure includes a normal distributed error of 4% amplitude. We see that the multiple local minima have disappeared, and that the presence of error in the data clearly flattens the minimum point decreasing in consequence the convergence of the optimization algorithm.

7.6 INITIAL ESTIMATION OF THE ELASTIC PROPERTIES

This section describes an original technique for the direct estimation of the Young's modulus, Poisson's ratio and thickness of the sample plate, from the experimentally obtained dispersion curves. The technique extracts these values by looking into the frequency: thickness product information of the vertical asymptotic behaviour for the high order modes, and the horizontal asymptotic behaviour of the low order modes.

The elastic properties obtained in this way are passed as initial values to an optimization inversion procedure applied over the Lamb waves' phase velocity information, for a more accurate estimation of their values. Notice that the initial estimation technique obtains the elastic property values based mainly in frequency:thickness product information, meanwhile the inversion technique optimizes these values based in complementary phase velocity information.

The current technique, like any technique based in Lamb wave propagation information, cannot measure E and ρ independently, only as E/ρ. However we assume the value of ρ to be the standard one for aluminium (2.7 gr/cm^3). Any variations of the plate's density from this value will propagate into variations of the estimated value for E.

The technique is based in three steps:

7.6.1 Calculate the bulk waves phase velocities (c_T, c_L) from the cut-off frequencies of the high order modes

The cut-off frequencies of the high order Lamb modes are the frequency:thickness products at which the different high order Lamb modes start to originate. The high order modes initiate as standing longitudinal and/or transversal waves across the thickness of the plate. This implies that the mode's group velocity must be null at these points, or equivalently their phase velocity must be infinite. These points are associated to a vertical asymptotic behaviour of the Lamb mode's phase velocity dispersion curves and to a null cross in the wavenumber dispersion curves.

Eqn. A.24 shows the relationship of the symmetric modes cut-off frequency:thickness product values with the bulk waves phase velocities, and eqn. A.25 shows the same relationship for the antisymmetric high order modes.

In the experimental dispersion curves for a rectangular aluminium plate plotted in fig. 6.18, the most accurately defined cut-off frequencies appear to be the modes S_1, S_2, S_5, A_1 and A_3. Their values together with the experimental errors are given in table 7.2, and the associated normalized bulk wave phase velocity is also calculated.

Mode	*Cut-off frequency:thickness value* (*MHz mm*)	*Normalized bulk wave phase velocity associated* (*Hz*)
S_1	2.67 ± 0.02	c_T / d = 2.67 ± 0.02
S_2	2.76 ± 0.02	c_L / d = 5.52 ± 0.04
S_5	8.235 ± 0.02	c_L / d = 5.49 ± 0.02
A_1	1.36 ± 0.03	c_T / d = 2.72 ± 0.06
A_3	5.498 ± 0.015	c_L / d = 5.498 ± 0.015

Table 7.2: Cut-off frequency thickness values of the most accurate experimental points and their associated normalized bulk wave phase velocity value.

Although all the experimentally measured normalized bulk wave phase velocity values agree within their error interval, we take those values of higher accuracy; c_L / d = 5.498 ± 0.015 *MHz mm* and c_T / d = 2.67 ± 0.02 *MHz mm*. The reason for normalizing the phase velocity values with respect to the thickness of the plate d, is due to the assumption that this thickness is unknown. We know that the original thickness of the plate was 1.18 *mm*, however the ablation regime for the laser ultrasonic generation has decreased the thickness slightly in the generation area.

7.6.2 Calculate ν from the values of c_T and c_L

As we already show in eqn. A.9 and A.10 the bulk waves phase velocities are related with the elastic properties (E, ν and ρ) in a way such that their quotient depends only in ν as shown in eqn. 7.19.

$$\nu = \frac{2\left(c_T / c_L\right)^2 - 1}{2\left[\left(c_T / c_L\right)^2 - 1\right]} \tag{7.19}$$

Substituting the previously obtained values for c_T and c_L, gives the initial estimation of the Poisson's ratio to be $\nu = 0.346 \pm 0.008$.

7.6.3 Calculate the plate's thickness from the values of c_T, ν and the Rayleigh wave phase velocity

As described in Appendix A, *Rayleigh waves* are the solution to the elastic wave equation for a wave propagating in the free surface of a half-space elastic medium. In opposition with Lamb waves, the Rayleigh waves are non-dispersive and their phase velocity is given by eqn. A.15.

Experimentally it can be shown that when the thickness of the plate d is twice or higher a Rayleigh wavelength λ_R, the low order Lamb modes (A_0 and S_0) have a great similarity with Rayleigh waves. They become non-dispersive, and they interfere with one another in such a way that the depth distribution of the displacements for the upper and lower halves of the plate is similar to that of the Rayleigh waves. This distribution transfers from one to the opposite surface of the plate every multiple of a distance L from the source, which is a complex function of d / λ_R [9]. At a distance from the source $<< L$ the low order Lamb modes become indistinguishable from a Rayleigh wave and their phase velocity satisfies eqn. A.15. In the experimental case here studied, for any frequency value $f > 5$ *MHz* then the condition $d > 2 \cdot \lambda_R$ is satisfied. Thus taking the point in the experimental dispersion curves at $f = 8.7$ *MHz*, with a phase velocity of the low order modes equal to $c = 2.885 \pm 0.015$ *km/s*, this gives a value for $L \approx 1.5$ *m*. In our experiments, the farthest distance source-sensor is less than 15 *cm* (as depicted in Chapter 6) then the measured phase velocity satisfies correctly eqn. A.15. By substitution of the obtained values of c_T / d and ν, we get a thickness of the plate equal to $d = 1.16 \pm 0.03$ *mm*. This value is then used together with the obtained c_L / d to get the initial estimation for Young's modulus, which corresponds to $E = 70 \pm 4$ *GPa*. The thickness estimated by this technique is more accurate than the technique described in [10] (at least for our experimental ultrasonic signals), however their technique does not require of previous calculation of any elastic property value and it only needs a single ultrasonic signal.

A good initial estimation of the elastic property values is important for the optimization routine of the inversion process to be more effective, and the technique here presented provide a very good initial estimation as we will see next.

7.7 APPLICATION TO EXPERIMENTAL DATA

Once a good initial estimation of the elastic and geometrical properties for the sample under test is known, the developed inversion algorithm is applied in order to optimize as much as possible these estimated values. The inversion algorithm consists in applying iteratively corrective values to the elastic properties in order to minimize the difference between the experimental dispersion curves and the modified theoretical ones. This difference is properly defined by the error function in eqn. 7.15. Based in that expression of the error function, the problem is a mean least-square fit criteria to the set of experimental points (c_i, f_i) selected for the inversion algorithm.

The experimental points to be used in the inversion process could be carefully selected based in the conclusions of section 7.5 in this chapter. In this way few very suitable points are used in the optimization, reducing effectively the computer power requirements of the inversion process. Other approach consists in increasing the number of selected experimental points in the different modes. In this way the effect of the experimental errors over the estimation of the elastic properties is decreased, as the experimental error is averaged out with a bigger number of experimental points. More number of experimental points in the inversion process also helps reducing the effect of local minima in the error function, as already seen. This last approach is the one taken here, where the experimental points are selected uniformly through the different modes' dispersion curves, avoiding the vertical asymptotic regions of the high order modes.

The section of the inversion algorithm that minimizes the error function for the selected set of experimental data pairs (c_i, f_i) is the optimization algorithm. Here we use and compare two different optimization techniques thoroughly described in Chapter 5, these are:

- *Downhill simplex algorithm* (DHS): It is capable of minimizing a function of several independent variables only requiring function evaluations, without the need of numerical or analytic derivatives. It is not very efficient in the number of function evaluations required, so although it could be a bit slow it can also be extremely robust. What make of it one of the most used nonlinear optimization techniques. This algorithm can handle discontinuities of the function to be minimized, but it might only give local solutions.

- *Gradient method and line search algorithm for nonlinear least-squares problem* (LSP): This algorithm uses gradient information of the object function by means of a quasi-Newton method, to dictate a direction of search where the minimum is thought to lie. Once the direction of search is known, the algorithm uses a line search procedure to know how far to move in that direction towards the minimum.

  This method uses not only function evaluation but also gradient information then it is more powerful than the downhill simplex algorithm, providing more accurate results. Gradient methods are also generally more efficient when the function to be minimized is continuous in its first derivative as it is our case, and this efficiency is further improved by optimizing this technique for least-squares problems as described in Chapter 5. However as in the previous method it might only give local solutions.

The inversion process is now applied over three different regions of the experimental dispersion curves obtained in Chapter 6. For each of these regions both optimization techniques will be compared. The three areas in which we divide the experimental dispersion curves are; the vertical asymptotic region associated to the cut-off frequencies of the high order modes, the horizontal asymptotic region at high frequency:thickness product values where the dispersion curves have a non-dispersive tendency, and finally the central region of the dispersive behaviour of the different modes.

7.7.1 Vertical asymptotic region

The experimental points in this region are the less adequate for the inversion process as explained in previous sections. As they are the points with higher experimental error associated. Figure 7.16 shows the selected points as black dots over the experimentally obtained dispersion curves in the phase velocity domain.

The obtained values for the elastic properties are:

- *DHS algorithm*: E = 73.0443 *GPa*; ν = 0.3418. Error function for optimized elastic properties = 4.2108. Processing time = 135 *sec*.
- *LSP algorithm*: E = 73.0443 *GPa*; ν = 0.3418. Error function for optimized elastic properties = 4.2108. Processing time = 155 *sec*.

We see how both optimization techniques give the same solution for the elastic properties but with the LSP algorithm takes slightly more processing time. Probably due to the fact that the error function presents a high discontinuity in the border of existence of the phase velocity for points in the cut-off frequency region, as seen previously.

The solution for the elastic properties seems too different from the estimated values of previous section, and the obtained value of E is too big for an aluminium plate.

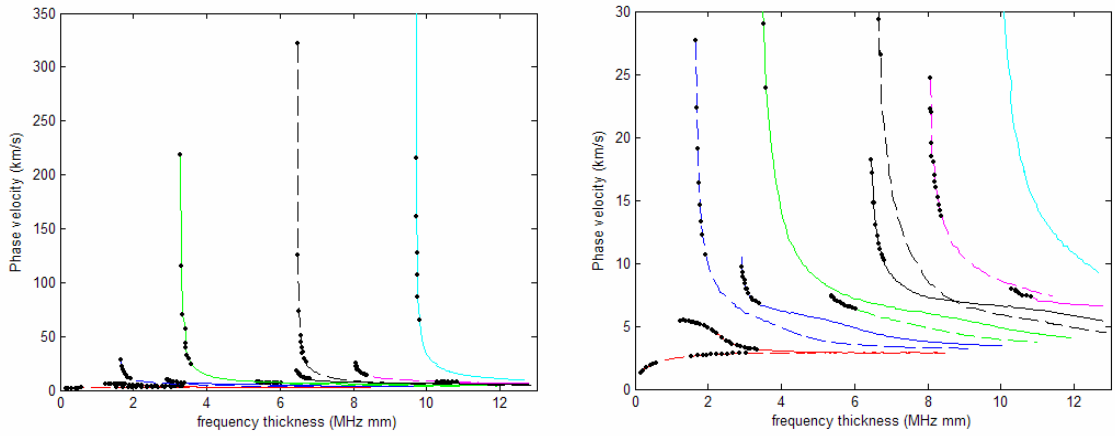

Figure 7.16: Selected points in the vertical asymptotic area of the high order modes: (*Left*) Plotted over the experimental phase velocity dispersion curves. (*Right*) Zoom of the left figure.

7.7.2 Horizontal asymptotic region

These points are the most accurate ones from the experimental error point of view (as seen in fig. 7.2-*right*). At high frequency:thickness product values the high order modes' phase velocity converge to the transversal bulk wave phase velocity meanwhile the low order modes converge to the Rayleigh phase velocity. Figure 7.17-*left* shows the points chosen in this case for the inversion algorithm.

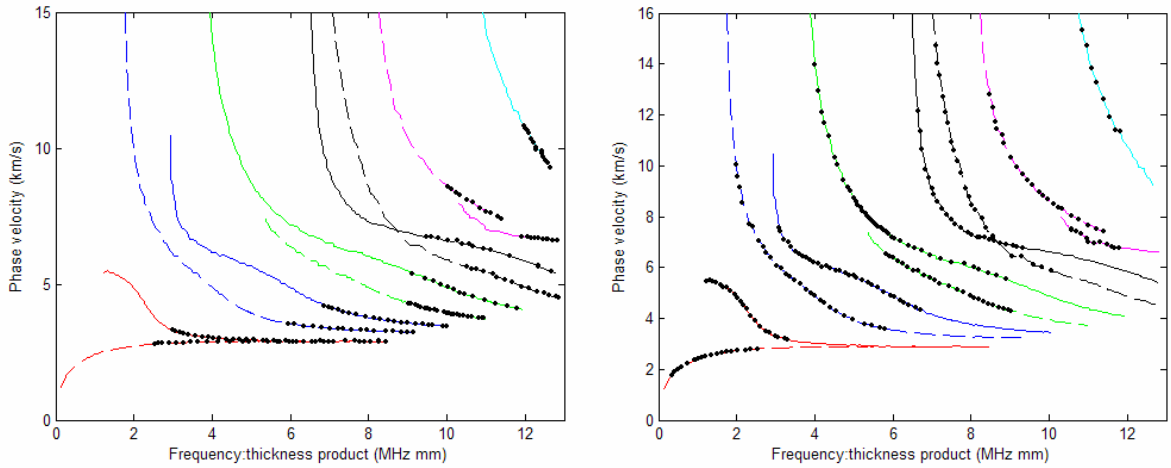

Figure 7.17: Selected experimental points for the inversion algorithm: (*Left*) Points taken from the horizontal asymptotic region. (*Right*) Points taken from the dispersive central region.

The obtained values for the elastic properties are:

- *DHS algorithm*: E = 70.5618 *GPa*; ν = 0.3528. Error function for optimized elastic properties = 0.0394. Processing time = 107 *sec*.
- *LSP algorithm*: E = 70.5618 *GPa*; ν = 0.3528. Error function for optimized elastic properties = 0.0394. Processing time = 20 *sec*.

Both optimization algorithms provide the same solutions for the elastic properties however now it is clear the much higher efficiency of the LSP algorithm as it requires five times less processing time than the DHS algorithm.

The optimized Young's modulus is now very similar to the estimated one, but the optimized Poisson's ratio differs slightly more than the previous case. The present value of the optimized elastic properties seems more adequate for an aluminium plate. The current better solution in comparison with the previous case has its origin in the smaller experimental error associated with the selected experimental points.

7.7.3 Dispersive region

Finally we look into the central region of the dispersion curves, where the different modes present high dispersion. The points chosen in this case are shown in fig. 7.17-*right*.

The obtained values for the elastic properties are:

- *DHS algorithm*: E = 71.7341 *GPa*; ν = 0.3488. Error function for optimized elastic properties = 0.1884. Processing time = 146 *sec*.
- *LSP algorithm*: E = 71.7341 *GPa*; ν = 0.3488. Error function for optimized elastic properties = 0.1884. Processing time = 36.5 *sec*.

Again the solutions given by both optimization algorithms are identical, but once again the LSP algorithm is several times faster than the DHS.

Both optimized elastic properties are now very similar to the estimated ones and within the range of accepted values for aluminium.

It is remarkable how the results of the inversion process in the present and previous cases are very consistent with the initial estimated values. Notice that meanwhile the estimated values were obtained from the asymptotic behaviour of the dispersion curves (both vertical and horizontal), mainly based in frequency:thickness product information. The optimized elastic property values from the inversion process are obtained from the non-asymptotic region of the experimental dispersion curves and they are based in phase velocity information. Both

techniques are applied over complementary information and nevertheless they provide a very consistent result.

7.7.4 Low experimental error region

The optimized elastic property values obtained in the horizontal asymptotic region and the dispersive region are very similar between them and very different from the values obtained from the vertical asymptotic region. As we know the later are associated with high experimental errors that obviously will affect negatively their effectiveness. In the other hand the horizontal and dispersive regions are data of the highest experimental resolution. It is also difficult to differentiate these two regions for high order modes and for the frequency:thickness product interval at which we work. This is why we have decided to finally apply the inversion process to a region which is combination of these two and with a relative irresolvable phase velocity error below 4% as shown in fig. 7.2-*right*. The optimization algorithm used will be the LSP because it provides results of equal accuracy than the DHS algorithm but with much less processing power requirements. This is important when the inversion process is applied to a big number of experimental points as it is the current case.

The obtained values for the elastic properties are:

- *LSP algorithm*: E = 71.0548 *GPa*; ν = 0.3516. Error function for optimized elastic properties = 0.274. Processing time = 52 *sec*.

This solution is in between the ones given in the previous two cases and so this is the one accepted as best solution for this experimental analysis.

7.7.5 Including the thickness of the plate as an unknown in the optimization algorithm

Until this point the inversion algorithm has not take into account the estimation of the thickness of the plate (1.16 *mm*). We have always considered the thickness to be 1.18 *mm*, which was the nominal thickness of the original plate. The difference between the nominal and estimated thickness lies in the erosion that the ablation regime for the optical source creates over the plate surface in the region of ultrasonic wave generation.

An improvement of the inversion algorithm has been done in order to include also the thickness as an optimization variable.

Testing the three variables optimization algorithm over theoretical dispersion curves

We have tested the three variables inversion algorithm applying it over uniformly distributed points through the theoretical dispersion curves for aluminium, avoiding the vertical asymptotic region as shown in fig. 7.18-*left*. A normal distributed error of amplitude 1% was added to the phase velocity data. We have used worse initial estimation than previously obtained (E_0 = 71.7 *GPa*, v_0 = 0.35 and d_0 = 1.15 *mm*). The optimized results for the three variables is: E = 70.8093 *GPa*, v = 0.337 and d = 1.1803 *mm*. These values very closely agree with the commonly accepted values for aluminium (E = 70.7584 *GPa*, v = 0.3375 and d = 1.18 *mm*), therefore validating the three variables optimization algorithm.

Application of 3 variables optimization algorithm over low experimental error region

If we use the three variables optimization algorithm over the experimental data of figure 7.2-*right*, the optimized results are:

- *LSP algorithm* for three variables: E = 69.6213 *GPa*; v = 0.3484; d = 1.1575 *mm*. Error function for optimized elastic properties = 0.1836. Processing time = 156 *sec*.

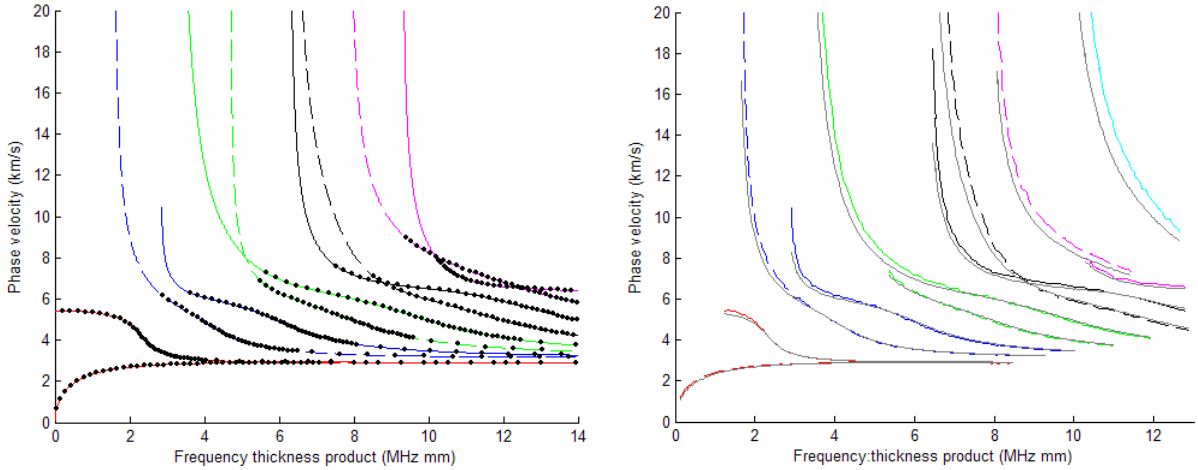

Figure 7.18: (*Left*) Selected points from theoretical dispersion curves to verify the three variable optimization algorithm. (*Right*) Comparison between experimental dispersion curves and theoretical ones (in grey) obtained using the Aluminium properties E= 70.7584 *GPa*, v = 0.3375, d = 1.16 *mm*.

Notice that now the optimized solution is even closer to the first estimated elastic property values and that the error function for the optimized values is now smaller than the previous case in which the thickness was not optimized. Obviously adding an extra variable for minimizing the error function will help in getting a better optimized error function value. Figure 7.18-*right* compares the experimental dispersion curves and the theoretical ones obtained with the commonly accepted values of the elastic properties for aluminium.

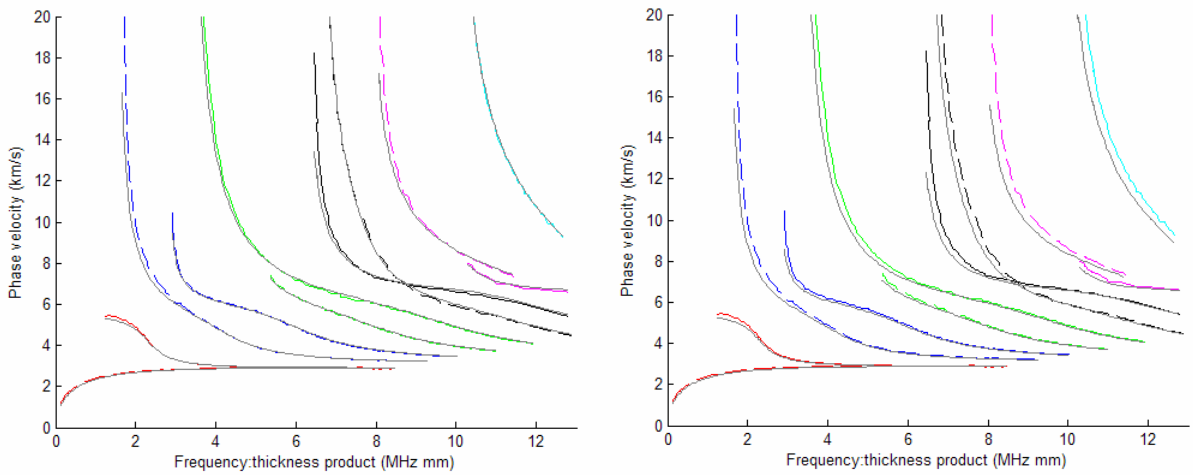

Figure 7.19: Comparison between experimental dispersion curves and theoretical ones associated to elastic property values: (*Left*) Obtained for the 3 variables optimization algorithm (E= 69.6213 GPa, v = 0.3484, d = 1.1575 mm). (*Right*) Obtained for the 2 variable optimization algorithm E= 71.0548 GPa, v = 0.3516, d = 1.16 mm.

The considerable disagreement on fig. 7.18-*right* is in contrast with the much better matching that takes place in fig. 7.19. The left graph of this figure compares the experimental dispersion curves with the theoretical ones for elastic properties obtained with the two variable optimization algorithm for points selected in the low experimental error region. In the right graph the theoretical dispersion curves are associated to elastic property values obtained with the three variables optimization algorithm. In both cases we appreciate important differences in the vertically asymptotic region mainly due to the higher experimental error associated to these points, the low experimental error region agrees considerably well, with in general a slight better agreement for the two variable optimization algorithm than for the three variables one

7.7.6 Global solution by genetic algorithms

We have already seen that the error function could have multiple local minima solutions. This damaging effect can be reduced by adding a big number of experimental data points and by providing an accurate first estimation to the optimization algorithm. Nonetheless because the previously used optimization algorithms can only provide local minimum solutions, it is a good idea to test the obtained optimized elastic and geometrical properties with a global optimization method like the genetic algorithm, described in Chapter 5. This algorithm is modelled based on the principles of evolutionary biology via natural selection. It is less susceptible to give local minima than the previous methods, and it improves the chances of

finding a global solution. However it tends to be computationally very expensive, this is why it is not implemented as a default optimization algorithm in the inversion process.

We used the implementation that MATLAB provides of this algorithm, considering only a two variables (E, v) problem. We applied the algorithm taking the default values for most of its options; population size of 20 (represent the number of individuals in each generation or iteration. An individual is a pair (E, v)), fitness scaling function used is *Rank* (it scales the raw fitness scores of each individual based on the position of the shorted score of each individual rather than in the score itself. This information is used by the selection function), the selection function used for choosing the parents of the next generation is S*tochastic uniform*, an Elite count of 2 is used in the Reproduction (it represents the number of individuals guaranteed to survive to the next generation) and a Crossover fraction of 0.8. A Gaussian mutation function is used with a scale value of 1 and a shrink value of 1. For the *stopping criteria* of the algorithm we have defined a maximum Generation of 100 (that is the maximum number of iterations allowed), a Time limit of 40 minutes (so if the algorithm is running longer than this time, it stops), a Fitness limit of 0.2 (based in the value of the error function for optimized elastic properties = 0.274 that we obtained with the LSP algorithm), a Stall generation limit of 15 (so if there is not improvement of the best fitness value in the number of iterations specified then the algorithm stops) and Stall time limit of 17 minutes (if there is not improvement in the best fitness value during the specified time, the algorithm stops). The genetic algorithm stops only if any of these stopping criteria are satisfied.

In order to make the algorithm more effective we have specified a lower and upper bound for the entries of the elastic property values of the initial population (also known as *initial range*), based in the knowledge of the experimental initial estimation previously presented. We started with an initial range of $E_{max} = 74\ GPa$, $E_{min} = 67\ GPa$, $v_{max} = 0.38$ and $v_{min} = 0.3$, after 27 generations and terminated by running more than the limited 40 minutes the global solution given by the Genetic Algorithm was $E = 71.67\ GPa$ and $v = 0.349$ with an error function evaluation for the optimized parameters of 0.374 (far bigger error than the obtained with the LSP algorithm). However if we used these values as initial estimation for the LSP algorithm (with better convergence capabilities than the Genetic Algorithm) it provided the same solution than before with the experimentally obtained initial estimation ($E = 71.0548\ GPa$; $v = 0.3516$), proving that effectively it is a global solution.

We tried making the initial range even more restrictive; $E_{max} = 73\ GPa$, $E_{min} = 68.5\ GPa$, $v_{max} = 0.37$ and $v_{min} = 0.32$. In this case the algorithm stopped because it exceeded the stall time limit of 17 minutes, giving after 17 generations a solution of $E = 71.12\ GPa$ and $v = 0.3506$

with an error function evaluation of 0.286. This solution is closer to the one obtained with the LSP algorithm previously, and again if we help to a better convergence of the optimized solution by applying the LSP algorithm we get again the solution (E = 71.0548 *GPa*; ν = 0.3516), proving once more that it effectively corresponds to a global solution.

7.8 EXPERIMENTAL VERIFICATION OF THE OBTAINED ELASTIC PROPERTY VALUES

In order to test the validity of the obtained elastic properties values, we look into a region of the dispersion curves that we have not used yet, nor for the initial estimation of the elastic properties, neither for the optimized values of the inversion process. This new region is the highly non-dispersive region of the S_0 mode at low frequency:thickness product values. From the Lamb wave characteristic equation, it is easy to probe that the phase velocity of the S_0 mode at low frequency:thickness product values can be approximated to eqn. A.22 [9].

Because the S_0 mode is highly non-dispersive in this region, the group velocity is very similar to the value of the phase velocity. For instance, in fig. 7.20-*left* we compare phase velocity (in blue) and group velocity (in red) for the S_0 mode in aluminium at low frequencies. Notice that the vertical axis plots the phase velocity between 5.4 and 5.44 *km/s*. In the frequency:thickness product region between 0 and 0.25 *MHz mm*, the phase velocity changes less than 0.1%. The group velocity at 0.25 *MHz mm* is only 0.2% smaller than the phase velocity. This region can accurately be considered non-dispersive, and because this plot is given for an aluminium plate of 1.17 *mm* thick then at frequencies below 200 *kHz* the group velocity satisfies eqn. A.22.

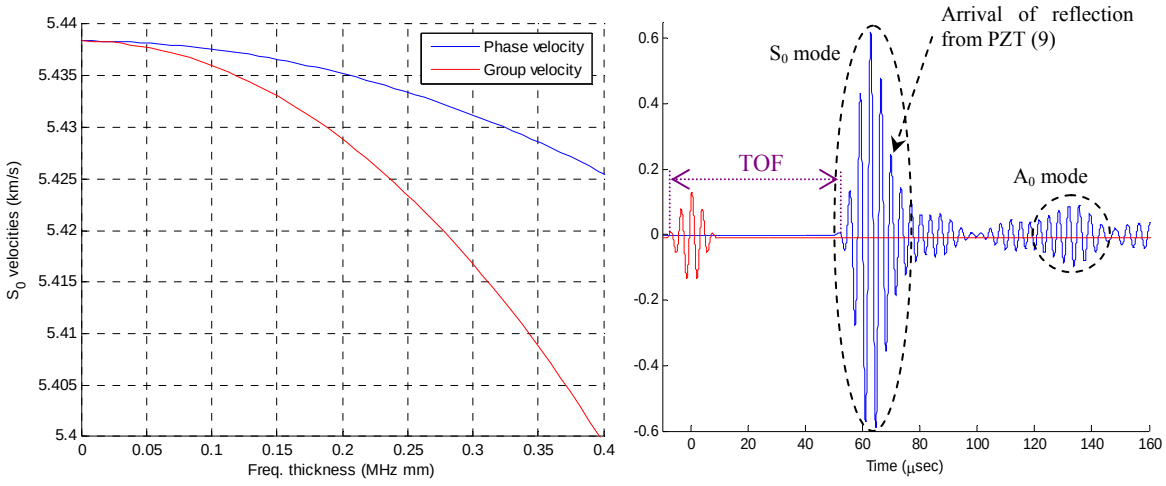

Figure 7.20: (*Left*) Comparison of the phase and group velocity for the S_0 mode in aluminium in the region of not dispersion. (*Right*) Ultrasonic signal detected in PZT_{ref} (in blue) with source at PZT_{10}. In red is the excited 4.5 cycles toneburst signal at 180 *kHz*.

In all materials the fastest propagating Lamb wave component is the S_0 mode at the previous group velocity. Thus, by analysing the time of arrival of the first ultrasonic perturbation of the broadband ultrasonic signals that we used in Chapter 6 to estimating the phase velocity dispersion curves, for which we know the distance source-sensor, we can experimentally measure this value. Later we compare it with the value given by eqn. A.22 by substitution of the elastic properties extracted with the inversion process in order to certificate the quality of the estimation.

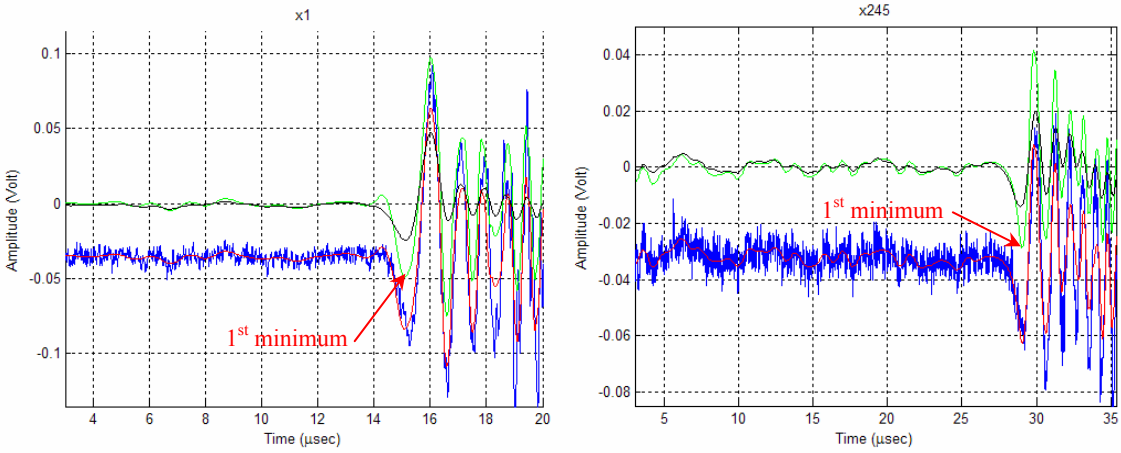

Figure 7.21: Comparison of the de-noised ultrasonic signal at two different source possitions to meassure the group velocity of the S_0 mode at low frequency:thickness product values. In blue is the detected ultrasonic data. In red after Daubechie wavelet de-noising till order 6 and full detail fitering apart of D_6. In green same wavelet de-noising plus 1st order Butterworth high pass filter at 30 *kHz*. In black same high pass filter as before plus 1st order Butterworth low pass filter at 500 *kHz*.

Fig. 7.21 shows in blue the received ultrasonic signals zoomed over the S_0 mode region, in the left for the closest distance source-sensor and in the right for the farthest. Although these distances are approximately known, they are not as accurate as the distance between both sources, as the position of the focused beam for the modified Mach-Zehnder interferometer system can not be accurately known. The distance between both sources is 74.37 ± 0.05 *mm*. In order to measure the difference in the time of arrival of the first perturbations between both signals we need to de-noise the signals. We have tried with three different de-noising techniques; (*red curve*) we apply a wavelet de-noising as explained in Chapter 5, for a Daubechie wavelet with a decomposition to order 6 and filtering fully all the details apart of D_6. This corresponds to a very selective low pass filtering, however the low frequency noise make difficult to see where begins the ultrasonic perturbation. (*Green curve*) same wavelet de-noising combined with a 1st order Butterworth high pass filter at 30 *kHz*, this helps with the low frequency noise. (Black curve) finally we compare with a situation with same high

pass filter as before and instead of wavelet de-noising, we apply a 1st order Butterworth low pass filter at 500 *kHz*, it is obvious the much better quality of the green signal. For instance the black curve does not show the first peak arriving at 14 μsec in fig. 7.21-*left*.

We look to the first minimum of the green curves in order to measure the TOF, being of 15.09 ± 0.03 μsec for the closest distance source-sensor and 29.06 ± 0.03 μsec for the farthest. The group velocity associated is $c_g = 5.32 \pm 0.02$ *km/s*.

The group velocity obtained by substitution of the optimized elastic property values in eqn. A.22 is $c_g = 5.48$ *km/s*, very different from the validation value. Does this mean that the inversion process is highly inefficient? The answer is not, a careful analysis of the 1st minimum oscillation in fig. 7.21 shows that it is associated to a frequency of between 450 to 500 *kHz*. This region is clearly dispersive as we can see from fig. 7.20 and so the eqn. A.22 does not apply. Furthermore, the theoretical group velocity of S_0 mode in aluminium at 500 *kHz* is effectively 5.31 *km/s*.

In conclusion the broadband ultrasonic data is not suitable to validate the estimated elastic properties based in eqn. A.22. Therefore an experiment has been developed with the sole purpose of achieving this validation. In the same experimental set up as the one used for directivity experiments in the wavefront integration analysis of Chapter 4 (see fig. 7.22-*left*), we use the property of the PZTs acting both as ultrasonic source and receiver.

We have taken two sets of measurements. First, having PZT_{ref} as detector we have excited a 4.5 cycles Hamming windowed sinusoidal toneburst (as shown in fig. 7.20-*right*) at 166.5 *kHz* to the PZTs in the circumference, numbered from (10) to (14) and in the line, numbered from (4) to (7). In order to avoid the perturbation of the reflection in adjacent PZTs to the PZT source, we define the time of flight (*TOF*) as the time distance between the first peak in the generated and received ultrasonic tonebursts as shown in fig. 7.20-*right*.

PZT_{source}	Distance to PZT_{ref} (*cm*)	TOF (μsec)
(4)	28.2	51.18
(5)	32.1	58.53
(6)	36.1	66.19
(7)	40.1	73.61
(10)	32	58.52
(11)	31.9	58.55
(12)	31.7	57.50
(13)	31.5	57.1479
(14)	31.1	56.48

Table 7.3: Experimental measurement of the TOF for the PZT lay out in fig. 7.22 for an excited ultrasonic signal of 4.5 cycles toneburst at 166.5 *kHz*.

The detected signals were wavelet de-noised with a Daubechies wavelet and decomposed to level 8 with a hard threshold, in order to improve the accuracy of the measurements. The resultant values are given in table 7.3.

Second, having PZT_{14} as receiver and excited same toneburst signal but at a frequency of 180 *kHz* now applied to the PZTs numbered (1), (3), (5) and (7). Because the thickness of the plate is 1 *mm* these frequency values warranty the condition of non-dispersion and the validity of eqn. A.22. The resultant values of the experiment are given in table 7.4.

PZT_{source}	**Distance to PZT_{14} (*cm*)**	**TOF (*μsec*)**
(1)	35	63.67
(3)	38.5	69.82
(5)	43.7	79.55
(7)	49.5	90.40

Table 7.4: Experimental measurement of the TOF for the PZT lay out in fig. 7.22 for an excited ultrasonic signal of 4.5 cycles toneburst at 180 *kHz*.

The obtained values of TOF versus distance source-sensor for both experiments are plotted as blue dots in fig. 7.22-*right*. The S_0 mode group velocity value is given by the slope of the line drawn by these points, so a linear curve fitting technique is applied. The obtained statistical results are; c_g = 5.48 *km/s* with a 95% confidence bounds of ± 0.02 and a goodness of fit SSE (Sum of Squares Due to Error) = 0.313. Value that slightly differs from the group velocity associated to the initial estimated elastic properties (c_g = 5.43 *km/s*).

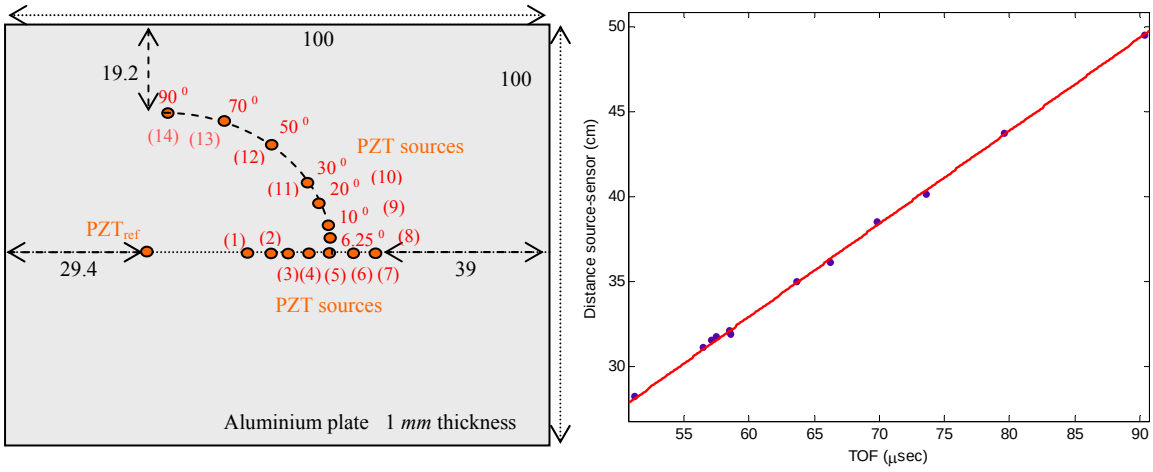

Figure 7.22: (*Left*) Experimental setup of the aluminium plate with bonded PZT ultrasonic sources and receivers (in red), for validation of the extracted elastic property values. All dimensions given in *cm*. (*Right*) Curve fitting of the experimental values of TOF and distance source - sensor, in order to calculate the phase velocity of S_0 mode at low frequencies.

The group velocity value associated to the optimization of the three variables (E = 69.6213 *GPa*; ν = 0.3484) is c_g = 5.42 km/s, but the one associated to the optimization of only E and ν

based in the experimental points of fig. 7.2-*right* perfectly agrees with the current experimental value c_g = 5.48 km/s. This shows a very positive validation of the presented inversion process.

We can estimate the interval of error in the elastic property values E and ν that would provide a group velocity value within the error interval of the experimentally obtained one c_g = 5.48 ± 0.02 *km/s*. Or equivalently c_g^2 = 30.0 ± 0.2 km^2/s^2. Applying the principles of error propagation in the expression of c_g as by eqn. A.22 we have:

$$\Delta c_g^2 = \frac{\rho\left(1-\nu^2\right)\cdot \Delta E + 2\rho E \nu \cdot \Delta \nu}{\rho^2\left(1-\nu^2\right)^2} \tag{7.20}$$

Substituting in eqn. 7.20 the values Δc_g^2 = 0.2, ρ =2.7 gr/cm^3 and the previously estimated values of E and ν we have that 0.2 = 0.4226·ΔE + 24.095·$\Delta \nu$. This relationship between the errors of the estimated values of E and ν that provide a value of c_g for the S_0 mode within the experimental error value Δc_g =0.02 *km/s* is a line plotted in fig. 7.23.

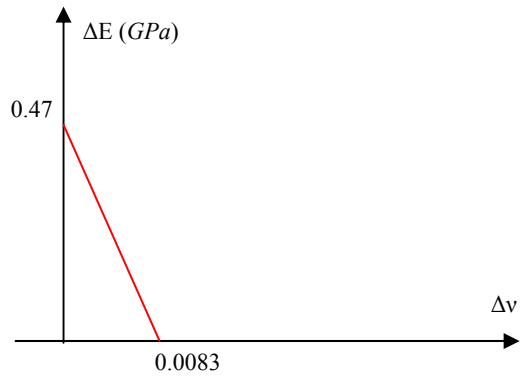

Figure 7.23: Relationship between the errors of the estimated values of E and ν that provide a value of c_{gr} for the S_0 mode within the experimental error Δc_{gr}=0.02 *km/s*.

This means that for the worst case scenario the estimated elastic properties have an error of 1% in E and 2% in the estimated ν value.

7.9 CONCLUSIONS

We have presented, implemented and analysed an inversion procedure based in the minimization of a nonlinear least square function of the difference between the phase velocity measured experimentally in previous chapter, of a selected number of points, and their theoretical phase velocity for varying values of E, ν and the thickness of the plate. The optimization algorithm was found to be very dependant in the frequency:thickness product value and modes of the selected experimental points, thus the Lamb waves sensitivity curves to changes of the elastic properties was studied. The sensitivity to changes in E is bigger than

to changes in v. We also analysed the experimental error distribution of the dispersion curves and rejected the vertical asymptotic regions of the high order modes for application in the inversion process. All these effects were taken into account for the analysis and adequate definition of the weighting factors associated to the error function of the inversion process.

The convergence of the inversion process was found to be improved when inflection points of the phase velocity dispersion curves were chosen, and when an accurate initial estimation of the elastic and geometrical properties was provided. For the later, a novel technique for simple extraction of a very accurate initial estimation of the elastic and geometrical properties based in frequency:thickness product information was presented.

We compared the application of two optimization algorithms (Downhill simplex algorithm and a gradient method and line search algorithm for least-squares problem) to the inversion process and concluded that the later was faster and gave more accurate solutions. Then the inversion process was applied over three regions of the phase velocity Lamb wave dispersion curves; the vertical asymptotic region or cut-off frequency region of the high order modes, the horizontal asymptotic region at high frequency:thickness product values and finally the central region of dispersive behaviour. The higher experimental error of the points associated to the first region provided a wrong estimation of the elastic property values, meanwhile the other two regions gave very similar values. Therefore we decided that the inversion process should always avoid the vertical asymptotic region.

The risk of existence of multiple local minima solutions, for the previous optimization algorithms, was avoided by selecting a big number of experimental points uniformly distributed along the different modes dispersion curves, and by applying the global solution characteristics of a genetic algorithm.

The technique was applied to the experimental data obtained in previous chapter for an aluminium plate, and the estimated material properties were: $E = 71.0\ GPa$; $v = 0.352$; $d = 1.16\ mm$. These values were positively validated by complementary experiments, within a worse case scenario error of 1% for E and 2% for v and d.

The high accuracy and reproducibility of the estimated mechanical parameters provided by the inversion technique presents high potential as a monitoring tool of their deviation, which can be used as an indicator of structural damage or deterioration.

The combined work of Chapters 6 and 7 present a powerful, all-optical remote inspection tool for NDT and SHM. Whilst this tool has thus far been only successfully proven and presented in a laboratory environment, we are optimistic that it can be used as the basis for a mechanical assessment tool for use in both; process validation and structural assessment.

The next development step of the current tool is to adapt it for application toward microstructural characterization. In Chapter 8 we present some areas of improvement and we also conclude this thesis with a review of the main tasks achieved within the present work.

7.10 REFERENCES

[1] Truell R., Elbaum C.and Chick B. B. *Ultrasonic methods in solid state physics*, Academic Press, 1969.

[2] Papadakis E. P. *The measurement of ultrasonic velocity*, Physical Acoustics, vol. **19**, pp. 81-106, 1990.

[3] Fei D., Chimenti D. E. and Teles S. V. *Material property estimation in thin plates using focused, synthetic-aperture acoustic beams*, J. Acoust. Soc. Am., vol. **113(5)**, pp. 2599-2610, 2003.

[4] Khoury M., Tourtollet G. E. and Schroder A. *Contactless measurement of the elastic Young's modulus of paper by an ultrasonic technique*, Ultrasonics, vol. **37**, pp. 133-139, 1999.

[5] Hayashi Y., Ogawa S., Cho H. and Takemoto M. *Non-contact estimation of thickness and elastic properties of metallic foils by the wavelet transform of laser-generated Lamb waves*, NDT&E International, vol. **32**, pp. 21-27, 1999.

[6] Rogers W. P. *Elastic property measurement using Rayleigh-Lamb waves*, Res. Nondestr. Eval. vol. **6**, pp. 185-208, 1995.

[7] Culshaw B., Pierce S. G. and Jun P. *Non-contact measurement of the mechanical properties of materials using an all-optical technique*, IEEE Sensors journal, vol. **3(1)**, pp. 62-70, 2003.

[8] Thursby G., Culshaw B., Sorazu B., Atique S. and Dong F. *Non-contact material evaluation for characterisation and wear detection using laser generated ultrasound and interferometric detection*, 11th International Symposium on Smart Structures and Materials SPIE, San Diego (USA), 14-18 March 2004.

[9] Viktorov I. A. *Rayleigh and Lamb waves – Physical theory and applications*, Plenum Press, New York, 1967.

[10] Dewhurst R. J., Edwards C., McKie A. D. W. and Palmer S. B. *Estimation of the thickness of thin metal sheet using laser generated ultrasound*, Appl. Phys. Letters, vol. **51(14)**, pp. 1066-1068, 1987.

Chapter 8

CONCLUSIONS AND FUTURE WORK

8.1 INTRODUCTION

Within a group of great experience in optical fibre sensors and with an in-depth interest in structural monitoring, emerges the goal of linking both areas. The work presented in this thesis is born in this union. We look into combining the advantages and structural integration capabilities of ultrasonic guided waves NDT technique with the unrivalled acoustic wave sensing performance and nonintrusive structural integration characteristics of modern optical fibre sensor technology. Therefore this work aims to contribute into the future of SHM which consists in integrating NDT monitoring technology into structural materials merging into a common discipline together with the field of smart structures.

We have successfully accomplished this in various ways and it is the purpose of this chapter to remember how. For that reason next we recapitulate the most important conclusions of the analytical and experimental results obtained in previous chapters, and at the end we discuss various paths of complementary and enhancement work to be done in the future.

8.2 SUMMARY OF FINDINGS

The starting chapter of this thesis in conjunction with some appendices has provided a state of the art review of the modern aspects involving SHM and NDT. We have also described and compared the most commonly used NDT techniques and decided that ultrasonic guided waves is the technique with greater implementation potential in a SHM system.

The body of our work presents a clear division of involvement in SHM and NDT.

8.2.1 NDT applications

The first part of the thesis (from Chapter 2 to Chapter 4) is concerned with the NDT aspects. Therefore we described the conventional ways in which ultrasonic guided waves can be generated and detected in plate-like structural materials. Based in their important limitations,

we decided to study more advantageous optical techniques for implementation in future on-board damage detection systems.

In Chapter 2 we presented the optical techniques for ultrasonic generation and the optical fibre ultrasonic detection systems used in this thesis; FBG sensors, two different configurations of an all-fibre Mach-Zehnder interferometer and a polarimetric sensor. We have compared their performance parameters and their different sensing characteristics, and in Chapter 3 we experimentally confirmed their suitability for ultrasonic wave detection. We describe their potential for damage detection and location applications due to their inherent high directivity. The processing techniques used for this purpose were described in Chapt. 5.

In Chapter 4 the wavefront integration response of an optical fibre sensor (such as polarimetric sensor or modified MZ interferometer) to varying length, distance and orientation from the source was modelled. The basic trends predicted were experimentally confirmed, demonstrating the huge potential of our model. The results indicate that optimum ultrasonic detection may be achieved through careful positioning and orientation of the optical fibre. These results may be applied, for example in NDT, where scattered ultrasound from defects introduces new effective sources that may be characterized by arrays of these integrating sensors.

We also show that a polarimetric sensor exhibits similar integration behaviour to that predicted for an interferometric system because positive and negative changes are produced in the fibre birefringence in a similar way to that expected for fibre refractive index.

8.2.2 SHM applications

In the second part of the thesis (from Chapter 6 and Chapter 7) a complete remote all-optical tool for structural material characterization has been developed and implemented. In order to do this we had to fully understand the full cycle of generation, propagation and structural ultrasonic interaction and detection of the Lamb waves. The broadband (in frequency and space) ultrasonic generation by Q-switch laser and detection by modified MZ interferometer provided a huge amount of the Lamb waves dispersion propagation characteristics which through 2D-FT and time-frequency analysis techniques could be converted into the material phase and group velocity dispersion curves. The full system was experimentally applied to various aluminium plate samples. A detailed analysis of the results led to the identification of the main areas for improvement (1D and 2D leakage, DC offset, radiation directivity of the line-source, etc). The implementation of their corrections allowed a very successful enhancement of the experimental dispersion curves.

It was found that although 2D-FT and time-frequency analysis provide the Lamb waves dispersion propagation characteristics, this information presents important differences as how it relates with the monitoring of the sample structural condition. Meanwhile the dispersion information provided by the 2D-FT can focus the material property analysis to specific areas of the sample, the time-frequency analysis monitors the full area between source and receiver. This makes a technique more suitable than the other depending in the application.

The system was later used to analyze temperature change sensitivity (using the 2D-FT technique) and for hole-damage detection applications (by the reassignment spectrogram). The results of these two applications have proved this inspection tool more than adequate.

In Chapter 7 we used this experimental dispersion information to extract the material elastic and geometric properties by the application of an inversion technique. This technique minimizes the differences between the experimentally obtained Lamb wave phase velocity information of a selected number of points, and their theoretical phase velocity for varying values of E, v and the thickness of the plate.

The optimization algorithm was found to be very dependant in the frequency:thickness product value and modes of the selected experimental points, thus the Lamb waves dispersion curves sensitivity to changes of the elastic properties was studied. The sensitivity to changes in E is bigger than to changes in v. We also analysed the experimental error distribution of the dispersion curves and rejected the vertical asymptotic regions of the high order modes for application in the inversion process.

The convergence of the inversion process was found to be improved when an accurate initial estimation was provided and when inflection points of the phase velocity dispersion curves were chosen. The risk of the existence of multiple local minima solutions was avoided by selecting a big number of experimental points uniformly distributed along the different modes dispersion curves, and by applying the global solution characteristics of a genetic algorithm. A new simple technique to obtain a very accurate initial estimation of the elastic properties was also presented.

The technique was applied to the experimental data obtained in previous chapter for an aluminium plate, and the estimated material properties were: E = 71.0 GPa; v = 0.352; d = 1.16 mm. These values were positively validated by complementary experiments, within a worse case scenario error of 1% for E and 2% for v and d.

8.2.3 Signal processing

Chapter 5 presented the various signal processing techniques required along this thesis with special emphasis of the 2D-FT and the time-frequency analysis. Some important conclusions were obtained for the former, such that the main domain of definition of the 2D-FT spectrum is divided into a section corresponding to the incident Lamb waves and other section associated to the Lamb waves reflected from the border of the plate or any present damage. This has obvious damage detection applications, plus it also help to experimentally identify the section of negative group velocity of the S_1 mode. Additionally it was proven that the 2D-FT spatial aliasing does not have the same negative effects as in the 1D-FT. So that most of the propagating Lamb waves dispersion information can be extracted. This is of great advantage because it allows us to work with smaller spatial sampling frequencies ($1/\Delta x$), thus increasing the spatial resolution of the experimental dispersion curves.

The most common time-frequency analysis of the STFT was replaced by a less known technique, named reassigned spectrogram by which the resolution of the experimental group velocity dispersion curves was greatly enhanced.

8.2.4 Software applications

A great percentage of the work of this thesis has consisted in programming (mainly in MATLAB) the signal processing techniques as well as the full realization of the inversion process. The huge number of code lines required for these complex programs has prevented me to add them as appendices in this thesis. Nonetheless they are of free access. Some of these programs are of general interest, these includes:

- Implementation of Rouard's method and coupled mode theory for calculation of uniform FBG reflectivity spectra. These programs were used for calculating the parameters of the FBGs used in Chapter 3 from the obtained experimental reflectivity spectra. Rouard's implementation has a great potential for further development, as it allows simulating complex gratings configurations otherwise difficult to deal with through the coupled mode theory.
- Calculation of the displacement and stress distributions of Rayleigh waves in a half space of an isotropic material.
- Numerical solution of the very unstable Lamb waves characteristic equations. This program allows resolving the Lamb wave phase and group velocity dispersion curves for high order modes by specifying the elastic property values of an isotropic material. Or the inverse, to obtain E, ν and the thickness of the plate through the experimental phase

velocity dispersion curves. This program also can calculate the particle displacement, velocity and acceleration components along the thickness of an isotropic plate for any propagating Lamb mode.

8.3 FUTURE WORK

In the area of work in which this thesis is framed, various points for improvement have been identified as presented next:

8.3.1 Heterodyne modified MZ interferometer

In numerous occasions along the experimental work of this thesis we have suffered the limited stabilization characteristics of the homodyne MZ interferometer used. We have started the investigations into the development of an all-fibre heterodyne version based on the one presented in [1]. Heterodyne interferometers work by shifting the optical frequency of the interferometer up by f_B usually through an acousto-optic modulator (AOM) in one of or both reference and sensing arms. The velocity of the particles in the surface of the sample modulates by Doppler effect the carrier light of the interferometer generating two sidebands [2]. Because the ultrasonic effect is now detected at high frequency shifted values then this detection systems is immune to the low frequency ambient vibration noise components. Thus the heterodyne interferometer does not require of a stabilization scheme, in contrast to the homodyne interferometer topology used along this thesis. On the other hand a heterodyne interferometer offer slightly less sensitivity and worse signal to noise ratios than the homodyne configuration [2].

8.3.2 Wavefront integration model

Improve the wavefront integration mathematical model by adding the differential stress of the particles displacement movement by the propagating Lamb waves, in the same way as we did for the birefringence analysis to prove why the polarimeter works in the same way as the MZ interferometer. Also we have identified areas for improvement in the theoretical analysis; to include a more precise modelling of specific propagating ultrasonic waves and the addition of the propagating wave dispersion effect. Improved models are currently in development.

8.3.3 Software improvement

- The wavefront integration algorithm needs to be improved to simulate better the experimental results. For this, a more precise modelling of specific propagating ultrasonic

waves and the addition of the propagating wave dispersion effect is required. Improved models are currently in development.

- Adaptation of the inversion process for the group velocity dispersion curves.

8.3.4 Estimation of elastic properties of material

Three different areas of improvement were found in the inversion process:

- In our work to date we have only concentrated on using the changes in the shape and shift of the material dispersion curves to derive the Young's modulus, Poisson's ratio and transversal dimensions of the structural material. However an enhancement of this technique would consist in the monitoring of the changes in these parameters and identify thresholds that provide a sensitive indication of structural damage or deterioration. Future work also will concentrate in extracting additional information from the perturbation of the dispersion curves such as a more advanced analysis of the effect caused by temperature changes (as started in Chapter 6) and structural loading.

- Improve the error estimation of the estimated elastic property values. The highly pessimistic estimation calculated in Chapter 7 is based only in the experimental error of the verification experiment. More accurate error estimation is needed to have a better idea of the method potential. We suggest evaluating the accuracy of the estimated elastic properties not as an error in their value but as a statistical analysis of the influence of the experimental error on the optimized elastic property values. This can be done as follows. In Chapter 7 we decided that the best region of the dispersion curves used for the elastic properties estimation was that with relative errors in the phase velocity values of less than 4% as shown in fig. 7.2. We multiply the phase velocity value of the chosen experimental points by 0.96 and 1.04 randomly to take into account the effect of the 4% normal distributed error. And we calculate again new estimations of the elastic properties for the new experimental point values. We repeat this process a given number of times (let's say 15 times) and then calculate the mean value of the different estimated elastic property values and their standard deviations. The value of the standard deviation should give us an idea of the accuracy of the estimated elastic property values and how sensitive this estimation is to experimental errors.

8.3.5 All-optical, remote inspection tool for material characterization

- In most cases, both for macroscopic or microscopic structural monitoring applications, the damage that the ablation regime causes over the sample is unacceptable. When a specific region of the structure is inspected by the 2D-FT technique, the ablation caused by the sources in the area to be inspected may alter the material's properties or at

least negatively affect the structure. Fortunately, the 2D-FT technique is completely reversible. This means that the range of source-detector distances in the regions to be inspected, can be adjusted by either moving the source or the detector. In our experimental setup in Chapter 6, we chose the former because of experimental convenience. However if the monitoring requirement of a totally non-damage, non-invasive technique must be satisfied then it is more suitable to fix the position of the ablation source in a region where slightly damage is allowed and then adjust position of the detectors in the area of interest.

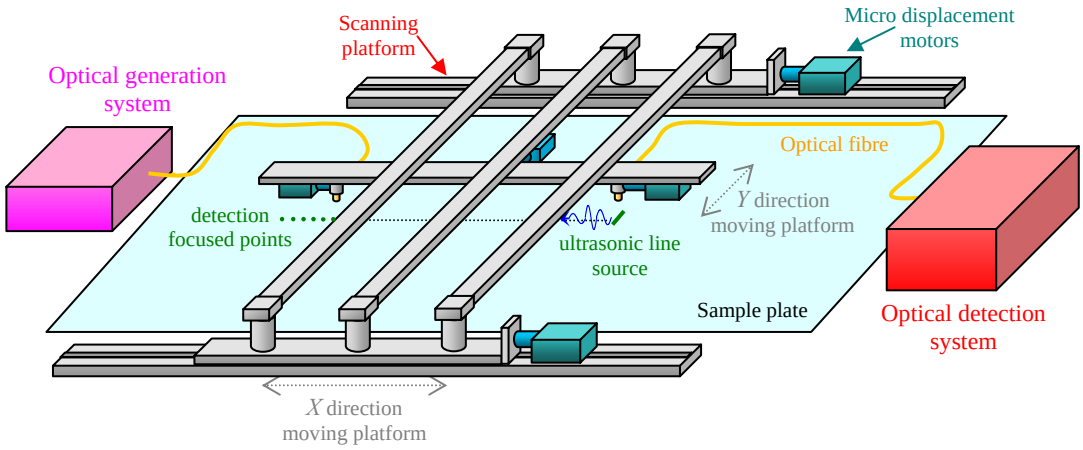

Figure 8.1: Possible setup of a fully automated scanning system based in the non-contact all optical monitoring system. The scanning platform can move in a plane parallel to the sample plate by several micro displacement motors. The plate can be scanned in multiple localized areas.

If the detected ultrasonic amplitude permits it, we could decrease the light power of the ultrasonic source by using a low power CW laser and an optical amplifier. In this case both fibre connectors (one each for the ultrasonic detection and generation stages) could be attached to a 2D moving micro stage platform, allowing an automatic movement of source and receiver parallel to the surface of the structure to be monitored (see fig. 8.1).

- We already described the full automation of operation potential of the non-contact all optical monitoring tool (see Chapter 6). This needs further development.

8.4 REFERENCES

[1] Kil H-G. *An automated scanning laser Doppler system for vibration measurements and wave vector analysis of vibration of shells*, PhD. thesis, Georgia Institute of Technology, 1995.

[2] Monchalin J-P. *Optical detection of ultrasound*, IEEE Transactions on ultrasonics, ferroelectrics and frequency control, vol. **UFFC-33(5)**, pp. 485-499, 1986.

APPENDICES

APPENDIX A: Elastic waves in solids

The most commonly used methods in NDT are listed in Table 1.2 of Chapter 1. These methods can be considered mature, because they have been used in the industry for quite a long time and have proved to be very effective in their respective applications. Yet between them all, only three can seriously be considered for their potential implementation in a SHM system; acoustic emission, modal analysis and ultrasonic guided waves.

For this thesis, ultrasonic guided waves have been chosen as the method with the highest potential. Ultrasonic guided waves are different from the conventional ultrasonic scanning method, not only because they use a different kind of ultrasonic wave; being guided waves for the former and bulk wave for the later. But also because they travel in different kind of media, with guided waves only travelling in bounded media. We will see in this appendix that in fact these two kinds of waves are not so different from each other and we will understand why guided waves are limited to only bounded media.

It is surprising that although the theory of propagation of elastic waves in solids is based on more than two centuries of work in the areas of wave mechanics and elasticity, it has not been until the late 1920's that ultrasonic waves were conceived as a means for NDT/E. Even more surprising is that the benefits of ultrasonic guided waves were not recognized until the late 1950's [1,2]. Since then the numerous advantages of ultrasonic guided waves in comparison with conventional methods have increased, with the most important being:

- Guided waves can inspect longer distances as they propagate with less attenuation because they remain contained in a wave guide.
- They provide better defect detection capabilities as guided waves can propagate in a high number of different modes and frequencies, allowing adequate tuning in relation to the characteristics of the damage. This also contributes in their capabilities for damage location, classification and size valuation.
- Conventional C-scanning provides a point-by-point through the thickness inspection, whereas guided waves can inspect the full strip thickness between the ultrasonic source and receiver probes at quite long distances (hundreds or thousands of ultrasonic wavelengths). This not only allows an improvement in the inspection speed of large areas but also in the inspection simplicity as it only requires a fixed location probe instead of a scanning one (see fig. A.1).

- Ability to inspect large areas of structures under water, concrete or surrounded by coatings and insulating materials, or even multi-layered structures, only needing to access them at a few points (see fig. A.1-*right*).
- Guided waves' propagation characteristics are sensitive to the principal material elastic properties and they are also dependent on structural loading or defects present within the material.
- The guiding characteristic of guided waves enables them to travel through curved regions and reach hidden areas or difficult to access for conventional ultrasonic methods (see fig. A.1-*left*).

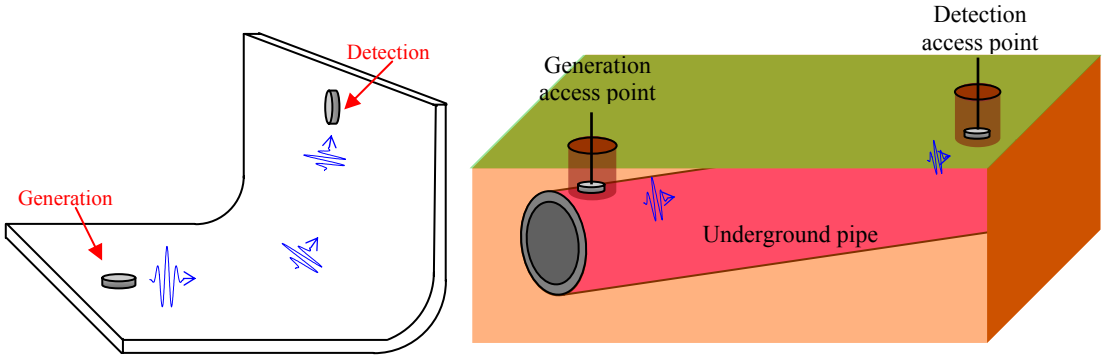

Figure A.1: (*Left*) Guided waves can inspect strip between source and receiver, travelling through difficult to access curved regions. (*Right*) Underground pipes can be fully inspected by only accessing the structure at a few points.

Yet ultrasonic guided waves have also some drawbacks; because they are very dispersive and they can propagate in multiple modes at the same time, the obtained data is complex and it requires a large amount of signal processing in order to extract the information that they store. Additionally in the case of plate guided elastic waves (Lamb waves), as shown later, it is required that the wavelength of the waves to be of the order of magnitude or larger than the thickness of the guiding structure. And because in a far field analysis, only discontinuities that are larger than one-half the size of the wave's wavelength can usually be detected, then the detectable flaws size is importantly limited. For most common guiding structures with thickness in the order of a millimeter or more, the detectable flaw's size is a fraction of a millimeter. If smaller defects need to be detected, an accurate study of the scattering characteristics of small defects in the near field is necessary, with decreasing sensitive the smaller the size of the damage.

Modern advances in computer power and in signal processing techniques have overcome some of these drawbacks, making ultrasonic guided waves as one of the most promising NDT methods for the near future.

This appendix provides the basic theoretical background of elastic waves to understand the physical characteristics of ultrasonic guided waves. The concepts of the material's elastic properties are defined through the characterization of the basics acoustic waves presented in all solid materials, bulk waves. Later we introduce the different ultrasonic guided waves, and justify why we only need to concentrate on Lamb waves for the particular applications of this thesis. A more detailed look into the propagation characteristics of Lamb waves helps to understand how they can be used to monitor the elastic properties of the inspected material and the presence of damage.

A.1 ELASTIC WAVES TYPES IN SOLIDS

We start this section with a maybe evident but necessary affirmation to understand what follows after; *Ultrasonic testing of materials is based in mechanical or elastic waves, which are composed of oscillations of discrete particles in the materials*.

It is logical then that in order to understand ultrasonic testing of materials it is necessary first to have an idea of the theory of elastic waves in solid media.

The theory of elastic waves in solid media has been already marvellously covered in a broad number of references, being, in my opinion, the most relevant ones [3-6,35]. In this section we give a brief introduction to this theory in order to introduce vital concepts that have been used along this work. We invite any reader seeking more detailed explanations to take a look at the references mentioned above.

A series of simplifying assumptions have been considered in the development of the next theory because these assumptions are satisfied along the work in this thesis. They are as follows; the material in which the waves propagate is *elastic*, so that the perturbation that the wave causes in the stationary state of the material particles requires a certain period of time to be transmitted along it. The material is *homogeneous* and *isotropic*, so that the density of the material is uniform. This allows us to accurately model the solid as consisting of uniformly separated particles with the same elastic behaviour in all the spatial directions. Each of these particles is the equivalent of an infinitesimal cube of mass as shown in fig. A.2. The propagating waves are considered *planar*, such that the magnitude of the perturbation is constant on a given plane of the material. The wave plane is named *wavefront* and it is normal to the direction of propagation of the wave.

Additionally the medium is considered perfectly elastic, which means that the mechanical energy of the propagating perturbation is conserved. This assumption can never be true in reality, because *internal friction* converts part of this energy into heat as the wave

propagates. Other effects like *mechanical relaxation* affect the conservation of the propagating mechanical energy. These effects constitute the main weakening causes of the *absorption* of materials. Other basic elastic wave weakening is the *scattering* or dispersion of the elastic energy into multiple propagation directions as a result of physical interactions with the material discontinuities, borders or structure. The combined effect of scattering and absorption is called *attenuation*. As a consequence the intensity of the elastic waves diminishes with the travelled distance. However the simplification of perfect elastic body is considered in order to extract a first solution of the equation of motion in solid media. The attenuation effect can be subsequently added to the obtained solutions.

In order to extract the equations of motion, a very useful model is to consider the solid material as being divided into elements or particles of infinitesimal volume as depicted in Figure A.2-*left*. The position of each of these elements is given by the position of its vertex P in the referential system *X, Y, Z*, which we consider to be (*x, y, z*). In this figure we show the different stress components acting over the faces of each element of material, as red and blue vectorial systems, parallel to the general system of reference. Because the chosen infinitesimal element is a parallelepiped then six different stress components will be acting parallel to each referential axis.

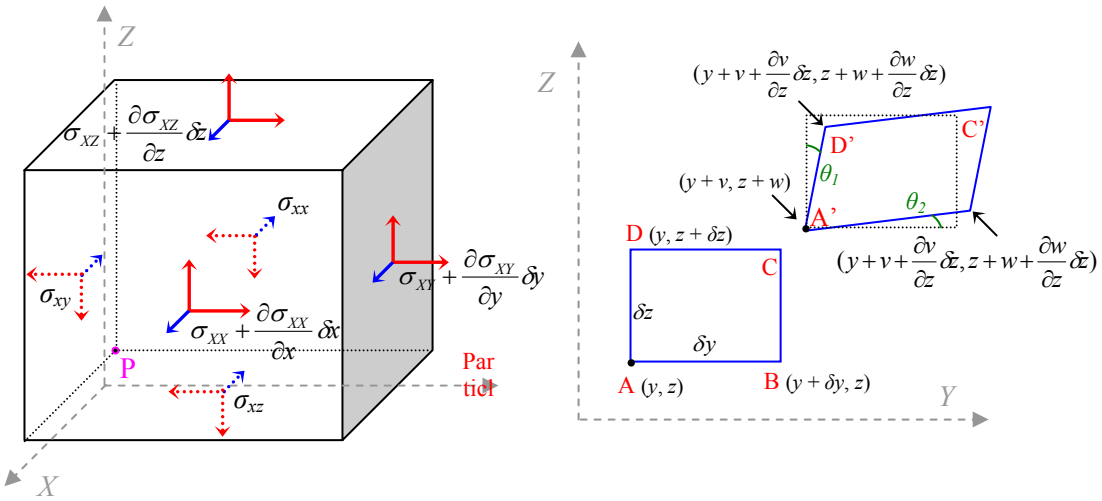

Figure A.2: (*Left*) Elements of infinitesimal dimensions in the elastic solid with stress components. (*Right*) Translation and displacement of one plane of an element for strain considerations.

The blue vectors in the figure are the stress components acting in the *X* direction, the addition of their value times the area they are acting over, represent the net force acting over the element in the *X* direction. This force can be expressed as:

$$\left(\frac{\partial \sigma_{xx}}{\partial x} + \frac{\partial \sigma_{xy}}{\partial y} + \frac{\partial \sigma_{xz}}{\partial z} \right) \cdot \delta x \delta y \delta z \qquad \text{(A.1)}$$

The first suffix in the stress components represents the direction of the stress and the second suffix is the plane in which it is acting.

A material in which a perturbation is propagating, is in a non equilibrium condition hence Newton's second law of dynamics must apply. If we neglect body forces such as gravity, we can express this law as:

$$\frac{\partial \sigma_{xx}}{\partial x} + \frac{\partial \sigma_{xy}}{\partial y} + \frac{\partial \sigma_{xz}}{\partial z} = \rho \cdot \frac{\partial^2 u}{\partial t^2} \tag{A.2}$$

Where ρ is the density of the material and u the displacement of the element in the X direction. By the same reasoning we obtain for the other referential directions:

$$\frac{\partial \sigma_{yx}}{\partial x} + \frac{\partial \sigma_{yy}}{\partial y} + \frac{\partial \sigma_{yz}}{\partial z} = \rho \cdot \frac{\partial^2 v}{\partial t^2} \tag{A.3}$$

$$\frac{\partial \sigma_{zx}}{\partial x} + \frac{\partial \sigma_{zy}}{\partial y} + \frac{\partial \sigma_{zz}}{\partial z} = \rho \cdot \frac{\partial^2 w}{\partial t^2} \tag{A.4}$$

Where v and w are the displacement of the element in Y and Z directions respectively.

The detailed steps followed for the development of the equation of motion have been relegated to Appendix B. They mainly consisted in the definition of the *Lamé's constants* λ and μ, and in rewriting the displacement vector in terms of a scalar potential ϕ and a vector potential $\vec{\psi}$, useful to express the equation of motion as two uncoupled equations:

$$\nabla^2 \phi = \frac{1}{(\lambda + 2\mu)/\rho} \cdot \frac{\partial^2 \phi}{\partial t^2} \qquad \nabla^2 \vec{\psi} = \frac{1}{\mu/\rho} \cdot \frac{\partial^2 \vec{\psi}}{\partial t^2} \tag{A.5}$$

Although the equation of motion has been obtained as a function of the Lamé's constants, however other two constants are normally used when describing the elastic properties of materials. These constants are *Young's modulus E* and the *Poisson's ratio v*, and as the *Lamé's constants* they also completely define the elastic behaviour of an isotropic solid [35].

The *Young's modulus* is commonly defined as the ratio between the applied stress and the fractional extension, when a cylindrical or prismatic specimen is subjected to a uniform stress over its plane ends and the lateral surfaces are free.

The *Poisson's ratio* is defined as the ratio between the lateral contraction and the longitudinal extension of the specimen with the lateral surface free.

Ref. [35] shows that the relationship between these constants and the Lamé's constants is:

$$E = \frac{\mu(3\lambda + 2\mu)}{\lambda + \mu} \qquad \nu = \frac{\lambda}{2(\lambda + \mu)} \tag{A.6}$$

The next sections look into the possible different solutions that the equation of motion provides in relation to the boundary conditions of the material. As we will see for an unbounded media only two kind of waves propagates, they are called *bulk waves*. When boundaries are added to the medium different kind of guided waves may appear. We will look to surface guided waves (Rayleigh waves), to plate guided waves (Lamb waves) and for completeness to other common guided waves, however they are not used in this work.

A.1.1 Bulk waves

If we look into the equation of motion eqn. B.6 as written in Appendix B, we notice that it is constituted of two very different and complementary parts; the first part is proportional to $\vec{\nabla} \cdot \vec{u} = \Delta$ which represents the dilatation or compression of the material, meanwhile the second part is proportional to the rotational of the displacement vector $\vec{\nabla} \times \vec{u}$ which accounts for the equivoluminal portion of the solution. Thus if the propagating perturbation involves no rotation ($\vec{\nabla} \times \vec{u} = 0$) then the equation of motion eqn. B.6 is equivalent to A.5-*left* with $\vec{u} = \vec{\nabla} \cdot \phi$. The solution of this equation, considering plane waves as the propagating perturbation, are of the type:

$$\vec{u} = A_1 \cdot e^{-i\left(\vec{k}\cdot\vec{r} - \omega t\right)} + A_2 \cdot e^{-i\left(\vec{k}\cdot\vec{r} + \omega t\right)} \tag{A.7}$$

Where $\vec{r}$ is the vector position of a given point in the planar wavefront, ω is the angular frequency of the wave and $\vec{k}$ is the wavenumber vector in the direction of propagation of the wave and it describes the wavelength (λ) and speed (c) of the perturbation as:

$$\lambda = 2\pi / |k| \qquad\qquad c = \omega / |k| \tag{A.8}$$

The general solution in eqn. A.7 corresponds to two planar waves travelling in opposite directions with amplitudes A_1 and A_2 (arbitrary constants).

The particular solution to the equation (A.5)-*left* gives a wave speed equal to:

$$c_L = \sqrt{\frac{(\lambda + 2\mu)}{\rho}} = \sqrt{\frac{E(1-\nu)}{\rho(1+\nu)(1-2\nu)}} \tag{A.9}$$

These waves are called *pressure waves* (P-wave) or *longitudinal waves*, because the displacement of the particles is along the direction of propagation.

Additionally if the propagating perturbation involves no dilatation ($\vec{\nabla}\cdot\vec{u}=0$) then the equation of motion eqn. B.6 is equivalent to eqn. A.5-*right* with $\vec{u}=\vec{\nabla}\times\vec{\psi}$. This gives an identical plane wave solution as in eqn. A.7 but with a different wave speed:

$$c_T=\sqrt{\frac{\mu}{\rho}}=\sqrt{\frac{E}{\rho 2(1+\nu)}} \tag{A.10}$$

These waves are called shear *waves* or *transversal waves*, because the displacement of the particles is transversal to the direction of propagation and parallel to the wavefront. For this kind of waves two different modes can coexist; Shear vertical or SV-wave and Shear horizontal or SH-wave. If a two dimensional plane of propagation is considered (as we are considering planar waves, the third dimension is redundant), then the SV mode is that with particle displacement direction within this plane and SH mode the one with the displacement being perpendicular to the plane. Shear waves, in opposition to longitudinal waves, require an acoustically solid material for effective propagation and so they do not propagate effectively in liquid and gas materials.

Longitudinal and shear waves propagate in an unbounded media without interaction, because the equations of motion in A.5 are independent of each other. Any plane wave propagating in this media must travel as one or the other mode. These waves are called *bulk waves*.

Finally, if we consider the attenuation characteristics of real materials, the amplitudes of the propagating waves given in eqn. A.7 should decrease as the waves propagate through the material. This amplitude reduction, for plane waves, is usually modelled by an exponential reduction with propagated distance:

$$A_i=A_{i0}\cdot e^{-\alpha r} \tag{A.11}$$

Where A_{i0} is the amplitude of the propagating wave at some location, r is the propagated distance from that initial location and α is the attenuation coefficient of the wave travelling in the material, its dimensions are *nepers per meter*, so that an attenuation of α nepers per meter means that a wave of unit amplitude is reduced to amplitude $e^{-\alpha}$ after travelling one meter.

We must notice here that as we are dealing with ideal planar waves there is not amplitude reduction by spreading of the wave as it would be the case for spherical or cylindrical waves.

A.1.2 Guided waves

When a boundary is added to the isotropic media then the bulk waves no longer travel independently and coupling of the modes take place during reflections and refractions in the boundaries.

Mathematically the boundaries are added to the equation of motion as physical boundary conditions, the problem can not always be solved analytically. Between the few guided wave cases with analytical solution, we will study those relevant to the work of this thesis. These are in chronological order of discovery; Rayleigh waves, Love waves, Lamb waves and Stoneley waves.

It is interesting to highlight that meanwhile in the case of an infinite body (unbounded media) we only have a finite number of propagating modes (P-wave, SV-wave and SH-wave), in a finite body (bounded media) an infinite number of modes can coexist.

A.1.2.1 Surface guided waves: Rayleigh waves

The first analytical solution of a guided wave was carried out by Lord Rayleigh in 1885 [7]. He proved that elastic waves could travel in the stress-free surface of a semi-infinite body. Their energy and displacement amplitude decaying exponentially with depth, being mainly concentrated within a wavelength thickness of the surface.

These waves are the effect of the superposition of longitudinal and shear waves travelling along the surface of the body with a common phase velocity, smaller than their respective velocities when propagating in the bulk of the material. This is the velocity of the Rayleigh wave, here represented as c_R.

In order to obtain the value of the particle displacement for this type of guided wave, we consider the system of reference shown in fig. A.3-*left*, where the surface is taken as the plane *XY* and the waves are propagating in the *X* direction. Notice the positive sign of *Z* (as the out-of-plane direction) towards the interior of the body.

As before, we look for a plane wave solution, that makes the displacements independent of the *Y* axis. Based in the potentials expression of the equation of motion the general expression of the solution is given by eqn. A.5. For this problem the scalar and vector potentials for waves propagating in the positive *X* direction can be written as:

$$\phi = D_1(z)\cdot e^{i(kx-\omega t)} \quad \vec{\psi} = \psi_y = D_2(z)\cdot e^{i(kx-\omega t)}\,\hat{j} \tag{A.12}$$

Where D_1 and D_2 are the amplitude of the potentials as a function only of the depth (z), as no material attenuation is considered for the ideal case of a perfect elastic body. We must notice

that for the vector potential $\vec{\psi}$ we only consider the component in the Y axis because the displacement in Y direction must be null making the other components zero or constant.

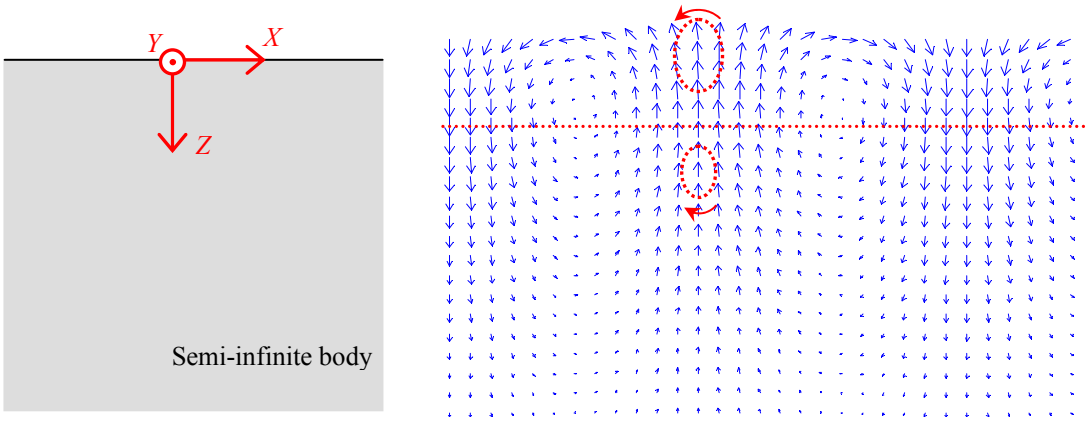

Figure A.3: (*Left*) Convention of the system of reference for Rayleigh wave particle displacements. (*Right*) Snapshot of particles displacements in a Rayleigh wave for a particular time instant.

Finally because the boundary condition in this problem is a stress-free surface then $\sigma_{zz} = 0$ and $\sigma_{xz} = 0$ at $z = 0$, which combined with the equations B.1, B.3, B.5, B.7, A.5 and A.12 give the next expressions for the X and Z components of the particles displacement:

$$u = Ak_R\left(e^{-q_R z} - \frac{2q_R s_R}{k_R^2 + s_R^2}e^{-s_R z}\right)\sin(k_R x - \omega t)$$
$$w = Aq_R\left(e^{-q_R z} - \frac{2k_R^2}{k_R^2 + s_R^2}e^{-s_R z}\right)\cos(k_R x - \omega t) \qquad \text{(A.13)}$$

Where $k_R = \omega/c_R$, $q_R = \sqrt{k_R^2 - k_L^2}$, $s_R = \sqrt{k_R^2 - k_T^2}$, $k_L = \omega/c_L$, $k_T = \omega/c_T$ and ω is the wave's angular frequency. The arbitrary constant A will depend on the energy of the propagating wave.

Equation A.13 shows that the particle displacement of Rayleigh waves depend on the material elastic properties through the bulk waves phase velocity as part of the wavenumbers k_L and k_T. However in order to resolve some values for specific materials we need to know k_R, which relates with the phase velocity of the Rayleigh waves c_R. It is not the intention of this section to show in detail how to get to this expression, but in the process of obtaining the expression of the displacement in eqn. A.13 a condition for the Rayleigh wave phase velocity must be satisfied:

$$\left(2 - \frac{c_R^2}{c_T^2}\right)^2 - 4\sqrt{\left(1 - \frac{c_R^2}{c_L^2}\right)\left(1 - \frac{c_R^2}{c_T^2}\right)} = 0 \qquad \text{(A.14)}$$

From this expression we realize that c_R does not depend on the ultrasonic wave's frequency, which means that Rayleigh waves are not dispersive and as a consequence a plane surface wave will travel without change in its shape. For values of c_L and c_T corresponding to real media only one solution exist to eqn. A.14 and as shown in [8] it can be approximated to the value:

$$c_R \approx \frac{0.87 + 1.12\nu}{1+\nu} c_T \tag{A.15}$$

With ν being the Poisson's ratio of the material. Because ν is limited, for real materials, between 0 and 0.5, then c_R is always smaller than c_T, which is also smaller than c_L.

In order to understand better the particle displacement characteristics of Rayleigh waves we compare, in fig. A.4, the depth dependence of displacement's amplitudes normalized against the amplitude of the perpendicular displacement in the surface *w(z=0)*. We also plot the stress amplitudes normalized against the amplitude of σ_{xx} in the surface. We must notice that this Figure has been obtained for the particular case of aluminium (ν = 0.3375), however it is not much different for most metals (with Poisson's ratio varying between 0.25 and 0.34).

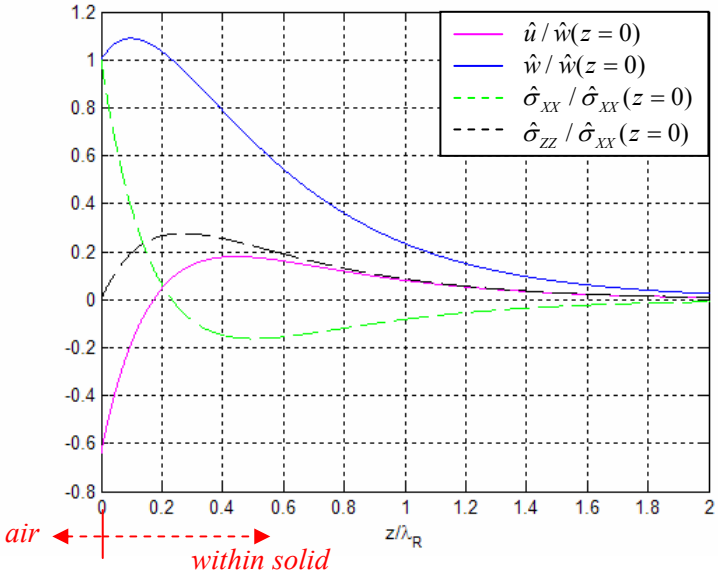

Figure A.4: Displacement and stress normalized amplitude values for Rayleigh waves with depth in aluminium.

Several important properties can be extracted from the particles displacement equation and from figure A.4:

- Rayleigh waves amplitude perturbation decrease exponentially with the depth into the solid (z), being negligible at a depth of twice the Rayleigh wavelength λ_R. Thus Rayleigh wave penetrates deeper the lower its wave frequency.

- The particle trajectory is an ellipse with the major axis perpendicular to the surface of the solid (*Z* direction) and the minor axis in the *X* direction as it can easily be deduced from the fact that displacement components *u* and *w* have a difference in phase of $\pi/2$ (see eqn. A.13). At the surface of the solid and for waves propagating in the *X* direction, the particles rotate counter-clockwise in their elliptical trajectories as shown in fig. A.3-*right* (snapshot of the particles displacement in a particular time instant) by a red dashed ellipse with the arrow indicating the rotation direction. As proved by the fact that at the surface the particle's displacement amplitudes have opposite sign, therefore for a given surface particle at position *x* as time increases the wave phase ($k_R x - \omega t$) decreases.

  As we go deeper into the solid, the major and minor axis of the particle trajectories decrease until *u* becomes zero at a depth of around 0.2 λ_R (for most metals), where the displacement is totally vertical (red dashed horizontal line in fig. A.3-*right*). Below this depth, the amplitudes of the displacement have the same sign, and then the particles' rotation reverses to clockwise. It is this change in the rotation that characterises the difference in Rayleigh waves from waves in water, where the rotation is always clockwise. In fig. A.3-*right* it is evident that the deformation of the solid's surface, by Rayleigh waves, is not sinusoidal.

- The stress component σ_{xx} has a maximum in the surface and then decreases until it cancels at a depth near $\lambda_R/4$, to change sign at deeper points. Whilst the stress component σ_{zz} is null in the surface, and it reaches a maximum at around 0.3 λ_R depth.

The application of Rayleigh waves in NDT is for the interrogation of the presence of surface and near surface flaws. With the advantage of being able to propagate long distance with low loss thanks to the absence of any wave component propagating into the bulk of the semi-infinite material. However these guided waves cannot give any information about the material elastic properties or presence of damage in the region deeper than a Rayleigh wavelength, and certainly they cannot provide information of the body's thickness.

These waves although theoretically associated to a semi-infinite body, can in practice be reproduced in any specimen with a thickness of the order of a few Rayleigh wavelengths.

A.1.2.2 Layer on a semi-infinite body: Love waves

Rayleigh waves are one of the most destructive waves generated during an earthquake as they propagate along the surface of the Earth. However other surface waves are also generated that travel faster than the Rayleigh waves and so are the first to be detected during an earthquake. These new waves induce a particle displacement in a direction perpendicular to the plane of wave propagation and parallel to the layer's surface where they propagate, as

shown in figure A.5[1] together with the coordinate system used in this section. In 1911 a British mathematician developed a theoretical model of these waves so that thereafter they were named after him, *Love waves* [9].

Love showed that these waves can only exist on layers over a half-space of different elastic properties. The solution for the particles displacement of the equation of motion is in this case only dependent on the *v* variables in both mediums (layer and half-space), as shown by the governing equation A.16 given in ref. [9].

$$\frac{\partial^2 v_n}{\partial x^2} + \frac{\partial^2 v_n}{\partial z^2} = \frac{1}{c_{T_n}^2}\frac{\partial^2 v_n}{\partial t^2} \qquad (n = 1,2) \tag{A.16}$$

Where $c_{T_n} = \mu_n / \rho_n$ are the transversal phase velocity of the respective mediums, with the subindex $n = 1$ associated to the layer and the subindex $n = 2$ associated to the half-space.

Applying the boundary conditions of this problem; $\sigma_{zy}^{(1)} = 0$ at $z = -d$, $\sigma_{zy}^{(1)} = \sigma_{zy}^{(2)}$ at $z = 0$ and $v^{(1)} = v^{(2)}$ at $z = 0$. And considering a planar wave solution, we obtain the next particle displacement solutions:

$$v_1 = D\cosh\left[\beta_1 k\left(z + d\right)\right]e^{i(wt - kx)} \quad \text{at } -d \le z \le 0 \tag{A.17}$$

$$v_2 = D\cosh\left(\beta_1 kd\right)\cdot e^{-\beta_2 kz}e^{i(wt - kx)} \qquad \text{at } z \ge 0 \tag{A.18}$$

Where $\beta_n = \sqrt{1 - c^2 / c_{T_n}^2}$ and *D* an arbitrary constant. The Love waves' phase velocity *c* is obtained from the Love characteristic equation:

$$\tan\left[\sqrt{\frac{1}{c_{T_1}^2} - \frac{1}{c^2}}\cdot \omega d\right] = \frac{\mu_2\sqrt{1 - c^2 / c_{T_2}^2}}{\mu_1\sqrt{1 - c^2 / c_{T_1}^2}} \tag{A.19}$$

The solutions to eqn. A.19 are real only if $c_{T2} > c_{T1}$ and they satisfy the condition $c_{T1} < c < c_{T2}$. The phase velocity is a function of the wave's frequency so Love waves are dispersive. As shown in eqn. A.18, Love waves amplitude decrease exponentially with depth in the half-space.

Love waves are interesting for NDT applications as they create stress fields in all the thickness of the top layer, giving information of it all. However their propagation is also affected by the surface of the half-space over which the layer rests.

Love waves opposite to surface waves can propagate in multiple modes. The bigger the value of the product *fd*, then the higher the number of existing modes.

---

[1] Original extracted from *http://www.geo.mtu.edu/UPSeis/waves.html*.

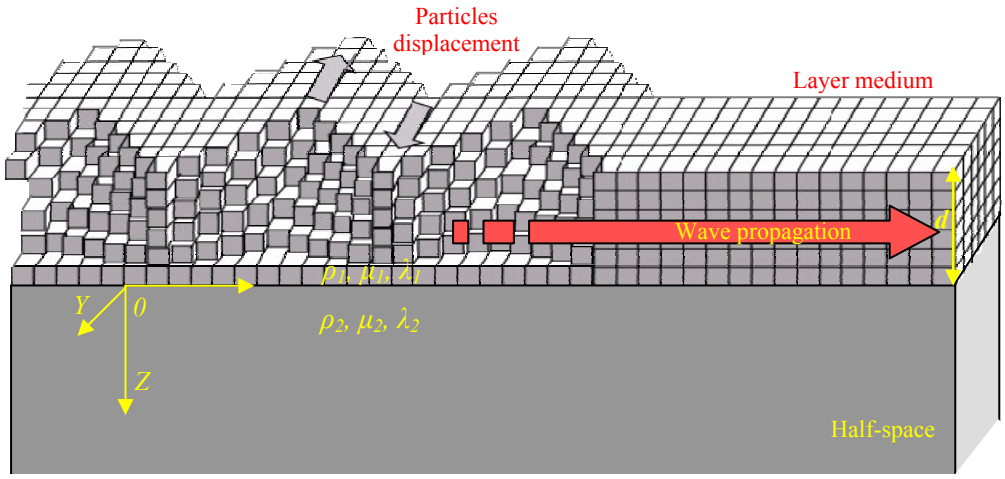

Figure A.5: Shear Horizontal displacement of Love waves in a layer over a half-space.

These waves are not presented in our experimental work as we do not satisfy the condition of having the plate (layer) over a half-space. Fortunately, another kind of guided waves can provide also the through thickness information of the layer without being affected by any other media. These waves are the ones used for the present work and they are described next.

A.1.2.3 Plate-like guided waves: Lamb waves

When a second surface parallel to the existing one is added to the semi-infinite body, then the elastic waves propagate as a new kind of guided wave in the plate-like solid. These new waves are called *Lamb waves* in honour to its theoretical discoverer Horace Lamb [10].

As a result of having the body bounded between two infinite surfaces, the bulk waves propagating within the body are reflected back and forth between the upper and lower bounding surfaces originating multiple reciprocal mode conversion. This results in an interference pattern along the thickness of the plate that guides the wave in a specific direction within it.

As already seen, the superposition of the transversal and compressive waves in each surface of the body generates Rayleigh waves. When these surfaces are close enough from each other, the propagating Rayleigh waves in the upper and lower surface couple, transforming into the new kind of elastic waves, Lamb waves. For this to happen, the thickness of the plate must be of the order or smaller than an ultrasonic wavelength.

Because Lamb waves are the effect of the coupling of surface Rayleigh waves, then Lamb waves spreading attenuation is of a two dimensional wave, in contrast of the three dimensional spreading attenuation associated to bulk waves. In consequence, Lamb waves can propagate larger distance with very low attenuation, and because they produce stress

fields throughout the bulk of the plate, they provide information of the body's entire thickness elastic characteristics. Although their range within the plate specimen depends on many parameters, interrogation distances of the order of hundreds or thousands of ultrasonic wavelengths can be realistically expected.

Solution of the equation of motion

The propagation characteristics of Lamb waves can be analysed once solved the particle displacement expressions associated to these waves. With this purpose in mind, the equation of motion must be solved under the current boundary conditions such that the associated traction force must cancel on the surfaces of the plate. Or equivalently that $\sigma_{XZ} = \sigma_{ZZ} = 0$ at $z = \pm d/2$. The solution is obtained based in the expression of potentials for the equation of motion and following the same reasoning as we did with the Rayleigh waves. However for this problem, the geometry and coordinates definitions are as in fig. A.6, where an infinite plate of thickness d is defined. Again we consider a planar harmonic wave solution so it will be independent of the coordinate perpendicular to the plane of propagation (in our case coordinate Y).

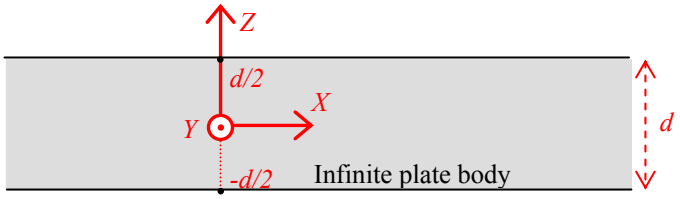

Figure A.6: Geometry of infinite free plate problem.

We will not develop in here the solution extraction process, which has already been done in a very detailed way in reference [8]. It is necessary though to highlight in this appendix the main conclusions of this process and the properties associated to Lamb wave's propagation characteristics.

The solution of Lamb waves to the equation of motion allows two groups of waves to travel in the plate independently of one another. Both groups are characterized by the symmetry of the normal displacement of the particles relative to the plate's neutral axis (plane $z = 0$). These groups are called *symmetric mode* when the displacement is symmetrical and *antisymmetric mode* where the displacement is antisymmetrical, as illustrated in figure A.7.

In order to characterize the two groups of solution, four equations are needed to express the Lamb wave particle displacements; in-plane and out-plane displacements for symmetric and antisymmetric modes. Their expressions are given in eqn. A.20.

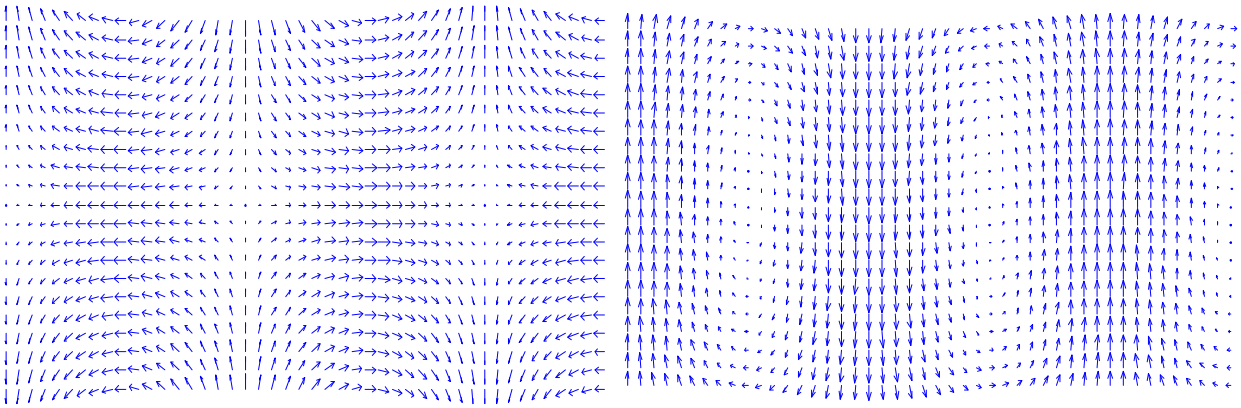

Figure A.7: Snapshot of Lamb waves particles displacements: (*Left*) For a symmetric S_o mode. (*Right*) For an antisymmetric A_o mode.

The subindex $_A$ is associated with the antisymmetric modes and the subindex $_S$ is associated with the symmetric modes. Additionally k_S, $k_A = \omega/c$ with c being the Lamb wave phase velocity (for symmetric mode in the case of k_S and for antisymmetric mode in the case of k_A), $q_S, q_A = \sqrt{k_{S,A}^2 - k_L^2}$, $s_S, s_A = \sqrt{k_{S,A}^2 - k_T^2}$. The arbitrary constants A and B will depend in the power density of the propagating wave.

$$
\begin{aligned}
u_S &= \mathrm{Re}\left[Ak_S \left(\frac{\cosh(q_S z)}{\sinh(q_S d/2)} - \frac{2q_S s_S}{k_S^2 + s_S^2} \frac{\cosh(s_S z)}{\sinh(s_S d/2)} \right) \cdot e^{i\left(k_S x - \omega t + \frac{\pi}{2}\right)} \right] \\
w_S &= \mathrm{Re}\left[Aq_S \left(\frac{\sinh(q_S z)}{\sinh(q_S d/2)} - \frac{2k_S^2}{k_S^2 + s_S^2} \frac{\sinh(s_S z)}{\sinh(s_S d/2)} \right) \cdot e^{i(k_S x - \omega t)} \right] \\
u_A &= \mathrm{Re}\left[Bk_A \left(\frac{\sinh(q_A z)}{\cosh(q_A d/2)} - \frac{2q_A s_A}{k_A^2 + s_A^2} \frac{\sinh(s_A z)}{\cosh(s_A d/2)} \right) \cdot e^{i\left(k_A x - \omega t + \frac{\pi}{2}\right)} \right] \\
w_A &= \mathrm{Re}\left[Bq_A \left(\frac{\cosh(q_A z)}{\cosh(q_A d/2)} - \frac{2k_A^2}{k_A^2 + s_A^2} \frac{\cosh(s_A z)}{\cosh(s_A d/2)} \right) \cdot e^{i(k_A x - \omega t)} \right]
\end{aligned}
\qquad \text{(A.20)}
$$

It is interesting to notice that the in-plane displacement of the antisymmetric modes (u_A) vanishes at the centre of the plate ($z = 0$), which characterize the predominantly out-of-plane component motion associated to this mode. In contrast, for the symmetric modes it is the out-of-plane displacement which cancels at the centre of the plate, evidencing their predominantly in-plane component of motion.

In Lamb waves the displacements of the particles take place both in the direction of the wave's propagation and in the direction perpendicular to the plane of the plate, as it is clear from the expressions in eqn. A.20. This behaviour is similar to the previously described

Rayleigh waves, and like them for each Lamb wave mode, the particles describe elliptical trajectories.

During the process of extracting the previous particle displacement expression, several conditions had to be satisfied. These conditions limit the values that the Lamb wave phase velocity *c* can take. And obviously, the phase velocity values must be known in advance, in order to get the values of the particle displacements for a specific material. The conditions that determine the range of *c* values for which Lamb waves exist in a material are given by the *Rayleigh-Lamb characteristic equations*:

$$\frac{\tan\left(\sqrt{1-\varsigma^2}\,\bar{d}\right)}{\tan\left(\sqrt{\xi^2-\varsigma^2}\,\bar{d}\right)}+\left[\frac{4\varsigma^2\sqrt{1-\varsigma^2}\sqrt{\xi^2-\varsigma^2}}{\left(2\varsigma^2-1\right)^2}\right]^{\pm 1}=0 \qquad \text{(A.21)}$$

Where the exponent $^{+1}$ is associated with the roots for the symmetric modes phase velocity and the exponent $^{-1}$ with the roots of the antisymmetric modes. We also have $\bar{d}=\pi(fd)/c_T$, $\varsigma^2={c_T}^2/c^2$ and $\xi^2={c_T}^2/{c_L}^2$.

Phase and Group velocity dispersion curves

Although eqn. A.21 looks rather simple, it only can be solved numerically. It sets the phase velocity at which a Lamb wave of a given frequency can propagate within the plate of a given thickness. As we can see from this equation the phase velocity is a function of the wave's frequency, so Lamb waves are dispersive. In fact it is a function of the product frequency times the plate's thickness. The numerical solution of the Rayleigh-Lamb equation gives the waves' dispersion relationship in what is known as the Lamb wave *dispersion curves*. Figure A.8-*left* shows an example of such curves for an aluminium plate.

Lamb waves can propagate simultaneously and independently in a different number of modes depending on the product of the wave frequency and the thickness of the plate, as shown in figure A.8. These modes belong to one of the two groups regarding the symmetry of their particles displacements, but they differ from one another in their phase and group velocity and distribution of displacement and stress through the thickness of the plate.

For low frequency:thickness product values only one root for each characteristic equation exist. These are the *null symmetric* (S_0) and *null antisymmetric* (A_0) modes and they exist for all the frequency:thickness product values. It is useful to obtain the expression of their phase velocity in the extreme cases of very small and very high values of *fd*. For ($fd \rightarrow 0$) we have:

$$\lim_{fd\to 0} c_{So}=\sqrt{\frac{E}{\rho(1-\nu^2)}} \qquad \text{(A.22)}$$

$$\lim_{fd \to 0} c_{Ao} = \sqrt[4]{\frac{E}{3\rho(1-\nu^2)}}\sqrt{\pi \cdot fd} \qquad \text{(A.23)}$$

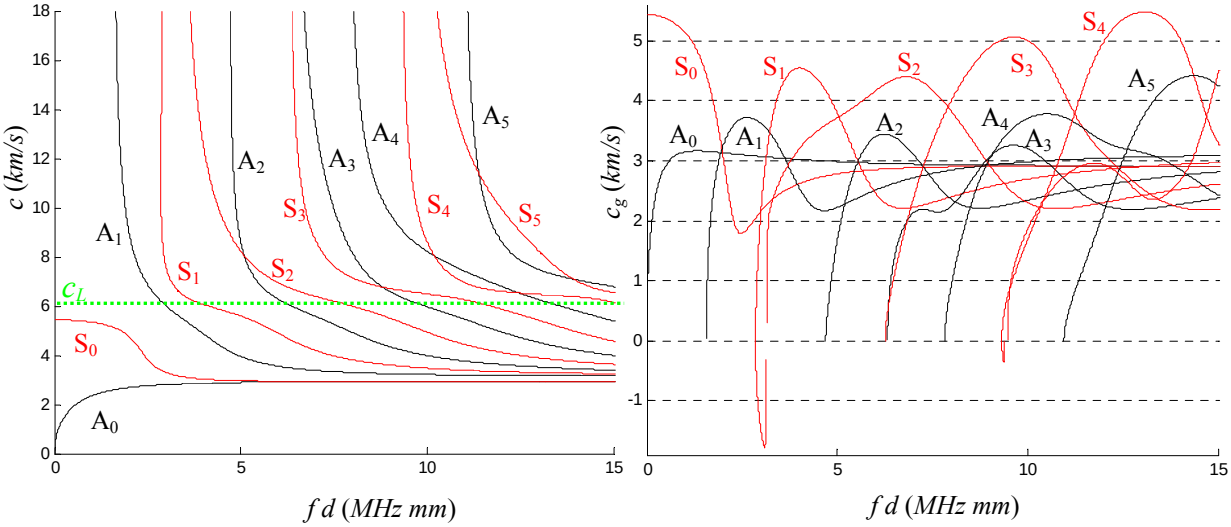

Figure A.8: Lamb waves dispersion curves for the first 6 symmetric (red) and antisymmetric modes (black) in aluminium: (*Left*) Phase velocity dispersion curves. (*Right*) Group velocity dispersion curves.

Equation A.22 shows that for low frequency:thickness product the S_0 has a constant phase velocity and so it is non dispersive, meanwhile eqn. A.23 shows that the A_0 mode's phase velocity increases linearly with fd being null at $fd = 0$.

As the frequency:thickness product increases to infinity, it is easy to prove mathematically that the null modes phase velocity tends to the Rayleigh waves value c_R. Experimentally can be shown that when the thickness of the plate d is twice or bigger the Rayleigh wavelength λ_R then the two null Lamb wave modes (A_0 and S_0) start having a great similarity with the Rayleigh waves. They become non-dispersive with their group and phase velocity near to the phase velocity of Rayleigh wave, and the depth distribution of the displacements in each of the waves for the upper and lower halves of the plate is similar to the distribution of the Rayleigh wave displacement.

In fact within the previous condition $d > 2 \cdot \lambda_R$ the ultrasonic source excites the modes A_0 and S_0 with nearly equal amplitudes and phases, being their displacements in the same direction in the surface of the plate where the source is located, and in opposite direction in the other surface of the layer. During their propagation, A_0 and S_0 modes interfere with one another such that near the ultrasonic source their total acoustic field is similar to the Rayleigh wave acoustic field. In this way, the null modes behave as a quasi-Rayleigh wave propagating in the same surface where the source is situated.

As we go farther from the source the phase difference between the null modes increases, becoming π at a distance L, which is a function of d / λ_R (see [8] for an approximated expression). At this distance the quasi-Rayleigh wave 'transfers over' to the opposite surface where the source is located. Repeatedly this 'transference' of the quasi-Rayleigh wave from one surface to the other happens every multiple of the mentioned distance L. When $d/\lambda_R \to \infty$ then $L \to \infty$ and the quasi-Rayleigh wave becomes a pure Rayleigh wave, which corresponds effectively to a half-space solid situation.

These null modes are pure, inhomogeneous interface waves that are originated from bulk wave mode conversion in the surfaces of the plate. But other Lamb modes are present in plate-like structures as we increase the frequency:thickness product from zero. The additional number of new roots, of both the symmetric and antisymmetric characteristic equations, increases successively as the frequency:thickness product increases. These are called *high order modes* and in opposition to the null modes, they originate in the body of the material. These modes are not present at all frequencies, as they are originated as standing waves related to one of the bulk waves. The frequency:thickness product values at which they appear are the *cut-off frequencies* and their expressions are given in eqns. A.24 and A.25. At these points, the phase velocity approaches asymptotically infinity and the group velocity tends to zero. This agrees with the affirmation of having the high order modes originated as standing longitudinal and/or transversal waves across the thickness of the plate, because a standing wave does not propagate energy thus its group velocity must cancel. If we rewrite the cut-off frequencies as a relation between thickness of plate and bulk wavelength (as shown in the right side of previous equations) we can clearly understand the transversal or longitudinal though-thickness standing wave origin of these high order modes.

For symmetric modes:

$$fd = \begin{cases} c_T, 2c_T, 3c_T, \ldots \equiv c_T(n+1) \\ \dfrac{c_L}{2}, \dfrac{3c_L}{2}, \dfrac{5c_L}{2}, \ldots \equiv (2n+1)\dfrac{c_L}{2} \end{cases} \equiv d = \begin{cases} \lambda_T, 2\lambda_T, 3\lambda_T, \ldots \equiv \lambda_T(n+1) \\ \dfrac{\lambda_L}{2}, \dfrac{3\lambda_L}{2}, \dfrac{5\lambda_L}{2}, \ldots \equiv (2n+1)\dfrac{\lambda_L}{2} \end{cases} \tag{A.24}$$

For antisymmetric modes:

$$fd = \begin{cases} c_L, 2c_L, 3c_L, \ldots \equiv c_L(n+1) \\ \dfrac{c_T}{2}, \dfrac{3c_T}{2}, \dfrac{5c_T}{2}, \ldots \equiv (2n+1)\dfrac{c_T}{2} \end{cases} \equiv d = \begin{cases} \lambda_L, 2\lambda_L, 3\lambda_L, \ldots \equiv \lambda_L(n+1) \\ \dfrac{\lambda_T}{2}, \dfrac{3\lambda_T}{2}, \dfrac{5\lambda_T}{2}, \ldots \equiv (2n+1)\dfrac{\lambda_T}{2} \end{cases} \tag{A.25}$$

Where n = 0, 1, 2 … Notice that left and right expressions are equivalent.

The cut-off frequencies are assigned to the Lamb waves modes, following increasing frequency:thickness product value with increasing mode order. However this incremental

order will depend on the values of the bulk waves phase velocities. For instance, in Table A.1 we show the cut-off frequencies associated to the first five symmetric and antisymmetric modes for the materials used in this thesis; aluminium, steel and Perspex. In this table we see that in Perspex and steel the assigned cut-off frequencies to the modes are the same, however they are different from the ones assigned to the symmetric modes in aluminium.

Material	Symmetric cut-off frequency:thickness		Antisymmetric cut-off frequency:thickness	
Aluminium c_T =3.13 c_L = 6.32	S_1	C_T	A_1	$C_T/2$
	S_2	$C_L/2$	A_2	$3C_T/2$
	S_3	$2C_T$	A_3	C_L
	S_4	$3C_T$	A_4	$5C_T/2$
	S_5	$3C_L/2$	A_5	$7C_T/2$
Steel c_T =3.26 c_L = 5.96	S_1	$C_L/2$	A_1	$C_T/2$
	S_2	C_T	A_2	$3C_T/2$
	S_3	$2C_T$	A_3	C_L
	S_4	$3C_L/2$	A_4	$5C_T/2$
	S_5	$3C_T$	A_5	$7C_T/2$
Perspex c_T =1.43 c_L = 2.73	S_1	$C_L/2$	A_1	$C_T/2$
	S_2	C_T	A_2	$3C_T/2$
	S_3	$2C_T$	A_3	C_L
	S_4	$3C_L/2$	A_4	$5C_T/2$
	S_5	$3C_T$	A_5	$7C_T/2$

Table A.1: Cut-off frequency:thickness products associated to the first five symmetric and antisymmetric modes for common materials. The bulk waves velocities are in km/s.

When the high order modes begin to travel (for frequency:thickness products over their cut-off values) they couple with the remaining bulk wave and create an inhomogeneous wave.

As the frequency:thickness product values increases to infinity, the phase velocity of the high order modes (both symmetric and antisymmetric) converge to the transversal bulk wave velocity value c_T.

It is remarkable that the high order symmetric modes' dispersion curves have a frequency: thickness product interval, just over their cut-off frequencies, where the phase velocity flattens. At the beginning of this region the modes' phase velocity reaches the longitudinal bulk wave value (shown as a green horizontal line in Figure A.8-*left*). These frequency:thickness product intervals are broader the higher the symmetric order mode. Additionally, the symmetric modes group velocities reach their maximum in these intervals, and the out-of-plane displacement of the symmetric modes vanishes in the surface of the

plate. This situation contributes to the already pointed affirmation that symmetric modes have preferential longitudinal mode behaviour.

The Lamb waves' dispersion characteristic is, as previously stated, commonly displayed in the form of phase velocity curves. But a more important and useful concept are the group velocity dispersion curves (Figure A.8-*right*), as they provide relevant information such as the time of arrival of wave packets. Group velocity dispersion curves show the velocity at which finite-time wave packets travel in the structure. In order to avoid an unnecessary extension of the length of this appendix and because of the particular difficulty and importance of understanding what group velocity represents and its difference with the phase velocity, we have dedicated the full length of Appendix D to this subject. We encourage any interested reader to have a look at it.

In a simple way, group velocity is defined as $c_g = d\omega/dk$, with k being the Lamb wavenumber $k = \omega/c$. It is easy to probe that c_g can be rewritten as:

$$c_g = c^2\left[c - (fd)\frac{dc}{d(fd)}\right]^{-1} \tag{A.26}$$

Equation A.26 shows that when the phase velocity c does not change with fd then $c_g = c$, as it is the case of non-dispersive systems. This happens to the S_0 mode at low values of fd or at high values for both S_0 and A_0 modes, as shown in figure A.8.

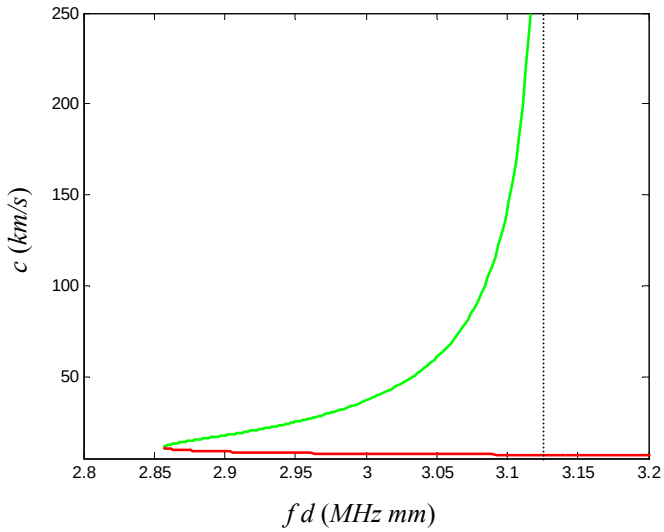

Figure A.9: S_1 mode phase velocity around its cut-off frequency:thickness value in aluminium. In green is the anomalous mode's region and in dashed black the cut-off frequency.

Finally we want to highlight the behaviour of S_1 mode around its cut-off frequency:thickness product (see fig. A.9). This mode is defined for frequency:thickness products below its cut-off frequency and it suffers of *anomalous dispersion* where $dc/df > 0$ (in green in fig. A.9)

and the mode's phase velocity appears to have double value. When d*c/df* is sufficiently negative, based in eqn A.26, the group velocity becomes negative, and the transportation of energy or information by the wave takes place in opposite direction to its phase velocity. In addition when rewriting the group velocity as $c_g = (d(1/\lambda)/df)^{-1}$, it is evident that a negative group velocity implies that the ultrasonic wavelength increases as the frequency increases, which is the opposite of the common situation.

The negative group velocity phenomena was considered at the beginning of the 20th century as unphysical and just of only mathematical consideration [11], and it is not until the middle 1960's that it was experimentally verified [12]. As shown in Chapter 6, the negative group velocity for S_1 mode in aluminium is present in our experimental work. This particularity although naturally associated to S_1 mode for all materials, it can also be present in other symmetric and antisymmetric high order modes for certain elastic materials. This is discussed further in Chapter 7 and in Appendix D.

The paradox of c_T and c_L as solutions of the Rayleigh-Lamb characteristic equation

It is not difficult to prove that $\varsigma = 1$ (which means $c = c_T$) is a solution of the Rayleigh-Lamb characteristic equation for the symmetric modes, for any value of $\bar{d}$ or alternatively for any value of the frequency:thickness product. Effectively for the symmetric mode we use the equation with positive exponent ($^{+1}$). Then for $\varsigma = 1$ we have that $\sqrt{1-\varsigma^2} = 0$ so $\tan\left(\sqrt{1-\varsigma^2}\cdot\bar{d}\right) = 0$ and then we have 0 = 0, which is a solution of the Lamb wave equation. The only possibility to avoid mathematically this solution is to get an indetermination of the kind 0/0 in the left side of the equation. Then we need $\tan\left(\sqrt{\xi^2-\varsigma^2}\cdot\bar{d}\right) = 0$, but because for real materials we have that $c_T < c_L$ then $\xi^2 < \varsigma^2$ and $\sqrt{\xi^2-\varsigma^2} = i\cdot\sqrt{\varsigma^2-\xi^2} = i\cdot\sqrt{1-\xi^2}$ is a complex number. Now considering the case of $\varsigma = 1$, we have $\tan\left(\sqrt{\xi^2-\varsigma^2}\cdot\bar{d}\right) = \tan\left(i\cdot\sqrt{1-\xi^2}\cdot\bar{d}\right) = i\cdot\tanh\left(\sqrt{1-\xi^2}\cdot\bar{d}\right)$. The only way to make this equal to 0 is doing $\sqrt{1-\xi^2}\cdot\bar{d} = 0$, which implies that $\bar{d} = 0$, option that does not have physical meaning.

This mathematical analysis concludes that the horizontal line $c = c_T$ should be a solution in the symmetrical modes dispersion curves. However it does not appear experimentally and it neither appears in fig. A.8.

A similar analysis over the antisymmetric characteristic equation (negative exponent $^{-1}$), would give $c = c_L$ as a solution of the antisymmetric modes for any value of the frequency: thickness product. Again this solution does not appear experimentally.

Lamb modes are generated by interference of the transversal and longitudinal bulk modes, and then the bulk modes by themselves cannot be a Lamb wave solution.

The answer to this paradox is that these solutions are a mathematical artefact. Although they satisfy Lamb wave characteristic equation, they do not satisfy the boundary conditions. When evaluating the stress field in the surface of the plate, using one of these bulk velocities, we find that the traction forces σ_{XZ} and σ_{ZZ} are not zero, hence they cannot be Lamb waves.

Lamb wave testing of materials

Phase and group velocity dispersion curves are highly sensitive to the principal material elastic properties (Poisson's ratio, Young's modulus) as shown by the dependence of the characteristic equation on the bulk waves phase velocity and on these with E and v as given on equations A.9 and A.10. Together with their highly dependence to structural loading or the presence of defects within the material, makes them very useful in NDT applications.

Conventional Lamb wave testing methodology, where usually a single frequency sinusoidal toneburst is used, looks to the differences between the detected ultrasonic signal for the damaged plate and a reference ultrasonic signal associated to the certainly known undamaged plate. These changes are associated to the reflections of the generated ultrasonic signal from the presented damage.

This conventional analysis is mainly carried on the time domain and it looks not only to changes in amplitude of the ultrasonic signal, but also to phase changes or even appearance of propagating new Lamb modes originated by mode conversion in an antisymmetric boundary [13]. The analysis is usually simplified by confining it to low values of frequency:thickness product such that only the fundamental modes S_0 and A_0 can propagate in the structure. This avoids the overlapping of high order modes arriving at same time to the detector, which would complicate considerably the time signals. For instance in aluminium the frequency:thickness product is usually restricted to be under 1.5 *MHz mm* (as shown in figure A.8).

The most common generation techniques used in conventional Lamb waves testing are; angle beam transducers, comb transducer or PZT transducers. These systems can be used to selectively launch a single fundamental mode [14,15], which although possible in theory it is a bit difficult in practice but effectively helps in the time domain signal interpretation. In addition, it is also of great help the fact that for low frequency:thickness products (below 1 *MHz mm*) the S_0 mode is non-dispersive and it is the fastest of the fundamental modes, being able to propagate for significant distances without losing temporal pulse definition and without interfering with any other presented mode. However its main disadvantage is that its

wavelength (around 1 *cm*) is large in comparison with the plate thickness (1 *mm*), thus placing a limit on the far field analysis attainable defect resolution. The A_0 mode in contrast has much smaller velocity values up to 0.5 *MHz mm* frequency:thickness product, however it is highly dispersive in this area, modifying considerably the launched signal and interfering with the reflections of the faster S_0 mode.

The signal processing advantage of the conventional technique proves its common uses in NDT applications where the damage resolution limitation is not a problem. This technique has been used in the experimental work of chapters 3 and 4.

Nonetheless, the limitations of the previous singlemode inspection technique obligate to develop alternative inspection techniques, in order to provide a higher defect resolution. One of such techniques utilises a broadband excitation of the Lamb wave spectrum, providing a much shorter ultrasonic wavelength. As a consequence of the broadband excitation a large number of high order modes are excited causing a very complex overlapped time signal, which requires the application of more complex signal processing techniques; such as those presented in Chapter 5 in order to extract the dispersion curves information. The technique is used in the experimental work of chapters 6 and 7.

Lamb wave mode selection

Lamb waves displacement and pressure distribution along the thickness of the inspected plate is rather complicate, changing dramatically not only as the mode's type changes, but also as the mode's order does. Even when we move along the same mode, by changing the frequency:thickness product value, the through-thickness distribution is very different. Figure A.10 is a good example of this, it compares the displacement distribution of the S_0 mode along the thickness of an aluminium plate, for two different frequency:thickness product values. The vertical axis z/λ represents the depth normalized against the ultrasonic wavelength. The value 0 is associated to the centre of the plate and the maximum and minimum values representing its top and bottom surface. In the other hand the horizontal axis shows the in-plane (*red*) and out-of-plane (*blue*) displacement values normalized against the out-of-plane displacement in the surface of the plate. At around 0.12 *MHz mm* the S_0 mode behaves as a longitudinal wave with a nearly null out-of-plane displacement and with the in-plane displacement almost constant across the plate's thickness, as shown in fig. A.10-*left*. However at around 2.34 *MHz mm* the situation is totally different with the out-of-plane displacement in the surface being much bigger than the in-plane one, and with the in-plane displacement energy concentrated mainly at the centre of the plate and cancelling at a certain depth, as we can see in fig. A.10-*right*. This is in contrast to the general preferential in-plane

behaviour of the symmetric modes as previously commented, and it helps in understanding that the symmetric modes cannot be thought of just an in-plane vibration.

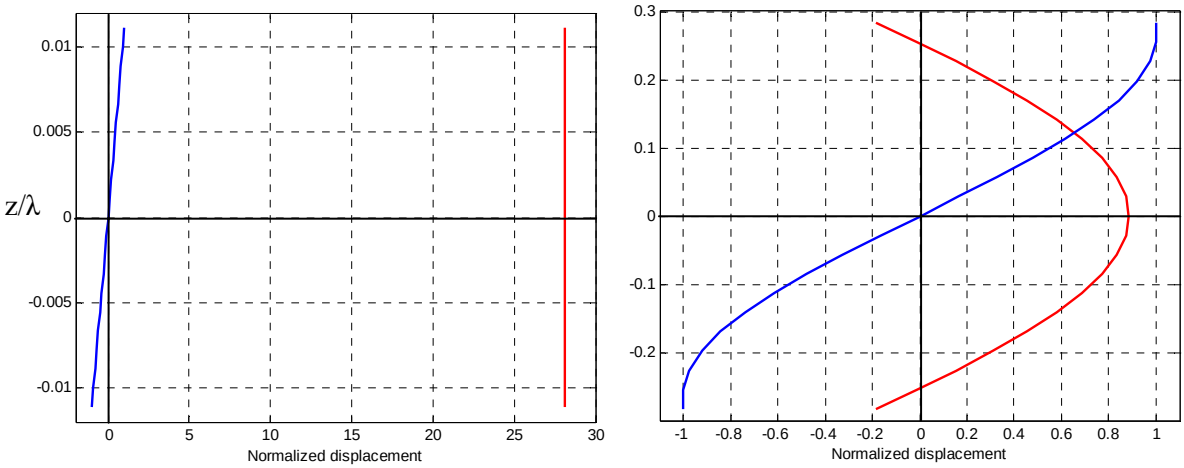

Figure A.10: In-plane (red) and out-of-plane (blue) displacement values for S_0 mode in aluminium: (*Left*) Frequency:thickness = 0.12 *MHz mm*. (*Right*) Frequency:thickness = 2.12 *MHz mm*.

Similar can be said of the antisymmetric modes, as not being just out-of-plane vibration modes. As an example we have fig. A.11, where two different frequency:thickness product values are considered for A_0 mode in aluminium.

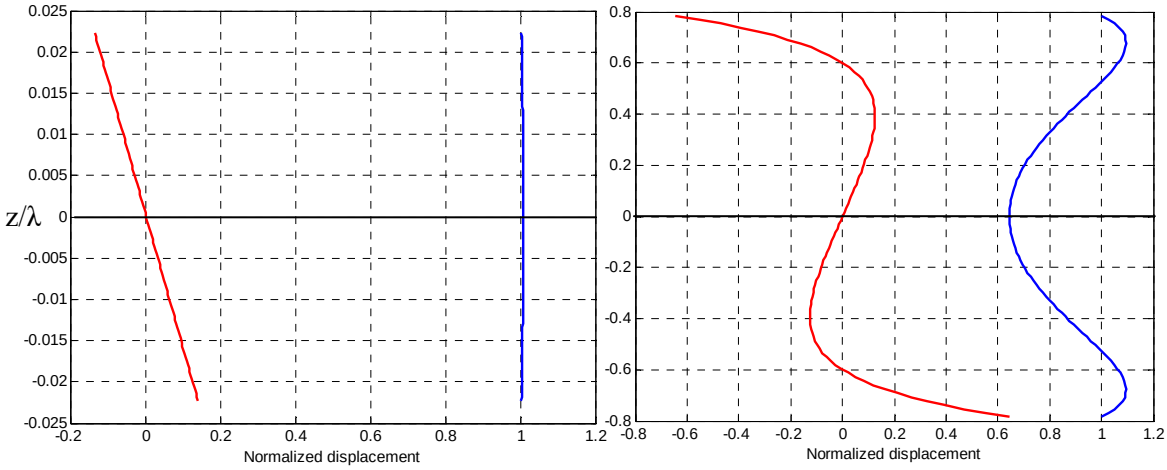

Figure A.11: In-plane (red) and out-of-plane (blue) displacement values for A_0 mode in aluminium: (*Left*) Frequency:thickness = 0.0195 *MHz mm*. (*Right*) Frequency:thickness = 4.53 *MHz mm*.

At low frequency:thickness product values the A_0 mode behaves as a transversal mode with an almost null in-plane displacement and a uniform though thickness out-of-plane displacement.

In contrast, as the frequency:thickness product increases (fig. A.11-*right*), the in-plane displacement increases considerably in the surface of the plate and the out-of-plane displacement energy moves as well towards the surface. This behaviour is a reminder of the mode's Rayleigh wave characteristic as the plate thickness is comparable to the ultrasonic wavelength.

The different energy distribution and behaviour of the different modes make important to understand the interaction characteristics of the chosen sensors with the ultrasonic waves and their embedded or bonded position within the inspected structure, in order to properly choose a Lamb mode and frequency:thickness value that maximize the sensitivity of the sensor. For instance, FBGs are known to be mainly sensitive to in-plane displacements [16]. Then for a surface bonded FBG sensor, certainly the case in fig. A.10-*left* would be the most suitable. Meanwhile for an out-of-plane displacement interferometric sensor, the case in A.11-*left* would be preferable.

It is also important to properly understand the interaction characteristics of the expected structural damage; for instance the through-thickness position of the damage should require a Lamb mode with considerable stress and energy distributions around the same depth as the damage is located. Or the affinity of the damage interaction to in-plane or out-of-plane displacements. For instance delaminations are known to be more sensitive to transversal stresses, so they will be better detected by the use of the ultrasonic wave in fig. A.10-*right* than by the wave in the *left* side of the same figure.

A.1.2.4 Interface waves : Stoneley waves

These waves exist at the interface of two half-space solids when the interface is capable of supporting the wave so that no energy is leaked into any of the materials. This is only possible for a very limited domain of material properties as given in [17].

It was R. Stoneley who by generalization of the single interface problem (Rayleigh waves) first gave a mathematical model to these waves in 1924 [18].

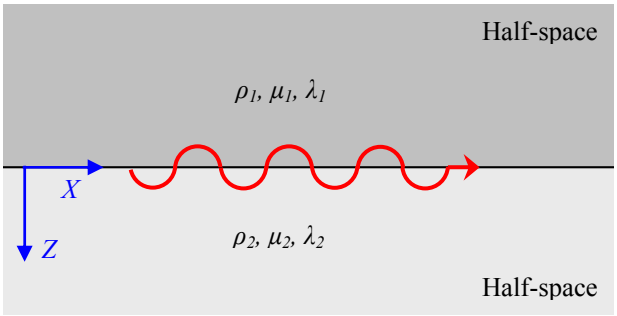

Figure A.12: Stoneley waves propagating within the interface of two half-space bodies.

Following the notation and coordinate system depicted on fig. A.12, and applying the boundary conditions for a perfect contact interface in $z = 0$ to the equation of motion; $u^{(1)} = u^{(2)}$, $w^{(1)} = w^{(2)}$, $\sigma_z^{(1)} = \sigma_z^{(2)}$ and $\sigma_{xz}^{(1)} = \sigma_{xz}^{(2)}$. Where the indices (1) and (2) associated to the upper and lower half-spaces respectively.

We obtain the Stoneley waves particles displacements:

$$\begin{aligned} u^{(1)} &= \left(A_1 e^{k\alpha_1 z} + B_1 \beta_1 e^{k\beta_1 z}\right) e^{i(kx-\omega t)} \\ w^{(1)} &= -i\left(A_1 \alpha_1 e^{k\alpha_1 z} + B_1 e^{k\beta_1 z}\right) e^{i(kx-\omega t)} \end{aligned} \quad \text{upper half-space } z < 0 \tag{A.27}$$

$$\begin{aligned} u^{(2)} &= \left(A_2 e^{-k\alpha_2 z} - B_2 \beta_2 e^{-k\beta_2 z}\right) e^{i(kx-\omega t)} \\ w^{(2)} &= i\left(A_2 \alpha_2 e^{-k\alpha_2 z} - B_2 e^{-k\beta_2 z}\right) e^{i(kx-\omega t)} \end{aligned} \quad \text{lower half-space } z > 0 \tag{A.28}$$

Where $\alpha_n = \sqrt{1 - c^2 / c_{L_n}^2}$, $\beta_n = \sqrt{1 - c^2 / c_{T_n}^2}$ and A_n, B_n are arbitrary constants with $n = 1,2$ for upper and lower half-space respectively. Notice that because β_n must be real then Stoneley waves' phase velocity c must be smaller than the smallest c_{Tn}. The displacement amplitude is higher in the interface ($z = 0$) and then it decreases exponentially with the depth in any of both materials.

In order to obtain the phase velocity value of the propagating Stoneley wave and to solve the four arbitrary constants then the real roots of the determinant in A.29 must be obtained.

$$\begin{vmatrix} -\left(1+\beta_1^2\right) & -2\beta_1 & \left(1+\beta_2^2\right)g & -2\beta_2 g \\ 2\alpha_1 & \left(1+\beta_1^2\right) & 2\alpha_2 g & -\left(1+\beta_2^2\right)g \\ 1 & \beta_1 & -1 & \beta_2 \\ -\alpha_1 & -1 & -\alpha_2 & 1 \end{vmatrix} = 0 \tag{A.29}$$

Where $g = \mu_2 / \mu_1$. Because no component of this determinant is a function of the wave's frequency, then Stoneley waves are not dispersive.

Stoneley waves are best suited for assessing the quality of bonded interfaces for bonded joint inspection as they are sensitive to microstructural changes and the degree of contact between the two media that create the interface in which they propagate [19]. However the main drawback of Stoneley waves is that they are inherently difficult to generate and detect.

In the work of this thesis Stoneley waves were avoided in the interface between the aluminium specimen plate and the supporting optical bench, by inserting paper sheets in between, or leaving an air gap. The only case in which Stoneley waves could appear is in the interface between the aluminium plate and the Epotex mould of the optical fibre sensors during the wavefront integration experiments described in Chapter 4. Nonetheless this interface does not allow the existence of Stoneley waves.

A.2 CONCLUSIONS

In this appendix we have presented the principles of the theory of elasticity, so that the reader could get familiar with the basic concepts of wave propagation in solid materials. We have introduced important concepts such as strain and stress fields, phase and group velocity, and we have defined the elastic properties that completely define the elastic behaviour of an isotropic solid material; Poisson's ratio and Young's modulus.

We have seen that the bulk waves presented in all solid materials can interfere to generate different kinds of ultrasonic guided waves. Between them special attention has been given to surface and plate-like guided waves, as they are the most involved within this thesis. However we have not forgotten that under adequate boundary conditions other guided waves may be presented, and we have justified why they are not relevant in our experiments.

Special attention has been given to the analysis of the dispersive and multimode propagation characteristic of Lamb waves and how this information can be used for testing of materials and for monitoring of its elastic properties. In addition, fundamental concepts such as phase and group velocity dispersion curves and high order modes cut-off frequency:thickness products were presented, preparing the reading for their use along the thesis.

APPENDIX B: Equation of motion in elastic solids

In order to develop the equation of motion we need to express the left side of Equations A.2-A.4 as a function of the element's displacement variables, for which we need to look at the stress-strain relationship of the material or Hooke's law. Based on this law, each of the six components of stress in the element of material can be expressed as a linear function of six components of strain. This gives 36 possible independent coefficients to relate stress and strain, however it can be shown [35] that for isotropic elastic media only two independent constants remain, they are named *Lamé's constants* and they are represented by the Greek letters λ and μ. The Lamé's constants completely define the elastic behaviour of an isotropic solid by the next relationship:

$$\begin{array}{ccc} \sigma_{xx} = \lambda\Delta + 2\mu\varepsilon_{xx} & \sigma_{yy} = \lambda\Delta + 2\mu\varepsilon_{yy} & \sigma_{zz} = \lambda\Delta + 2\mu\varepsilon_{zz} \\ \sigma_{yz} = \mu\varepsilon_{yz} & \sigma_{zx} = \mu\varepsilon_{zx} & \sigma_{xy} = \mu\varepsilon_{xy} \end{array} \qquad \text{(B.1)}$$

Where $\Delta = \varepsilon_{xx} + \varepsilon_{yy} + \varepsilon_{zz}$ represents the change in volume of a unit cube and is named *dilatation*; ε_{xx}, ε_{yy}, and ε_{zz} are the *normal strain* components; ε_{xy}, ε_{yz}, and ε_{zx} are the *shear strain* components. Figure A.1-*right* helps to understand how the strain components are defined as it looks to an infinitesimal translation and deformation of the two dimensional plane *YZ* of the material's elements defined in appendix A.

The *normal strains* correspond to the fractional expansions and contractions of the infinitesimal element's line edges parallel to the main axis. Following the notation in Figure A.1-*right* we can express ε_{yy} and ε_{zz} by:

$$\varepsilon_{yy} = \frac{A'B' - AB}{AB} \qquad \varepsilon_{zz} = \frac{A'D' - AD}{AD} \tag{B.2}$$

Under the approximations of small strain and deformations the normal strains can be rewritten as:

$$\varepsilon_{xx} = \frac{\partial u}{\partial x} \qquad \varepsilon_{yy} = \frac{\partial v}{\partial y} \qquad \varepsilon_{zz} = \frac{\partial w}{\partial z} \tag{B.3}$$

The *shear strains* correspond to the angular deformation of the infinitesimal elements in the different planes, such that following the notation in Figure A.1-*right* we can express ε_{yz} as:

$$\varepsilon_{yz} = \theta_1 + \theta_2 \tag{B.4}$$

Again under the approximations of small deformations and by analogy with the other planes:

$$\varepsilon_{xy} = \frac{\partial v}{\partial x} + \frac{\partial u}{\partial y} \qquad \varepsilon_{yz} = \frac{\partial w}{\partial y} + \frac{\partial v}{\partial z} \qquad \varepsilon_{zx} = \frac{\partial u}{\partial z} + \frac{\partial w}{\partial x} \tag{B.5}$$

Finally the *equation of motion* for an elastic isotropic solid in the absence of body forces, as a function of the particle displacements is obtained by substituting Equations B.1, B.3 and B.5 in A.2-A.4, and after applying some algebraic manipulations:

$$(\lambda + 2\mu)\vec{\nabla} \cdot \left(\vec{\nabla} \cdot \vec{u}\right) + \mu\vec{\nabla} \times \left(\vec{\nabla} \times \vec{u}\right) = \rho \cdot \frac{\partial^2 \vec{u}}{\partial t^2} \tag{B.6}$$

Where $\vec{u} = (u\hat{i} + v\hat{j} + w\hat{k})$ is the displacement vector and $\vec{\nabla}$ the gradient operator.

This expression can be simplified by the application of Helmholtz decomposition [36] over the displacement vector, such that it can be written in terms of a scalar potential ϕ and a vector potential $\vec{\psi}$ as:

$$\vec{u} = \vec{\nabla} \cdot \phi + \vec{\nabla} \times \vec{\psi} \tag{B.7}$$

If we substitute (B.7) into (B.6):

$$\vec{\nabla}\cdot\left[(\lambda+2\mu)\nabla^2\phi-\rho\cdot\frac{\partial^2\phi}{\partial t^2}\right]+\vec{\nabla}\times\left[\mu\nabla^2\vec{\psi}-\rho\cdot\frac{\partial^2\vec{\psi}}{\partial t^2}\right]=0 \tag{B.8}$$

This equation is satisfied only if both terms are null, so the equation of motion can be decomposed into two uncoupled equations:

$$\nabla^2\phi=\frac{1}{(\lambda+2\mu)/\rho}\cdot\frac{\partial^2\phi}{\partial t^2} \qquad \nabla^2\vec{\psi}=\frac{1}{\mu/\rho}\cdot\frac{\partial^2\vec{\psi}}{\partial t^2} \tag{B.9}$$

APPENDIX C: Most sensitive polarization state of light output in the polarimetric sensor

In chapters 2 and 3 we presented the operation and set up of the polarimetric sensor system for ultrasonic wave detection. There it was mentioned that the ultrasonic signal amplitude produced by the system set-up was dependent both on the input state of polarisation of the light to the system, and the orientation of the polariser at the output. Here we present a theoretical analysis of the polarimetric system sensitivity dependency with the polarization state of the light at the output of the optical fibre sensor and the orientation of the linear polarizer. In order to do this, we compare the maximum variation of the optical intensity passing through the polarizer in its optimum orientation due to a small change in its polarization state, for the three cases in which the output light of the sensing fibre (before the polariser) is linear, circular and a general elliptical case.

In this analysis we have considered several realistic simplifying assumptions; a linear birefringence induced by the ultrasonic wave [33], a monochromatic and plane wave light progressing in either direction along the *z* axis corresponding to the axis of the fibre, and the only changes in the polarization state of the light caused by the acoustic wave are changes in the phase difference between the two electric field components and not in their associated amplitude.

The Jones' algebra [34], developed by R. C. Jones in 1941, is specially adapted to the description of the polarized states of light and their coherent superposition, therefore is the notation chosen for this analysis. The state of polarization of a propagating light wave may be completely defined by stating the amplitudes and phases of the *X* and *Y* components of the

electric vector of the light wave. Thus at any fixed point along the *Z* axis, the electric field may be written as:

$$\vec{E} = a_X \cos(\tau + \delta_X)\hat{i} + a_Y \cos(\tau + \delta_Y)\hat{j} \tag{C.1}$$

Where a_X and a_Y are the amplitude of the two orthogonal electric fields. δ_X and δ_Y are arbitrary phase values of each electric field component so that we can define $\delta = \delta_X - \delta_Y$ as their difference in phase. We also define $\tau = \omega t - kz$.

Jone's algebra represents these electric fields components in a matrix notation with an orthogonal base of two vectors of dimension 2x1 representing the linear states *X* and *Y* as given by eqn. C.2.

$$|e_1\rangle = \begin{bmatrix} 1 \\ 0 \end{bmatrix} \qquad |e_2\rangle = \begin{bmatrix} 0 \\ 1 \end{bmatrix} \tag{C.2}$$

Hence any electric field (or polarization state) associated to a plane wave light can be expressed as a combination of these orthogonal base vectors as shown next:

$$|E\rangle = \langle e_1|E\rangle \cdot |e_1\rangle + \langle e_2|E\rangle \cdot |e_2\rangle \tag{C.3}$$

Where $\langle e_i|E\rangle$ represents the projection of the electric field polarization state to the base vector component $|e_i\rangle$ with i = 1,2. The effect of any optical element (f.i. a polarizer) on the light can be represented as a linear operator acting upon the electric vector of the light wave. The operator is expressed as a 2x2 matrix in Jone's algebra.

Linearly polarized light

In a linearly polarized light the two electric field orthogonal components propagate in phase ($\delta = 0$) or equivalently the electric field vector evolves with time along a line in the plane of polarization as shown in fig. C.1-*left*. The linearly polarized light can be expressed in Jone's algebra by eqn. C.4.

$$|E_{LIN}\rangle = r \begin{bmatrix} \cos\gamma \\ sen\gamma \end{bmatrix} \tag{C.4}$$

Where $r = \sqrt{a_X^2 + a_Y^2}$ and γ is the *remanent angle of polarization* defined as $\gamma = tan^{-1}(a_Y/a_X)$ and it represents the angle of the diagonal line of the polarization plane with respect to the horizontal axis as shown in fig. C.1-*left*. For a line polarized line this diagonal line agrees with the line along which the electric field vector evolves with time (in red in fig. C.1-*left*).

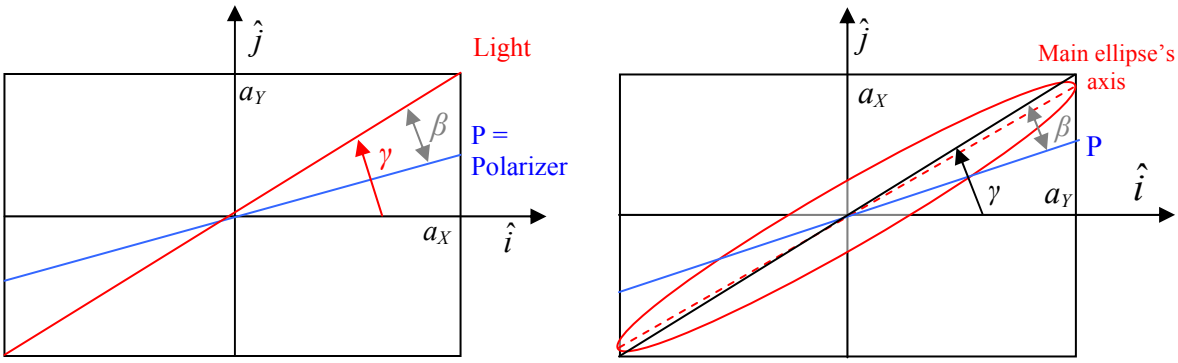

Figure C.1: (*Left*) Linear polarized light in the plane of the wave. The electric field of the light evolves in time along the red line. (*Right*) Ultrasonic wave perturbation of the linear polarization state into a slightly elliptical one. In blue we show an arbitrary position of the linear polarizer.

When a polarizer acts over the electric field of the propagating light, the effect can be represented in Jone's algebra as a 2x2 matrix. In the case of a linear polarizer oriented at an angle β respect to electric field line (shown by a blue line in fig. C.1-*left*) this matrix is defined as:

$$|P\rangle = \begin{bmatrix} \cos^2(\gamma-\beta) & sen(\gamma-\beta)\cos(\gamma-\beta) \\ sen(\gamma-\beta)\cos(\gamma-\beta) & sen^2(\gamma-\beta) \end{bmatrix} \tag{C.5}$$

Therefore, following the description of Jone's algebra presented in [34] now we can express the optical intensity or irradiation of the light coming out the polarizer as:

$$I_{PL} = \langle E_{LIN}|P*P|E_{LIN}\rangle = \langle E_{LIN}|P|E_{LIN}\rangle = r^2\begin{bmatrix}\cos\gamma & sen\gamma\end{bmatrix}\cdot$$

$$\begin{bmatrix} \cos^2(\gamma-\beta) & sen(\gamma-\beta)\cos(\gamma-\beta) \\ sen(\gamma-\beta)\cos(\gamma-\beta) & sen^2(\gamma-\beta) \end{bmatrix}\cdot\begin{bmatrix}\cos\gamma \\ sen\gamma\end{bmatrix} = r^2\cos^2\beta \tag{C.6}$$

Where we have applied the property associated to a polarizer operator for which $\langle P|P\rangle = |P\rangle^2 = |P\rangle$.

Now when the propagating ultrasonic wave pressure field interact with the optical fibre sensor where the light wave is progressing, the polarization state of the light is disturbed by a slight change in the phase difference between the two electric field components so that $\delta = \Delta\delta \rightarrow 0$. As we mentioned in our assumptions the induced birefringence does not change the amplitude of the electric field components a_X and a_Y and so neither the angle γ. The new polarization state will be slightly elliptical as shown in fig. C.1-*right* and it is given by:

$$\left| E'_{LIN} \right\rangle = r \begin{bmatrix} \cos\gamma \\ sen\gamma \cdot e^{-i\Delta\delta} \end{bmatrix} \tag{C.7}$$

The irradiation through the polarizer situated in the same orientation as before β would be given in this case by:

$$I'_{PL} = \left\langle E'_{LIN} \left| P \right| E'_{LIN} \right\rangle = r^2 \cos^2\beta - \frac{r^2}{2} sen\gamma \cdot \cos\gamma \cdot sen\left[2(\gamma-\beta)\right] \cdot (\Delta\delta)^2 \tag{C.8}$$

Thus the acoustic wave causes a variation on the optical intensity after the polarizer equal to the difference between eqns. C.6 and C.8:

$$I_{PL} - I'_{PL} = \frac{r^2}{2} sen\gamma \cdot \cos\gamma \cdot sen\left[2(\gamma-\beta)\right] \cdot (\Delta\delta)^2 \tag{C.9}$$

We can see from this equation that the changes in the intensity will cancel if $\gamma = \begin{cases} 0 \\ \pm\dfrac{\pi}{2} \end{cases}$, which is logical because this correspond to the case in which a_X or a_Y are 0. Therefore only one of the two components of the electric field is present and in this case δ has not meaning.

It also cancels when $\beta = \begin{cases} \gamma \\ \pm\dfrac{\pi}{2} - \gamma \end{cases}$ which corresponds to having the polarizer in one of the two main axis ($\hat{i}$ or $\hat{j}$). In such case there will not be changes in the optical intensity without changes in γ.

We can look to which orientation of the polarizer β we can get more sensitivity (or maximum value of the intensity difference in eqn. C.9). For a given value of $\Delta\delta$ and γ the maximum happens at maximum values of $\left|\sin\left[2(\gamma-\beta)\right]\right|$, which corresponds to values $\beta = \gamma - (2n+1)\dfrac{\pi}{4}$ or equivalently a maximum sensitivity for linearly polarized light occurs when the polarizer is situated at 45 degrees respect to the main axis of the plane of polarization. Minimum sensitivity occurs when $\beta = \gamma - 2n\dfrac{\pi}{4}$, for $n = 0,1,2,...$

Circular polarization

In the case of a circular polarized light before the arrival of the acoustic wave perturbation, the two electric components of light have same amplitude $a_X = a_Y$ and out of phase ($\delta = \pm \pi/2$) and $\gamma = \pi/4$. The electric field vector evolves in time along a circumference in plane of the wave of light as shown in fig. C.2-*left*, the direction of the rotation depending in the sign

of δ. However this does not have any effect over the optical intensity passing through the polarizer.

In Jone's algebra the circular polarization state is given by the vector:

$$\left| E_{CIR} \right\rangle = \frac{r}{\sqrt{2}} \begin{bmatrix} 1 \\ e^{-i\frac{\pi}{2}} \end{bmatrix} \tag{C.10}$$

The optical intensity coming out through the polarizer situated at an angle β from the diagonal of the plane of the wave (as shown in fig. C.2-*left*) is given by eqn. C.11.

$$I_{PC} = \left\langle E_{CIR} \left| P \right| E_{CIR} \right\rangle = \frac{r^2}{2} \tag{C.11}$$

The intensity through the polarizer in a circular polarization is obviously constant.

As the propagating ultrasonic wave pressure field interact with the optical fibre sensor the circular polarized light changes slightly its polarization state towards a elliptical polarization of low eccentricity, caused by a slight change in the phase difference between the two electric field components so that $\delta = \pm \pi/2 + \Delta\delta$, with $\Delta\delta \rightarrow 0$. The change in the ellipticity of the electric field vector trajectory is shown in fig. C.2-*right*, as before the amplitude of the electric field components is unchanged.

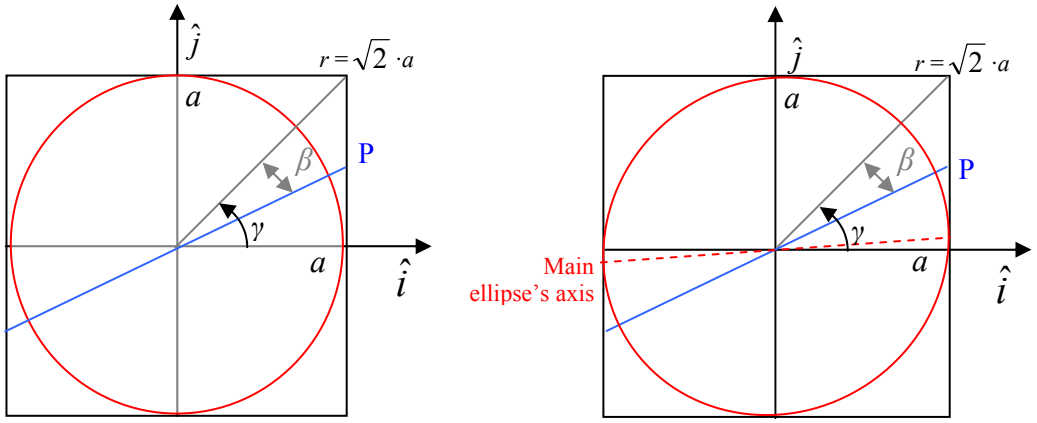

Figure C.2: (*Left*) Circular polarized light in the plane of the wave. The electric field of the light evolves in time along the red circle. (*Right*) Ultrasonic wave perturbation of the circular polarization state into a low eccentricity elliptical one. In blue we show an arbitrary position of the linear polarizer.

The new Jones' vector associated to this modified polarization state is given by:

$$\left| E'_{CIR} \right\rangle = \frac{r}{\sqrt{2}} \begin{bmatrix} 1 \\ e^{-i\left(\frac{\pi}{2}+\Delta\delta\right)} \end{bmatrix} \tag{C.12}$$

The irradiation through the polarizer situated in the same orientation as before β would be now equal to:

$$I'_{PC} = \left\langle E'_{CIR} \middle| P \middle| E'_{CIR} \right\rangle = \frac{r^2}{2} - \frac{r^2}{2} sen\left[2\left(\frac{\pi}{4} - \beta \right) \right] \cdot \Delta\delta \tag{C.13}$$

Hence the variation on the optical intensity after the polarizer caused by the acoustic wave is given by:

$$I_{PC} - I'_{PC} = \frac{r^2}{2} sen\left[2\left(\frac{\pi}{4} - \beta \right) \right] \cdot \Delta\delta \tag{C.14}$$

The change in the optical intensity through the polarizer is null for orientations of the polarizer associated to $\beta = \begin{cases} \pi/4 \\ \pm\pi/2 \pm \pi/4 \end{cases}$, which is equivalent to putting the polarizer in one of the main axis. For the case of circular polarized light at the output of the optical fibre sensor the maximum sensitivity of the polarimetric system is achieved with the orientation of the polarizer at angles $\beta = -n\frac{\pi}{2}$, for $n = 0,1,2,...$

General elliptical polarization

Finally we analyse the general case of an elliptically polarized plane wave light, where the amplitude of the electric field components can be different and with an arbitrary phase difference value. This general state of polarization is described by the Jone's algebra vector:

$$\left| E \right\rangle = r \begin{bmatrix} \cos\gamma \\ sen\gamma \cdot e^{-i\delta} \end{bmatrix} \tag{C.15}$$

The optical intensity coming out through the polarizer situated at an angle β from the diagonal of the plane of the wave (as shown in fig. C.3-*left*) is given by:

$$\begin{aligned} &I_{PE} = \left\langle E \middle| P \middle| E \right\rangle = \\ &r^2 \left[\cos^2(\gamma - \beta)\cos^2\gamma + sen^2(\gamma - \beta) sen^2\gamma + sen(\gamma - \beta)\cos(\gamma - \beta) sen\gamma \cos\gamma \cdot 2 \cdot \cos\delta \right] \end{aligned} \tag{C.16}$$

After slight perturbation of the elliptical polarization by the presence of the acoustic wave, we have a variation of the optical intensity through the polarizer equal to:

$$I_{PE} - I'_{PE} = \frac{r^2}{2} \sin[2(\gamma - \beta)] \cdot \sin\gamma \cdot \cos\gamma \cdot \left(\cos\delta \cdot (\Delta\delta)^2 + 2 \cdot \sin\delta \cdot \Delta\delta \right) \tag{C.17}$$

The equation C.17 is the most general expresion for the sensitivity of the polarimetric system and it is a function of the three variables; β, γ and δ. We can study how to maximize this function respect to each of the variables independently. Thus the maximum respect to β is

achieved under the same conditions as with the linear polarization, that is $\beta = \gamma - (2n+1)\frac{\pi}{4}$. After substitution of this value of β in eqn. C.17 we get a maximum of the function respect to γ when it is satisfied $\gamma = (2n+1)\frac{\pi}{4}$, which represents that $a_X = a_Y$. Again subtituting this value in eqn. C.17 gives us also the value of the variable δ that together with the previous values of the other two variables provide the maximum sensitivity of the polarimetric system, that is $\delta = (2n+1)\frac{\pi}{2}$ for $n = 0,1,2,...$, which is identical to a circular polarization state.

The value of the three variables that maximize the sensitivity of the polarimetric system corresponds to a circular polarization state of the light at the output of the optical fibre sensor with the polarizer oriented at any of the two diagonals of the plane wave of light as shown in fig. C.3-*right*.

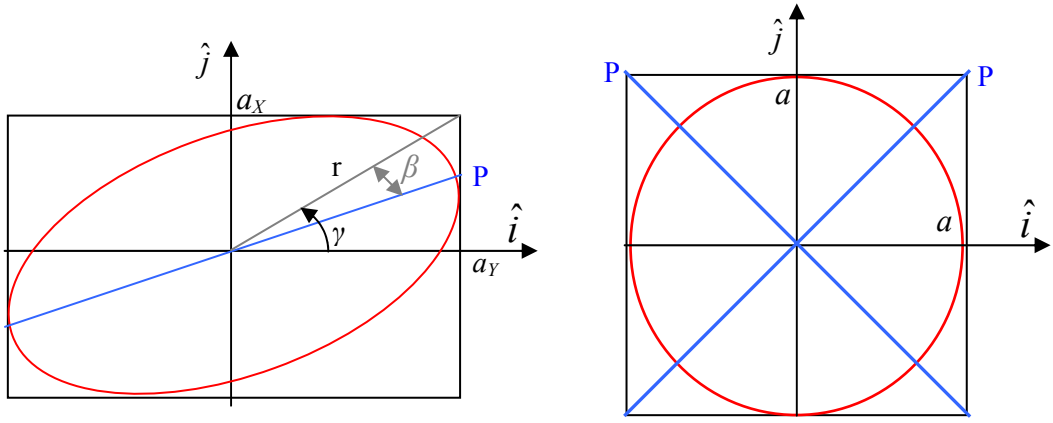

Figure C.3: (*Left*) Elliptical polarized light in the plane of the wave. The electric field of the light evolves in time along the red ellipse. (*Right*) Situation of maximum sensitivity of the polarimetric system; circular polarized light with the polarizer oriented at any of the two diagonals of the plane wave.

APPENDIX D: Physical interpretation of phase and group velocity

The definition of the *velocity* of a wave could lead to confusion, not only because of the existence of multiple and different kind of waves but also because it depends in which aspects of the wave motion we try to quantify.

There are two aspects which are of high importance when describing a wave or group of waves, these are; the phase velocity and the group velocity.

D.1 PHASE VELOCITY

The phase velocity is a definition usually associated to *monochromatic* waves, these are waves of a single constant frequency oscillation. It characterizes the velocity with which wave's points of fixed phase propagate through the medium. Let us consider a plane wave propagating in the X direction:

$$y(x,t) = A \cdot e^{-i(k \cdot x - \omega t)} \tag{D.1}$$

Where the complex term $\varphi = kx - \omega t$ is called the *phase* of the wave. Then, following the previous definition we can obtain the phase velocity as the partial derivative of the spatial variable with respect to the time variable as the phase is kept constant, as shown in eqn D.2.

$$c = \left(\frac{\partial x}{\partial t}\right)_{\varphi} = \frac{-\left(\partial \varphi / \partial t\right)_x}{\left(\partial \varphi / \partial x\right)_t} = \frac{\omega}{k} \tag{D.2}$$

With ω being the angular frequency and k the wave wavenumber. From a practical description point of view, the phase velocity characterizes the speed at which the wave's profile moves, i.e. if we consider the wave profile as a solid entity then the phase velocity is the speed at which this entity slides through the medium.

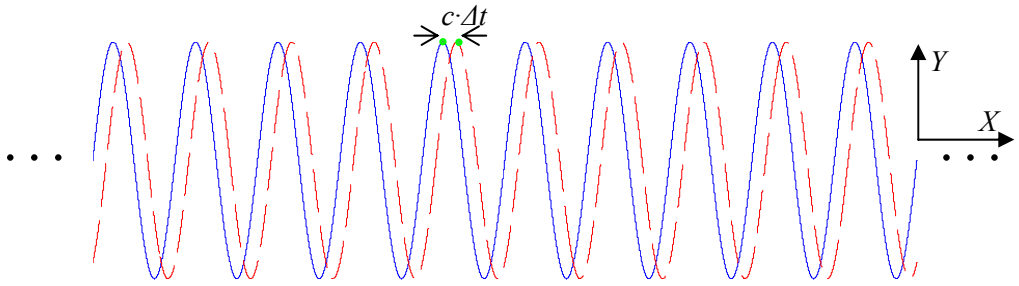

Figure D.1: Monochromatic wave moving towards increasing x values. In blue at a particular time t_0 and in dashed red after Δt. The points in green represent a particular phase value.

For instance, if we look to one particular point of the monochromatic wave profile shown in fig. D.1, in particular the green point corresponding to one of the peaks. As the wave moves through the medium, the speed at which this point propagates is the phase velocity.

From a physical point of view, the waves considered in this work are perturbations of the equilibrium position of the medium's elementary particles or *oscillators* as described in appendix A. Thus, considering the wave's perturbation $y(x,t)$ as the particle's displacement perpendicular to the direction of propagation of a planar transversal wave, then although the wave propagates laterally in the X direction, no medium's particle motion takes place in this direction. In this case the phase velocity does not describe a physical entity. Monochromatic waves, as the ones described previously, do not transmit energy or information through the medium because they are of infinite extent in space, so that for any value t the spatial variable x varies from $-\infty$ to ∞. Then the perturbation is always in the entire medium. The physical entity representing the velocity of the particles displacements is given as $\partial y/\partial t = -c \cdot \partial y/\partial x$ and so it is different from the phase velocity c.

Notice that in the expression of eqn. D.2 the sign of the phase velocity is positive, as in order the phase φ to be constant when t increases then x must also increase, therefore the wave moves in the direction of increasing x. Complementarily, if we express the phase as $\varphi = kx+\omega t$, when t increases then x must decrease in order the phase to keep constant. In this case $c = -\omega/k$, is negative.

When the phase velocity is dependent of the wave's frequency then it is said to be *dispersive*. This name is easily understood if we consider a pulse wave made up of several monochromatic components of different frequencies. If these components are *non-dispersive* then all of them propagate together with the same velocity, and the pulse which is their sum, retains its original shape as it propagates. In opposition, if the waves are dispersive, then as they propagate with different velocities; some components propagate faster meanwhile others propagate slower than the average, as a result the pulse is broadened or dispersed as it travels through the medium (see fig. D.2).

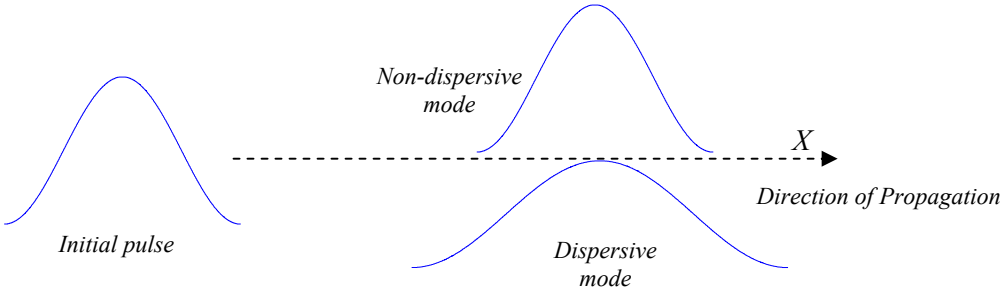

Figure D.2: Dispersion effect over a pulse wave propagating under a dispersive mode.

We mentioned that monochromatic waves are infinite in extension, nonetheless waves in real experiments are, as the previous pulse wave, always confined in space. A wave in order to transmit information or energy cannot be an infinitely extended periodic signal, but a combination of periodic signals of different frequencies. The velocity at which the energy or information stored in this group of waves is transmitted is called *group velocity*.

D.2 GROUP VELOCITY

The distinction between a wave's group velocity and its phase velocity was first proposed by W. R. Hamilton in 1839 [37]. However it is Stokes who in 1876 made of it a commonly used concept, as he proposed it as the topic of a Smith's Prize examination paper [38]. The simplest way in which he presented the concept of group velocity is by considering a group of two monochromatic waves of same amplitude and slightly different frequencies and wavelengths. These waves are propagating, with different phase velocities, towards increasing values of x:

$$y(x,t) = A\cdot\cos\left[(k-\Delta k)x-(\omega-\Delta\omega)t\right]+A\cos\left[(k+\Delta k)x-(\omega+\Delta\omega)t\right] \tag{D.3}$$

The expression in eqn. D.3 represents the propagating waves perturbation and by simple trigonometric identities it can be easily rewritten as an amplitude modulated wave:

$$y(x,t) = 2A\cdot\cos\left[\Delta k\cdot x-\Delta\omega\cdot t\right]\cdot\cos\left[kx-\omega t\right] \tag{D.4}$$

Equation D.3 shows that the group of waves can be understood as a carrier of frequency ω and phase velocity ω/k with amplitude modulated by an *envelope* of frequency $\Delta\omega$ and phase velocity $\Delta\omega/\Delta k$ (as shown in fig. D.3, in blue the carrier wave and in dashed red line the envelope).

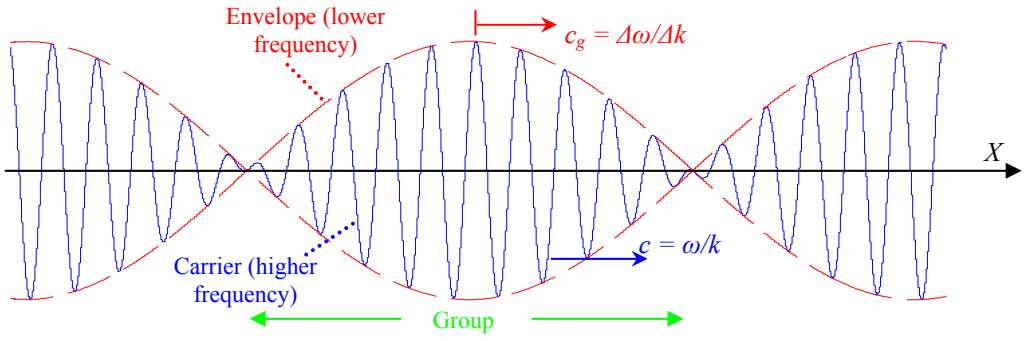

Figure D.3: Envelope of a superposition of two waves to define group velocity.

It is important to notice that the peaks of the envelope wave are associated to those situations (proper combinations of time and position values) in which the monochromatic components

are in phase. Meanwhile the minimums are those cases in which their phase is in opposition. Therefore, the phase velocity of the modulating function or envelope describes the speed of any feature of a wave that relies on different frequencies remaining in phase. Hence for a more general situation of a pulse wave of finite width containing a packet of waves of similar frequencies, the envelope phase velocity defines the speed at which the peak of the pulse propagates. It expresses the velocity at which the group of monochromatic waves propagate as a whole, therefore its name of *group velocity*. In the present case of nearly equal frequency components, the group velocity can be expressed as $d\omega/dk$. Since $\omega = k \cdot c$ and $k = 2\pi/\lambda$ it can be proved that the group velocity can be related to the phase velocity by eqn. D.5.

$$c_g = c - \lambda \frac{dc}{d\lambda} \tag{D.5}$$

We must notice that a wave in order to transfer energy or information, it must be modulated and it is this modulation that represents the signal content.

Following with the simple case of a group constituted by a superposition of two monochromatic waves as shown in eqn. D.3, we can define its energy density as:

$$\hat{E} = \rho \cdot d^2 y / dt^2 \tag{D.6}$$

Where ρ is the density of the medium in which the group of waves propagate. If the energy density is averaged over several periods of the carrier wave (during which the envelope does not change too much), then as shown in [39] we obtain for a lossless media that:

$$\left\langle \hat{E} \right\rangle \cong 2\rho \cdot \omega^2 \cdot A^2 \cdot \cos^2(\Delta k \cdot x - \Delta\omega \cdot t) \tag{D.7}$$

Equation D.7 clearly suggest that the time-averaged energy density of the packet of waves propagates with the group velocity.

Thus, group velocity is the speed at which the content or energy in a wave is transported. Therefore Lamb wave's *group velocity* dispersion curves show the velocity at which finite-time wave packets travel; they are therefore useful for the calculation of the travel times of the wave pulsed toneburst signals [44].

The group velocity represent the speed of energy propagation only under the condition that the group velocity does not exceed the phase velocity of the waves of the group [40]. If this is not satisfied, the group velocity does not necessarily represent the actual propagation speed of any information or energy and the envelope propagation is just an artefact of the way the different frequencies are slipping in and out of phase. This contradicts the paradox

of experiments consisting on transmitting a superposition of electromagnetic waves with a group velocity exceeding the speed of light, advertising them as astonishing overturns of the theory of relativity [41,42].

The relation between the phase and group velocity values distinguishes three main cases;

- $\boldsymbol{c > c_g}$, this is the conventional case of *normal dispersion*. Where the phase velocity is a function of the frequency and it decreases as the frequency increases (as it can be seen from another way of expressing the group velocity shown in appendix A, eqn. A.26).
- $\boldsymbol{c = c_g}$, this corresponds to a *non-dispersive* case. From eqn. D.5 it is obvious that this case corresponds to a phase velocity independent of the frequency as $dc/d\lambda = 0$.
- $\boldsymbol{c < c_g}$, this case is known as *anomalous dispersion*. Like the first case the phase velocity is now also a function of the frequency but opposite to the normal dispersion, now the phase velocity increases with frequency $dc/df > 0$. Even more, as A. Schuster first noted in 1904 [43], if the value d*c/df* is sufficiently positive, based in eqn A.26, the group velocity becomes negative. The implications of a negative group velocity are; first the ultrasonic wavelength increases as the frequency increases, which is the opposite of the common situation, and second the transportation of energy or information by the wave takes place in opposite direction to the waves' phase velocity.

This exciting and not always considered physically possible phenomenon of negative group velocities is presented in some Lamb waves' high order modes and indeed it has been observed in our experimental work as shown in Chapter 6. Therefore let us have a closer look to it.

D.2.1 Negative group velocity in Lamb waves high order modes

A detailed numerical analysis of the manifestation of negative group velocity in the Lamb wave dispersion curves by changing the elastic properties of the material, gave me some interesting interpretations of the conditions under which a negative group velocity appears. We present here only the results of those analyses.

It was found that negative group velocities occur for both symmetric and antisymmetric high order modes and only in the region of vertical asymptotic behaviour or cut-off frequency:thickness product values. In fact for a given set of elastic property values we have observed that a negative group velocity only appear when the cut-off frequency of adjacent modes of the same type (symmetric or antisymmetric) are proportional to different bulk wave phase velocity (one mode's cut-off frequency is proportional to c_L and the other to c_T).

And only when these cut-off frequencies are close enough. The mode with the smallest cut-off frequency:thickness product value gets negative group velocity and never the other. It was also found that we can never have two consecutive high order modes of the same type with negative group velocity. The negative group velocity is shown in the phase velocity dispersion curves as an elbow with the concave section pointing towards smaller frequency:thickness product values (as in fig. A.9). Thus having double phase velocity solution associated to a same frequency:thickness product value.

A graphical explanation of these aspects of the negative group velocity is as follow. The cut-off frequency is defined as the frequency:thickness product at which the high order modes tends asymptotically to infinite as the frequency:thickness product reaches that value. When two adjacent modes of the same type tend asymptotically to infinity in a close region, they would intersect in some point near the region where they behave asymptotically. This intersection is not allowed as that would mean that different modes of the same type (either symmetric or antisymmetric) would have same frequency:thickness product value and same phase velocity. Therefore both modes would have same particle displacements, hence they would be the same mode. In order to avoid this intersection both modes should tend to infinity from different sides of their respective cut-off frequencies as shown in the diagrams of fig. D.4 (where the cut-off frequency:thickness product values of two adjacent symmetric modes is given by the vertical dashed lines). These figures, from left to right, show the changes commonly experienced in the dispersion curves of two adjacent modes of the same type (symmetric in this example) as their cut-off frequencies get closer to each other.

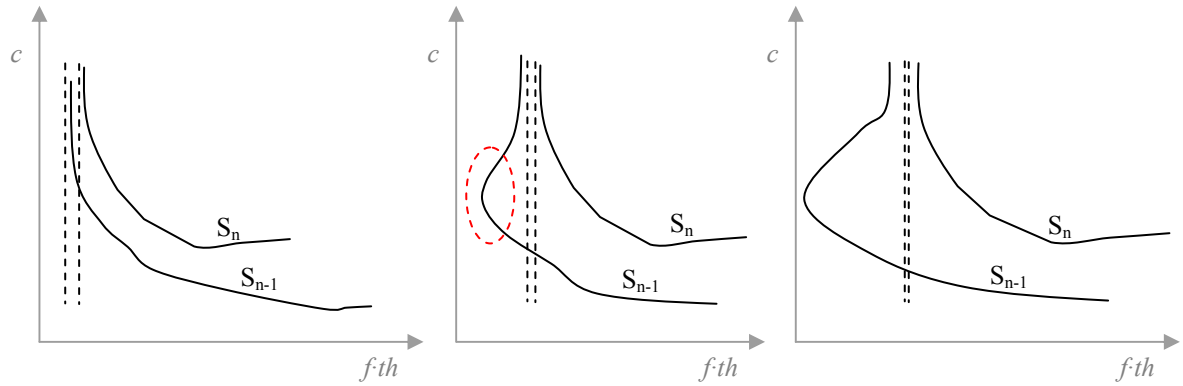

Figure D.4: Graphical interpretation of the aspects of negative group velocity. From left to right the cut-off frequencies of adjacent modes of the same type get closer thus accentuating the effects of negative group velocity.

In fig. D.4-*left* the cut-off frequencies of adjacent modes are far enough, and then no negative group velocity effects are experienced. The phase velocity dispersion curves of both modes have asymptotic tendency to their cut-off frequencies from their right (from higher frequency:thickness products). As the modes' cut-off frequencies get closer (as the elastic

properties of the material change) to avoid intersection of the modes' dispersion curves the smaller order mode takes the asymptotic tendency from the left side of its cut-off frequency (from smaller frequency:thickness products), which creates a small elbow (red circled area in fig. D.4-*centre*). The closer the cut-off frequencies of adjacent modes get, the more pronounced the elbow appears, thus the more negative the group velocity value (as shown in fig. D.4-*right*).

It was found that the negativity of the group velocity is not only affected by how close the modes' cut-off frequencies are, but also by the value of these frequencies (or mode order). We found that the higher the mode order, the closer the adjacent modes can get before interfering into a negative group velocity. A more rigorous mathematical analysis can be found in the references [45-47].

APPENDIX E: Tone burst signal

The tone burst signal is the most common driving signal for time analysis NDT applications with ultrasonic guided waves, because of its localization in time and narrow frequency bandwidth characteristics. No wonder then that these signals appear broadly in this thesis, not only for damage detection and characterization as shown in Chapters 3 and 4, but also for measuring the Lamb waves group velocity as shown in Chapter 7. Based on this we have considered necessary to include the present appendix in order to properly describe this type of signals and explain their advantages. In addition, this appendix also describes the fundamental problems associated with processing finite and discrete data; such as leakage and scalloping loss, and the most common window function used for their correction; such as the Hamming and Hanning windows.

E.1. BURST SIGNAL

A *burst* is a signal constituted of a specific number of cycles of a given waveform. This waveform is chosen sinusoidal in most cases and certainly as well in this thesis, because as shown in [48] this is the pulse shape that most efficiently excites Lamb wave harmonics. Additionally this shape is the one that dedicates more energy to the desired driving frequency or *carrier frequency*, defined as the repetition rate of the burst waveform ($f_{carrier}$).

Thus providing a stronger narrow bandwidth Lamb wave in comparison with other kind of waveforms. Figure E.1 shows graphically this parameter in addition to the *burst rate* (f_{rate}), which specifies the interval between bursts. It usually has a small enough value such that the reflections on the borders of the plate from a given burst do not interfere with the signal from the next excited burst.

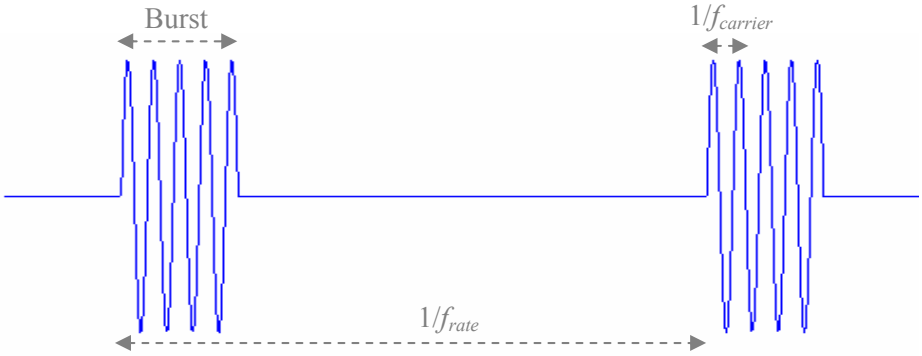

Figure E.1: Definition of the parameters of a burst.

Burst signals are well localized in time and they are easy to identify within the sample record. This is a very important characteristic for time analysis in order to be able to distinguish the arrival time of the features not only for the different excited Lamb modes but also for their reflections at the geometrical borders and discontinuities or imperfections of the structure under test

In order to make a properly use of the time localization benefits of these signals, an upper limit in the number of excited cycles should be consider, with a trade off between the number of cycles and the proximity of abrupt features in the structure. Also a low limit in the number of cycles must be considered, as the smaller the number of cycles excited then the broader the number of frequency components excited. Thus generating a higher number of Lamb modes with smaller amplitude because the energy of the excited signal must be distributed into the different modes, causing a reduction in the SNR of the signal and in the sensitivity of the system. These multiple modes propagate with different velocities, causing signal spreading by dispersion, which again decreases the time resolution of the system so that the reflection from structural features in close proximity may not be separately observed in the detected signal. Indeed choosing the right number of cycles for each specific case is one of the most complicated decisions to be made in the inspection of structures by guided waves. Wilcox et. al. present in [49] an analysis for the optimum number of cycles in the input signal that minimises the duration of the received signal and so maximises the time resolution. The optimum number of cycles very much depends in the propagation distance of

the pulse to the receiver, as well as in the frequency:thickness product of the carrier and the selected Lamb wave mode.

It is very convenient to use an integer and a half number of cycles so that a symmetric sinusoidal pulse is generated (see fig. E.2-*left*), which make easier to detect visually the central peak that characterizes the group velocity propagation of the dispersive signal. Although some experiments did not require this symmetry. We have experimentally observed that 4.5 or 5 cycles are highly acceptable for most of the applications in this thesis.

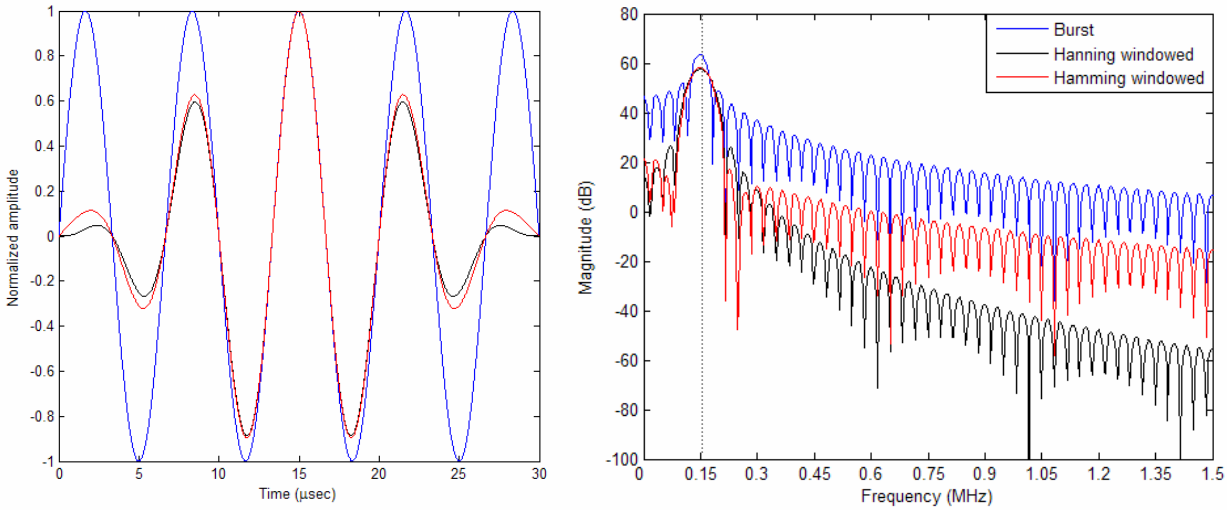

Figure E.2: Window functions applied to a sinusoidal burst signal of carrier frequency at 150 kHz in blue; Hamming window in red and Hanning window in black. (*Left*) Time domain smoothing effect of the window functions. (*Right*) Frequency domain minimization of the spillover frequencies.

Although the burst shown in fig. E.1 are purely sinusoidal, a more common approach is to apply a window function to the waveform. The window function smoothly brings to zero the signal data at its boundaries, reducing the order of the discontinuity at the boundaries of the tone burst signal. Further narrowing the bandwidth of the burst signals by minimizing *spill-over* components from neighbouring frequencies, as shown in fig. E.2. This helps to further focus the maximum energy into the actuating frequency, providing more accurate phase velocity calculations which help to get a more sensitive and reliable damage detection capability.

Window functions have an additional beneficial effect, related with the fact that the contact transducer for the generation of ultrasonic waves, such as PZTs have a complex mechanical impedance (see Chapter 2). Its reactive component causes not only a time delay in the response of the transducer's mechanical oscillation with respect to the driving signal, but it also causes a transitory interval of amplitude increasing mechanical oscillation from a state of rest till it reaches the stationary constant amplitude oscillating state of the driving electric

signal. Once the oscillations of the driving signal stops, the transducer still continues to oscillate in an amplitude decreasing transitory interval. The smooth amplitude increment at the start of a windowed burst and the smooth decreasing amplitude at the end, decreases considerably the difference between the electrical driving signal oscillations and the transducer's mechanical ones.

The most common used windows are Hanning and Hamming windows, which although very similar they have some slight differences making one or another more suitable for different applications. Next we briefly compare both windows and if the reader is interested in a more detailed analysis we suggest the references [50,51].

E.2. WINDOW FUNCTIONS

Window functions are used in the DFT spectral analysis environment in order to deal with problems associated to the finite extent of the data signals processed in real life situations. Between these problems, the two most common are spectral leakage and scalloping loss as briefly described next.

E.2.1 Spectral leakage

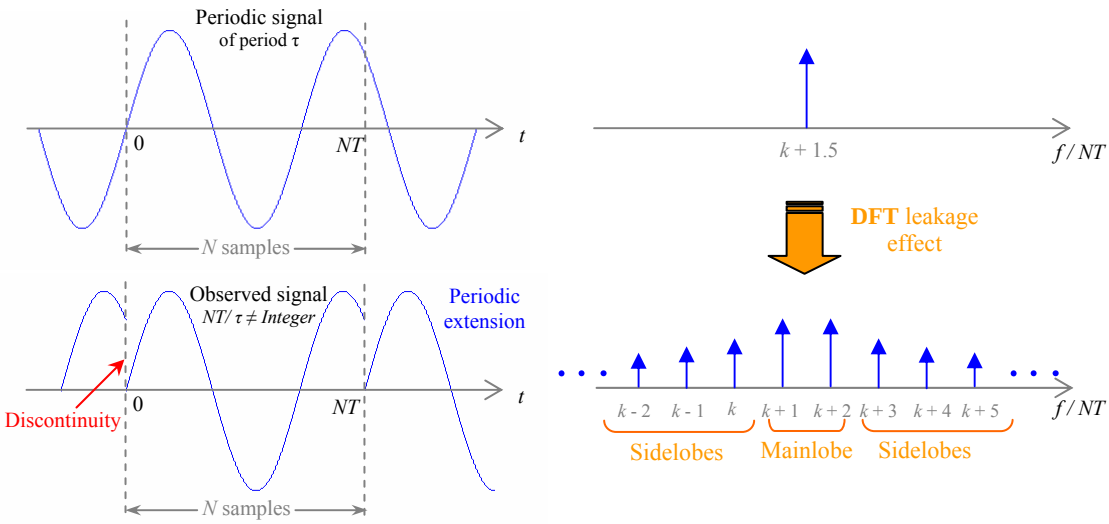

Figure E.3: Spectral leakage as a consequence of the discontinuities shown in the periodic extension of the time signal. (*Left*) from a time domain point of view. (*Right*) from a frequency domain point of view.

This phenomena occurs when the periodic extension associated to the DFT of a finite length discrete data signal exhibits discontinuities at the boundaries of each periodic extension, as shown in fig. E.3-*left*. The discontinuity is a consequence of a finite length signal having frequency components that do not coincide with the FFT bin values, or are not multiples of the bin width given by $1/NT$ where N is the number of total samples for the finite signal and

T the sampling period. As a consequence, these frequency components will have non zero projections or 'leak out' over the entire frequency set, as shown in fig. E.3-*right* for an input signal with frequency in the middle of two frequency bins.

The window functions smoothly bring to zero the finite length data at the boundaries, highly reducing the discontinuity of the periodic extension in many orders of derivative, thus reducing the leakage effect. This is the way in which the window functions narrow the apparent frequency bandwidth of the burst signals.

E.2.2 Scalloping loss

It is also known as the *picket-fence effect*, and it is a property related to the minimum detectable frequency signal component. This effect is related with the signal detection loss due to the reduction in the signal levels for those frequency components that are off the DFT bins $1/NT$, as already seen in fig. E.3-*right*. The spectrum of a signal given by the DFT is analogous to looking at it through a 'picket-fence' because the exact frequency behaviour can only be observed at discrete points. The maximum signal loss occurs when the frequency components of the signal are at the frequency midway between adjacent frequency bins.

This signal loss obviously decreases the SNR of the processed signal with respect to the SNR of the input signal (before calculating its DFT). In fact as mentioned in [50], the scalloping loss represents the maximum SNR reduction of the processed signal.

The window functions can help to reduce these losses as they can modify the frequency response of the original signal. The picket-fence effect can also be reduced by increasing the number of points in each periodic extension through the technique called *zero padding*, where zeros are added at the end of the original finite signal, while maintaining the original record intact. This process artificially changes the locations of the frequency bins, as N is increased, without altering the continuous form of the original spectrum. In the new set of frequency bins, spectral components that originally were between bins now can be closer to the new set, reducing their scalloping losses.

E.2.3 Window functions comparison

In this section we present the most commonly used window functions in NDT applications. These are the Hamming and the Hanning windows, however as comprehensively analysed in [50] they are not the best of the available windows. Nonetheless because they are easy to generate and they have a very good performance, they have become the most popular in a great variety of applications.

Hanning window

This window is a member of the cos^{α} (X) window functions with $\alpha = 2$. More accurately the Hanning window is defined as:

$$w(n) = 0.5\left[1 - \cos\left(2\pi n / N\right)\right] \tag{E.1}$$

Where $n = 0, 1, 2, \ldots, N-1$ and N being the length of the window.

The Hanning window is continuous till its first derivative so the sidelobes fall off at 18 *dB* per octave as it can be seen in fig. E.4-*right* in black. Notice from the time domain representation in the same figure that this window cancels out in its boundaries.

Some important characteristics of the Hanning window are: *Leakage factor*, defined as the ratio of power in the sidelobes to the total window power = 0.05%, First sidelobe attenuation = -31.5 dB, Mainlobe width (-3dB) = 0.042969 ($\times\pi$ *rad/sample*) (for the case in the previous figure with N= 64). Scalloping Loss = 1.42 dB.

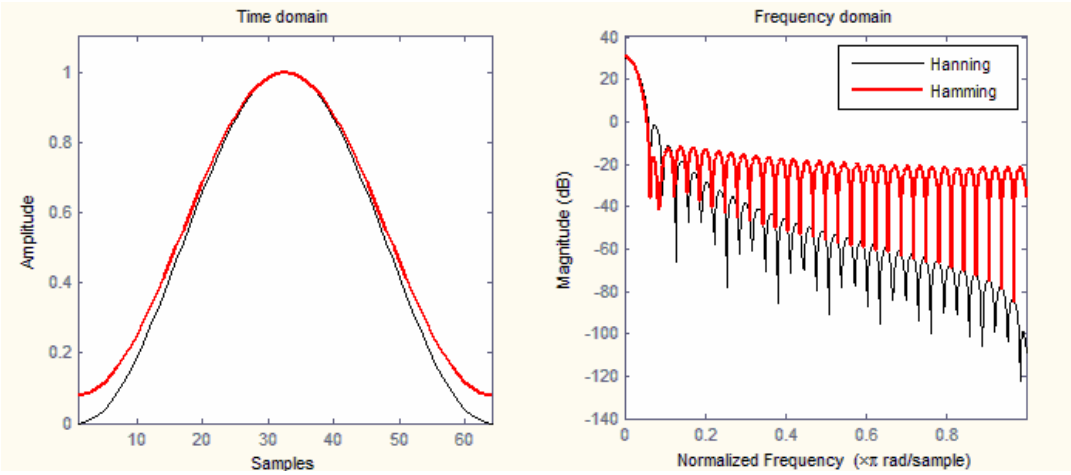

Figure E.4: Comparison of window functions; Hamming window in red and Hanning window in black. (*Left*) Time domain weightening values of the window of length 64 points. (*Right*) Normalized frequency spectrum of the windows in a logarithmic amplitude scale.

Hamming window

The Hamming window is a slightly modified Hanning window, such that provides a high improvement in the attenuation of the first sidelobe levels.

$$w(n) = 0.54 - 0.46\cos\left(2\pi n / N\right) \tag{E.2}$$

Where $n = 0, 1, 2, \ldots, N-1$ and N being the length of the window.

The first sidelobe attenuation is now -42.5 dB, much lower than before. However the Hamming window presents a small discontinuity at its boundaries resulting in only a 6 dB

per octave rate of fall off. In consequence the high order sidelobes are much higher in amplitude than for the Hanning window, as shown in red in fig. E.4-*right*. We may notice from the time domain representation that this window does not cancel in its boundaries, allowing more energy of the signal to which it is applied to pass into the frequency spectra.

Finally the rest of the Hamming window characteristics are: *Leakage factor* = 0.03%, Mainlobe width (-3dB) = 0.039063 ($\times\pi$ *rad*/*sample*) (for the case in the previous figure with N= 64). Scalloping Loss = 1.78 dB.

Comparison of both window functions

The comparison of the values for the Hamming and the Hanning window characteristics makes it difficult to specify one of the windows as better than the other. For instance meanwhile the Hamming window has a much smaller first sidelobe magnitude, however it has higher sidelobe levels as a consequence of its slower sidelobes fall off rate. In consequence the statistical accuracy of the estimated frequencies when the Hamming window is applied is reduced respect to the Hanning window, due to the higher leakage effect of the former. This is also related with a higher scalloping loss for the Hamming window and so a worse SNR of the processed finite signal. In contrast the Hamming window has a narrower mainlobe frequency width, therefore it provides a better frequency resolution than the Hanning window. The selection of the window functions is a trade-off between spectral smoothing (for which the Hanning window is better) and frequency resolution (for which the Hamming window is more adequate).

The decision of choosing one or the other will depend highly on the particular applications. For instance in the time analysis application of damage detection discussed in Chapter 3 a narrower bandwidth burst signal was desirable in order to generate a purer single frequency mode, then here a Hamming window is clearly more adequate. Opposite in the 2D-FT applications for the extraction of the dispersion curves in Chapter 6, we were more interested in the sidelobes effect decrement, as they would worsen the resolution of the dispersion curves by spreading them as a consequence of the leakage effect and affecting also the frequency values estimation, so a Hanning window was chosen instead.

APPENDIX F: Comparison of experimental and irresolvable error of the experimental dispersion curves

The experimentally obtained phase velocity dispersion curves based in the 2D-FT (as shown in Chapter 6), have an uncertainty in the values of the curves, given by the frequency and wavenumber bins spacing, called *irresolvable error* in Chapter 7. However the obtained dispersion curves may have a bigger error due to the temporal and spatial experimental error sources. The temporal experimental error source is associated with the time sampling error, of which the unique origin is the oscilloscope sampling inaccuracy. A Tektronix TDS 3014 oscilloscope was used during the experiments with a sampling rate accuracy of ±200 *ppm*. For the 100MS/s sampling rate used, it means an error of 0.02 MS/s, which corresponds to a sampling period error of $T_s = 10 \pm 0.002$ *nsec*, or a 0.02% temporal sampling error.

The spatial experimental error source is double; from one side we have the irregularity of the Q-switch laser synchronization trigger and from the other the spatial positioning error of the beam source. The laser synchronization trigger error of the Brilliant B Quantel used in the experiments is given by the laser's Jitter with respect to the Q-switch trigger and the manufacturer characterizes it as being 0.25 *nsec*. The error in the trigger affects the time origin of the measured ultrasonic data. This is equivalent to have an error in the position of the source by a distance equal to the travelling distance of the propagating ultrasonic wave. The broadband ultrasonic source of our experiments has various modes propagating at different velocities. Nevertheless, we are not much interested on the components travelling at speeds over 10 *km/s* because the conversion error from wavenumber to the phase velocity information is too high for these cases. Thus considering the fastest travelling wave to have a speed of 7 *km/s*, it has a spatial sampling error associated of $\Delta x_{error} = 0.25\ 10^{-9} \cdot 7 \cdot 10^{6} = 1.75\ 10^{-3}$ *mm*, which for a spatial sampling period of $\Delta x = 0.3048$ *mm* it corresponds to a relative error of approximately 0.5%.

In the other hand we also have to consider the spatial sampling error associated to the motor displacement error that positions the ultrasonic laser source. The motor used is a McLennan Digital Linear Actuator (DLA) L92211-P2 series, controlled by a two axis programmable stepper motor control board. Experimentally it was observed an error of less than 0.1% in the displacement. In conclusion, the spatial error is dominated by the Q-switch trigger Jitter, and it will be considered of being 1%.

Let us see the effect that these experimental errors causes over the frequency bins for the temporal and spatial Fourier transforms, considering evenly sampled data of different sampling frequencies.

The temporal ultrasonic signals from the oscilloscope have 10000 points with a $T_s = 10^{-8}$ sec. In the 2D-FT these are zero padded to the closest power of 2 for a faster computation of the FFT. This makes $N_t = 16384$, so the frequency bins are $m\frac{1}{T_s N_t} = m \cdot 6.1035\, kHz$ with $m = 0,1,$ 2 … $N_t/2$. Notice that the data is filtered for frequencies over 12 *MHz* so the frequency bins plotted in the experimental dispersion curves are only until bin $m = 2000$.

Now if we consider the sampling period to be $T_s = 1.0002 \cdot 10^{-8}$ *sec* so that the oscilloscope inaccuracy is included, then the new frequency bins are $m \cdot 6.1023$ *kHz* for m defined as before. The difference is only of 0.0012 *kHz*. We must realize that calculating the 2D-FT considering evenly sampled data only take into account the value of the sampling frequencies to define the bins. Then the spectrum is the same, it only changes the grid dimensions and values. In the case of bigger sampling period the temporal part of the grid has its bins closer to each other. But each segment of the grid agrees perfectly, so that for the maximum bin of consideration $m = 2000$, it has an associated discrepancy of only 40%. This obviously means that the uncertainty of the bins provides a bigger error in the dispersion curves than the experimental error associated with the oscilloscope.

In relation to the spatial sampling period, we have that the number of samples is 245, which zero padding to the closer power of 2 gives an $N_s = 256$. The spatial sampling period without considering any error is $\Delta x = 0.3048$ *mm*. Then the spatial frequency bins (in wavenumber dimension $1/\lambda$) are $n \cdot 0.0128$ (1/*mm*) for $n = 0,1, 2 \ldots N_s - 1$. Now we consider the new spatial sampling value $\Delta x = 0.3065$ *mm* to include the experimental error. The space frequency bins are now $n \cdot 0.01275$ (1/*mm*) for n as before. Again it is a very small change in the values of the bins. For bin associated to the higher $n = N_s - 1$, we see it is moved a full distance between bins (0.0128 (1/*mm*)) toward smaller values, however we do not use information for n over 200, which has a coincidence between both spatial sampling values grids of 22%.

From this analysis it is obvious that it is a good approximation to consider the measurement error to be dominated by the uncertainty of the Fourier transform (or distance between frequency bins).

APPENDIX G: Horizontal shift of the phase velocity sensitivity curves to *E* and *ν*

In the analysis carried out in Chapter 7 about the phase velocity sensitivity curves s_E and s_ν for various sets of elastic property values as pictured in fig. 7.4. We noticed that the sensitivity curves shifted towards lower frequency:thickness product values as the elastic property values decrease. In this appendix, we show that this shift is related with an equivalent shift of the phase velocity dispersion curves as a consequence of the changes that the perturbations in the elastic properties causes over their associated cut-off frequency:thickness product values.

As we already defined in appendix A, the cut-off frequencies represent the frequency:thickness product values at which the high order modes begin. The cut-off frequencies are proportional to one of the bulk waves phase velocities (c_T, c_L) as shown in eqn. A.24 and A.25, which are also dependant on the elastic property values as given by eqn. A.9 and A.10. Thus, to understand how the sensitivity curves changes with changes in the elastic properties we need first to understand how the bulk waves change.

First, we look into the perturbation that a change in E and ν given by $(1+\Delta_E)\cdot E_0$ and $(1+\Delta_\nu)\cdot \nu_0$ respectively, causes over the inverse of the transversal mode's phase velocity $1/c_T$:

$$1/c_T = \sqrt{\frac{2\rho(1+(1+\Delta_\nu)\nu_0)}{(1+\Delta_E)E_0}} = \sqrt{\frac{2\rho(1+\nu_0)+2\rho\Delta_\nu\nu_0}{(1+\Delta_E)E_0}} = \frac{1}{\sqrt{1+\Delta_E}}\sqrt{\frac{1}{{c_{T_0}}^2}+\frac{2\rho\Delta_\nu\nu_0}{E_0}} \qquad \text{(G.1)}$$

Where c_{T0} is the transversal mode phase velocity associated to E_0 and ν_0. The relationship between Δ_E and Δ_ν that makes $c_T = c_{T0}$ is given by:

$$\Delta_\nu = \left(\frac{E_0}{2\rho\nu_0{c_{T_0}}^2}\right)\Delta_E \qquad \text{(G.2)}$$

Figure G.1-*left* shows the contour plot of the inverse of eqn. G.1 as a function of (Δ_E, Δ_ν). In black line it is shown the combinations of (Δ_E, Δ_ν) that make $c_T = c_{T0}$ as characterized in eqn. G.2. An identical analysis can easily be done with the longitudinal bulk wave phase velocity c_L, and fig. **G.1**-*right* shows the contour plot of constant values of c_L as a function of (Δ_E, Δ_ν) with the black line representing those combinations that make $c_L = c_{L0}$.

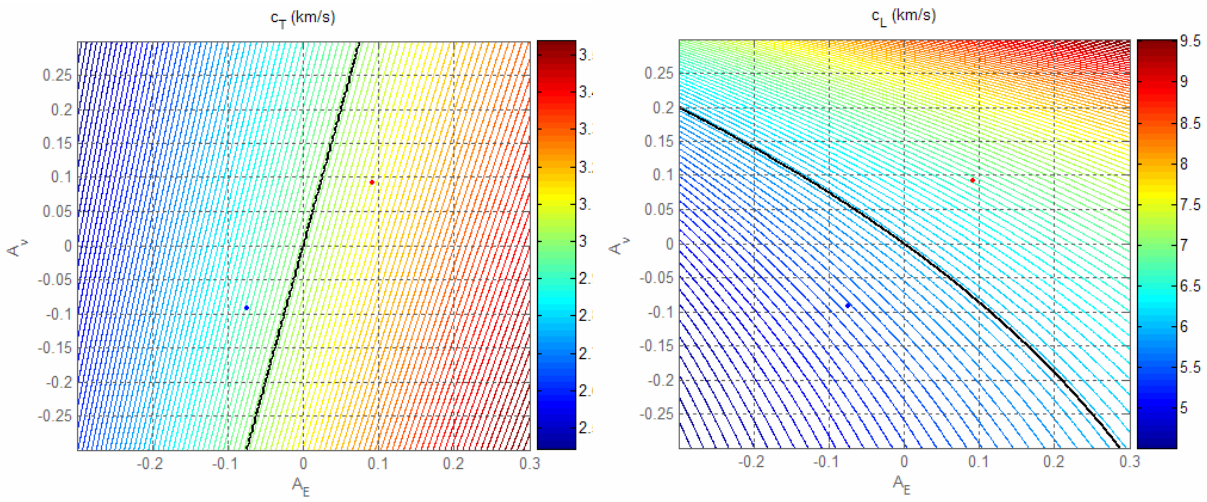

Figure G.1: Change in the bulk waves phase velocities by changes in the elastic constants (E, ν) = [(1+ Δ_E) E_0, (1+Δ_ν) ν_0]: (*Left*) Contour plot of c_T, the black contour is c_{T0} associated to elastic constants (E_0, ν_0) = (64.8 *GPa*, 1/3). (*Right*) Contour plot of c_L, in black the contour for c_{L0}.

The previous contour plots show graphically that an increment of any of the elastic property values individually ($\Delta_E > 0$ or $\Delta_\nu > 0$) will make c_L to increase. Then those high order modes with cut-off frequency proportional to this bulk wave phase velocity will be shifted towards higher frequency thickness product values. With the most intensive shift associated to a simultaneous increment of both elastic property values as it corresponds to a perpendicular movement along the contour lines towards the red coloured area (higher values of c_L). In the other hand, an increment in the value of only E will also make c_T to increase and thus shift the dispersion curves with cut-off frequency proportional to this bulk wave phase velocity towards higher frequency:thickness product values. However an increment in ν would make c_T to decrease and so cause a shift towards smaller frequency:thickness values. From fig. G.1-*left* we clearly see that c_T is more sensitive to changes in E than to changes in ν, and a combined increment of both elastic property values will cause a very small increment of c_T as it corresponds to a shift almost parallel to the contour lines.

To explain the different shifts of the sensitivity curves shown in fig. 7.4 for different cases of elastic property values, we first need to know the cut-off frequencies associated to each mode curve. The cut-off frequencies are given for the symmetric and antisymmetric modes in eqn. A.24 and A.25, however the assignment of each value to each order mode depends in the value of the elastic properties, as shown in table A.1. This table clearly shows that the antisymmetric modes cut-off frequency assignment is always the same:

$$\boldsymbol{A_{1cutoff}} = c_T/2;\ \boldsymbol{A_{2cutoff}} = 3c_T/2;\ \boldsymbol{A_{3cutoff}} = c_L;\ \boldsymbol{A_{4cutoff}} = 5c_T/2 \qquad \text{(G.3)}$$

However the cut-off frequency thickness products associated to the symmetric modes will depend on the value of v:

- For cases with $v = 0.364$:

$$\boldsymbol{S_{1cutoff}} = c_T;\ \boldsymbol{S_{2cutoff}} = c_L/2;\ \boldsymbol{S_{3cutoff}} = 2c_T;\ \boldsymbol{S_{4cutoff}} = 3c_T \tag{G.4}$$

- For cases with $v = 1/3$:

$$\boldsymbol{S_{1cutoff}} = c_L/2 \text{ or } c_T;\ \boldsymbol{S_{2cutoff}} = c_T \text{ or } c_L/2;\ \boldsymbol{S_{3cutoff}} = 2c_T;\ \boldsymbol{S_{4cutoff}} = 3c_L/2 \text{ or } 3c_T \tag{G.5}$$

If we compare the figures 7.4-*top* where only E changes incrementally from left to right, we see that all the sensitivity curves are shifted towards higher frequency:thickness product values, as it would be expected from the associated increment of both c_L and c_T as previously discussed. The higher the order mode the bigger this shift is. Look for instance the sensitivity curves of modes A_1 and S_3. This is due to the fact that the higher the mode's order, the bigger the proportional constant of the cut-off frequency values with the bulk waves phase velocity (as shown in eqn. G.3 and G.5). In the previous example the cut-off frequency for A_1 is $c_T / 2$, meanwhile for S_3 it is $2c_T$, so the shift of the cut-off frequency in S_3 will be four times bigger than in A_1 for a similar change in the value of c_T.

It is perceivable in fig. 7.4 that as the cut-off frequency values shift, then the sensitivity curve's shapes also shift in more or less similar quantity. Look for instance to the peaks of the sensitivity curves for order one and two. For higher order modes the sensitivity curves suffer important shape transformations in addition to the horizontal shift.

In the other hand, if we compare figs. 7.4-*top left* and *bottom right* where there is a change in both elastic properties, then a bigger increment in the c_L value than in the previous case should be expected, and a very small incremental change in c_T. Effectively this is what we see, for instance looking to the sensitivity curve associated to mode A_3, with cut-off frequency equal to c_L, a bigger shift towards higher frequency:thickness values is shown in fig. 7.4-*bottom right* than in the *top right* one. Now if we look to the sensitivity curve of mode S_3, with cut-off frequency proportional to c_T, we notice that the shift in fig. 7.4-*top right* although being small it is bigger than in the *bottom right* figure, as predicted.

Finally we notice that if only v is increased then a decrement in c_T, and an increment in c_L are expected. Again this is what we see as we compare figs. 7.4-*top left* and *bottom left*. Where all the modes with cut-off frequency proportional to c_L (for instance the modes S_2 and A_3) have an appreciable shift towards higher frequency:thickness product values, meanwhile the rest of modes with cut-off frequency proportional to c_T has a smaller shift to smaller frequency:thickness product values (as it happens with modes S_3 and A_1). Notice that the shift towards higher frequency:thickness product values of the sensitivity curves associated

to cut-off frequencies proportional to c_L is much bigger than the shift towards smaller frequency:thickness product values of those proportional to c_T by a given change in v. This is expected from the different changes in c_T and c_L as shown in fig. G.1.

REFERENCES

[1] Worlton D. C. *Ultrasonic testing with Lamb waves*, Non-Destructive Testing, vol. **15**, pp. 218-222, 1957.
[2] Worlton D. C. *Experimental confirmation of Lamb waves at Megacycles frequencies*, Journal of Applied Physics, vol. **32**, pp. 967-971, 1961.
[3] Rose J. L. *Ultrasonic waves in solid media*, Cambridge University Press, Cambridge, 1999.
[4] Achenbach J. D. *Wave propagation in elastic solids*, North Holland, Amsterdam, 1973.
[5] Graff K. F. *Wave motion in elastic solids*, Dover Publications, New York, 1991.
[6] Briggs A. *Acoustic Microscopy*, Oxford Science Publications, Oxford, 1992.
[7] Rayleigh L. *On waves propagated along the plane surface of an elastic solid*, Proc. Lond. Math. Soc., vol. **17**, pp. 4-11, 1885.
[8] Viktorov I. A. *Rayleigh and Lamb waves – Physical theory and applications*, Plenum Press, New York, 1967.
[9] Love A. E. H. *Some problems of geodynamics*, Cambridge University, London, 1911.
[10] Lamb H. *On waves in an elastic plate*, Proceedings of the Royal Society of London, Series A, vol. **93**, pp. 114-128, 1917.
[11] Brillouin L. *Wave propagation in periodic structures*, McGraw-Hill, New York, 1946.
[12] Meitzler A. H. *Backward-wave transmission of stress pulses in elastic cylinders and plates*, J. Acoust. Soc. Am., vol. **38**, pp. 835-842, 1965.
[13] Diligent O., *Interaction Between Fundamental Lamb Modes And Defects in Plates*, PhD Thesis, Imperial College, London, 2003.
[14] Rose J. L. *A baseline and vision of ultrasonic guided wave inspection potential*, Journal of pressure vessel technology, vol. **124**, pp. 273-282, 2002.
[15] Giurgiutiu V. and Cuc A. *Embedded non-destructive evaluation for structural health monitoring, damage detection and failure prevention*, The shock and vibration digest, vol. **37(2)**, pp. 83-105, 2005.
[16] Betz D. *Application of optical fibre sensors for Structural Health and usage monitoring*, PhD thesis, University of Sheffield, 2004.
[17] Scholte J. G. *The range of existence of Rayleigh and Stoneley waves*, Monthly Notices of the Royal Astronomical Soc., Geophysical Supp., vol.5, pp. 120-126, 1947.
[18] Stoneley R. *Elastic waves at the surface of separation of two solids*, Proceedings of the Royal Society of London, Series A, vol. **106**, pp. 416-428, 1924.
[19] Hsieh T. M., Lindgren E. A. and Rosen M. *Effect of interfacial properties on Stoneley wave propagation*, Ultrasonics, vol. **29(1)**, pp. 38-44, 1990.
[20] Staszewski W. J., Boller C., and Tomlinson G. R. *Health Monitoring of Aerospace Structures: Smart Sensor Technologies and Signal Processing*, Eds. Chichester: Jon Wiley & Sons Inc, 2003.
[21] Hull B., John V. *Nondestructive Testing*, Macmillan, UK, 1998.
[22] Munns J. and Georgiou *Non-destructive testing methods for adhesively bonded joint inspection - a review*, Insight, vol. **37(12)**, pp. 941-952, 1995.
[23] Khan M. A. U. *Non-destructive testing applications in commercial aircraft maintenance*, Proceedings of the 7th European Conference on Non-Destructive Testing, vol. **4**, 1999.
[24] Vest C. V. *Holographic interferometry*, John Wiley & Sons, New York, 1979.
[25] Miller R. K., McIntire P. *Non-Destructive Testing Handbook*, 2nd edition, Vol. 5: *Acoustic Emission Testing*, American Society for Non-Destructive Testing, 1987.
[26] Maldague X. *Introduction to NDT by Active Infrared Thermography*, Materials Evaluation vol. **6(9)**, pp. 1060-1073, 2002.

[27] Zweschper Th., Dillenz A., Riegert G. and Busse G. *Lockin thermography methods for the NDT of CFRP aircraft components*, NDT.net, vol. **8(2)**, 2003.
[28] Nieminen A. O. and Koenig J. L. *NMR imaging – a promising new adhesive evaluation technique*, J. Adhesion Sci. Technol., vol. **2** (6), pp. 407-414, 1988.
[29] Vallen H. *AE Testing Fundamentals,Equipment, Applications*, , NDT.net, vol. **7(9)**, 2002.
[30] Doebling S. W., Farrar C. R., Prime M. B. and Shevitz D. W. *Damage identification and Health Monitoring of structural and mechanical systems from changes in their vibration characteristics: a literature review*, Los Alamos National Laboratory, Technical report LA-13070-MS, 1996.
[31] Krautkramer J. and Krautkramer H. *Ultrasonic Testing of Materials*, Springer-Verlag, New York, 1990.
[32] Moulson A. J. and Herbert J. M. *Electroceramics: Materials, properties, applications*, Chapman & HallLondon, 1990.
[33] Thursby G., Sorazu B., Dong F., Betz D. and Culshaw B. *Damage Detection in Structural Materials using a Polarimetric Fibre Optic Sensor*, 10th International symposium on Smart Structures and Materials SPIE, 2003.
[34] Jones R. C. *A new calculus for the treatment of optical systems. I. Description and discussion of the calculus*, J. Opt. Soc. Am., vol. **31**, pp. 488-493, 1941.
[35] Kolsky H. *Stress waves in solids*, Dover Publications, New York, 1963.
[36] Morse P. M. and Feshbach H. *Methods of theoretical physics*, McGraw-Hill Book Company, pp. 52-53, 1953.
[37] Hamilton W. R., *Researches respecting vibration, connected with the theory of light*, Proc. Roy. Irish Acad., vol. **1**, pp. 341-349. (Accessible in www.emis.de/classics/Hamilton/VibLight.pdf)
[38] Stokes G. G. Smith's Prize examination, Cambridge, 1876. (Reprinted in Mathematics and Physics Papers, vol. **5**, pp. 362, Cambridge university Press, 1905)
[39] Miklowitz J *The theory of elastic waves and waveguides*, North-Holland, New York, 1978.
[40] http://www.mathpages.com/home/kmath210/kmath210.htm
[41] Woodley J. F. and Mojahedi M. *Negative group velocity and group in left-handed media*, Physical Review E, vol. **70**, pp. 046603-1 - 046603-6, 2004.
[42] Wang L.J., Kuzmich A. and Dogariu A. *Gain-assisted superluminal light propagation*, Nature, vol. **406**, pp. 277-279, 2000.
[43] Lamb H., On group-velocity, Proc. London Math. Soc., vol. **1**, pp. 473-479, 1904.
[44] Lowe M.J.S., Alleyne D. N. and Cawley P. *Defect detection in pipes using guided waves*, Ultrasonics, vol. **36**, pp. 147-154, 1998.
[45] Tolstoy I. and Usdin E *Wave propagation in elastic plates: Low and high modes dispersion*, J. of the Acous. Soc. Am., vol. **29(1)**, pp. 37-42, 1957.
[46] Werby M. F. and Uberall H. *The analysis and interpretation of some special properties of higher order symmetric Lamb waves: The case for plates*, J. Acous. Soc. Am., vol **111(6)**, pp. 2686-2691, 2002.
[47] Wolf J., Ngoc T. D. K., Kille R. and Mayer W. G. *Investigation of Lamb waves having a negative group velocity*, J. Acous. Soc. Am., vol. **83(1)**, pp. 122-126, 1988.
[48] Kessler S. S. and Spearing S. M. *Damage detection in built-up composite structures using Lamb wave methods*, Journal of Intelligent Material Systems and Structures, submitted 2005.
[49] Wilcox P., Lowe M. and Cawley P. *Long range Lamb wave inspection: The effect of dispersion and modal selectivity*, Review in Progress in Quantitative Nondestructive Evaluation, vol. **18**, pp. 151-158, 1999.
[50] Harris F. J. *On the use of windows for harmonic analysis with the discrete Fourier transform*, Proceedings of the IEEE, vol. **66(1)**, pp. 51-83, 1978.
[51] DeFatta D. J. *Digital signal processing:A system design approach*, J. Willey & Sons Ltd. 1988.

LIST OF PUBLICATIONS

B. Sorazu, G. Thursby, B. Culshaw, F. Dong, S. G. Pierce, Y. Yao and D. Betz *Optical generation and detection of ultrasounds*, Journal of Strain, vol. 39 (3), pp. 111-114, 2003.

B. Sorazu, G. Thursby, Brian Culshaw and F. Dong *Ultrasonic wavefront integration using interferometric optical fiber sensors*, Smart Structures and Materials 2003: Smart Sensor Technology and Measurement Systems, Edited by Inaudi, Daniele; Udd, Eric. Proceedings of the SPIE, vol. 5050, pp. 23-33, 2003.

B. Sorazu, G. Thursby, B. Culshaw and F. Dong *Wavefront integration optical fibre sensors for damage detection using ultrasound techniques*, Proceedings of 16th International Conference on Optical Fibre Sensors, ISBN 4-89114-036-4, pp. 222-225, Nara (Japan), 13-17 October, 2003.

B. Sorazu, B. Culshaw, S. G. Pierce, et. al. *Optically non-contact extraction of the elastic properties of materials*, 2nd European Workshop on Optical Fibre Sensors. Edited by Lopez-Higuera, Jose M.; Culshaw, Brian. Proceedings of the SPIE, vol. 5502, pp. 204-207, 2004.

B. Sorazu, B. Culshaw and G. Pierce *Optical technique for examining materials' elastic properties*, Smart Structures and Materials 2005: Smart Sensor Technology and Measurement Systems. Edited by Udd, Eric; Inaudi, Daniele. Proceedings of the SPIE, vol. 5758, pp. 177-188, 2005.

B. Sorazu, B. Culshaw and S. Atique *Inversion technique for an all-optical inspection of material's elastic properties*, Smart Structures and Materials 2006: Smart Sensor Monitoring Systems and Applications. Edited by Inaudi, Daniele; Ecke, Wolfgang; Culshaw, Brian; Peters, Kara J.; Udd, Eric. Proceedings of the SPIE, vol. 6167, pp. 166-177, 2006.

B. Sorazu, S. Atique, B. Culshaw and G. Thursby *A non-contact method of determining material properties and structural integrity through the analysis of laser generated ultrasound*, Proceedings of 3rd European Workshop on Structural Health Monitoring, Edited by Alfredo Güemes, ISBN: 1-932078-63-0, Granada (Spain) 5-7 July, 2006.

The author has also contributed to the following publications:

G. Thursby, F. Dong, Y. Yong, B. Sorazu, D. Betz and B. Culshaw .*Fibre optic polarimetric detection of lamb waves*, Proceedings of 15th Optical Fiber Sensors Conference Technical digest 2002 (OFS 2002), ISBN: 0-7803-7289-1, vol. 1, pp. 321-324, 2002.

G. Thursby, B. Sorazu, F. Dong , D. Betz and B. Culshaw *Damage Detection in Structural Materials using a Polarimetric Fibre Optic Sensor*, Smart Structures and Materials 2003: Smart Sensor Technology and Measurement Systems, Edited by Inaudi, Daniele; Udd, Eric. Proceedings of the SPIE, Vol. 5050, pp. 61-70, 2003.

F. Dong, G. Thursby, B. Sorazu and B. Culshaw *RF sub-carrier based fibre strain sensor for lifetime monitoring on carbon fibre composite pressure vessels*, Proceedings of 16th International Conference on Optical Fibre Sensors, ISBN 4-89114-036-4, pp. 444-447, Nara (Japan), 13-17 October, 2003.

G. Thursby, B. Sorazu *Comparison of point and integrated fibre optic sensing techniques for ultrasound detection and location of damage*, Smart Structures and Materials 2004: Smart Sensor Technology and Measurement Systems, Edited by Inaudi, Daniele; Udd, Eric. Proceedings of the SPIE, vol. 5384, pp. 287-295, 2004.

G. Thursby, B. Culshaw, B. Sorazu, S Atique and F Dong *Non-contact material evaluation for characterization and wear detection using laser-generated ultrasound and interferometric ultrasonic detection*, Smart Structures and Materials 2004: Smart Sensor Technology and Measurement Systems, Edited by Inaudi, Daniele; Udd, Eric. Proceedings of the SPIE, vol. 5384, pp. 296-304, 2004.

S. Atique, B. Culshaw, G. Thursby, F. Dong, B. Sorazu and H. S. Park *Generation of ultrasound for material testing using low power diode laser*, Proceedings of 2nd European Workshop on Structural Health Monitoring, Edited by Christian Boller & Wieslaw J. Staszewski, ISBN 1-932078-41-X, pp. 933-940 Munich (Germany) 7-9 July, 2004.

G. Thursby, B. Sorazu, D. Betz, W. Staszewski and B. Culshaw *The Use of Fibre Optic Sensors for Damage Detection and Location in Structural Materials*, Applied Mechanics and Materials (ISSN: 1660-9336), vols. 1-2, pp. 191-196, 2004.

S. Atique, D. Betz, B. Culshaw, F. Dong, H. S. Park, B. Sorazu and G. Thursby *Detecting ultrasound using optical fibres*, Journal of Optics (India), vol. 33(4), pp. 239-253, 2004.

G. Thursby, B. Sorazu, D. Betz and B. Culshaw *Novel methods of Lamb wave detection for material damage detection and location*, Health Monitoring and Smart Nondestructive Evaluation of Structural and Biological Systems IV. Edited by Kundu, Tribikram. Proceedings of the SPIE, vol. 5768, pp. 313-322, 2005.